

# Universidade de Vigo



---

## **Acidification and transports of water masses and CO<sub>2</sub> in the North Atlantic**

---

Memoria para optar al grado de Doctora por la  
Universidad de Vigo con Mención  
Internacional presentada por la Licenciada en  
Ciencias del Mar:

**María Isabel García Ibáñez**

PhD Thesis

Tesis Doctoral

Vigo, Mayo 2015





El Profesor de Investigación del Departamento de Oceanografía del Instituto de Investigaciones Marinas (IIM) perteneciente al Consejo Superior de Investigaciones Científicas (CSIC), **Dr. Fiz Fernández Pérez**, en calidad de director de esta Tesis Doctoral,

#### HACE CONSTAR

que la presente memoria, titulada “**Acidification and transports of water masses and CO<sub>2</sub> in the North Atlantic**”, presentada por la Lcda. en Ciencias del Mar **María Isabel García Ibáñez** para optar al grado de Doctora por la Universidad de Vigo con Mención Internacional, ha sido realizada bajo su dirección, cumpliendo con las condiciones exigidas para su presentación, la cual autoriza.

Y para que así conste y surta los efectos oportunos, firma la presente en Vigo, 7 de mayo de 2015.

Prof. Dr. Fiz Fernández Pérez







Memoria de Tesis presentada por la Lcda. en Ciencias del Mar **María Isabel García Ibáñez** para optar al grado de Doctora por la Universidad de Vigo con Mención internacional.

La presente Tesis Doctoral fue realizada dentro del Grupo de Oceanología (Departamento de Oceanografía) del Instituto de Investigaciones Marinas (IIM) perteneciente al Consejo Superior de Investigaciones Científicas (CSIC). María Isabel García Ibáñez fue beneficiaria de una beca predoctoral de Formación de Personal Investigador (FPI-MICINN) del Programa Nacional de Formación de Recursos Humanos de Investigación, en el marco del Plan Nacional de Investigación Científica, Desarrollo e Innovación Tecnológica 2008–2011, financiada por el Gobierno de España a través del Ministerio de Economía y Competitividad. Los trabajos recogidos en esta memoria se desarrollaron dentro del proyecto “Carbon Transport and Acidification Rates In the North Atlantic” (CATARINA) (CTM2010-17141) financiado por el Ministerio de Ciencia e Innovación, cofinanciado por el Fondo Europeo de Desarrollo Regional 2007–2012 (FEDER). Esta Tesis Doctoral se enmarca dentro del programa de doctorado “Marine Science, Technology and Management” (DO\*MAR) de la Universidad de Vigo.

Vigo, 7 de mayo de 2015







## TABLE OF CONTENTS

<b>RESUMEN</b> .....	1
<b>AGRADECIMIENTOS</b> .....	7
<b>PART I.- INTRODUCTION</b> .....	9
<b>Chapter 1.- Introduction</b> .....	11
1.1.- General Background.....	13
1.2.- Physical Perspective: The North Atlantic Ocean .....	16
1.2.1.- Topographic features .....	17
1.2.2.- Large-scale circulation .....	18
1.2.2.1.- Surface Currents .....	18
1.2.2.2.- Deep-ocean Currents or the Meridional Overturning Circulation .....	21
1.2.3.- Water masses .....	22
1.2.4.- The North Atlantic Oscillation (NAO).....	26
1.3.- Chemical Perspective: The seawater CO <sub>2</sub> system.....	29
1.3.1.- The role of the CO <sub>2</sub> in the ocean .....	29
1.3.1.1.- Variables of the seawater CO <sub>2</sub> system .....	31
1.3.2.- Ocean Acidification.....	34
1.3.3.- Anthropogenic Carbon and Seawater .....	36
<b>PART II.- AIM OF THE STUDY AND DATA</b> .....	43
<b>Chapter 2.- Acidification and transports of water masses and CO<sub>2</sub> in the North Atlantic: Aim of the PhD</b> .....	45
<b>Chapter 3.- Oceanographic cruises in the North Atlantic</b> .....	47
3.1.- WOCE A25 section.....	49
3.1.1.- Measurements.....	50
3.1.1.1.- CTD measurements .....	51
3.1.1.2.- Oxygen (O <sub>2</sub> ) sampling and measurement .....	51
3.1.1.3.- Total dissolved inorganic carbon (C <sub>T</sub> ) sampling and measurement .....	52
3.1.1.4.- pH sampling and measurement .....	52
3.1.1.5.- Total alkalinity (A <sub>T</sub> ) sampling and measurement .....	53
3.1.1.6.- Nutrients sampling and measurement .....	54
3.1.1.7.- Salinity (S) sampling and measurement .....	54
3.1.1.8.- Acoustic Doppler Current Profiler (ADCP) measurements .....	55

<b>PART III.- RESULTS AND DISCUSSION .....</b>	<b>57</b>
<b>Chapter 4.- Structure, transports and transformations of the water masses in the Atlantic Subpolar Gyre.....</b>	<b>59</b>
4.1.- Resumen .....	59
4.2.- Abstract .....	59
4.3.- Introduction .....	60
4.4.- Data and methods .....	62
4.4.1.- Biogeochemical data.....	62
4.4.2.- Optimum MultiParameter (OMP) analysis.....	63
4.4.2.1.- Water mass characterization .....	63
4.4.2.2.- Methodology of the analysis .....	68
4.4.3.- Velocity field .....	72
4.4.4.- Combining the water mass distributions with the velocity fields.....	73
4.5.- Water mass distributions for the first decade of the 2000s .....	73
4.5.1.- Upper waters .....	75
4.5.2.- Intermediate waters.....	75
4.5.3.- Overflows and deep waters.....	76
4.6.- Time variability of the water mass distributions between 1997 and 2010.....	77
4.7.- Water mass volume transports, recirculation and transformations in the Subpolar North Atlantic .....	80
4.8.- Conclusions .....	86
<b>Chapter 5.- Observed trends of the stressors of the CO<sub>2</sub> system in the Irminger and Iceland Basins .....</b>	<b>89</b>
5.1.- Resumen .....	89
5.2.- Abstract .....	90
5.3.- Introduction .....	91
5.4.-Material and Methods.....	92
5.4.1.- Dataset .....	92
5.4.2.- pH change deconvolution: anthropogenic and non-anthropogenic components .....	95
5.4.3.- Water mass characterization .....	96
5.5.- Temperature, Salinity and AOU fields.....	97
5.6.- Alkalinity trends .....	102
5.7.- C <sub>ANT</sub> trends .....	103
5.8.- Acidification trends .....	107
5.9.- Changes in the CaCO <sub>3</sub> saturation horizon.....	110
5.10.- Future changes in the variables of the seawater CO <sub>2</sub> system.....	112
5.11.- Conclusions .....	113

<b>Chapter 6.- Variability of the transport of anthropogenic CO<sub>2</sub> at the Greenland–Portugal OVIDE section: controlling mechanisms</b> .....	115
6.1.- Resumen .....	115
6.2.- Abstract .....	115
6.3.- Introduction .....	116
6.4.- Data sets .....	118
6.5.- Method: transport of anthropogenic CO <sub>2</sub> and its decomposition.....	123
6.6.- Results .....	124
6.6.1.-Transport of anthropogenic CO <sub>2</sub> across the Greenland–Portugal section ....	124
6.6.2.- Decomposition of the transport of anthropogenic CO <sub>2</sub> across the Greenland–Portugal section.....	125
6.6.3.- Variability of the transport of anthropogenic CO <sub>2</sub> .....	128
6.6.3.1.- Variability of the components of the T <sub>CANT</sub> .....	129
6.6.3.2.- A simplified estimator for the variability of the T <sub>CANT</sub> .....	129
6.6.3.3.- The effect of the anthropogenic CO <sub>2</sub> concentration changes on the variability of the T <sub>CANT</sub> .....	131
6.7.- Discussion and conclusions.....	132
<b>PART IV.- SUMMARY AND CONCLUSIONS</b> .....	137
<b>Capítulo 7.- Resumen y conclusiones</b> .....	139
7.1.- Capítulo 4: Estructura, transportes y transformaciones de las masas de agua del Giro Subpolar del Atlántico.....	139
7.2.- Capítulo 5: Tendencias observadas en los factores de estrés del sistema del CO <sub>2</sub> en las cuencas del Irminger e Islandia. ....	141
7.3.- Capítulo 6: Variabilidad del transporte de CO <sub>2</sub> antropogénico en las secciones OVIDE entre Groenlandia y Portugal: mecanismos controladores.....	142
<b>REFERENCES</b> .....	145
<b>APPENDIX</b> .....	167
<b>Appendix A.- Acronyms, abbreviations and symbols</b> .....	169
<b>Appendix B.- List of Tables</b> .....	175
<b>Appendix C.- List of Figures</b> .....	177





## UNIVERSIDADE DE VIGO

RESUMENTesis Doctoral**Acidification and transports of water masses and CO<sub>2</sub> in the North Atlantic**por **María Isabel García Ibáñez**

La atmósfera de la Tierra contiene gases que absorben la radiación infrarroja, los cuales son conocidos como gases de efecto invernadero. Entre ellos destaca el dióxido de carbono (CO<sub>2</sub>). Las actividades antropogénicas, es decir, las actividades humanas, han ido aumentando paulatinamente la concentración de este gas en la atmósfera desde la Revolución Industrial (1750). Las emisiones antropogénicas de CO<sub>2</sub> alteran el ciclo natural del carbono que lo redistribuye entre la atmósfera, el océano y las tierras emergidas. La absorción de CO<sub>2</sub> por el océano ha limitado el aumento de su concentración en la atmósfera y, por tanto, el calentamiento debido a los gases de efecto invernadero. Pero esta absorción ha dado lugar a una serie de cambios químicos conocidos colectivamente como acidificación oceánica, entre los que se incluyen la disminución del pH y del grado de saturación de carbonatos. Estos cambios pueden modificar los principales ciclos biogeoquímicos marinos, por lo que la acidificación oceánica tiene el potencial de afectar dramáticamente a organismos y ecosistemas marinos. La principal inquietud del colectivo científico es la tasa de cambio de pH, que supera cualquiera conocida durante los últimos cientos de miles de años. Estos cambios son tan rápidos que pueden reducir de forma significativa la capacidad tampón de los procesos naturales que han amortiguado los cambios en la química de los océanos en la mayor parte del tiempo geológico. Esta alta tasa de cambio también podría dar lugar a que ciertas especies formadoras de estructuras calcáreas no puedan adaptarse lo suficientemente rápido como para sobrevivir, alterando así las redes tróficas marinas.

Aunque la acidificación oceánica tiene lugar en los océanos de todo el mundo, existen marcadas diferencias regionales debido a los diferentes procesos que afectan al sistema del CO<sub>2</sub> oceánico. Por ejemplo, los efectos de la acidificación oceánica tienden a ser más severos en los océanos de latitudes altas debido a las bajas temperaturas de sus aguas superficiales (que propician una mayor disolución del CO<sub>2</sub> atmosférico), en combinación con sus altos factores de Revelle, es decir, a su baja capacidad tampón (que da lugar a mayores cambios de pH para una perturbación de CO<sub>2</sub> atmosférico dada). De hecho, las aguas al norte de Islandia están acidificándose a una tasa del 5% por década, mientras que las aguas del Océano Pacífico Norte occidental (al sur de Japón) lo hacen a una tasa del 3% por década. Por otra parte, mientras que la concentración de CO<sub>2</sub> en las capas superficiales del océano aumenta conforme lo hace el CO<sub>2</sub> en la atmósfera, su penetración en el océano profundo depende de la lenta mezcla vertical de la columna de agua y del transporte de las masas de agua. Alrededor de la mitad del CO<sub>2</sub> antropogénico se encuentra en los primeros 400 m de la columna de agua, mientras que la otra mitad penetra hacia las capas más profundas. Sin embargo, en algunas regiones donde los movimientos verticales son relativamente rápidos, como es el caso del Atlántico Norte Subpolar, la escala de tiempo necesaria para la penetración profunda del CO<sub>2</sub> antropogénico es del orden de décadas en lugar de siglos, por lo que la exposición a los efectos de la acidificación oceánica de origen antropogénico es más rápida.

El Atlántico Norte lleva siendo un sumidero de CO<sub>2</sub> desde antes de la Revolución Industrial debido a la acción de la circulación termohalina. La circulación termohalina es el resultado de los cambios de densidad que sufren las aguas oceánicas. En el Océano Atlántico las aguas superficiales del Hemisferio Sur fluyen hasta las latitudes polares del Hemisferio Norte en la rama superior de la circulación termohalina del Atlántico. Debido a los largos tiempos de residencia en las regiones subtropicales y ecuatoriales, las frías aguas procedentes del Hemisferio Sur se calientan y salinizan, y llegan prácticamente a estar en equilibrio con las concentraciones de CO<sub>2</sub> atmosférico. Al norte de alrededor de los 15–20°N, estas aguas comienzan a enfriarse al ser transportadas hacia el norte por la Corriente del Golfo, tendiendo a captar más CO<sub>2</sub> atmosférico. Gran parte de estas aguas alcanzan el Giro Subpolar del Atlántico Norte, el Mar de Labrador, el Océano Ártico y los mares nórdicos, donde se densifican lo suficientemente como para hundirse y comenzar un viaje sub-superficial hacia el sur en corrientes de fondo que conforman la rama inferior de la circulación termohalina del Atlántico, proceso conocido como circulación de retorno. El efecto neto de la circulación de retorno y de la ventilación termoclina es la captación de CO<sub>2</sub> atmosférico y la liberación de calor hacia la atmósfera. Por lo tanto, la circulación termohalina juega un papel fundamental en la regulación del clima terrestre.

Todo lo anteriormente expuesto motivó el estudio de la acidificación y la circulación del Atlántico Norte llevado a cabo en esta tesis. Concretamente, se estudiaron la acidificación y los transportes de masas de agua y de CO<sub>2</sub> en el Giro Subpolar del Atlántico Norte. Los resultados de los estudios que conforman la presente tesis doctoral se estructuraron en tres grandes apartados. El primero apartado recoge los resultados del estudio de la distribución de las principales masas de agua del Giro Subpolar del Atlántico Norte, y su variabilidad entre 1997 y 2010; así como de la estimación de los transportes de las principales masas de agua y sus transformaciones dentro del Giro Subpolar. El segundo apartado recoge los resultados de la evaluación de la captación de CO<sub>2</sub> de origen antropogénico, y los cambios químicos derivados de ésta en las principales masas de agua de las cuencas del Irminger e Islandia durante el periodo 1981–2014. Por último, el tercer apartado recoge los resultados del estudio del transporte del CO<sub>2</sub> de origen antropogénico en el Atlántico Norte Subpolar entre 1997 y 2010, poniendo el foco en comprender los mecanismos que controlan su variabilidad.

Un componente importante de la circulación termohalina global se lleva a cabo en las altas latitudes del Atlántico Norte. Los procesos de formación de masas de agua en el Atlántico Norte Subpolar, el Mar de Labrador, el Océano Ártico y los mares nórdicos afectan a la circulación termohalina del Atlántico en escalas de tiempo largas. La Oscilación del Atlántico Norte (NAO), el modo dominante de la variabilidad atmosférica en la región subpolar del Atlántico Norte, influye en la formación de las masas de agua y, por lo tanto, en la intensidad de la circulación termohalina del Atlántico. En consecuencia, conocer la distribución de las masas de agua, su transporte y transformación es importante para determinar el efecto de los cambios en la circulación oceánica en la captación y almacenamiento del CO<sub>2</sub> de origen antropogénico. En el primer apartado de esta tesis se discuten la distribución y el transporte de las principales masas de agua en la región subpolar del Atlántico Norte, concretamente en el Giro Subpolar, para la primera década de los 2000 (2002–2010); así como la variabilidad interanual en la estructura de las masas de agua entre 1997 y 2010. Las distribuciones de las principales masas de agua del Giro Subpolar del Atlántico Norte, cuantitativamente evaluadas por medio de un análisis multiparamétrico optimizado (OMP), se combinaron con los campos de velocidad (derivados de

modelos inversos previamente resueltos) con el fin de obtener los transportes de volumen de las masas de agua. También se evaluó la contribución relativa a la circulación termohalina del Atlántico de las principales masas de agua que caracterizan el Giro Subpolar del Atlántico Norte, identificando qué masas de agua contribuyeron a la variabilidad de la circulación termohalina del Atlántico entre 1997 y la década de los 2000. Este lapso temporal estuvo marcado por la transición entre un alto índice NAO (con una circulación horizontal asociada más intensa) y un índice NAO neutro/bajo (con una circulación horizontal asociada más débil). La reducción de la intensidad de la rama superior de la circulación termohalina del Atlántico entre 1997 y la década de los 2000 se asocia con la reducción en el transporte hacia el norte de las Aguas Centrales. Esta reducción del transporte hacia el norte de la rama superior de la circulación termohalina del Atlántico queda parcialmente compensada con la reducción del transporte hacia el sur de la rama inferior, asociada con la disminución de los transportes de Agua Polar Intermedia y Agua Modal Subpolar en la cuenca del Irminger. También se dedujo la transformación de las masas de agua dentro del Giro Subpolar del Atlántico Norte en base a un modelo de cajas. Las Aguas Centrales ( $2,1 \pm 1,8$  Sv;  $1 \text{ Sv} = 10^6 \text{ m}^3 \cdot \text{s}^{-1}$ ), el Agua del Mar de Labrador ( $2,4 \pm 2,0$  Sv), el Agua Intermedia Subártica ( $4,0 \pm 0,5$  Sv) y el Agua de desbordamiento de Islandia–Escocia ( $0,9 \pm 0,9$  Sv) circulan desde la cuenca Este del Atlántico Norte hacia la cuenca del Irminger por encima del Reykjanes Ridge. Una vez llegadas a la cuenca del Irminger, estas masas de agua se transforman y/o densifican, pasando de la zona de aguas superiores e intermedias a la zona de aguas profundas. Los resultados también dan información acerca de las transformaciones de las Aguas Centrales (1,1 Sv) y el Agua Intermedia Subártica (2,2 Sv) en las diferentes variedades de Agua Modal Subpolar.

La acidificación del océano provoca cambios en el equilibrio del sistema del CO<sub>2</sub> oceánico, afectando a todas las especies químicas y a todos los parámetros medibles salvo uno. Concretamente aumenta el carbono inorgánico disuelto total (C<sub>T</sub>), la presión parcial de CO<sub>2</sub> (pCO<sub>2</sub>) y las concentraciones de CO<sub>2</sub>, iones bicarbonato (HCO<sub>3</sub><sup>-</sup>) y protones (H<sup>+</sup>); disminuye la concentración de iones carbonato (CO<sub>3</sub><sup>2-</sup>) y el pH ( $-\log_{10}[\text{H}^+]$ ); mientras que la alcalinidad total (A<sub>T</sub>) no cambia. En el segundo apartado de esta tesis se evaluaron las tendencias temporales en la captación del CO<sub>2</sub> antropogénico y sus efectos sobre el pH y la saturación de CaCO<sub>3</sub>, así como los cambios en la A<sub>T</sub> en las cuencas del Irminger e Islandia durante los tres últimos decenios, concretamente durante el periodo 1981–2014. Los cambios a largo plazo de la concentración del CO<sub>2</sub> antropogénico, del pH, la A<sub>T</sub> y la saturación de CaCO<sub>3</sub>, esta última en términos de saturación de aragonito ( $\Omega_{\text{Arag}}$ ), se evaluaron en las principales masas de agua de las cuencas del Irminger e Islandia y se discutieron en el contexto de la circulación oceánica. Se observa que las aguas de las cuencas del Irminger e Islandia están ganando CO<sub>2</sub> de origen antropogénico, lo que da lugar a que todas las masas de agua del Giro Subpolar del Atlántico Norte presenten tasas de acidificación significativas. Las mayores tasas de aumento de la concentración del CO<sub>2</sub> antropogénico se encuentran en las capas superiores de ambas cuencas, como resultado de su contacto directo con la atmósfera, lo que se traduce en unas tasas de descenso del pH de  $-0.011 \pm 0.002$  unidades de pH por década en ambas cuencas. Las aguas profundas de la cuenca del Irminger presentan unas tasas de acidificación muy similares a las de las capas superficiales, resultado de su reciente contacto con la atmósfera. La columna de agua de la cuenca del Irminger presenta unas tasas de aumento de la concentración de CO<sub>2</sub> de origen antropogénico mayores que las encontradas en la cuenca de Islandia, lo que refleja la mayor proximidad de la cuenca del Irminger a las zonas de formación de masas de agua. Estas mayores tasas dan lugar a unos descensos de pH mayores en la cuenca del Irminger que los encontrados en la cuenca de Islandia. Para estudiar las causas de los cambios de

pH se evaluaron sus componentes antropogénico (derivado de la captación del CO<sub>2</sub> antropogénico;  $\Delta\text{pH}_{\text{C}_{\text{ANT}}}$ ) y no antropogénico (no directamente relacionado con la captación de CO<sub>2</sub> antropogénico;  $\Delta\text{pH}_{\text{V}_{\text{AR}}}$ ). En estado estacionario, el término  $\Delta\text{pH}_{\text{V}_{\text{AR}}}$  sería constante y todos los cambios de pH se explicarían por el término  $\Delta\text{pH}_{\text{C}_{\text{ANT}}}$ . Sin embargo, en las capas superiores de ambas cuencas la acción del  $\Delta\text{pH}_{\text{V}_{\text{AR}}}$  (debida a la advección de aguas subtropicales) contrarresta el efecto del  $\Delta\text{pH}_{\text{C}_{\text{ANT}}}$ , dando lugar a que las tasas de acidificación observadas sólo representen un 72–87% de las tasas esperadas derivadas de la captación de CO<sub>2</sub> de origen antropogénico. En cambio, en las aguas intermedias de la cuenca del Irminger, el efecto del  $\Delta\text{pH}_{\text{V}_{\text{AR}}}$  (producido por el envejecimiento de las aguas) refuerza la acidificación derivada de la captación del CO<sub>2</sub> antropogénico, lo que da lugar a que la tasa de acidificación de estas aguas sea un 34% mayor que la esperada por la acción del  $\Delta\text{pH}_{\text{C}_{\text{ANT}}}$ . Los descensos de pH observados dan lugar a que la  $\Omega_{\text{Arag}}$  muestre tendencias de descenso significativas en todas las masas de agua de ambas cuencas. Las aguas intermedias de ambas cuencas presentan unas tasas de descenso de la  $\Omega_{\text{Arag}}$  de entre  $-2,4$  y  $-3,8 \cdot 10^{-3} \text{ año}^{-1}$ , lo que da lugar a un ascenso del horizonte de saturación de  $\sim 10 \text{ m} \cdot \text{año}^{-1}$ . En base a los cambios de pH y de  $\Omega_{\text{Arag}}$  observados durante el periodo 1981–2014, se infirieron los cambios esperados para final de siglo. Cuando la concentración de CO<sub>2</sub> atmosférico alcance los 800 ppm se espera que el pH de las capas superiores descienda  $\sim 0,31$  unidades de pH respecto a los valores de la era preindustrial. Las capas profundas de la cuenca del Irminger sufrirán descensos de pH similares a los de las capas superficiales. Estos descensos de pH alcanzados cuando la concentración de CO<sub>2</sub> atmosférico sea de 800 ppm darán lugar a que toda la columna de agua de las cuencas del Irminger e Islandia esté sub-saturada en aragonito. Sin embargo, las aguas intermedias alcanzarán el estado de sub-saturación mucho antes, concretamente cuando la concentración de CO<sub>2</sub> atmosférico alcance los 500 ppm. Esta somerización del horizonte de saturación de las aguas del Atlántico Norte podría tener consecuencias nefastas para las poblaciones de corales de aguas frías que las habitan. Los datos aquí recopilados también muestran la influencia del aumento de la descarga de los ríos árticos en la  $A_T$  de las aguas profundas de la cuenca del Irminger, que presentan unas tendencias significativas de aumento de la  $A_T$ .

El Atlántico Norte se comporta como un sumidero de CO<sub>2</sub>, sin embargo no todo el CO<sub>2</sub> que almacena es de origen antropogénico. En las latitudes medias del Atlántico Norte, los intercambios de CO<sub>2</sub> entre la atmósfera y el océano están dominados por el componente antropogénico; mientras que en la región subpolar del Atlántico Norte los intercambios de CO<sub>2</sub> están dominados por el componente natural, derivado de los procesos naturales del sistema terrestre. Es decir, la absorción de CO<sub>2</sub> de origen antropogénico se produce casi exclusivamente en el giro subtropical, siendo luego lateralmente advechado hacia la región subpolar del Atlántico Norte, constituyendo este transporte lateral el principal suministro de CO<sub>2</sub> antropogénico del Atlántico Norte Subpolar. Otro elemento importante en el almacenamiento de CO<sub>2</sub> de origen antropogénico en el Atlántico Norte Subpolar es la advección de masas de agua recién ventiladas como el Agua del Mar de Labrador. Por lo tanto, es importante cuantificar y comprender la forma en que se transporta el CO<sub>2</sub> antropogénico para así comprender cómo el océano lo almacena, y para modelar el papel del océano en la amortiguación del futuro aumento del CO<sub>2</sub> atmosférico causado por las actividades humanas. En el tercer y último apartado de esta tesis se investiga la variabilidad interanual a decenal en el transporte de CO<sub>2</sub> antropogénico a través del Atlántico Norte Subpolar durante el período 1997–2010. Este apartado se ha centrado en el estudio del aspecto físico del transporte de CO<sub>2</sub> antropogénico en el Atlántico Norte Subpolar con el fin de comprender los mecanismos que lo controlan. Se obtuvo un transporte promedio de CO<sub>2</sub>

antropogénico de  $254 \pm 29 \text{ kmol}\cdot\text{s}^{-1}$  para el período 1997–2010. Para evaluar el efecto de los diferentes elementos de la circulación oceánica en el transporte de CO<sub>2</sub> antropogénico, éste se dividió en sus componentes diapícnico (el transporte de CO<sub>2</sub> antropogénico a través de las isopícnas) e isopícnico (el transporte de CO<sub>2</sub> antropogénico a lo largo de las isopícnas). La concentración de CO<sub>2</sub> antropogénico juega un papel importante en los dos componentes implicados en el transporte de CO<sub>2</sub> de origen antropogénico: el gradiente horizontal de CO<sub>2</sub> antropogénico en el Atlántico Norte Subpolar es el responsable de su transporte isopícnico hacia el sur, principalmente en las aguas intermedias y profundas de la cuenca del Irminger; mientras que el flujo hacia el norte de las aguas cargadas de CO<sub>2</sub> antropogénico es el responsable del alto transporte diapícnico de CO<sub>2</sub> antropogénico hacia el norte. La descomposición del transporte de CO<sub>2</sub> antropogénico en sus diferentes componentes también muestra que el componente de diapícnico es su principal contribuyente, cuyo valor medio durante el período 1997–2010 es de  $400 \pm 29 \text{ kmol}\cdot\text{s}^{-1}$ , además de ser el principal responsable de la variabilidad del transporte de CO<sub>2</sub> antropogénico a través del Atlántico Norte Subpolar. Tanto la intensidad de la circulación termohalina como el aumento del CO<sub>2</sub> antropogénico en la columna de agua afectan de forma importante a la variabilidad del componente diapícnico y al propio transporte de CO<sub>2</sub> antropogénico. A escalas de tiempo interanuales a decenales, la variabilidad de la circulación termohalina domina la variabilidad del transporte de CO<sub>2</sub> antropogénico, pero a escalas de tiempo mayores es el aumento del CO<sub>2</sub> antropogénico el que parece controlar el cambio del transporte de CO<sub>2</sub> antropogénico, siendo muy probable que esto cause un aumento del transporte de CO<sub>2</sub> antropogénico a través del Atlántico Norte Subpolar conforme vaya aumentando la concentración de CO<sub>2</sub> en la atmósfera.

El continuo aumento de la concentración de CO<sub>2</sub> en la atmósfera debido a las actividades humanas ha sido suavizado por la absorción oceánica. Pero, ¿cuánto tiempo va a seguir actuando el océano como sumidero de este gas de efecto invernadero? y ¿qué consecuencias se esperan de esta absorción de CO<sub>2</sub>? La absorción de CO<sub>2</sub> en el Giro Subpolar del Atlántico Norte da lugar a tasas de acidificación significativas en toda la columna de agua, que producen una somerización del horizonte de saturación del CaCO<sub>3</sub>. Se espera que la concentración de CO<sub>2</sub> antropogénico en ambas ramas de la circulación termohalina del Atlántico se vincule a la variabilidad de la circulación termohalina, pero la escala de tiempo necesaria para ello depende de la advección de aguas subtropicales en la rama superior, y de los procesos de formación de aguas intermedias y profundas en la rama inferior. Extrapolando el aumento de la diferencia de concentración de CO<sub>2</sub> antropogénico observado en ambas ramas de la circulación termohalina del Atlántico y considerando la desaceleración del 25% de la circulación termohalina prevista para el año 2100, se espera que el transporte de CO<sub>2</sub> antropogénico a través del Atlántico Norte Subpolar aumente en  $430 \text{ kmol}\cdot\text{s}^{-1}$  durante el siglo XXI. En consecuencia, se podría producir un aumento en la tasa de almacenamiento de CO<sub>2</sub> antropogénico en el Atlántico Norte Subpolar, lo que conllevaría a un aumento de las tasas de acidificación de sus aguas.



## ***AGRADECIMIENTOS***

---

Gracias a todos aquellos y aquellas que me han alentado, aconsejado, animado, reconfortado... durante estos cuatro años. Sin vuestro apoyo esta tesis no habría sido un éxito.

En primer lugar me gustaría agradecer al director de esta tesis, Dr. D. Fiz Fernández Pérez su capacidad de trabajo, paciencia, comprensión y confianza durante estos años. Gracias por tu orientación y ayuda, por transmitirme el amor por la ciencia, por tu disponibilidad fuera la hora que fuera, y por todo lo que me he has enseñado. Sin tu guía este camino no habría sido lo mismo. Gracias también a Dra. D<sup>a</sup> Aida Fernández Ríos por tener siempre un momento y una sonrisa, y por ser el tercer punto de apoyo de esta tesis.

A los compañeros del Grupo de Oceanología del Instituto de Investigaciones Marinas de Vigo (CSIC), por el ambiente genial que siempre hay en el laboratorio, por las risas y por el compañerismo que han hecho que cada día de trabajo haya sido estupendo. Gracias a todos y cada uno, tanto los que siguen aquí: Antón, Carmen, Des, Fer, Isabel, Mar, María, Miguel, Rocío, Rosa, Trini, Vane... como a los que ya se fueron: Javi, Kico, Mónica, Nico, Eva... Gracias por esos riquísimos dulces a la hora del café rodeados de gente aún más dulce, por la recopilación de frases míticas, por los rankings de colesterol y por tantos otros momentos compartidos. Un gracias enorme a mis “niñas CSIC” que se han convertido en grandes amigas: Alba María y Alba Marina, Clara, Elisa, Eva, Lidia, Noe, Bea y Pau. Gracias por todos los momentos compartidos y por siempre estar ahí con una sonrisa cuando más lo necesitaba. Gracias por hacerme parte de vuestras vidas, me siento muy afortunada de haberos encontrado en mi camino. Gracias a Alba María por compartir el desasosiego del programa de doctorado y por tus ánimos en la recta final. Gracias a Alba Marina por ser esa estupenda compi de camarote durante mi primera campaña y por tus recetas colombianas. Gracias a Clari por tu humor ácido, por tus millones de emoticonos en las conversaciones que siempre me sacan una sonrisa y por ser la mejor organizadora de planes de nenis. Gracias a Elisa por alegrarnos con cada una de tus visitas y por haberte convertido en una más aun estando lejos. Gracias a Eva por los planes de fin de semana que me ayudaron a desconectar y por siempre buscar ese rallito de sol que tanto escasea aquí en Galicia. Gracias a Lidia por allanarme el camino en el grupo LPO y por ser tan agradable aunque siempre digas que eres un poco “toxiño”. Gracias a Noe por hacer de jefa chungu y por compartir los momentos más importantes de tu vida con nosotras. Gracias a Bea por su organización infinita, sin la cual habríamos estado todas tan perdidas, y gracias a la Bea del pasado que se acordó de dejarle una notita a la Bea del futuro. Gracias a Pau por su infinita paciencia, por sus sabias palabras y consejos, por hacer de mentora en la sombra y siempre tener un momento para dedicármelo. A todos vosotros, gracias por haberme hecho sentir parte de vuestra “pequeña” familia gallega.

I would like to thank Dr. Herlé Mercier, from the Laboratoire de Physique des Océans (IFREMER, Brest, France) and Dr. Nicholas R. Bates, from the Bermuda Institute of Ocean Sciences (BIOS, Bermuda), who kindly gave me the opportunity to work in their labs. Thank you both for your support, your wise comments, and for expanding my knowledge about ocean circulation and ocean chemistry. Working with you has made me progress towards my Ph.D. Thanks also to Pascale Lherminier for welcoming me into your home, and make me feel like in my own home. Thank you for your eternal smile and for your great capacity for work. Gracias a estas

estancias me encontré con grandes de batallas de los que me llevo grandes amistades, entre ellas la de Patri. Gracias Patri por todos los momentos “brestois” compartidos, por tu personalidad y por sacarme siempre una sonrisa con tus historias.

A las tripulaciones de los buques *B.O. Sarmiento de Gamboa*, *B.O. Hespérides* y *N/O Pourquoi Pas?*, gracias por hacerme sentir como en casa en el mar. A todos los compañeros de campaña, con los que viví tantos momentos memorables. Me los llevo todos conmigo. Espero que volvamos a coincidir muy pronto. Gracias a Noe y Alba por venir a despertarme para ver “¡ballenas!”. A Mónica y Antón por vuestra disponibilidad y vuestro buen humor. Gracias a Estela, Suso, Miquel, Pedro y Alberto por los momentos “osobuco”. Gracias a Fer y Lidia por las carreras en el Mario Kart y las vacaciones en Toronto.

Como no, gracias a mi familia, especialmente a mis padres, mi hermano y mi querida abuela por su apoyo incondicional y sus ánimos, sin los cuales no habría podido llegar hasta donde he llegado. Gracias mamá y papá por estar ahí en todo momento y nunca negarme mis sueños. Gracias por aceptar mis muchas ausencias. Por las llamadas de los domingos, que me hacen sentir que estoy en casa aun estando lejos. Gracias Miguel por tu bondad, por tu alegría y tu cercanía. Gracias por confiar en mí cuando tienes problemas, sean del tipo que sean. Por las llamadas inesperadas y por los besos sin ningún motivo especial. No podría tener un mejor hermano. Gracias abuela por los millones de besos cada vez que nos vemos y por preocuparte porque todos estemos bien. Gracias a mis ti@s y prim@s por siempre alegrarse por mis éxitos. Gracias a mis amigas del cole, que siempre han estado cuando las he necesitado aunque estemos a kilómetros de distancia. Adriana, Marisa y Michelle, no me olvido de vosotras.

Y gracias a tantos otros que no aparecen en esta pequeña lista y me han ayudado a conseguir llegar a la meta doctoral. Gracias a todos, pues sin vosotros esto no habría sido posible.



# PART I.- INTRODUCTION



ARCHIMEDES



HYPATIA



LEONARDO DA VINCI



NICOLAUS COPERNICUS



GALILEO GALILEI



JOHANNES KEPLER



RENÉ DESCARTES

IF I HAVE SEEN FURTHER IT IS BY STANDING ON THE SHOULDERS OF GIANTS.



ISAAC NEWTON



BENJAMIN FRANKLIN



HENRY CAVENDISH



ANTOINE LAVOISIER



MICHAEL FARADAY



CHARLES DARWIN



GREGOR MENDEL



LOUIS PASTEUR



NIKOLA TESLA



MAX PLANCK



MARIE CURIE



ALBERT EINSTEIN



ALEXANDER FLEMING



NIELS BOHR



JACQUES-YVES COUSTEAU



JAMES WATSON



FRANCIS CRICK

# PARTE I.- INTRODUCCIÓN



ARCHIMEDES



HYPATIA



LEONARDO DA VINCI



NICOLAUS COPERNICUS



GALILEO GALILEI



JOHANNES KEPLER



RENÉ DESCARTES

SI HE VISTO  
MÁS LEJOS ES  
POR ESTAR  
A HOMBROS  
DE GIGANTES.



ISAAC NEWTON



BENJAMIN FRANKLIN



HENRY CAVENDISH



ANTOINE LAVOISIER



MICHAEL FARADAY



CHARLES DARWIN



GREGOR MENDEL



LOUIS PASTEUR



NIKOLA TESLA



MAX PLANCK



MARIE CURIE



ALBERT EINSTEIN



ALEXANDER FLEMING



NIELS BOHR



JACQUES-YVES COUSTEAU



JAMES WATSON



FRANCIS CRICK

## **Chapter 1.- Introduction**

---

This introductory chapter starts with a general background of CO<sub>2</sub> as a greenhouse gas, its atmospheric increase since the industrial revolution, and the consequences of this increase on the oceans. The physical perspective section of this chapter describes the main features of the North Atlantic Ocean, with an emphasis on the subpolar region that is the main area of study in this thesis. A brief description of the major topographical features is performed, as well as the main characteristics of the circulation and water masses present in the North Atlantic. The chemical perspective section describes the oceanic carbon system, considering its anthropogenic perturbation and its consequences on the ocean chemistry.



## 1.1.- General Background

A small portion of the Earth's atmosphere is composed of gases that absorb and contain infrared radiation, which warm the Earth's surface and atmosphere; they are referred to as greenhouse gases (GHGs). Water vapour is the most important GHG, followed by carbon dioxide (CO<sub>2</sub>), methane (CH<sub>4</sub>), nitrous oxide (N<sub>2</sub>O), sulphur hexafluoride (SF<sub>6</sub>) and ozone (O<sub>3</sub>). Anthropogenic activities have been gradually increasing the CO<sub>2</sub> concentrations in the atmosphere since the Industrial Revolution, from ~277 parts per million (ppm) in 1750 (Joos and Spahni, 2008) to a global average of 400 ppm (2015; (Dlugokencky and Tans, 2015), i.e., the average content of CO<sub>2</sub> has increased by more than 120 ppm in 265 years. However, the rate of increase has not been constant over time. The growth rate decreased between the 1960s (4.5% yr<sup>-1</sup>) and the 1990s (1.0% yr<sup>-1</sup>), and began to increase again in the 2000s (3.4% yr<sup>-1</sup>), decreasing slightly for the last decade (2004–2013; 2.5% yr<sup>-1</sup>) (Le Quéré et al., 2014). The continuous monitoring of the atmospheric CO<sub>2</sub> in Mauna Loa Observatory (Hawaii) since 1958 (Keeling et al., 1976), and later in other observatories such as Barrow, Alaska Observatory; American Samoa Observatory or the South Pole Observatory highlights this CO<sub>2</sub> increase (Figure 1).

Anthropogenic CO<sub>2</sub> (C<sub>ANT</sub>) emissions occur on top of an active natural carbon cycle that circulates carbon between the atmosphere, ocean and terrestrial biosphere reservoirs (Figure 2) on timescales from days to millennia, while exchanges with geologic reservoirs have even longer timescales (Archer et al., 2009). The ocean dominates the storage of CO<sub>2</sub> due to its high solubility in seawater and its sequestration through seawater sinking. In fact, the global ocean contains ~50 times the amount of CO<sub>2</sub> in the atmosphere (Figure 2). The absorption of CO<sub>2</sub> by the oceans has limited the rise in atmospheric CO<sub>2</sub> concentrations and hence GHG warming. But this absorption leads to a suite of chemical changes collectively known as ocean acidification (e.g., Raven et al., 2005; Doney et al., 2009; Feely et al., 2009). Because it is another consequence of C<sub>ANT</sub> emissions, it has been dubbed “the other CO<sub>2</sub> problem” (Turley, 2005) and “the evil twin of global warming” (Pelejero et al., 2010). Ocean acidification includes seawater chemical changes such as the lowering of seawater pH and carbonate saturation, and has the potential to dramatically affect marine organisms and ecosystems (e.g., Langdon et al., 2000; Riebesell et al., 2000; Pörtner et al., 2004; Gattuso et al., 2014) and also to modify the major marine biogeochemical cycles (Gehlen et al., 2011; Matear and Lenton, 2014). The main concern is the rate of change of pH, which exceeds any known for at least hundreds of thousands of years (Feely et al., 2004; Raven et al., 2005). These changes are so rapid that they can significantly reduce the buffering capacity of the natural processes that have moderated changes in the ocean chemistry over most of the geological time (Raven et al., 2005). Also this rapid rate of change could cause that certain calcifying species do not adapt fast enough to survive, thus altering the marine food webs (e.g., Orr et al., 2005; Doney et al., 2009).

Since the industrial revolution, less than half of the C<sub>ANT</sub> emitted to the atmosphere (555 ± 85 PgC; 1 PgC = 10<sup>15</sup> gC) has remained in it (240 ± 10 PgC); the remaining has been absorbed by the ocean and terrestrial ecosystems, both of these known as “carbon sinks” (Ciais et al., 2013; Rhein et al., 2013). The oceans have absorbed ~30% of the C<sub>ANT</sub> emitted to the atmosphere between 1750 and 2013 (DeVries, 2014; Le Quéré et al., 2014). But this C<sub>ANT</sub> is not evenly distributed throughout the oceans (Sabine et al., 2004), entering preferentially in regions of upwelling and convective overturn (Maier-Reimer and Hasselmann, 1987; Sarmiento et al.,



1992). The thermohaline circulation or Meridional Overturning Circulation (MOC) makes the North Atlantic one of the most important  $C_{ANT}$  sinks of the global ocean, storing 25% of the global oceanic  $C_{ANT}$  despite covering only 15% of the global ocean area (Sabine et al., 2004). The Atlantic MOC transports  $CO_2$ -laden waters from the Equator to the northern North Atlantic (Watson et al., 1995; Wallace, 2001), where the water mass formation processes, i.e., the sinking of surface waters, provide the pathway for  $C_{ANT}$  to pass from the surface mixed layer to the deep ocean (Lazier et al., 2002; Pérez et al., 2008; Steinfeldt et al., 2009). The uptake and storage of  $C_{ANT}$  by the oceans depends on the ventilation, formation and transport of the water masses (Tanhua et al., 2006; Rhein et al., 2007; Steinfeldt et al., 2009; Pérez et al., 2013). In fact, the lateral advection of  $C_{ANT}$ -laden water masses is an important contributor to the  $C_{ANT}$  storage in the Subpolar North Atlantic region (Pérez et al., 2013).

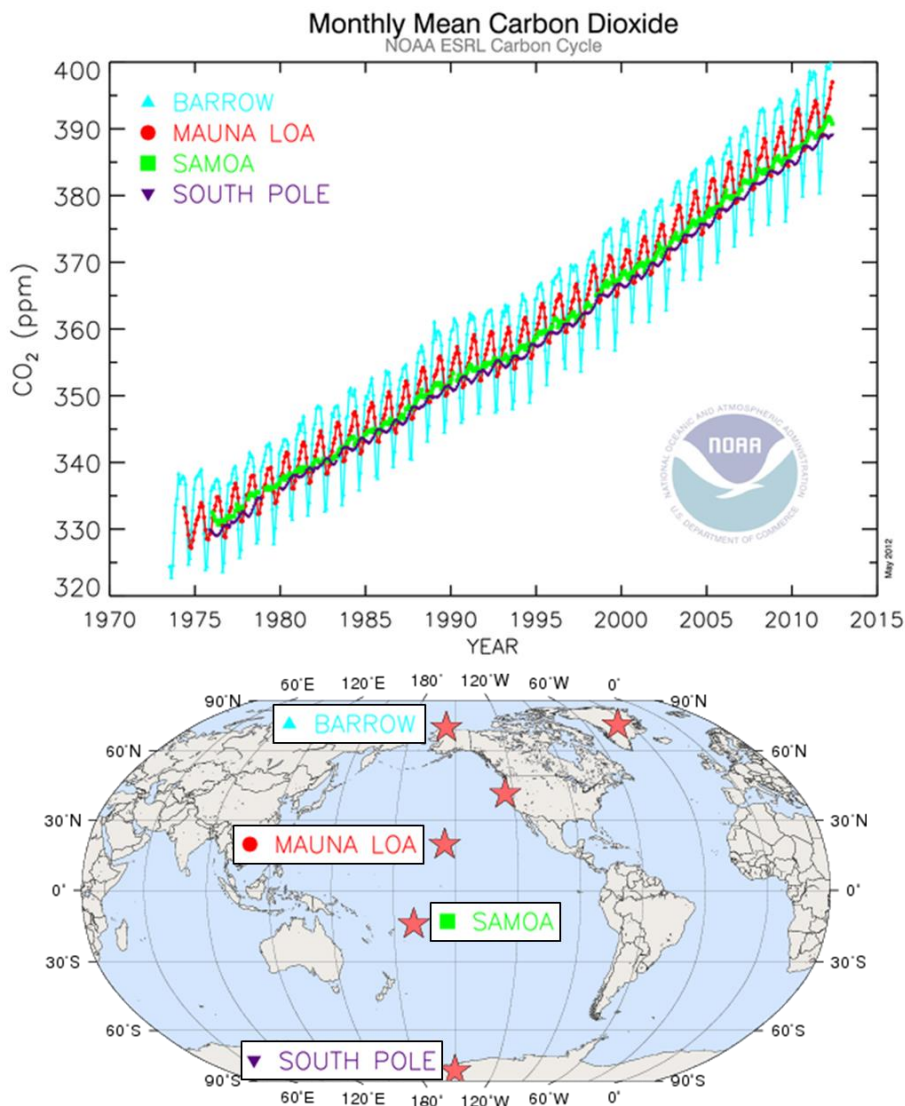


Figure 1.- At the top, monthly average instrument data for atmospheric carbon dioxide ( $CO_2$ ) mixing ratios determined from the continuous monitoring programs at the four Baseline Observatories of Barrow (cyan triangle), Mauna Loa (red dot), American Samoa (green square) and South Pole (purple inverted triangle). At the bottom, locations of the observatories. Modified from Tans (2012).

This thesis focuses on the Subpolar North Atlantic that plays an important role in the European climate and in the absorption (sink) and transport of CO<sub>2</sub> into the deep ocean through the thermohaline circulation. The subtropical warm waters carried northwards by the North Atlantic Current (NAC), release heat to the atmosphere contributing to temperate Western Europe winters (Stommel, 1958; Seager et al., 2002). The progressive cooling of these waters as they are transported to the Subpolar North Atlantic leads to their transformation into subpolar waters, which eventually reach the formation regions in the Labrador and Nordic Seas. The CO<sub>2</sub> sequestration occurred during this circulation and its subsequent transport to the ocean interior maintains the carbon absorption capacity of the North Atlantic waters.

The remainder of Chapter 1 is separated into two sections. Firstly discussing the Physical Perspective, with respect to circulation within the North Atlantic at all depths, and secondly discussing the Chemical Perspective of this research for the assessment of changes in ocean carbon content. Both perspectives will provide the focus for the following thesis Chapters.

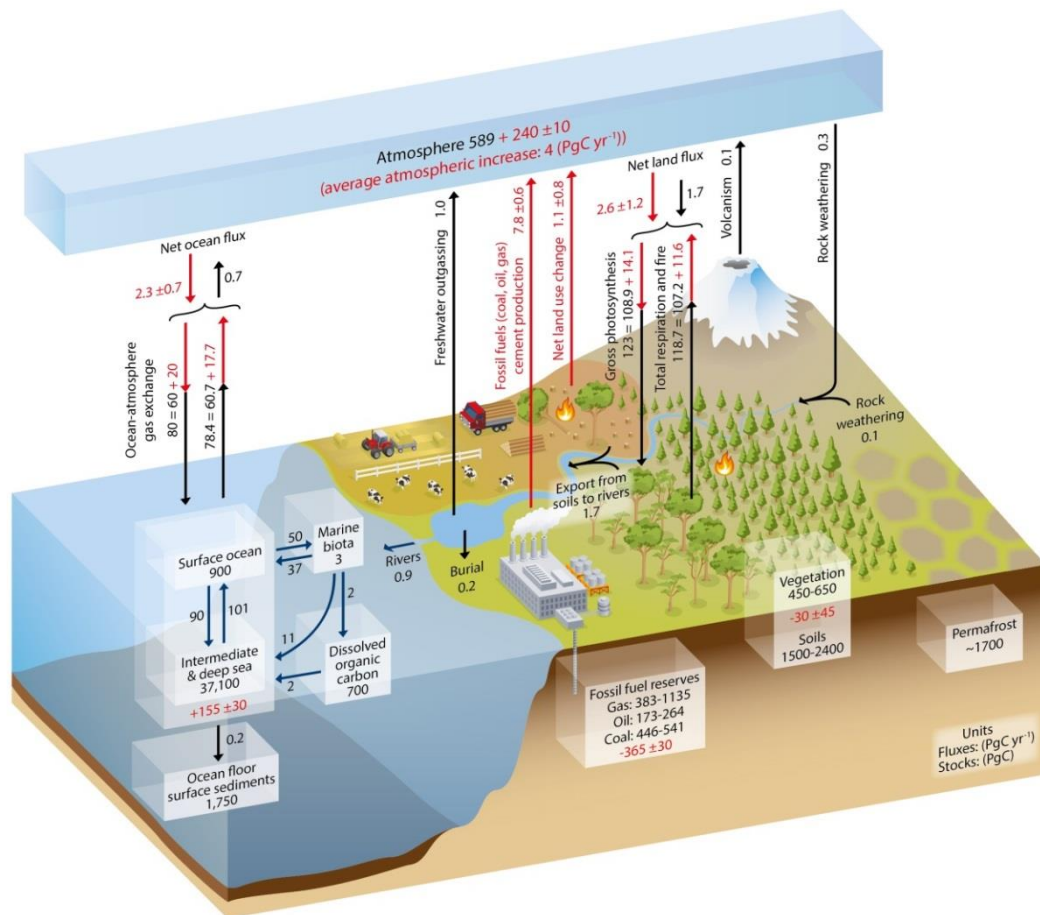


Figure 2.- Scheme of the global carbon cycle. Numbers represent mass reservoirs in PgC (1 PgC = 10<sup>15</sup> gC) and annual carbon exchange fluxes (in PgC·yr<sup>-1</sup>). Black numbers and arrows indicate mass reservoirs and exchange fluxes estimated for the time prior to the Industrial Era (~1750). Red arrows and numbers indicate annual anthropogenic fluxes averaged over the 2000–2009 time period. These fluxes are a perturbation of the carbon cycle during Industrial Era (post 1750). The red arrows parts of Net land flux and Net ocean flux are the uptake of anthropogenic CO<sub>2</sub> by the ocean and by terrestrial ecosystems (carbon sinks). Red numbers in the reservoirs denote cumulative changes of anthropogenic carbon over the Industrial Period 1750–2011. By convention, a positive cumulative change means that a reservoir has gained carbon since 1750. Uncertainties are reported as 90% confidence intervals. Source: Ciais et al. (2013).

## 1.2.- Physical Perspective: The North Atlantic Ocean

The Atlantic Ocean occupies about 23% of the total world ocean area, extending from the Arctic Ocean to the Southern Ocean. The Equator artificially divides it into North Atlantic and South Atlantic. Within the North Atlantic domain (Figure 3), the Subpolar North Atlantic area is the best understood and most intensively studied of all the ocean basins. The Subpolar North Atlantic is the region north of 40°N, south of the Greenland–Scotland Ridge and bordered to the east by the European continental shelf and to the west by the Davis Strait, the Hudson Strait and the Canadian continental shelf (Figure 3). The North Atlantic Ocean plays a key role in regulating the climate of the continents it washes, mainly because of the heat exchanges that happen during the northward flow of the warm tropical waters. Once these surface warm waters reach the Subpolar North Atlantic area, they cool, consequently increasing their density, and finally sink. This is the start process of the thermohaline circulation or Meridional Overturning Circulation (MOC). The complex system of surface and bottom currents that constitutes MOC not only moves water and salt around the planet but it also carries prodigious amounts of heat to various parts of the world thus significantly influencing the global climate (Figure 4).

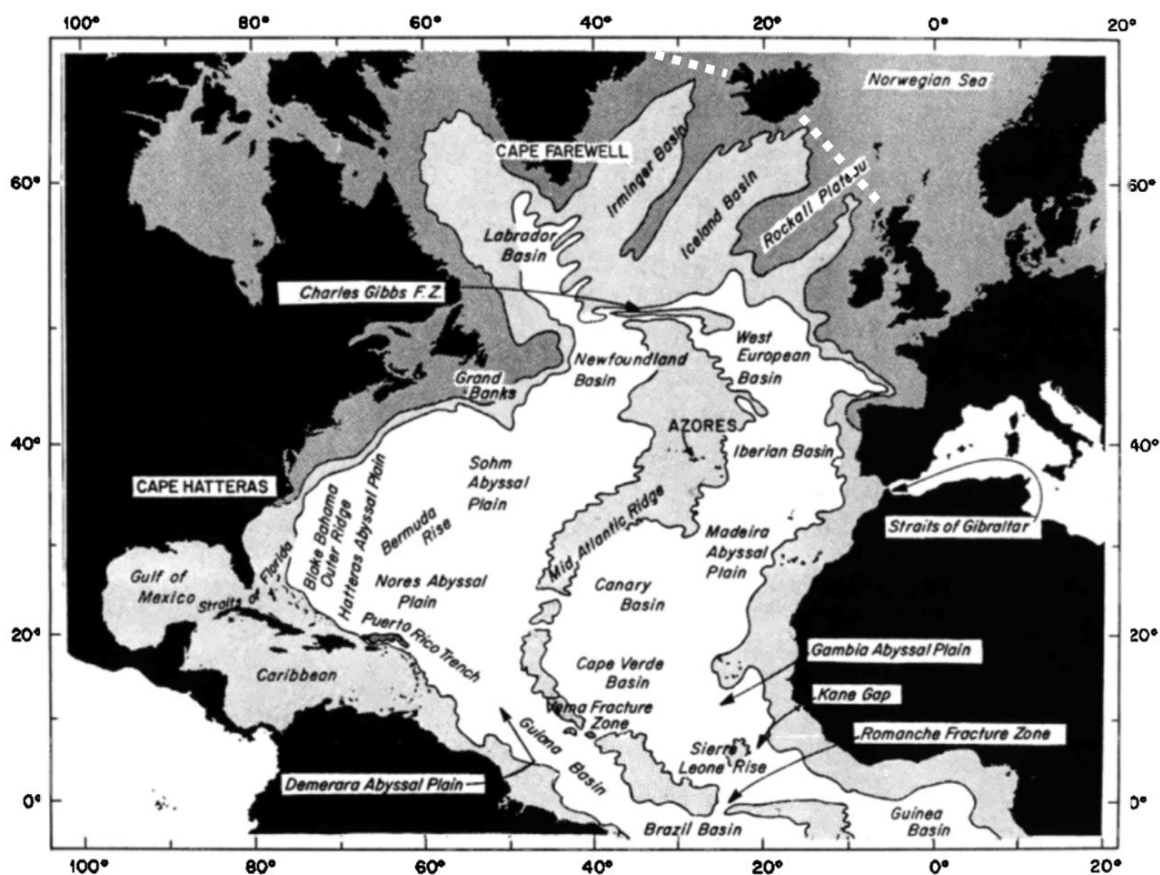


Figure 3.- A topographic and feature nomenclature map for the North Atlantic. The dotted white line between Greenland and Scotland represents the Greenland–Scotland Ridge. Modified from Schmithz and McCartney (1993).



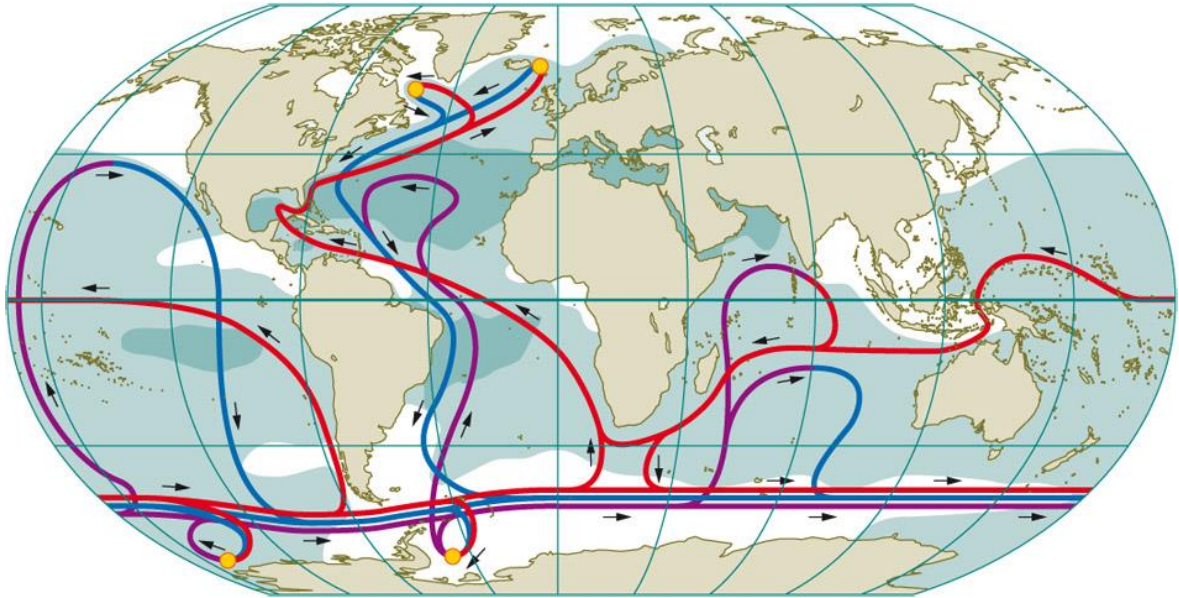


Figure 4.- Simplified sketch of the Meridional Overturning Circulation (MOC). The red lines represent the surface currents (MOC upper limb), and the blue and purple lines the deep and bottom currents (MOC lower limb), respectively. The black arrows indicate the direction of the circulation. The dark areas indicate high salinity waters (> 36) and the white areas low salinity waters (< 34). The yellowish circles indicate the main regions of deep water formation. Source: Bollmann et al. (2010).

### 1.2.1.- Topographic features

The topographic features strongly affect ocean circulation, especially deep currents. The principal feature of the bottom topography of the Atlantic Ocean is the Mid-Atlantic Ridge (MAR), which is formed by the confluence of four tectonic plates: Eurasian, North American, South American and African. The MAR, with characteristic depths between 1500 and 2000 m, divides the North Atlantic Ocean into two main basins, eastern and western, constituting a barrier for the circulation of deep and bottom waters. Nevertheless, the existence of some deep passages crossing the MAR allows deep water transport between the eastern and western basins. Three of the most important ones are the Charlie-Gibbs Fracture Zone (CGFZ) at about 50°N with a maximum depth of 3000 m, and the Vema (10°N) and Romanche Fracture Zones at the Equator with a maximum depth of 4500 m (Figure 3). Concretely, the part of the MAR extending from Iceland to the southwest until the CGFZ is known as the Reykjanes Ridge. At about 57°N the Bight Fracture Zone crosses the ridge with sill depths of about 2000–2500 m.

Another important topographic feature is the Greenland-Scotland Ridge (GSR; Figure 3). The GSR runs northwest to southeast through Iceland and forms the border between the North Atlantic Ocean and the Nordic and Arctic Seas. The sills along the GSR are generally less than 500 m depth, and no greater than ~850 m in the deepest channels. These sills control the overflow of the waters coming from the Nordic and Arctic Seas. The part of the ridge between Iceland and the Faroes is known as the Iceland-Faroe Ridge. The threshold depths are 430 m off Iceland and 470 m off the Faroes. Between Iceland and East Greenland, the ridge is known as the Greenland-Iceland Ridge, which runs on the bottom of the Denmark Strait.

Transverse ridges running between the continents and the MAR divide the ocean floor into numerous basins. Some of the larger basins in the Subpolar North Atlantic area are, from north to south: Irminger, Iceland, Labrador, West European and Iberian. The Irminger and Iceland Basins are the northernmost regions of the North Atlantic Ocean. The Irminger Basin or Irminger Sea is located south of the Denmark Strait, between southeast Greenland and the Reykjanes Ridge. Its northern limit is the Greenland–Iceland Ridge, which connects the Irminger Basin with the Greenland Sea. To the southwest, the Irminger Basin reaches to Cape Farewell, the southern tip of Greenland, and meets the Labrador Basin at this point. The Iceland Basin with depths exceeding 2000 m is bordered by the Reykjanes Ridge in the northwest with depths less than 1000 m, by the Icelandic margin in the north, and by the Iceland–Faroe Ridge in the northeast with depths less than 500 m. To the south-east the basin is bordered by several banks extending from the Faroes, at the west, to the Hatton Bank and Rockall Bank, at the east. The Labrador Basin, located between the Labrador Peninsula, Canada and Greenland, reaches depths of 3400 m. It connects to the north with the Baffin Bay through the Davis Strait, and to the west with the Hudson Bay through the Hudson Strait. The Iberian Basin is mainly constituted by the Iberian Abyssal Plain, located in front of the west coast of the Iberian Peninsula. The West European Basin is located north of the Iberian Basin, between the European coast and the Reykjanes Ridge, being its northern limit the Rockall Bank. It is constituted by two main abyssal plains: the Porcupine Abyssal Plain, adjacent to the Irish continental margin; and the Biscay Abyssal Plain or Bay of Biscay, located off the north coast of Spain and the west coast of France.

### ***1.2.2. - Large-scale circulation***

Ocean currents transport enormous amounts of heat around the world. This makes them one of the most important driving forces of climate. Ocean currents can be classified into surface currents and deep-ocean currents. The wind-driven surface currents are fast horizontally flows that move about 10% of all ocean water. In contrast, the slow deep-ocean currents have a significant vertical component, which is caused and driven by density differences that ultimately result in the MOC. It accounts for 90% of all ocean waters.

#### **1.2.2.1.- Surface Currents**

The upper ocean circulation is driven by the friction of wind on the atmosphere–ocean interface. Wind-driven currents decline with depth and are generally limited to the permanent pycnocline (100–400 m depth), but in some cases they may go as deep as 1000 m depth. Surface currents play a significant role in transporting heat from equatorial to polar latitudes. They are also involved in gas exchanges, especially oxygen ( $O_2$ ) and  $CO_2$ .

The combined action of the wind stress, the Coriolis Effect and the continental deflection causes that the surface currents form gyres, i.e., large circular-moving currents. Depending on its latitudinal position, those oceanic gyres are classified into subtropical (centred at about  $30^\circ N$  or  $30^\circ S$ ) and subpolar (centred at about  $60^\circ N$  or  $60^\circ S$ ). The subtropical gyres dominate the circulation at midlatitudes in each one of the five ocean basins (North and South Atlantic, North and South Pacific and Indian), whereas the cyclonical subpolar gyres are smaller and fewer (Figure 5). The subtropical gyres are not symmetrical and present a western intensification that leads to western boundary currents. Western boundary currents are narrower, deeper and faster than the eastern boundary currents. Some western boundary currents also carry waters as part of the

thermohaline circulation, involving inter-gyre and inter-basin exchanges as shown by green flow lines in Figure 5.

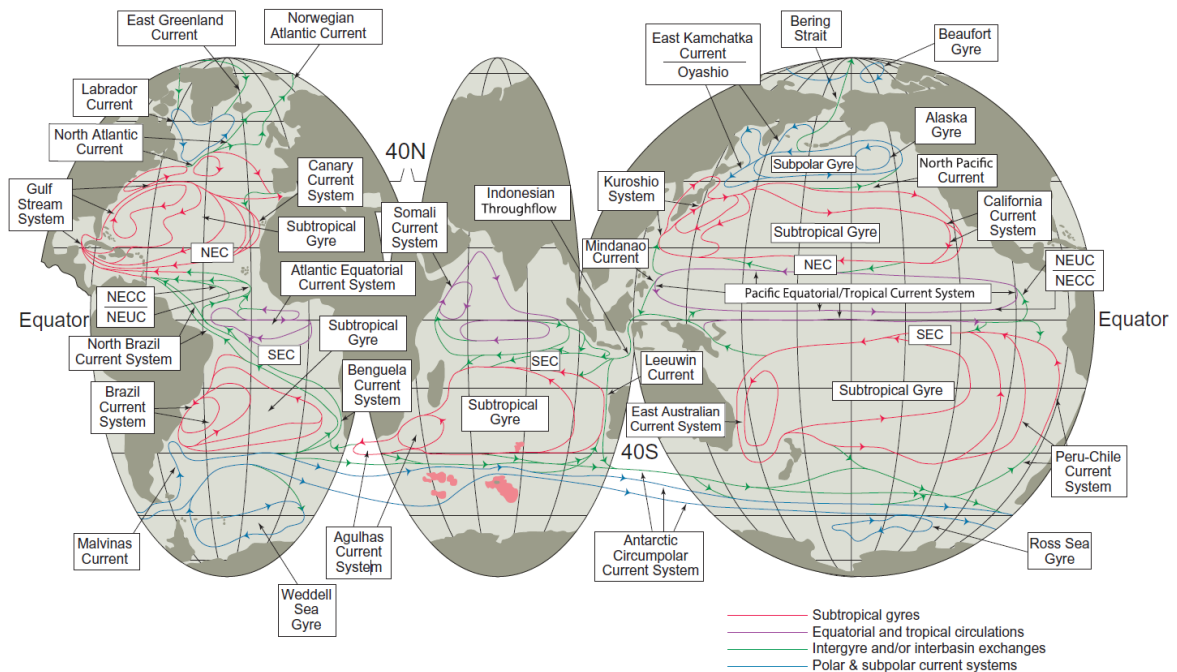


Figure 5.- Surface circulation scheme. NEC and SEC denote the Northern and Southern Equatorial Currents, NEUC and NECC are the Northern Equatorial Under and Counter Currents, respectively. Source: Talley et al. (2011).

The North Atlantic's subtropical gyre, like all subtropical gyres, is asymmetric, with strong, narrow western boundary currents and broad southward flow throughout the central and eastern subtropics. The subtropical western boundary current is composed of two connected portions: the Gulf Stream System south of about  $40^{\circ}\text{N}$ , and part of the NAC system east of Newfoundland and north of  $40^{\circ}\text{N}$ . The Gulf Stream System consists of a series of poleward western boundary currents, whose main components are shown in Figure 6. The subtropical Gulf Stream System begins where the North Equatorial Current enters the Caribbean Sea, and leaves it through the Florida Straits as the Florida Current and the Gulf Stream. The Florida Current/Gulf Stream flows along the continental shelf break of the eastern United States to the latitude of Cape Hatteras (about  $35^{\circ}\text{N}$ ,  $75^{\circ}30'\text{W}$ ), where it separates from the continental shelf and flows north-eastwards as a single free jet. East of its separation at Cape Hatteras, the Gulf Stream is one of the most powerful currents in the world's oceans in terms of volume transport (up to  $140\text{ Sv}$ ;  $1\text{ Sv} = 10^6\text{ m}^3\cdot\text{s}^{-1}$ ), maximum velocity (up to  $250\text{ cm}\cdot\text{s}^{-1}$ ) and average velocity (about  $150\text{ cm}\cdot\text{s}^{-1}$ ). Near the Grand Banks and southeast the Newfoundland Ridge ( $40^{\circ}\text{N}$ ,  $50^{\circ}\text{W}$ ), the Gulf Stream extends southwards into the abyssal plain, decreases in transport and splits into several branches, including the NAC.

The NAC extends to the highest latitude among any of the world's subtropical western boundary currents, about  $52^{\circ}\text{N}$  (Figure 6). As such, it represents the continuation of the northward heat transport as part of the thermohaline circulation. The NAC begins as a northward western boundary current east of the Grand Banks of Newfoundland, fed by a branch of the Gulf Stream. Near  $52^{\circ}\text{N}$ , the NAC separates from the boundary and turns abruptly eastwards, in a

feature referred to as the *Northwest Corner* (Rossby, 1996, 1999), as a multibranching meandering flow towards the MAR. The southward branches become part of the North Atlantic's anticyclonic subtropical circulation. The northward branches, which retain locally intense frontal structures, feed into the subpolar circulation and northwards into the Nordic Seas. Therefore the Subpolar Front constitutes the boundary between the warm waters in the subtropical gyre and the cooler and less saline waters in the subpolar gyre (Rossby, 1999).

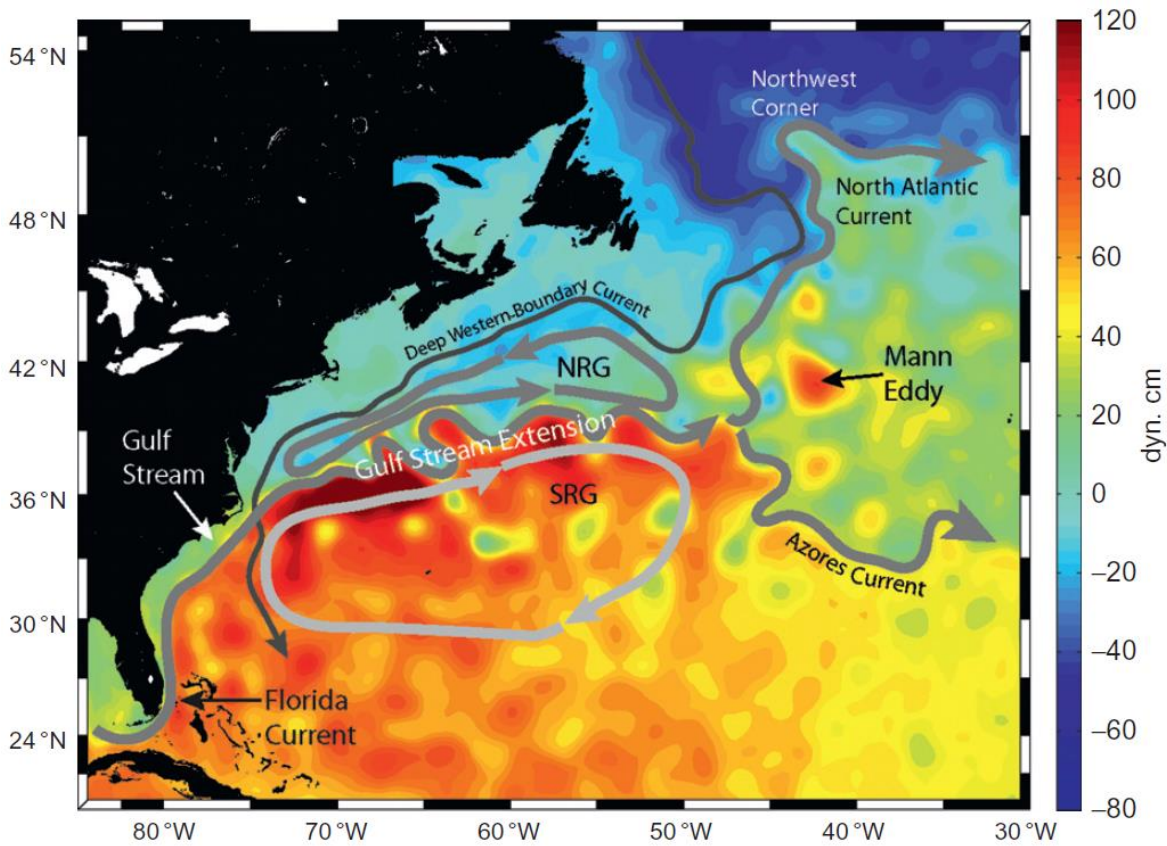


Figure 6.- Map of Absolute Dynamic Topography (in dynamic cm; colour shading) on September 21, 2011 for the western North Atlantic from AVISO (Archiving, Validation, and Interpretation of Satellite Oceanographic Data) Web site (<http://www.aviso.oceanobs.com>), with a scheme of the currents in the Gulf Stream System, including the Northern and Southern Recirculation gyres (NRG and SRG). Source: Imawaki et al. (2013).

The subpolar gyre is less asymmetric and more strongly controlled by topography than the subtropical gyre. It is divided into western and eastern regimes at the Reykjanes Ridge. The western subpolar domain is characterized by a cyclonic gyre in the Labrador and Irminger Seas. On the western flank of the Reykjanes Ridge, there is a northward flow called the Irminger Current. In the northern part of the Irminger Basin, the Irminger Current splits into two, with a branch that continues northwards through the Denmark Strait and the other (almost 85% of the initial current; Pickart et al. (2005)) that recirculates cyclonically in the Irminger Basin and joins the southward flow of the East Greenland Current (EGC) coming from the Nordic Seas, the northward flow of the West Greenland Current and the southward flow of the Labrador Current along the Labrador coast. The eastern subpolar domain is influenced by the NAC and is characterized by the north-eastward surface flow of several topographically-controlled branches of

the NAC that continue northwards and crosses the Iceland–Faroe–Shetland ridge into the Nordic Seas.

#### 1.2.2.2.- Deep-ocean Currents or the Meridional Overturning Circulation

Deep-ocean currents are driven by density changes, whose derived flow is known as thermohaline circulation or MOC. The global MOC is a key component of the Earth's climate system, acting as a heat redistribution modulator through the world's ocean, and participating in the biogeochemical cycles and gas exchanges with the atmosphere, thus modulating the GHGs distribution (Rahmstorf, 2002).

Surface seawaters are exposed to changes in salinity through evaporation, precipitation and sea-ice formation, and in temperature through heat exchange with the atmosphere. The density changes derived from the processes of mass and energy exchange with the atmosphere may occasionally produce surface waters denser than the underlying ones, thus forcing them to sink into the ocean interior. This process is known as water mass formation. The sinking of water in polar latitudes is balanced by the upwelling and return of water from ocean depths to the surface. The regions where water mass formation occurs are key points for the MOC. At large scale, there are three main regions where water mass formation takes place (Figure 4): the North Atlantic Ocean, the Ross Sea and the Weddell Sea (Rahmstorf, 2002).

Within the context of the global MOC, the Atlantic Ocean is the place with the "youngest" waters, thus presenting the highest  $O_2$  and lowest nutrient concentrations (Worthington, 1976). In a very simplistic manner, the Atlantic MOC carries warm and salty upper waters to high latitudes of the North Atlantic (upper limb), where they become denser by cooling and sink, returning southward as deep and bottom waters (lower limb). The heat exchange that happens during this circulation results in the Atlantic MOC playing an active role in the regulation of the European climate. In addition, the water mass formation processes also contribute to the  $CO_2$  sequestration. In fact, the North Atlantic Ocean stores 25% of the  $C_{ANT}$  stored in the oceans, despite representing only 15% of the global ocean surface (Sabine et al., 2004).

Figure 7 represents a very general outline of the North Atlantic MOC. The conversion of upper ocean waters to denser intermediate and deep waters in the northern North Atlantic is associated with a deep circulation, including Deep Western Boundary Currents (DWBCs). In the North Atlantic, the DWBC flows east of Greenland in the Irminger Sea between 700 and 4000 m depth, running southwards beneath the Gulf Stream and carrying dense waters from the Nordic Seas (overflowing the Greenland–Scotland Ridge). Then it flows around the Labrador Sea, incorporating water from this basin. This enhanced DWBC continues southwards towards the Equator, where part of the flow turns eastwards along the Equator and part continues into the South Atlantic, leaving the western boundary at 25°S to 40°S (Talley et al., 2011).



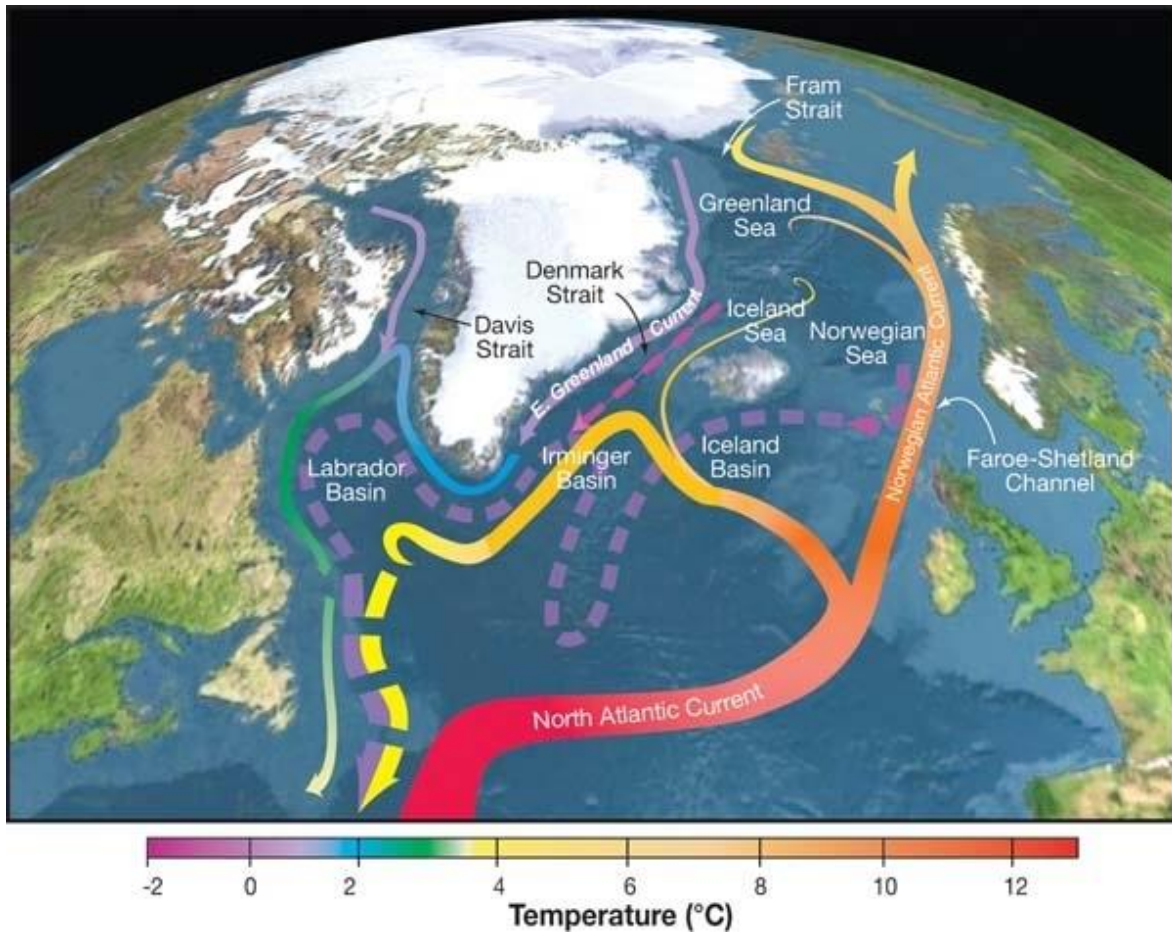


Figure 7.- Topographic map of the Nordic Seas and subpolar basins with schematic circulation of surface currents (solid curves) and deep currents (dashed curves) that form a portion of the Atlantic Meridional Overturning Circulation. Colours of curves indicate approximate temperatures. Source: R. Curry, Woods Hole Oceanographic Institution/Science/USGCRP.

### 1.2.3.- Water masses

A water mass is defined as a volume of water with a common formation history, whose physicochemical properties are distinct from the surrounding waters (Tomczak, 1999). The formation of a water mass is considered as the process by which surface waters become denser than the underlying ones, thus producing their sinking into the ocean interior. Three physical processes are known to produce water masses:

- convection: formation process result of the modification of seawater properties by contact with the atmosphere and the subsequent homogenization by mixing in the convection region, which leads to extremely uniform water properties over a large depth range. During this process, surface seawaters densify by cooling or by evaporation and sink. The depth that an isolated convection event reaches tend to be around a few hundred meters, however, water mass formation through convection usually occurs by the cumulative effect of many convection events, which leads to greater convection depths.
- subduction: process of water mass formation in the permanent pycnocline through a combination of wind action and cooling. During this process, a convergence in the wind-

driven surface current field (Ekman pumping) pushes water down along isopycnal surfaces. Although subduction is a permanent process, water mass formation occurs only in late autumn and winter, so that the properties of the water subducted are determined by the surface water properties during late winter only (Tomczak and Godfrey, 1994). In practical situations convection and subduction are sometimes found to act together to form a water mass.

- subsurface mixing: the only formation process which does not rely on air–sea exchange of properties. It occurs when two or more water masses mix so thoroughly that the mixing results in a water volume with well-defined properties distinctly different from those of the contributing water masses. The resulting water volume is then considered a newly formed water mass.

After formation, the water masses retain their properties, in particular their potential temperature ( $\theta$ ) and salinity ( $S$ ) (Tomczak and Godfrey, 1994), thus allowing identifying them in a  $\theta/S$  diagram. However, the water masses mix and interact throughout the ocean, so that these distinctive features are lost over time.

The water mass formation processes lead to the ventilation and renewal of the deep ocean. Concretely, in the North Atlantic it constitutes a major pathway for the meridional transport at depth of heat, freshwater and chemical constituents, such as nutrients or  $O_2$  (Álvarez et al., 2002; Dickson et al., 2008). The regional water mass structure of the North Atlantic Ocean is extremely complex due to the inputs of intermediate and deep waters formed in marginal sea. This makes the North Atlantic a region with a large variety of water masses. Figure 8 shows a  $\theta/S$  diagram with the main water masses of the Atlantic Ocean.

The Atlantic waters are influenced by the Mediterranean Water (MW), which enters the North Atlantic from the Mediterranean Sea. MW is formed by the mixture of the Atlantic waters and the saline waters from the Strait of Gibraltar at 36°N (Zenk, 1975). It is detected as a maximum in  $S$  ( $>36.1$ ) and  $\theta$  (9–10°C) between 600 and 1700 m depth in the eastern North Atlantic (Harvey, 1982; Tsuchiya et al., 1992; van Aken and Becker, 1996; Álvarez et al., 2004). Its core is characterized by low relative concentrations of  $O_2$  and nutrients, due to its origin in the oligotrophic Mediterranean Sea (Tsuchiya et al., 1992). MW causes that the waters of the eastern Atlantic, between about 30 and 40°N and 1000 and 3000 m depth, are the most warm and saline, not only of the Atlantic Ocean (Wüst and Defant, 1936), but of the world's oceans (Levitus, 1983). MW flows principally northwards along the European coast (at 1000 m depth in the NAC), with part of the flow being transported westwards due to the movement of the intermediate anticyclonic Mediterranean eddies, meddies (Shapiro and Meschanov, 1996; van Aken, 2000a).

The warmer North Atlantic waters are influenced by the North Atlantic Central Water (NACW), whose well-defined characteristics derived mainly from air–sea interaction (Iselin, 1936). East of the MAR in the North Atlantic, there are two varieties of this water mass: the west NACW (WNACW), closer to the ridge; and the east NACW (ENACW), in the eastern part of the basin (Harvey, 1982; Pollard et al., 1996; Read, 2000). ENACW is formed by winter convection in the intergyre region (Ríos et al., 1992; Pollard et al., 1996), being 0.1 units more saline than WNACW (Iselin, 1936; Harvey, 1982; Ríos et al., 1992; Pollard et al., 1996). Within ENACW two subclasses can be identified depending on their source area (Fiúza, 1984; Ríos et al.,

1992), a colder subpolar variety ( $ENACW_p$ ), moving southwards offshore of the northwest of the Iberian Peninsula; and a warmer subtropical variety ( $ENACW_T$ ), moving north-eastwards towards the Iberian Peninsula as a salt wedge between Azores and Portugal (Barbero et al., 2010).  $ENACW_p$  forms between the Subpolar and Subtropical Gyres (40–50°N) (McCartney and Talley, 1982; Ríos et al., 1992), presenting  $\theta$  lower than 12.2°C (Fraga et al., 1982; Harvey, 1982; Fiúza, 1984; Pollard et al., 1996).  $ENACW_T$  is formed at the northern margin of the Azores Current (Pollard and Pu, 1985; Ríos et al., 1992), being characterized by higher  $\theta$  (>13°C) than the  $ENACW_p$ . There is a zone of permanent superficial convergence between both water varieties within the latitudinal range 43°–44°N (Fraga et al., 1982; Ríos et al., 1992).

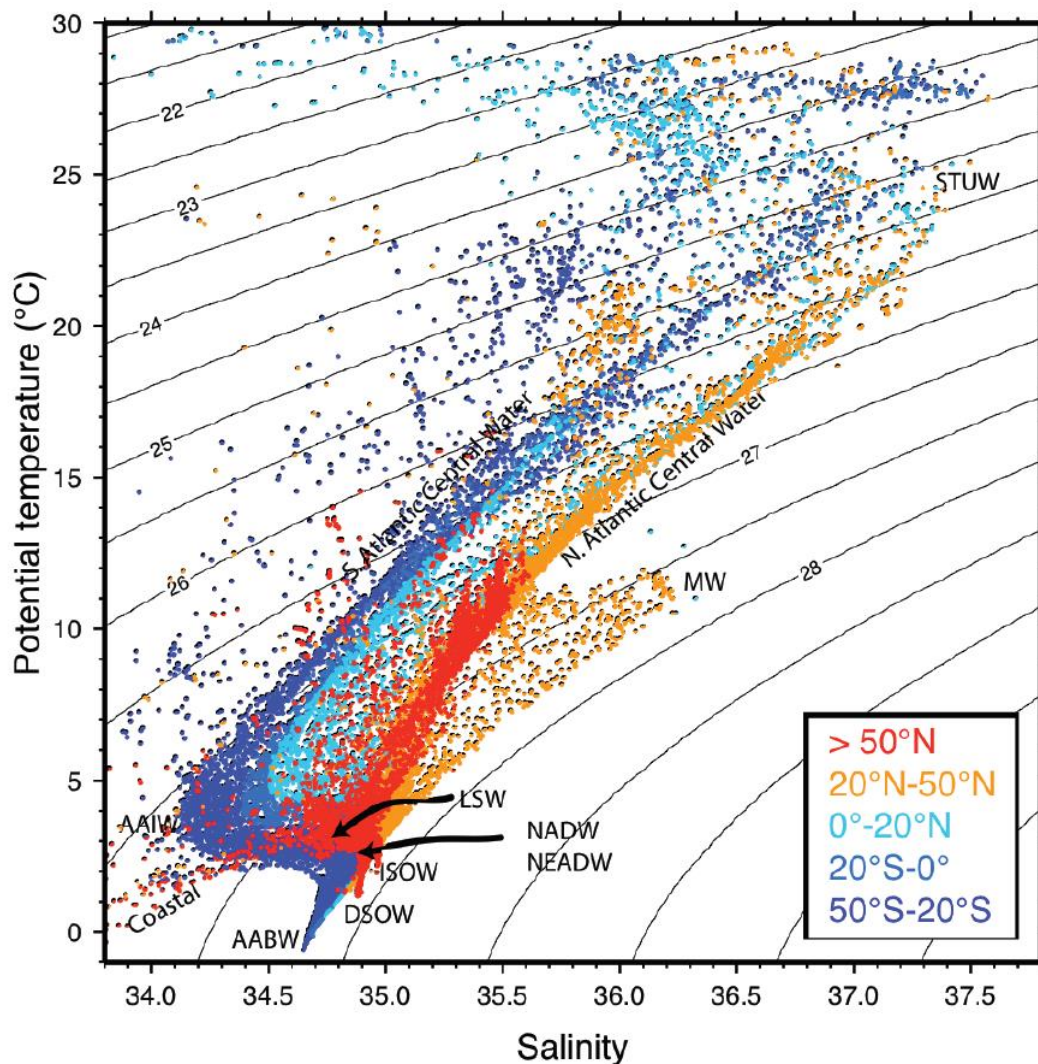


Figure 8.- Potential temperature (°C) vs. salinity for the Atlantic Ocean. Colours indicate the latitude range. Data are from the World Ocean Circulation Experiment (1988–1997). Contours are potential density referenced to 0 dbar. Acronyms indicate the principal water masses: Antarctic Bottom Water (AABW), Antarctic Intermediate Water (AAIW), Denmark Strait Overflow Water (DSOW), Iceland–Scotland Overflow Water (ISOW), Labrador Sea Water (LSW), Mediterranean Water (MW), North Atlantic Deep Water (NADW), North East Atlantic Deep Water (NEADW) and Subtropical Underwater (STUW). Source: Talley et al. (2011).

Part of the Central Waters carried by the NAC recirculates in the West European Basin, and part of them spreads towards the Iceland Basin leading to the formation of Subpolar Mode



Water (SPMW) (McCartney and Talley, 1982; Tsuchiya et al., 1992; van Aken and Becker, 1996; Brambilla and Talley, 2008). The core of this water mass is vertically homogenized in a layer of low stability between the seasonal and permanent pycnoclines (van Aken and Becker, 1996). Due to its convective origin, SPMW can be recognised by its lower potential vorticity (van Aken and de Boer, 1995), with the lowest vorticity values on the north-western part of the Reykjanes Ridge (Brambilla and Talley, 2008). The hydrographic properties of SPMW vary spatially due to air–sea interaction processes, presenting the highest  $\theta$  and  $S$  on the Rockall Channel (9–11°C and 35.30–35.50, respectively). In the Iceland Basin it is cooler, and is distributed over a wider range (5–9°C and 34.95–35.25), while when it reaches the Norwegian Sea near the Faroes Islands, the range of its parameters is more limited (7–9°C and 35.15–35.30) (van Aken and Becker, 1996).

The last stage of the transformation of SPMW in the Subpolar Gyre is the Labrador Sea Water (LSW) (Talley and McCartney, 1982). It forms in the Labrador Sea by extreme winter heat loss combined with the Subpolar Gyre circulation (Álvarez et al., 2004; Read, 2000; Yashayaev et al., 2008), being the coldest and most dense modal water in the Atlantic Ocean (Yashayaev et al., 2007a). LSW can be traced by its low potential vorticity, relatively low  $S$  and high  $O_2$  content ( $> 275 \mu\text{mol}\cdot\text{kg}^{-1}$ , the largest of all the world's oceans) (McCartney and Talley, 1982; Tsuchiya et al., 1992; van Aken and de Boer, 1995). Once formed, LSW is advected at intermediate depths in three main directions: northwards to the Irminger Sea; southwards to the DWBC; and south-eastwards across the MAR south of the CGFZ and thence to the Iceland Basin and the Rockall Channel (Talley and McCartney, 1982; Read, 2000; Álvarez et al., 2004). LSW production is strongly affected by the phase and persistence of the North Atlantic Oscillation (NAO) (Dickson et al., 1996; Yashayaev et al., 2008), showing marked inter-annual and inter-decadal changes in its thickness and thermodynamic properties (Yashayaev et al., 2008). During the high NAO index period of 1987–1994, characterized by cold and stormy winters, a large volume of a LSW variety, known as classical LSW (cLSW), was formed (Lazier et al., 2002; Yashayaev, 2007). cLSW is the coldest, densest and deepest LSW since 1930s (Yashayaev et al., 2008). Then the NAO index shifted to very negative values and the formation of cLSW ceased. At the beginning of 2000 the NAO index fluctuated between slightly positive and slightly negative values, but the atmospheric forcing at the beginning of this period (1999–2000) was strong enough to trigger again the deep winter convection in the Labrador Sea, forming a less dense and shallower LSW variety, called upper LSW (uLSW) (Yashayaev, 2007; Yashayaev et al., 2007a).

The Subarctic Intermediate Water (SAIW) originates in the western boundary of the Subpolar Gyre (Arhan, 1990). It presents  $\theta$  between 4 and 7°C and  $S$  below 34.9 (Bubnov, 1968), both characteristics reflecting its origin from Arctic waters (Read, 2000). Concretely, it is the result of the mixing between the warm and salty waters of the NAC with the cold and low-salinity waters of the Labrador Current (Iselin, 1936; Read, 2000). After its formation, SAIW subducts into the permanent thermocline and spreads southwards (Arhan, 1990), northwest of the Azores Plateau (25°W; Worthington (1976)), but it is also found south of the NAC as far as east of 20°W, between 49 and 53°N (Harvey, 1982; Pollard et al., 1996). The thermohaline properties of SAIW vary due to its spreading and subduction in a region characterized by a complex circulation, with horizontal and vertical mixing, recirculation processes and mesoscale variability, among other processes (Bubnov, 1968; Arhan, 1990).

Coming from the Arctic Ocean and the Nordic Seas, the Denmark Strait Overflow Water (DSOW) and the Iceland–Scotland Overflow Water (ISOW) are dense enough to reach the

bottom of the Atlantic Ocean. Both overflows are complex mixtures of several water masses. ISOW is formed when the Norwegian Sea waters overflow and entrain the overlying warm saline Atlantic waters (SPMW and LSW) (van Aken and de Boer, 1995; Dickson et al., 2002; Fogelqvist et al., 2003). After crossing the Iceland–Scotland sill, ISOW is advected westwards, flowing baroclinically following the topography (van Aken and de Boer, 1995). Part of it crosses the MAR by the CGFZ (Leffanue and Tomczak, 2004), and flows either southwards or northwards. In its norward flow, it enters the Irminger Sea, where it mixes with DSOW (Smethie and Fine, 2001). As for DSOW, it is a well-ventilated young water that flows through the Denmark Strait into the Atlantic Ocean. Due to the fact that the Denmark Strait is a dynamically active area with short-term variability (e.g., Macrander et al., 2005) that hampers to trace the DSOW sources (Tanhua et al., 2008), the DSOW origin is still matter of discussion. On the one hand, it is assumed that the main formation area of this water mass is the EGC, but the source water could be either the Arctic Atlantic Water (Mauritzen, 1996), or a mixing of the Arctic Intermediate Water (AIW) and the recirculated Atlantic Water (Strass et al., 1993). On the other hand, some authors believe that the main precursor of DSOW is the water from the Iceland Basin (Swift and Aagaard, 1981; Smethie and Swift, 1989; Rudels et al., 2002; Jonsson and Valdimarsson, 2004), with either large proportions of AIW (Swift et al., 1980; Rudels et al., 1999) or of the densest fraction of the overflow waters of the Greenland Sea (Smethie and Swift, 1989). According to Rudels et al. (2003), the wind forcing is the variable that controls which is the source area, the Iceland Basin or the EGC, on timescales of months to years. While on longer timescales, the responsible for this control is the convection in the Greenland Sea (Köhl, 2010). In addition, some authors have reported dense Greenland shelf water cascading down to the DSOW layer in the Irminger Sea (Olsson et al., 2005; Tanhua et al., 2005, 2008; Falina et al., 2012). The characteristics of the cascading waters are very similar to those of the Polar Intermediate Water (PIW) (Tanhua et al., 2005).

The different entrainments that suffers ISOW along its journey through the Iceland Basin, lead to the formation of the North East Atlantic Deep Water (NEADW) (van Aken, 2000b). NEADW recirculates in the Iberian Basin and mixes with the surrounding waters, including the bottom waters coming from the Southern Ocean (Antarctic Bottom Water, AABW; also named Lower Deep Water, LDW) (van Aken and Becker, 1996). The  $\theta/S$  properties of NEADW below 2500 m depth in this basin can be approximated as a line (Saunders, 1986; Mantyla, 1994) whose end points represent the upper (NEADW<sub>u</sub>) and lower (NEADW<sub>l</sub>) varieties of NEADW.

LSW together with the overflows (DSOW and ISOW) ultimately flow southwards in the DWBC and mainly compound the North Atlantic Deep Water (NADW), together with the modified AABW (Dickson and Brown, 1994). NADW represents the largest volume in the North Atlantic, whose formation, together with the formation of AABW, is perhaps the most important component of the global thermohaline circulation (Smethie and Fine, 2001; Lacan and Jeandel, 2004). NADW can be detected as a maximum of S at 2500–3000 m depth (Read, 2000). Since the water masses that form NADW are influenced by the NAO, especially LSW, NADW could also vary with the NAO changes (Dickson et al., 1996, 1999; Biastoch et al., 2003).

#### ***1.2.4.- The North Atlantic Oscillation (NAO)***

The NAO is the dominant mode of boreal winter climate variability over the North Atlantic sector (Walker and Bliss, 1932; Barnston and Livezey, 1987). The NAO is characterised

by a dipole oscillation in the North Atlantic sea-level pressure between the subpolar (Icelandic) low pressure and subtropical (Azores) high pressure regions (Saunders and Qian, 2002). An NAO index can be defined as the standardised difference in sea-level pressure between these regions:

$$\text{NAO} = P_{\text{AH}} - P_{\text{IL}}$$

where  $P$  denotes standardised sea-level pressure anomalies at stations in the Azores High (AH) and the Icelandic Low (IL), respectively. Positive (negative) numerical values of the winter NAO index are associated with strong (weak) zonal flow between these stations (Rogers, 1984).

The climatic impacts of changes in the phase (sign) of the winter NAO index are observed in winter temperature, precipitation and storminess over the whole North Atlantic (Hurrell, 1995; Trigo et al., 2002). The local and teleconnected climatic impacts of these NAO variations are shown in Figure 9. During periods of positive NAO index the pressure centres are more intense, thus resulting in stronger and more frequent storms. In contrast, during periods of negative NAO index both pressure centres are weaker and storms are less frequent.

Since the phase of the NAO index affects the wind field, atmospheric and oceanic effects associated with the winter NAO index are observed over a wide area surrounding the North Atlantic. Large-scale changes in the atmospheric forcing associated with multiyear changes in the NAO affect the ocean circulation and air–sea exchange of heat and freshwater. This results in changes in the upper-ocean hydrographic conditions and deep convection intensity in the Subpolar North Atlantic and Nordic Seas and therefore affects the properties of the intermediate and deep waters formed in the region (Dickson et al., 1996; Bersch, 2002; Sarafanov, 2009). During periods of positive NAO index, the north-eastward flow of the NAC intensifies, thus also intensifying the Subpolar Gyre (Flatau et al., 2003). The intensification of the Subpolar Gyre is manifested through its expansion, resulting in the strengthening and eastward displacement of the Subpolar Front and, in consequence, an intensification of the whole winter convection (Sarafanov, 2009). Sarafanov (2009) found that the changes in the NAO-related atmospheric forcing may account for up to two-thirds of the thermohaline changes at intermediate and deep levels in the Subpolar North Atlantic on a decadal timescale. Two factors dominate the link between the NAO and the decadal changes in  $\theta$  and  $S$  of the intermediate and deep-water in the region: (i) intensity of convection in the Labrador Sea controlling injection of relatively cold freshwater into the intermediate layer, and (ii) zonal extension of the Subpolar Gyre that regulates the relative contribution of cold fresh subpolar water and warm saline subtropical water to the formation of deep waters.

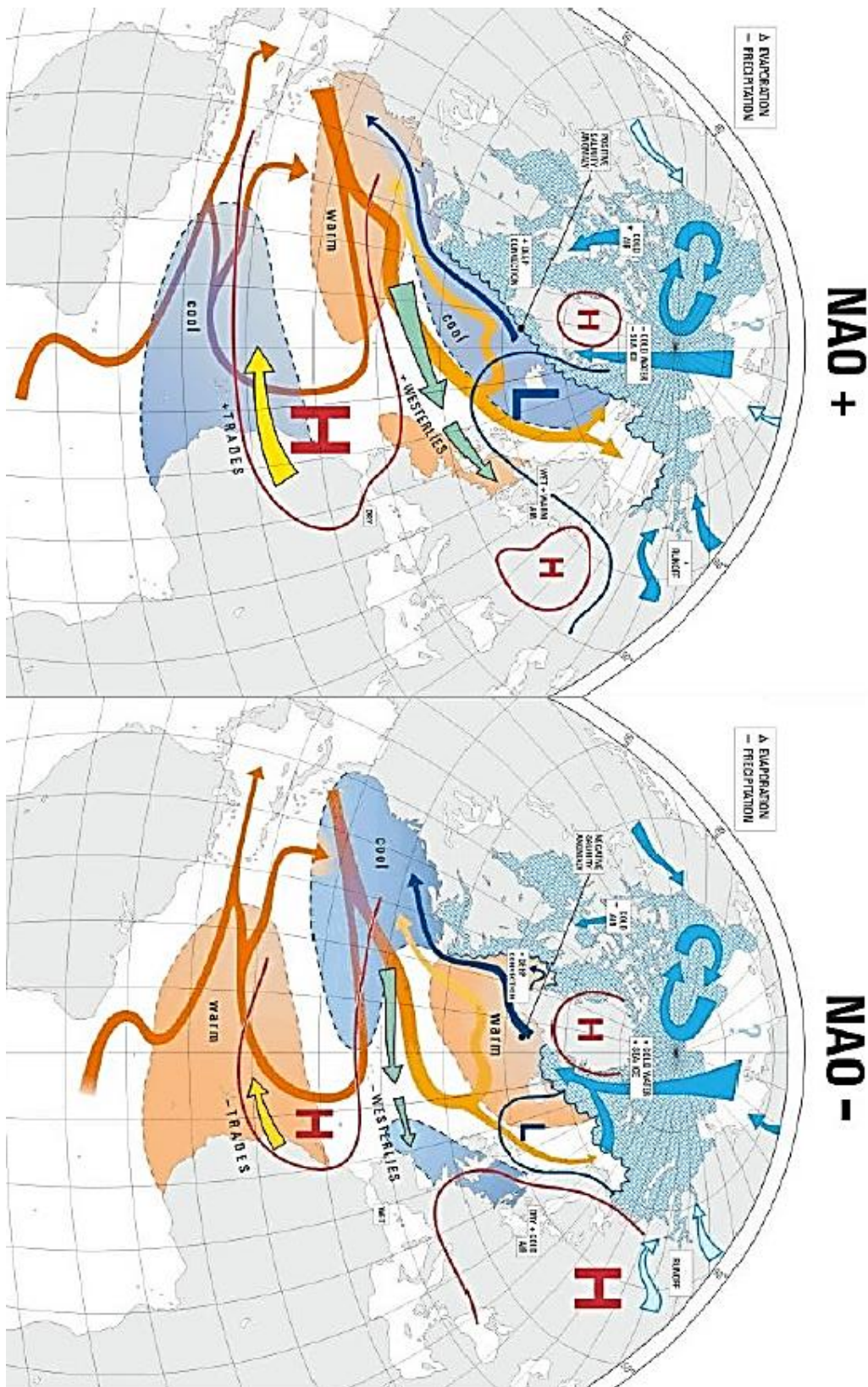


Figure 9.- Scheme showing the regional climatic impacts of the positive (left) and negative (right) phases of North Atlantic Oscillation (NAO). Surfaces mark sea surface temperatures and sea ice extension, arrows show the flow systems in ocean, atmosphere and rivers, blue and red lines indicate near-surface sea-level pressures and white rectangles describe characteristic climate conditions or important processes. Source: Fletcher (2005).

### 1.3.- Chemical Perspective: The seawater CO<sub>2</sub> system

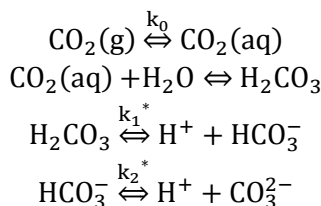
The global carbon system involves reactions within and exchange among the major global reservoirs: atmosphere, ocean and land (Figure 2). Exchange between each reservoir is facilitated by CO<sub>2</sub> gas exchange, flow of total dissolved inorganic carbon (C<sub>T</sub>) in rivers and burial of inorganic forms, such as calcium carbonate (CaCO<sub>3</sub>) (Emerson and Hedges, 2008). Continuous interaction between the atmosphere and ocean allows CO<sub>2</sub> to be readily absorbed into the surface ocean. The CO<sub>2</sub> buffering property of the marine carbon reservoir provides a large uptake capacity for additional CO<sub>2</sub>, that is, C<sub>ANT</sub>. The complex internal dynamics of the ocean is the major determining factor for the atmospheric CO<sub>2</sub> content over timescales of centuries and longer. Therefore even small changes in the natural components of the marine carbon cycle bear the potential to significantly feedback to the Earth's climate system.

#### 1.3.1.- The role of the CO<sub>2</sub> in the ocean

The absorption of CO<sub>2</sub> by seawater and the subsequent equilibrium reactions within this medium give rise to a complex chemical system, often referred to as the seawater CO<sub>2</sub> system or marine carbonate system. The seawater CO<sub>2</sub> system is responsible for about 95% of the acid–base buffering capacity of seawater and hence essentially controls the pH of ocean waters. This system has a major impact on key processes such as the precipitation and dissolution of CaCO<sub>3</sub> in the ocean, predominantly in the form of particulate inorganic carbon. This complex chemical system is influenced by physical, chemical, biological and geological processes in the ocean, such as:

- The solubility pump or physical pump, which is responsible for the exchange of CO<sub>2</sub> in the ocean–atmosphere interface. It is controlled by thermodynamic and kinetic processes, and results from the combined action of the solubility of CO<sub>2</sub> in seawater and the ocean buffer capacity (Zeebe and Wolf-Gladrow, 2001). The solubility pump is dependent on the MOC (Denman et al., 2007) through the enhancement of the CO<sub>2</sub> solubility in high latitude.
- The biological pump, which is constituted by processes such as photosynthesis, respiration and/or remineralisation of organic matter.
- The carbonate pump, which is driven by the formation of carbonate particles through biological activity and its subsequent dissolution.

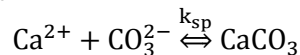
The solubility of CO<sub>2</sub> is the responsible of the physical pump. When CO<sub>2</sub> dissolves in seawater to produce aqueous CO<sub>2</sub> (CO<sub>2</sub>(aq)) it also forms carbonic acid (H<sub>2</sub>CO<sub>3</sub>), which rapidly dissociates into bicarbonate ions (HCO<sub>3</sub><sup>-</sup>), which in turn can also dissociate into carbonate ions (CO<sub>3</sub><sup>2-</sup>):



where  $k_0$  is the temperature and salinity-dependent solubility coefficient of CO<sub>2</sub> in seawater (Weiss, 1974) and  $k_1^*$  and  $k_2^*$  are the temperature and salinity-dependent first and second dissociation constants of carbonic acid, respectively. Both dissociation reactions produce hydrogen ions (H<sup>+</sup>) and therefore lower the pH of the solution. These reactions buffer the pH of surface seawater. Note that there is so little carbon in the form of H<sub>2</sub>CO<sub>3</sub> at any one moment in time, that the concentrations of CO<sub>2</sub>(aq) and H<sub>2</sub>CO<sub>3</sub> are usually combined as [CO<sub>2</sub>]. The seawater CO<sub>2</sub> system is thus comprised of four inorganic carbon species (CO<sub>2</sub>, H<sub>2</sub>CO<sub>3</sub>, HCO<sub>3</sub><sup>-</sup> and CO<sub>3</sub><sup>2-</sup>) which are connected through chemical equilibria that have been thermodynamically characterized to rather high accuracy (e.g., refs in Dickson et al., 2007).

The biological pump consists on the transformation in the ocean surface of dissolved inorganic carbon into organic matter, whose deposition creates a flow of organic carbon to the deep ocean. Phytoplankton, the base of the oceanic food webs, absorbs dissolved CO<sub>2</sub> to synthesize organic matter. During all the steps of the food webs, the organic matter is transported to deeper layers of the oceans by sedimentation, being oxidized and decomposed. Part of this organic material reaches the seafloor, joining seabed sediments.

The carbonate pump, on the contrary, releases CO<sub>2</sub> in the ocean surface layer through the synthesis of CaCO<sub>3</sub> skeletons carried out by some marine organisms such as coccolithophores and foraminifera. This CaCO<sub>3</sub>, found mainly as calcite or aragonite, precipitates during photosynthesis and sinks to the bottom. During the calcification process the total alkalinity (A<sub>T</sub>) decreases as CO<sub>3</sub><sup>2-</sup> is consumed, while the CaCO<sub>3</sub> dissolution increases A<sub>T</sub>:



where  $k_{sp}$  is the equilibrium constant defined as the solubility product ( $k_{sp} = [\text{Ca}^{2+}]_{\text{sat}} \cdot [\text{CO}_3^{2-}]_{\text{sat}}$ , where 'sat' means saturation). The fraction that remains undissolved can be determined by the saturation state ( $\Omega$ ) of seawater:

$$\Omega = \frac{[\text{Ca}^{2+}]_{\text{in situ}}[\text{CO}_3^{2-}]_{\text{in situ}}}{k_{sp}}$$

The  $\Omega$  expression reflects the equilibrium point between the tendency of ions dissolved in seawater to attach to the crystal surface (precipitation) and ions detaching from the surface to enter solution (dissolution). Since in the open ocean [Ca<sup>2+</sup>] variations are rather small and closely related to variations in S, [CO<sub>3</sub><sup>2-</sup>] mainly determines  $\Omega$

$$\Omega = \frac{[\text{CO}_3^{2-}]_{\text{in situ}}}{[\text{CO}_3^{2-}]_{\text{sat}}}$$

Supersaturated ( $\Omega > 1$ ) conditions, with an excess of [CO<sub>3</sub><sup>2-</sup>], promote inorganic CaCO<sub>3</sub> precipitation, and undersaturated ( $\Omega < 1$ ) conditions promote inorganic CaCO<sub>3</sub> dissolution. [CO<sub>3</sub><sup>2-</sup>] strongly depends on pressure, temperature, S and the C<sub>T</sub>:A<sub>T</sub> ratio. All else being equal, [CO<sub>3</sub><sup>2-</sup>]<sub>sat</sub> decreases with increasing pressure, which leads to a transition of CaCO<sub>3</sub> rich ( $\Omega > 1$ ) to CaCO<sub>3</sub> depleted ( $\Omega < 1$ ) waters with depth. The particular crystal structure form of CaCO<sub>3</sub> is also important, being the aragonite form more soluble than the calcite form.

### 1.3.1.1.- Variables of the seawater CO<sub>2</sub> system

The seawater CO<sub>2</sub> system or seawater carbonate system can be described by six fundamental parameters in thermodynamic equilibrium: C<sub>T</sub>, A<sub>T</sub>, [CO<sub>2</sub>], [HCO<sub>3</sub><sup>-</sup>], [CO<sub>3</sub><sup>2-</sup>] and [H<sup>+</sup>] (determined by the pH). The dissociation of water, the Henry's law, the first and second dissociation constants of H<sub>2</sub>CO<sub>3</sub> and the definitions of C<sub>T</sub> and A<sub>T</sub> (explained below) result in a system of four equations with six unknowns. Thus, the system can be solved by knowing the values of two parameters. Of all the carbonate species and parameters of the seawater CO<sub>2</sub> system, only the partial pressure of CO<sub>2</sub> (pCO<sub>2</sub>), pH, C<sub>T</sub> and A<sub>T</sub> can be determined analytically (Dickson et al., 2007). However, if any two parameters and total dissolved boron are known, all the parameters (pCO<sub>2</sub>, [CO<sub>2</sub>], [HCO<sub>3</sub><sup>-</sup>], [CO<sub>3</sub><sup>2-</sup>], pH, C<sub>T</sub> and A<sub>T</sub>) can be calculated for a given temperature, S and pressure (Zeebe and Wolf-Gladrow, 2001).

The CO<sub>2</sub> transfer from the atmosphere to the ocean surface occurs by molecular diffusion through the air–water interface and is directed by the differences in pCO<sub>2</sub> between the two fluids. In thermodynamic equilibrium, the CO<sub>2</sub> concentration in seawater ([CO<sub>2</sub>]) is related to the gaseous CO<sub>2</sub> in the atmosphere via the Henry's law:

$$[\text{CO}_2] = k_0 \cdot \text{pCO}_2$$

where  $k_0$  is the temperature and salinity-dependent solubility coefficient of CO<sub>2</sub> in seawater (Weiss, 1974). The pCO<sub>2</sub> assigned to a seawater sample refers to pCO<sub>2</sub> in the gas phase that is in equilibrium with that seawater. pCO<sub>2</sub> decreases with increasing temperature, since CO<sub>2</sub> solubility decreases. In fact, pCO<sub>2</sub> in the gas phase in equilibrium with seawater doubles with every 16°C increase in temperature (Takahashi et al., 2002).

The pH scale describes how acidic or basic a substance is, which is determined by the concentration of H<sup>+</sup> (-log<sub>10</sub>[H<sup>+</sup>]). The principal weak acids and bases that can exchange H<sup>+</sup> in seawater and are thus responsible for controlling its pH are inorganic carbon species and, to a lesser extent, borate (B(OH)<sub>4</sub><sup>-</sup>). Both pH and pCO<sub>2</sub> are dependent on temperature, S and pressure (Dickson et al., 2007).

Collectively, CO<sub>2</sub>, HCO<sub>3</sub><sup>-</sup> and CO<sub>3</sub><sup>2-</sup> are known as C<sub>T</sub>, which expression keeps track of the carbon:

$$C_T = [\text{CO}_2] + [\text{HCO}_3^-] + [\text{CO}_3^{2-}]$$

Within the ocean, C<sub>T</sub> is distributed according to both the solubility pump and the biological pump (Raven and Falkowski, 1999; Emerson and Hedges, 2008). The distribution of C<sub>T</sub> between the different species varies with seawater pH (Figure 10). Typically, the modern ocean surface waters have a relative contribution of each of the carbon species of 90:9:1 for HCO<sub>3</sub><sup>-</sup>, CO<sub>3</sub><sup>2-</sup> and CO<sub>2</sub>, respectively. Therefore, the CO<sub>2</sub> involved in the air–sea exchange is a minor part of C<sub>T</sub>.

A<sub>T</sub> is related to the charge balance in seawater, and reflects the acid binding capacity of seawater. In a simple way, the alkalinity is the ability of the water to neutralize acids or to accept protons. The accepted alkalinity definition, proposed by Dickson (1981), is “*the number of moles of H<sup>+</sup> ions equivalent to the excess of proton acceptors (bases formed from weak acids with a dissociation constant  $K \leq 10^{-4.5}$  at 25°C and zero ionic strength) over proton donors (acids with  $K > 10^{-4.5}$ ) in one kilogram of sample*”. The expression of A<sub>T</sub> in seawater following this definition is:



$$A_T = [\text{HCO}_3^-] + 2[\text{CO}_3^{2-}] + [\text{B}(\text{OH})_4^-] + [\text{OH}^-] + [\text{HPO}_4^{2-}] + 2[\text{PO}_4^{3-}] + [\text{SiO}(\text{OH})_3^-] + [\text{HS}^-] + 2[\text{S}^{2-}] \\ + [\text{NH}_3] - [\text{H}^+]_F - [\text{HSO}_4^-] - [\text{HF}] - [\text{H}_3\text{PO}_4]$$

where the carbonate species define about 96% of the seawater  $A_T$ . Both  $C_T$  and  $A_T$  are conservative quantities, i.e., their concentrations measured in gravimetric units ( $\mu\text{mol}\cdot\text{kg}^{-1}$ ) are unaffected by changes in temperature or pressure, for instance, and they obey the linear mixing law. Therefore, they are the preferred tracer variables in numerical models of the ocean's carbon cycle.

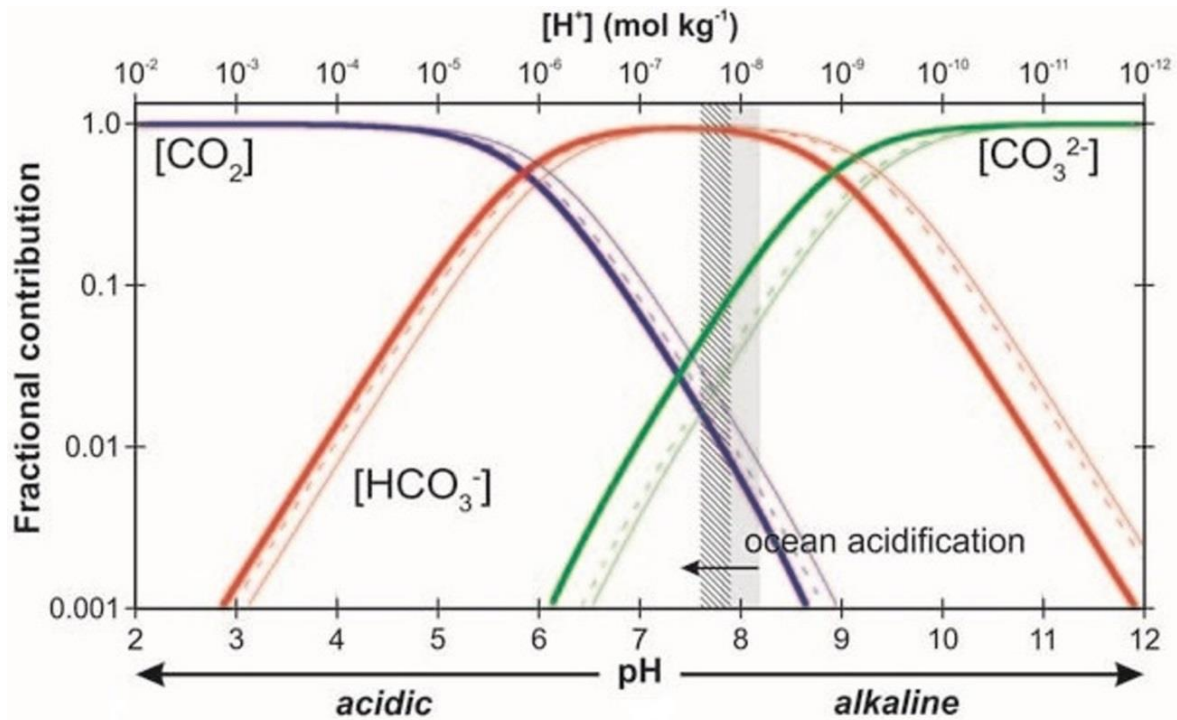


Figure 10.- Bjerrum plot showing the relative proportions of  $[\text{HCO}_3^-]$ ,  $[\text{CO}_3^{2-}]$  and  $[\text{CO}_2]$  to the total dissolved inorganic carbon in seawater at different salinities (S), temperatures (T), and pressures (P) (heavy curves are for  $S = 35$ ,  $T = 25^\circ\text{C}$ ,  $P = 0$  dbar; narrow curves are  $S = 35$ ,  $T = 0^\circ\text{C}$ ,  $P = 0$  dbar; dashed curves are  $S = 35$ ,  $T = 0^\circ\text{C}$ ,  $P = 3000$  dbar). The shaded region reflects the range of modern ocean surface (annual average), with the hashed region reflecting the corresponding projected year 2100 range taken from the global ocean geochemistry model projections of Turley et al. (2010). Modified from Barker and Ridgwell (2012).

Physical and biogeochemical processes affect the variables of the seawater CO<sub>2</sub> system. The invasion of CO<sub>2</sub> from (or release to) the atmosphere decreases (increases) pH and increases (decreases)  $C_T$ , while  $A_T$  stays constant because the charge balance is not affected (Figure 11). CaCO<sub>3</sub> precipitation (dissolution) decreases (increases)  $C_T$  and  $A_T$  in a ratio of 1:2, which results in higher (lower) CO<sub>2</sub> levels and lower (higher) pH. Photosynthesis (respiration) reduces (increases)  $C_T$  and slightly increases (decreases)  $A_T$  due to nutrient release (uptake). Temperature and S also affect the seawater CO<sub>2</sub> system variables, particularly in surface seawaters, since they influence the coefficient of solubility and the dissociation constants. For instance, CO<sub>2</sub> is less soluble at higher temperatures, leading to outgassing to the atmosphere and hence to a local decrease of  $C_T$ . Therefore, warm regions tend to have higher  $[\text{CO}_3^{2-}]$  and be more saturated with respect to carbonate minerals than colder regions. S changes are also associated with the process of evaporation (precipitation) causing increases (reductions) of the concentration of  $C_T$  and  $A_T$  in a 1:1 ratio. Pressure also influences CO<sub>2</sub> solubility, increasing it when increasing pressure. For all



these reasons, the distribution of the variables of the seawater CO<sub>2</sub> system in the ocean presents vertical and latitudinal gradients as well as temporal changes.

The CO<sub>2</sub> system is then the natural buffer of the seawater pH. The seawater pH buffer is mainly a result of the capacity of HCO<sub>3</sub><sup>-</sup> and CO<sub>3</sub><sup>2-</sup> ions to accept protons. One specific buffer factor, the so-called Revelle factor (Revelle and Suess, 1957), is important in the context of the oceanic uptake of CO<sub>2</sub>. The Revelle factor is given by the ratio of the relative change of [CO<sub>2</sub>] to the relative change of C<sub>T</sub>:

$$\text{Revelle factor} = \frac{\Delta[\text{CO}_2]/[\text{CO}_2]}{\Delta C_T/C_T}$$

Typical Revelle factor values in the ocean are between 8 and 15 (Figure 12), depending mainly on changes in pCO<sub>2</sub> and on the ratio of C<sub>T</sub> to A<sub>T</sub>. These Revelle factor values mean that upon an 1% increase of C<sub>T</sub>, the surface ocean [CO<sub>2</sub>] would increase by 8% to 15%, or what is the same, when the ocean takes up CO<sub>2</sub>, the relative increase in C<sub>T</sub> is approximately 1/10 of the relative increase in [CO<sub>2</sub>]. A high Revelle factor indicates that, for a given atmospheric CO<sub>2</sub> perturbation, the oceanic equilibrium concentration of CO<sub>2</sub> will be lower than that for low-Revelle factor waters, i.e., the lower Revelle factor, the larger the buffer capacity of seawater. The current Revelle factors are about one unit higher than they were in the preindustrial ocean (Sabine et al., 2004). An underappreciated consequence of ocean carbonate chemistry is that the fractional uptake of CO<sub>2</sub> (i.e., the amount of CO<sub>2</sub> taken up per amount of CO<sub>2</sub> emitted) will decrease significantly under high-pCO<sub>2</sub> scenarios, since seawater CO<sub>2</sub> chemistry leads to stronger rises in pCO<sub>2</sub> for a given addition of CO<sub>2</sub> when C<sub>T</sub> is already high.

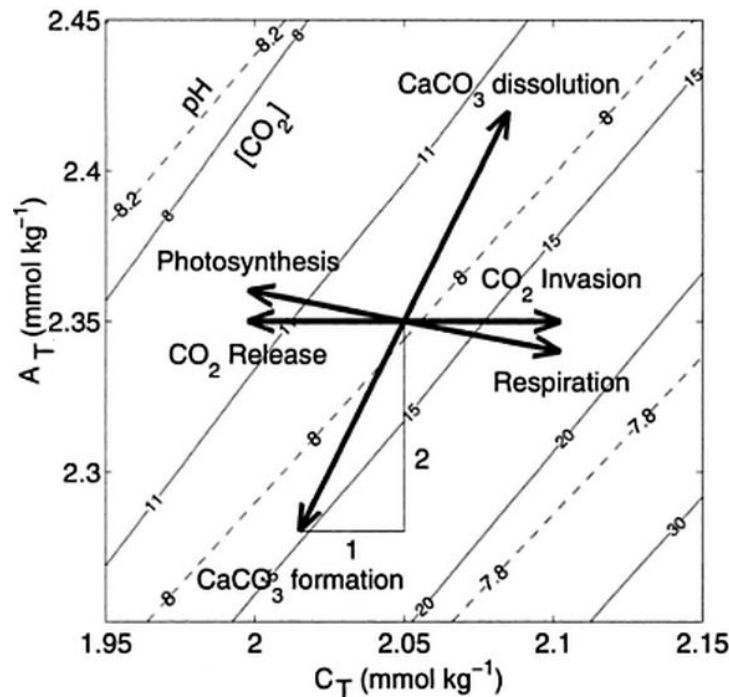


Figure 11.- Effect of various processes on total dissolved inorganic carbon (C<sub>T</sub>) and total alkalinity (A<sub>T</sub>) at 1 atm, 15°C and salinity of 35. Solid lines indicate levels of constant dissolved CO<sub>2</sub> (in μmol·kg<sup>-1</sup>) and dashed lines indicate levels of constant pH as a function of C<sub>T</sub> and A<sub>T</sub>. Modified from Zeebe and Wolf-Gladrow (2001).

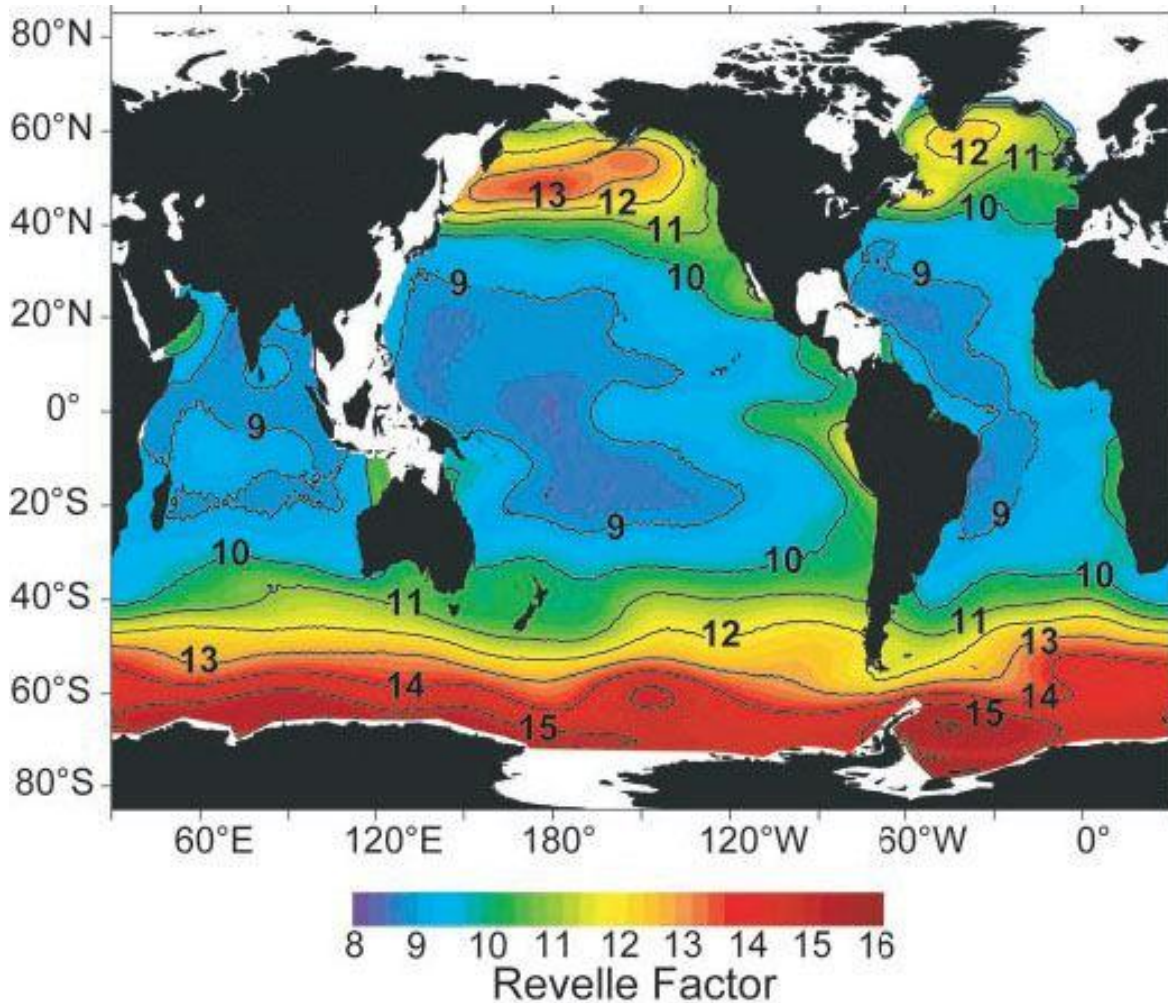


Figure 12.- The geographical distribution of the Revelle factor in ocean surface waters in 1994, averaged for the upper 50 m of the water column. Source: Sabine et al. (2004).

### 1.3.2.- Ocean Acidification

The exchange of CO<sub>2</sub> at the air–sea interface is relatively fast, taking place on timescales from months to a year so that, on average, the concentration of CO<sub>2</sub> in surface seawater remains approximately at equilibrium with the atmosphere. As atmospheric CO<sub>2</sub> increases due to anthropogenic emissions, the CO<sub>2</sub> dissolved in surface seawater increases proportionally. The uptake of the anthropogenic “excess” of CO<sub>2</sub> by the global ocean causes shifts in the balance of the seawater CO<sub>2</sub> system, which affects all species and all but one measurable parameter such that the concentration of CO<sub>2</sub>, HCO<sub>3</sub><sup>-</sup>, H<sup>+</sup>, C<sub>T</sub>, and pCO<sub>2</sub> increases, CO<sub>3</sub><sup>2-</sup> and pH decreases while A<sub>T</sub> remains unchanged. All these changes in seawater acid–base and inorganic carbon chemistry are termed ocean acidification (Feely et al., 2009).

The seawater CO<sub>2</sub> system is the natural buffer of the seawater pH. When CO<sub>2</sub> dissolves in seawater it does not fully dissociate into CO<sub>3</sub><sup>2-</sup> and the number of H<sup>+</sup> produced (and the drop in pH) is therefore smaller than expected. Thanks to this buffering effect the ocean acidification is much smaller than for an un-buffered system. All else being equal, as more CO<sub>2</sub> is added to seawater the pH will slowly decrease and the balance between the three carbonate species will

change, with [CO<sub>2</sub>] and [HCO<sub>3</sub><sup>-</sup>] increasing and [CO<sub>3</sub><sup>2-</sup>] decreasing (Figure 10). The ability of seawater to buffer changes in its pH as CO<sub>2</sub> is added depends on [CO<sub>3</sub><sup>2-</sup>]. As more CO<sub>2</sub> is added and CO<sub>3</sub><sup>2-</sup> is progressively consumed, the buffering capacity of seawater will decrease. This produces an increase in the proportion of CO<sub>2</sub> that remains as CO<sub>2</sub>(aq) as more CO<sub>2</sub> is added, an effect quantified by the Revelle Factor (Revelle and Suess (1957); see Section 1.3.1.1.). The proportion of C<sub>T</sub> present as CO<sub>2</sub> is also affected by temperature (Figure 10). As the ocean warms, less C<sub>T</sub> will be partitioned into the form of CO<sub>2</sub> (and more as CO<sub>3</sub><sup>2-</sup>), hence enhancing the buffering and providing a negative feedback on rising atmospheric CO<sub>2</sub>. But the warming of the ocean surface decreases the solubility of the CO<sub>2</sub> gas, which greatly outweighs the negative feedback described above. This means that as the ocean surface warms, even more of the emitted CO<sub>2</sub> will remain in the atmosphere.

Although acidification occurs in the world ocean, it presents marked regional differences due to the different processes that influence the seawater CO<sub>2</sub> system. For example, the impacts of ocean acidification tend to be stronger in the high latitude oceans due their higher Revelle factors in combination with their colder surface temperatures (Orr et al., 2005; McNeil and Matear, 2008). In fact, the waters north of Iceland are acidifying at a rate of 5% per decade (Olafsson et al., 2009), whereas the waters from the western North Pacific Ocean (south of Japan) acidify at a rate of 3% per decade (Midorikawa et al., 2010). Moreover, while the CO<sub>2</sub> concentration in the surface ocean tracks the increasing values in the atmosphere, the CO<sub>2</sub> penetration into deep water depends on the slow vertical mixing of the water column and the transport of water masses. About half of the C<sub>ANT</sub> is found in the upper 400 m, while the other half penetrates to deeper layers of the ocean (Feely et al., 2004). However, in some regions where the vertical movement is relatively fast, i.e., in regions of water mass formation such as the North Atlantic, the timescale for deep penetration of C<sub>ANT</sub> is on the order of decades instead of centuries (Sabine et al., 2004), thus being faster exposed to the acidification effects.

Recent studies show that the current uptake of CO<sub>2</sub> by the oceans and subsequent acidification is about a hundred times faster than during the last Ice Age (20,000 years ago) (Feely et al., 2004; Raven et al., 2005). In fact, according to models, the average pH of ocean surface waters has decreased by about 0.1 units (equivalent to ~30% increase in [H<sup>+</sup>]) since the preindustrial era (Orr et al., 2005). Continuing emissions into the future may drive an additional 0.3–0.4 drop by the end of the century, even under optimistic scenarios (Caldeira and Wickett, 2005; Orr et al., 2005) (Figure 13). This projected decline in seawater pH might be three-times larger than the observed glacial–interglacial variability in seawater pH, and will probably occur ~100-times faster than during glacial terminations, when globally averaged surface seawater pH changed fastest over the last two million years (Pelejero et al., 2010). This rate of decrease far exceeds the regulation capability of natural Earth system feedbacks to restore the system to pre-industrial conditions, suggesting that the perturbation in ocean chemistry from the release of C<sub>ANT</sub> will take up to a million years to complete (Archer, 2005; Ridgwell and Zeebe, 2005). It also highlights the overwhelming challenge that faces the biology of the ocean in terms of adapting to changes which are several orders of magnitude greater than any seen over the past several million years (Hoegh-Guldberg et al., 2007).

The pH decrease results in a readjustment of all minor acid–base species, in addition to inorganic carbon and borate. These include a myriad of trace organic compounds, inorganic species such as phosphate and ammonium, and trace metals bound to inorganic or organic

compounds. The effect of pH on these chemical species is of interest because several are important nutrients and the chemical forms affect bioavailability. Therefore, there is growing concern about how ocean acidification may impact marine organisms at a range of levels, from molecular to physiological and developmental processes, and competitive interactions among organisms to food web dynamics and hence global biogeochemical cycles, and climate. However, the better studied, and potentially more serious, implication of ocean acidification on marine life is that affecting the calcifying marine organisms, such as coccolithophores, foraminifera and corals. Those organisms produce CaCO<sub>3</sub> skeletons that can dissolve as ocean acidification proceeds. While modern surface ocean waters (where the majority of carbonate-secreting organisms live) are generally supersaturated ( $\Omega > 1$ ), there are regions of the ocean surface which are already close to undersaturation (Figure 14). The area covered by undersaturated waters is increasing due to shoaling of the CaCO<sub>3</sub> saturation horizon ( $\Omega = 1$ ) by around 1 m·yr<sup>-1</sup> caused by ocean acidification (Turley et al., 2010), ultimately reaching the surface in certain regions. High latitude surface waters will be some of the first to become undersaturated, later this century (Orr et al., 2005). In addition, because CaCO<sub>3</sub> saturation decreases with increasing pressure, organisms living at depth in areas with fast CO<sub>2</sub> uptake will on average be exposed to undersaturated waters before surface dwelling organisms, a process which is predicted to start to occur by 2080 (Guinotte et al., 2006).

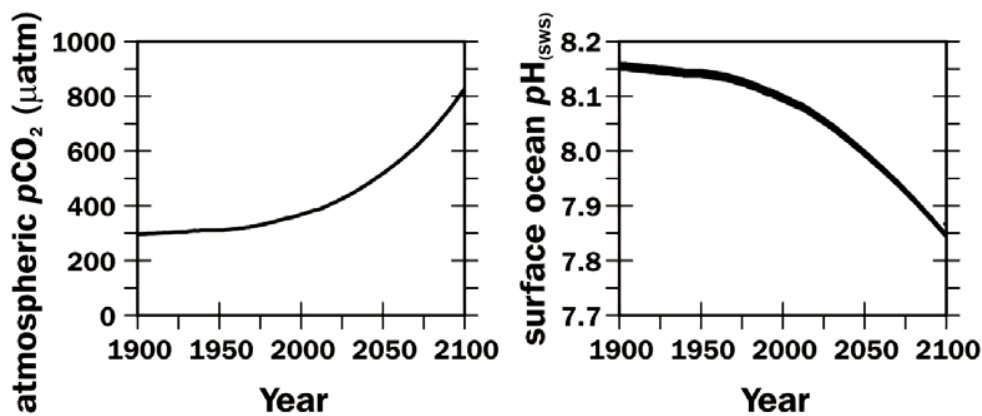


Figure 13.- Global ocean surface average of atmospheric partial pressure of CO<sub>2</sub> (pCO<sub>2</sub>) (left) and pH at Seawater Scale (pH<sub>sws</sub>) (right). Source: Turley et al. (2010).

### 1.3.3.- Anthropogenic Carbon and Seawater

With the onset of the Industrial Revolution in the eighteenth century, humanity has released large amounts of CO<sub>2</sub> into the atmosphere ( $C_{ANT}$ ), resulting in a progressive increase of the atmospheric CO<sub>2</sub> levels. The global ocean has absorbed ~30% of the  $C_{ANT}$  emitted to the atmosphere between 1750 and 2013 (DeVries, 2014; Le Quéré et al., 2014), thus minimizing the GHG effect, and reducing potential heating by emissions. The prediction of the amount of  $C_{ANT}$  that can be absorbed by the ocean needs the determination of the oceanic uptake of  $C_{ANT}$  and the net air-sea CO<sub>2</sub> fluxes at regional and global scales. Quantifying the uptake and storage of  $C_{ANT}$  in the interior ocean requires a distinction between the natural and anthropogenic contributions to changes in  $C_T$  over time. But estimating the storage of  $C_{ANT}$  in the ocean is a difficult task for a variety of reasons. First,  $C_{ANT}$  is not a directly measurable quantity, since it is not distinguishable from natural CO<sub>2</sub> (except for its isotopic signature); it has to be inferred using indirect means. Second, the  $C_{ANT}$  signal in the ocean is only a small perturbation (of the order of ~3%) on the



natural or preindustrial background distribution of carbon. A further complication is that carbon in the ocean participates in complex in situ biogeochemical processes. Lastly, the  $C_{ANT}$  distribution in the ocean is rather heterogeneous. As a consequence, unlike the atmosphere, which is relatively well mixed and where observations (both direct and from ice cores) extend back many thousands of years, the ocean is much more challenging in this regard. Reason why much effort has been devoted to study the accumulation, spatiotemporal distribution and transport of  $C_{ANT}$  in the ocean.

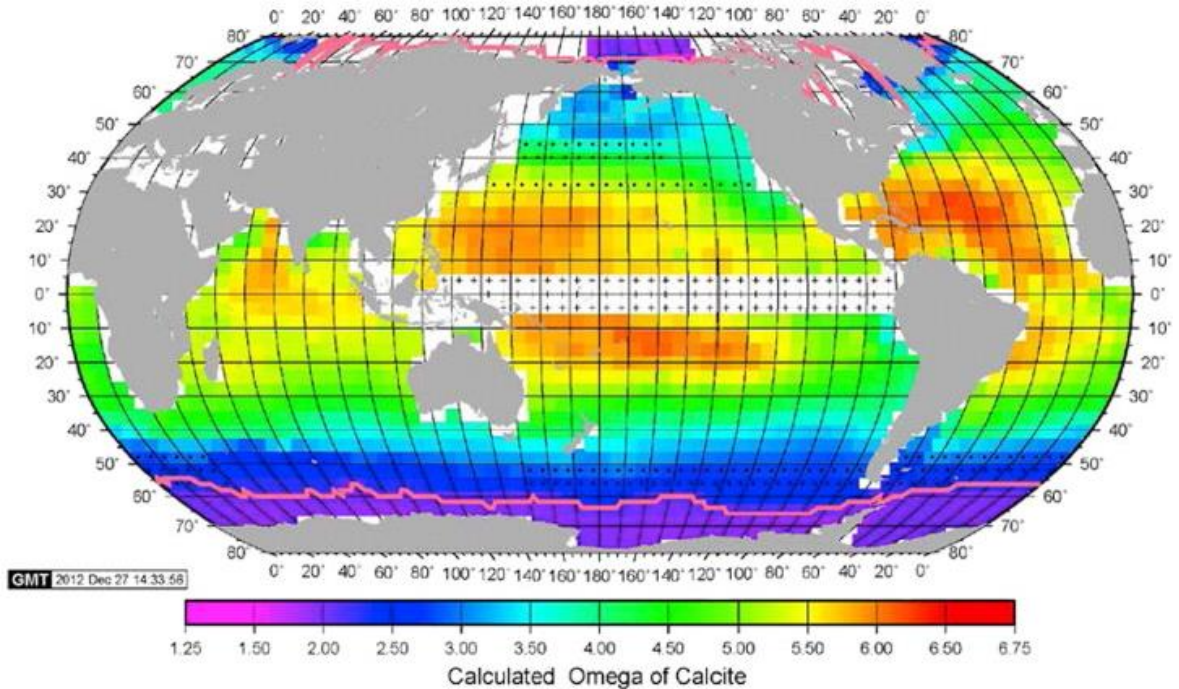


Figure 14.- The climatological mean distribution of aragonite saturation level (omega) in the global ocean surface water in August for the reference year 2005. The pink curves indicate the positions of the mean equatorward front of seasonal ice fields. The “+” symbol indicates the box areas affected by the El Niño events, and no value is given. The boxes with black dots indicate transition zones between oceanographic regimes (such as subtropical to subpolar regimes), where the omega values are highly variable. These values are interpolated from the adjacent box values. Note that the Arctic Ocean is slightly undersaturated (omega < 1), whereas the seasonal ice zone in the Southern Ocean is 10% to 20% above the saturation. Source: Takahashi et al. (2014).

Several methods have therefore been developed to estimate  $C_{ANT}$ . Fundamentally, these calculations are approached either by (1) back-calculation methods based on measurements of the seawater CO<sub>2</sub> system, together with biogeochemical variables such as O<sub>2</sub> and nutrients, or (2) based on measurements of transient tracers that provide information about the ventilation characteristics of the interior ocean. All observationally based  $C_{ANT}$  methodologies to date rely on the assumption that  $C_{ANT}$  penetrates the ocean as a passive, inert tracer responding to an evolving history in surface waters.

Back-calculation methods attempt to separate the small anthropogenic perturbation from the large background distribution of carbon based on the premise that the  $C_{ANT}$  concentration can be isolated from measured  $C_T$  values ( $C_m$ ) by subtracting the contribution of the biological pumps ( $\Delta C_{bio}$ ) and the physical processes involving the preindustrial end-members and the effects of the solubility pump ( $C_{phys}$ ):

$$C_{ANT} = C_m - \Delta C_{bio} - C_{phys}$$

This general approach is based on the assumption that ocean circulation and the biological pump have operated in steady state since preindustrial times. These approaches correct for the biological term using changes in  $A_T$  to estimate the CaCO<sub>3</sub> effect and apparent oxygen utilization (AOU; the difference between the O<sub>2</sub> at saturation and the measured O<sub>2</sub> concentration (Ito et al., 2004)) together with a Redfield ratio to correct for changes due to organic matter decomposition. Back-calculation methods include the  $\Delta C^*$  method (Gruber et al., 1996), and variations thereof such as the  $\phi C_T^0$  method (Vázquez-Rodríguez et al., 2009a) and the TrOCA (tracer combining O<sub>2</sub>, C<sub>T</sub> and A<sub>T</sub>) method (Touratier et al., 2007).

The  $\Delta C^*$  and  $\phi C_T^0$  methods are mainly based on the principles of the back-calculation  $C_T^0$  method established by Brewer (1978) and Chen and Millero (1979). The main difference between  $C_T^0$  and the other two techniques is in how the  $C_{phys}$  term is handled. The first fundamental difference between them is how they approach the changes in the properties of the subsurface waters. In the  $C_T^0$  method the changes of the properties of the subsurface layer are referenced to the mean deep-water values. In the  $\Delta C^*$  approach the water column is divided into isopycnal intervals and the changes of the properties of the subsurface layer are referenced back to the outcrop region for each interval. In the  $\phi C_T^0$  method the data of the sub-surface layer (100–200 m) is used as reference, thus avoiding biases due to the seasonal variability of surface properties. The  $\Delta C^*$  and  $\phi C_T^0$  techniques also take a different approach to estimating the  $C_{phys}$ . Rather than attempting to determine a preformed  $C_T$  ( $C_T^0$ ) concentration based on an empirical relationship between temperature and  $C_T$ , as the  $C_T^0$  method does, the  $C_{phys}$  term is divided into two terms: (i) the amount of  $C_T$  that the waters would have in equilibrium with a preindustrial atmosphere ( $C_{eq}$ ) and (ii) a term that corrects for the fact that, because CO<sub>2</sub> gas exchange is slow relative to the surface water biological and physical processes that can change CO<sub>2</sub>, surface waters are rarely in complete equilibrium with the atmosphere ( $C_{diseq}$ ).

$$C_{ANT} = C_m - \Delta C_{bio} - C_{phys} - C_{eq} - C_{diseq} = C^* - C_{diseq}$$

where  $C^* = C_m - \Delta C_{bio} - C_{phys} - C_{eq}$ , as defined by Gruber et al. (1996).

The disequilibrium term is by far the largest fraction of the preformed concentration and can be calculated using the equilibrium inorganic carbon constants, preformed  $A_T$ , and the preindustrial atmospheric CO<sub>2</sub> concentration. The main difference between the  $\Delta C^*$  and  $\phi C_T^0$  methods lies in the treatment of  $A_T$  and the disequilibrium term. While the  $\Delta C^*$  method assumes  $A_T$  and the disequilibrium to be constant, the  $\phi C_T^0$  method takes into account the temporal variability of both terms.

The TrOCA method, which means Tracer combining Oxygen, C<sub>T</sub> and A<sub>T</sub>, estimates  $C_{ANT}$  based on one equation valid for the world ocean:

$$C_{ANT} = \frac{\text{TrOCA} - \text{TrOCA}^0}{a}$$

where TrOCA is a tracer which temporal variation is directly related to the  $C_{ANT}$  accumulation,  $\text{TrOCA}^0$  is a quasi-conservative tracer similar to TrOCA, and  $a$  is a constant, which value is  $1.279 \pm 7.3 \cdot 10^{-3}$ . The TrOCA tracer can be determined by the expression:

$$\text{TrOCA} = O_2 + 1.279 \left( C_T - \frac{1}{2} A_T \right)$$

The quasi-conservative tracer  $\text{TrOCA}^0$  is the surface boundary condition of the artificial tracer TrOCA, i.e., the TrOCA value that a water mass would have at the time of its formation in pre-industrial atmospheric conditions. The quasi-conservative tracer is similar to those of NO and PO (Broecker, 1974). The  $\text{TrOCA}^0$  value was estimated by regressing TrOCA against  $\theta$  and  $A_T$ :

$$\text{TrOCA}^0 = e^{\left[7.511 - (1.087 \cdot 10^{-2})\theta - \frac{7.81 \cdot 10^5}{A_T^2}\right]}$$

Equation proposed by Touratier et al. (2007) based on the study of the distributions of  $\Delta^{14}\text{C}$  and CFC-11 in the Indian Ocean. The TrOCA method assumes that (i)  $A_T$  is constant over time; (ii) the surface layers of the ocean present an  $\text{O}_2$  concentration equal to saturation; and (iii) the values of  $A_T$  and  $\text{O}_2$  are not affected by the rise in atmospheric  $\text{CO}_2$ .

Transient tracer-based methods treat  $C_{\text{ANT}}$  as a passive tracer with a well-known input function that can be calculated with the knowledge of the ocean ventilation rates. These approaches use the fact that the  $C_{\text{ANT}}$  concentration at any point in the ocean interior should be related to the history of the  $C_{\text{ANT}}$  concentration at the surface and the spectrum of times it took the water to reach the interior ocean location. These methods are based on measures of other tracers to estimate the transport from the surface mixed layer into the ocean. However, it is difficult to find a tracer that behaves like  $\text{CO}_2$ . Most of the considered tracers are non-reactive gases, unlike  $\text{CO}_2$ . Moreover, many of the tracers used are post- $C_{\text{ANT}}$  and, therefore, their penetration and transport to certain regions will depend much on the year of introduction. The most commonly used transient tracer-based approaches are the transit time distribution (TTD) method (e.g., Hall et al., 2002, 2004; Waugh et al., 2004) and the more complex variation thereof, i.e., the “Green Function method” (Khatiwala et al., 2009). The transient tracer-based methods are based in the radioactive transient tracers ( $^{39}\text{Ar}$ ,  $^{14}\text{C}$  or tritium) or in the so-called transient anthropogenic tracers (CFCs,  $\text{SF}_6$  or  $\text{CCl}_4$ ). By measuring the concentration of these tracers it is possible to estimate the age of the water masses and, therefore, their  $C_{\text{ANT}}$  concentration at the time they were formed. These methods assume that the tracer concentration in the ocean interior reflects the surface concentration at the time of the water mass formation. The surface history is estimated using the equilibrium inorganic carbon chemistry equations, temperature, the preformed  $A_T$  (estimated from S), and the atmospheric  $\text{CO}_2$  record. Thus, the age of a water mass is determined by the difference between the sampling year and the year in which the tracer’s surface concentration was equal to the sample concentration. Taking into account the ocean mixing processes, the age is determined through a probability function of transit times or TTD (e.g., Hall and Plumb, 1994; Beining and Roether, 1996; Delhez et al., 1999; Haine and Hall, 2002), which are approximated by inverse Gaussian functions, known as Green’s function, i.e., a solution to the advection–diffusion equation for the ocean with an impulse boundary condition at the surface of the ocean. Each tracer, due to their different boundary conditions or decay rates, will result in different ages. The approach then only requires measurements of temperature, S and a transient tracer if one assumes that biology is not involved, that circulation is in steady state, and that a single surface source region dominates the interior water so there is no spatial dependency in the source waters. Based on the TTD technique, Khatiwala et al. (2009) developed an inverse technique to apply the full Green function formalism known as “Green function method”. Specifically, they (i) applied a maximum entropy deconvolution technique (Tarantola, 2005) to constrain the Green function with multiple steady and transient tracers and thus account for the mixing of waters of both different ages and different end-member types and (ii) allowed the air–sea

disequilibrium to evolve in space and time. In order to estimate the  $C_{ANT}$  surface history, they impose the condition that the rate of change of inventory of  $C_{ANT}$  is equal to the instantaneous air–sea flux of  $C_{ANT}$ . The latter flux is proportional to the change in surface disequilibrium of CO<sub>2</sub> relative to the preindustrial disequilibrium, which, in turn, is assumed to be proportional to the  $C_{ANT}$  perturbation in the atmosphere (Matsumoto and Gruber, 2005). Khatiwala et al. (2009) applied this method to gridded fields of six different tracers from the GLODAP data set (CFC-11, CFC-12, natural <sup>14</sup>C, S, temperature, and PO<sub>4</sub><sup>\*</sup> (Broecker et al., 1998)) to arrive at the first data-based estimate of the time-evolving, three-dimensional history of  $C_{ANT}$  in the ocean over the industrial period.

Another methodologies estimate directly the  $C_{ANT}$  inventory. One of them is based on multiple linear regression (MLR) techniques (Wallace, 1995) or extended MLR (eMLR) techniques (Friis et al., 2005). The MLR/eMLR techniques compare the  $C_T$  changes from two hydrographic occupations along the same transect separated in time, thus allowing the assessment of  $C_T$  and  $C_{ANT}$  changes along isopycnal surfaces. These techniques take advantage of the exponential nature of the atmospheric  $C_{ANT}$  increase and explore the transient steady state concept (Gammon et al., 1982). An exponentially changing tracer will, after a certain time, reach transient steady state, meaning that, e.g., a depth profile of  $C_{ANT}$  will have constant shape over time, and the concentrations will increase proportionally to the surface layer increase. This way of calculating the  $C_{ANT}$  concentration has the advantage that assumptions such as the preindustrial air–sea disequilibrium become irrelevant, since it will cancel out in the comparison. The MLR method creates a predictive equation for  $C_T$  from the available hydrographic and chemical parameters, and  $C_{ANT}$  is estimated as the residual between the predicted and the observed  $C_T$ . Firstly, for the earlier cruise, a mathematical relationship is derived between the measured  $C_T$  and the values of the ancillary properties, which are independent of increasing  $C_{ANT}$  and represent the natural processes affecting  $C_T$ : water mass mixing, organic matter formation/remineralisation and CaCO<sub>3</sub> formation/dissolution. The derived MLR is used to compute the residuals  $C_{residual,1}^{MLR}$ . Subsequently, for the latter cruise, the MLR relationship of the first cruise is combined with the ancillary values of the second cruise to derive  $C_{residual,2}^{MLR}$ . Finally, by comparison of the depth profiles of  $C_{residual,1}^{MLR}$  and  $C_{residual,2}^{MLR}$  the apparent increase due to  $C_{ANT}$  is derived. The eMLR approach extends the MLR approach by creating a second predictor equation for the more recent cruise dataset. The eMLR is favoured for minimising the error propagation and providing a smoother spatial structure, eliminating the effect of water mass motion on the predictor variables. However, the resulting non-Gaussian residual distributions suggest that part of the real  $C_T$  signal remains in the residuals (Brown et al., 2010). As described in Brown et al. (2010), the value of an eMLR generated anthropogenic signal relies on the ability in the selection of the predictor variables. The main caveat is the necessity to assume that the ocean is in steady state, i.e., the relationships between the predictors and  $C_T$  are time invariant. For instance,  $C_{ANT}$  input causes  $C_T$  change without affecting the concentration of the predictor variables.

Although substantial differences were observed between the results obtained with the different methodologies, it is still very difficult to determine which method gives the best estimates. Vázquez-Rodríguez et al. (2009b) compared the  $C_{ANT}$  estimates for the Atlantic Ocean resulting from different methodologies and conclude that the  $C_{ANT}$  inventory estimates obtained with the  $\phi C_T^0$  method are in close agreement with those resulting from the TTD method and in reasonable agreement with the  $\Delta C^*$  estimates. Based on this, in this thesis, the  $C_{ANT}$




concentrations were estimated by the  $\phi C_T^0$  method, and contrasted with the estimated by the  $\Delta C^*$  method.



PART II.- AIM OF THE STUDY AND DATA

I KNOW A PLACE WHERE THE SUN NEVER SHINES.



IT'S AT THE BOTTOM OF THE OCEAN.

A CRACK IN THE CRUST THERE EXUDES CHEMICALS AND HEATS THE WATER TO BOILING POINT.

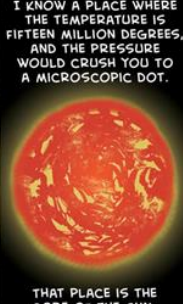


THIS WOULD KILL A HUMAN INSTANTLY.




BUT THERE ARE CREATURES THERE, BACTERIA, THAT THRIVE THEY EAT THE SULFUR FROM THE VENT, AND EXCRETE SULFURIC ACID.

I KNOW A PLACE WHERE THE TEMPERATURE IS FIFTEEN MILLION DEGREES, AND THE PRESSURE WOULD CRUSH YOU TO A MICROSCOPIC DOT.



THAT PLACE IS THE CORE OF THE SUN.

I KNOW A PLACE WHERE THE MAGNETIC FIELDS WOULD RIP YOU APART, ATOM BY ATOM.



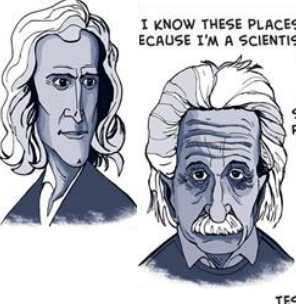
THE SURFACE OF A NEUTRON STAR, A MAGNETAR.

I KNOW A PLACE WHERE LIFE BEGAN, BILLIONS OF YEARS AGO.



THAT PLACE IS HERE, THE EARTH.

I KNOW THESE PLACES BECAUSE I'M A SCIENTIST.



SCIENCE IS A WAY OF FINDING THINGS OUT.

IT'S A WAY OF TESTING WHAT'S REAL.

IT'S WHAT RICHARD FEYNMAN CALLED:



A WAY OF NOT FOOLING OURSELVES.

YOU CAN EXPERIENCE THE THRILL OF DISCOVERY, THE INCREDIBLE, VISCERAL FEELING OF DOING SOMETHING NO ONE HAS EVER DONE BEFORE, SEEN THINGS NO ONE HAS SEEN BEFORE.



KNOW SOMETHING NO ONE ELSE HAS EVER KNOWN.




WELCOME TO SCIENCE.

YOU'RE GONNA LIKE IT HERE.  
-PHIL PLAIT



# PARTE II.- OBJETIVO DE LA TESIS Y DATOS

CONOZCO UN LUGAR DONDE EL SOL NUNCA BRILLA.



ESTÁ EN EL FONDO DEL OCEANO

UNA GRIETA EN LA CORTEZA QUE EXUDA SUSTANCIAS TÓXICAS Y CALIENTA EL AGUA HASTA EL PUNTO DE EBULlicIÓN.



ESO MATARÍA A UN SER HUMANO AL INSTANTE.

PERO HAY CRIATURAS AHÍ, BACTERIAS, QUE PROSPERAN ALIMENTÁNDOSE DEL AZUFRE QUE EMANA Y EXCRETANDO ÁCIDO SULFÚRICO.



CONOZCO UN LUGAR DONDE LA TEMPERATURA ES DE 15 MILLONES DE GRADOS, Y LA PRESIÓN TE APLASTARÍA HASTA UN PUNTO MICROSCÓPICO.



ESE LUGAR ES EL NÚCLEO DEL SOL.

CONOZCO UN LUGAR DONDE LOS CAMPOS MAGNÉTICOS TE DESPEDAZARÍAN, ÁTOMO POR ÁTOMO.



LA SUPERFICIE DE UNA ESTRELLA DE NEUTRONES, UN MAGNETAR.

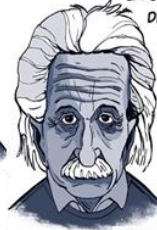
CONOZCO UN LUGAR DONDE LA VIDA COMENZÓ HACE MILES DE MILLONES DE AÑOS.



ESE LUGAR ES AQUÍ, LA TIERRA.



CONOZCO ESTOS GARES PORQUE SOY UN CIENTÍFICO. LA CIENCIA ES UNA FORMA DE DESCUBRIR COSAS.



ES UNA FORMA DE PROBAR LO QUE ES REAL.

ES LO QUE RICHARD FEYNMAN LLAMÓ:

UNA FORMA DE NO ENGAÑARNOS A NOSOTROS MISMOS



PUEDÉS EXPERIMENTAR LA EMOCIÓN DEL DESCUBRIMIENTO, EL INCREÍBLE, EL VISCERAL SENTIMIENTO DE HACER LO QUE NADIE ANTES HABÍA HECHO, DE VER LO QUE NADIE ANTES HABÍA VISTO.



SABER ALGO QUE JAMÁS HA SABIDO NADIE ANTES




BIENVENIDO A LA CIENCIA

TE VA A GUSTAR ESTAR AQUÍ

-PHIL PLAIT



## Chapter 2.- Acidification and transports of water masses and CO<sub>2</sub> in the North Atlantic: Aim of the PhD

---

The oceans are an essential part of the Earth's climatic system by virtue of their large capacity to store and transport heat. Additionally, they have an immense capacity to absorb and store the excess of (or anthropogenic) CO<sub>2</sub> in the atmosphere derived from human activities.

The CATARINA (CARbon Transport and Acidification Rates In the North Atlantic) project proposes an innovative research to study the oceanic perturbation and its consequences in response to the rise of the atmospheric CO<sub>2</sub> due to human activities at different timescales. The main goals of the CATARINA project are organized in two main activities: (i) circulation in the North Atlantic and the anthropogenic CO<sub>2</sub> (C<sub>ANT</sub>) uptake, and (ii) past and recent acidification impacts. Concretely, the main objectives are:

- To quantify the Meridional Overturning Circulation (MOC) and water mass ventilation changes and their effect on the changes in the oceanic uptake of C<sub>ANT</sub> and storage capacity.
- To evaluate the effect of present and past atmospheric CO<sub>2</sub> concentrations in the production and preservation of CaCO<sub>3</sub> in the North Atlantic.

This dissertation is part of the CATARINA project and directly contributes to accomplish the CATARINA objectives since it thoroughly analyses the water mass structure, circulation and transformation in the Subpolar North Atlantic, as well as the contribution of each water mass to the Atlantic MOC. It also quantifies the acidification trends for the Irminger and Iceland Basins and its impacts on the CaCO<sub>3</sub> saturation.

The CATARINA project contributes to continue the sampling along the WOCE (World Ocean Circulation Experiment) A25 Greenland–Portugal hydrographic section whose first occupation was in 1997 and then it was repeated every other year from 2002 to 2010 within the OVIDE (Observatoire de la Variabilité Interannuelle et DÉcennale en Atlantique Nord) project. The CATARINA cruise was carried out in June–July 2012.

Each chapter of this PhD is designed as an independent entity, and structured as a typical publication in a scientific journal, through sections such as abstract; introduction; data set and methods; results and discussion; and conclusions. All of them are also preceded by a summary in Spanish. Each chapter contributes to the accomplishment of the specific objectives of this dissertation:

- Determination of the water mass distribution, transport and transformation in the Subpolar North Atlantic region (Chapter 4). The water mass structure of the WOCE A25 Greenland–Portugal hydrographic sections was solved by an Optimum MultiParameter (OMP) analysis, performing a detailed study of the inter-annual to decadal variability of the most prominent water masses of the Subpolar North Atlantic

region. The results from the OMP analysis were combined with the velocity fields (calculated by the LPO-IFREMER group) to obtain the water mass transports and their contributions to the Atlantic MOC. The results also give insights about the water mass transformations within the Subpolar North Atlantic region.

- Evaluation of the trends of the stressors of the seawater  $\text{CO}_2$  system in the Subpolar North Atlantic region (Chapter 5). The trends of  $C_{\text{ANT}}$  and its effects on pH and  $\text{CaCO}_3$  saturation, as well as the changes in alkalinity were evaluated in the Irminger and Iceland Basins for the last three decades, concretely for the period 1981–2014. In order to disentangle the drivers of the pH changes, the pH changes were decomposed into those directly related to the  $C_{\text{ANT}}$  absorption and those indirectly related to the  $C_{\text{ANT}}$  uptake or caused by natural processes.
- Evaluation of the  $C_{\text{ANT}}$  transports (Chapter 6). The inter-annual to decadal variability of the  $C_{\text{ANT}}$  transport across the Subpolar North Atlantic region was studied by coupling the results of geostrophic inverse models with the  $C_{\text{ANT}}$  estimates of the WOCE A25 sections. The transport of  $C_{\text{ANT}}$  was decomposed according to the net, the diapycnal and the isopycnal circulation in order to understand the mechanisms controlling the variability of the  $C_{\text{ANT}}$  transport.

This dissertation ends with the main conclusions derived of this work.



## Chapter 3.- Oceanographic cruises in the North Atlantic

An important component of the Meridional Overturning Circulation (MOC) takes place at high latitudes of the North Atlantic Ocean. The warm and salty upper waters transported northwards by the Gulf Stream and the North Atlantic Current (NAC) gain  $\text{CO}_2$  as they cool. Once they reach the North Atlantic Subpolar Gyre, these  $\text{CO}_2$ -laden waters are transformed into subpolar waters and eventually reach the Labrador and Nordic Seas, where they sink transporting  $\text{CO}_2$  to the ocean interior where it remains sequestered for centennial timescales. The heat and  $\text{CO}_2$  exchanges that happen during this circulation result in the Atlantic MOC playing an active role in the regulation of the European climate and in the North Atlantic Ocean as one of the greatest  $\text{CO}_2$  sinks of the global ocean.

For all these reasons, there are an increasing number of cruises conducted in the North Atlantic Ocean (Figure 15) to study in more detail, not only the biogeochemical cycles and their possible disruption, but also the physical processes, such as currents, transports and formation rates of the water masses. Since repeated sections allow studying the patterns and/or changes in the circulation and transport of both the water masses and the most relevant biogeochemical variables, the main scientific effort has been directed to the research programs focused on the repetition of oceanographic sections (Figure 16). Concretely, this dissertation focuses on the study of the Greenland to Portugal WOCE (World Ocean Circulation Experiment) A25 section that has been repeated eight times thanks to the joint action of the OVIDE (Observatoire de la Variabilité Interannuelle et DÉcennale en Atlantique Nord), CATARINA (CARbon Transport and Acidification Rates In the North Atlantic) and GEOVIDE (An international GEOTRACES study along the OVIDE section in the North Atlantic and in the Labrador Sea) projects.

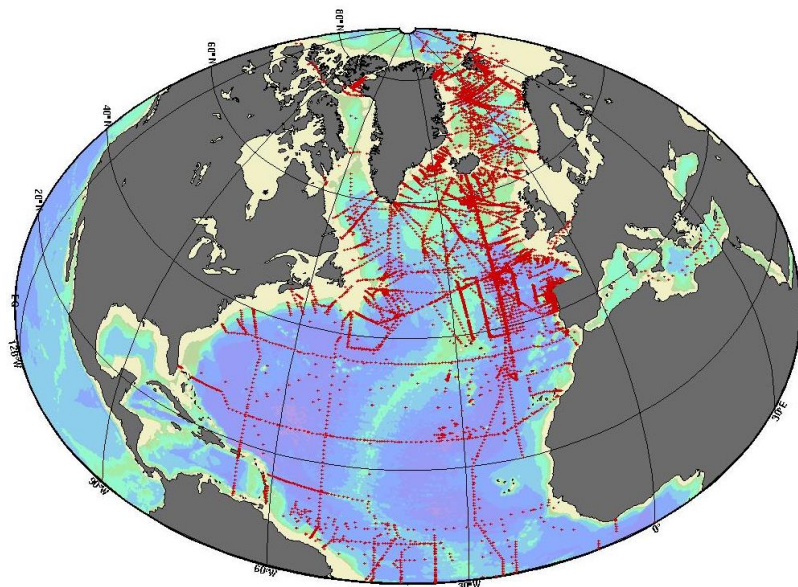


Figure 15.- Cruises conducted in the North Atlantic Ocean included in the international database CARINA (CARbon dioxide IN the Atlantic Ocean). Source: <http://cdiac.ornl.gov/oceans/CARINA>.



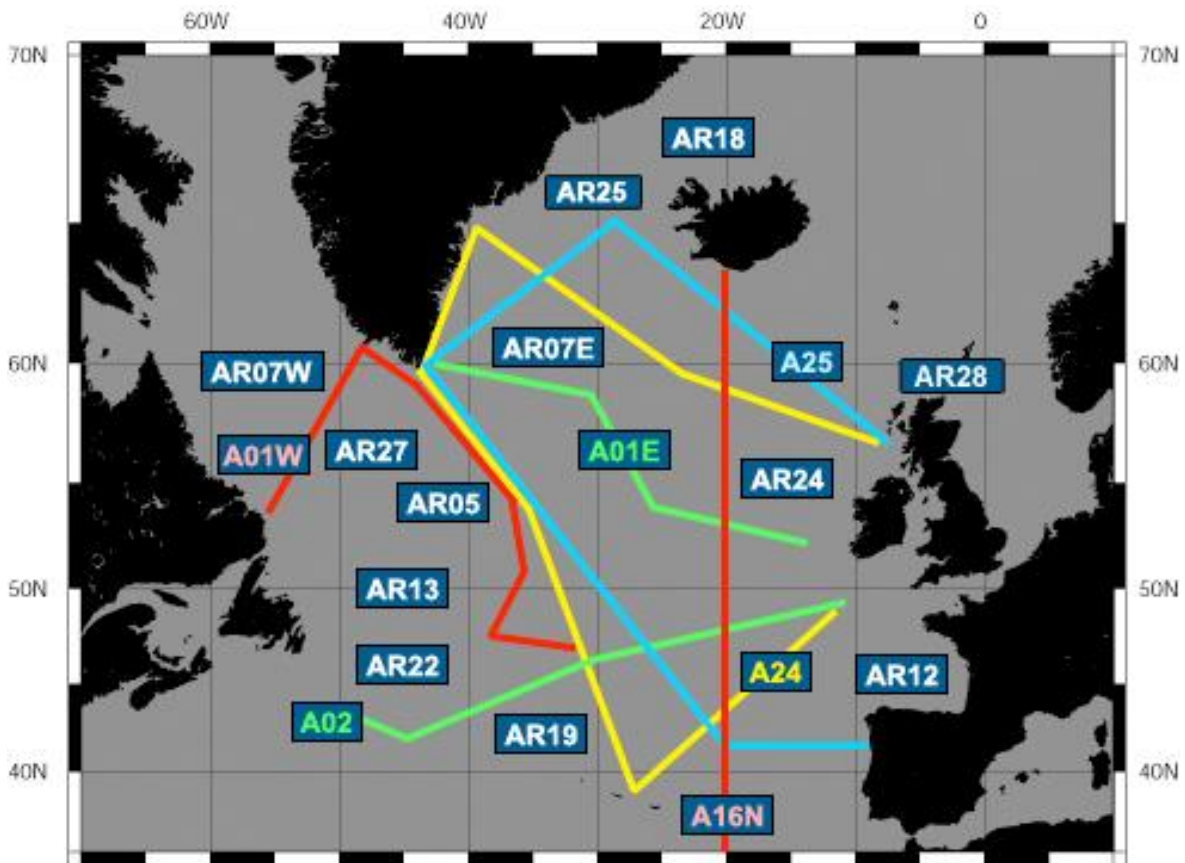


Figure 16.- Repeated sections conducted in the North Atlantic Ocean included in the international database CCHDO (CLIVAR and Carbon Hydrographic Data Office). Source: <http://cchdo.ucsd.edu>.

### 3.1.- WOCE A25 section

The WOCE A25 Greenland–Portugal hydrographic section crosses the main currents of the North Atlantic Subpolar Gyre and some regions where water mass formation takes place (Figure 17). This section also crosses the main currents of the Subpolar Gyre, i.e., the NAC and the East Greenland Current, as well as the overflows from the Nordic Seas and the Arctic Ocean. Therefore, this oceanographic section allows studying a wide variety of water masses coming from the Greenland, Norway, Labrador and Mediterranean Seas, even from the Antarctic Ocean. The long-term time-series of this section allows evaluating the inter-annual to decadal variability in the surface currents, the Atlantic MOC, the ventilation of the water masses, and the anthropogenic carbon ( $C_{ANT}$ ) storage and transport. The WOCE A25 section is part of the CLIVAR/IOCCP (Climate and Ocean: Variability, Predictability, and Change / International Ocean Carbon Coordination Project) and GOSHIP (Global Ocean Ship-based Hydrographic Investigations Project) international programs.

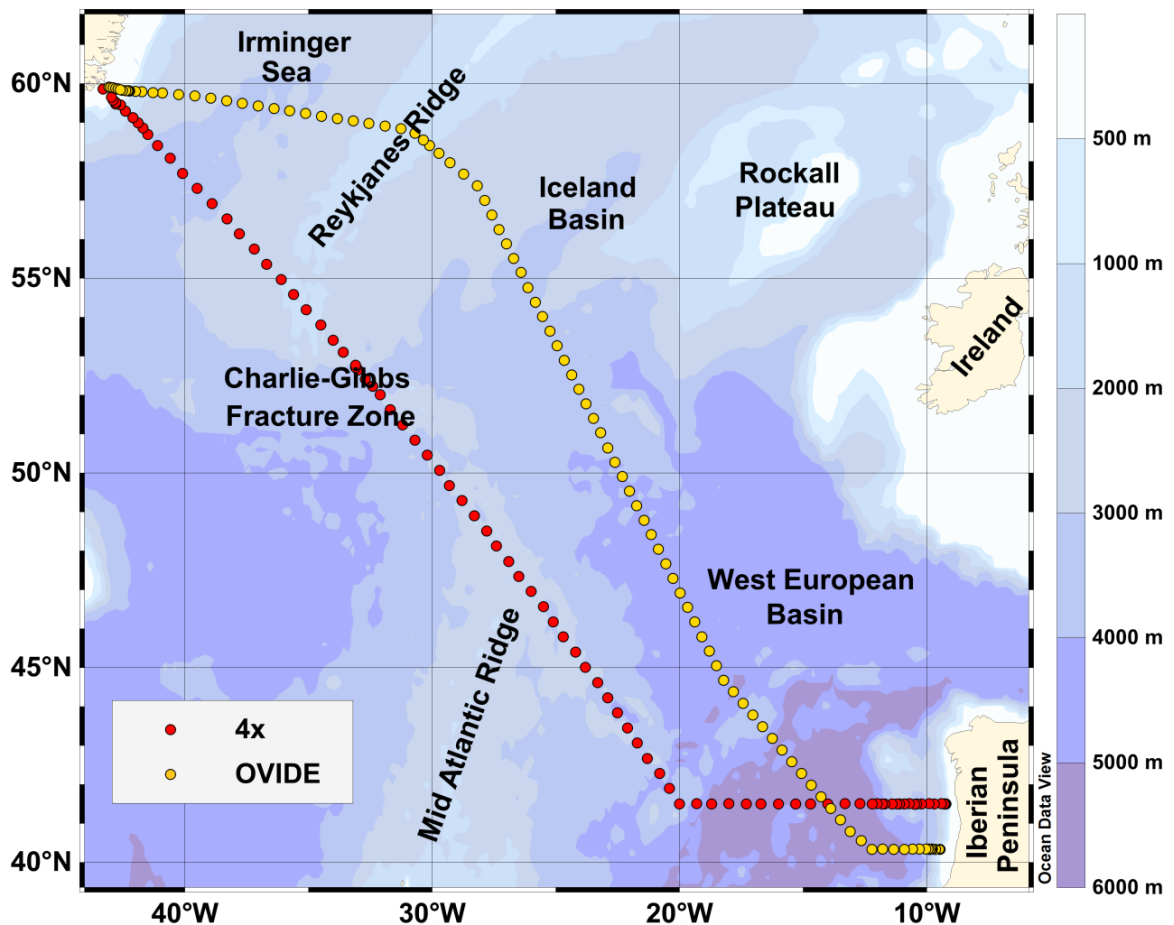


Figure 17.- Location of the 4x and OVIDE hydrographic stations and major topographical features of the Subpolar North Atlantic.

The first sampling of the WOCE A25 section was conducted during the 4x section in August 1997 as part of the WOCE. The cruise was called 4x because it is a repeat of the section 4 sampled during the International Geophysical Year (Dietrich, 1969). In summer 2002 the cruise

was repeated again in the frame of the OVIDE project, slightly changing the section pathway to better characterize the main currents in the Subpolar North Atlantic. The OVIDE line was specially designed to run perpendicularly across the main North Atlantic currents to minimize the transports due to eddies. Since then, it has been repeated every other summer until 2014. The 2012 cruise was held by the CATARINA project and the 2014 cruise by the GEOVIDE project. The section is going to be repeated again in 2016 in the frame of the BOCATS (Biennial Observation of Carbon, Acidification, Transport and Sedimentation in the North Atlantic) project led by the CSIC (Consejo Superior de Investigaciones Científicas). Cruise data is available in the CCHDO (CLIVAR & Carbon Hydrographic Data Office) webpage (<http://cchdo.ucsd.edu>).

The main goal of WOCE is to determine the large-scale oceanic circulation as a basis for developing and testing ocean circulation models and coupled climate-change models.

The OVIDE project, led by IFREMER (Institut Français de Recherche pour l'Exploitation de la MER), aims to document and understand the variability of both the circulation and the properties of the water masses in the northern North Atlantic within the context of global change. The OVIDE project contributed to PNEDC (Programme National d'Etude de la Dynamique du Climat) and to the international program CLIVAR.

The CATARINA project, led by CSIC, aims to study the MOC and the ventilation of the water masses in the North Atlantic, as well as the consequences of the  $C_{ANT}$  uptake at different timescales. The CATARINA project is part of the international program IMBER (Integrated Marine Biogeochemistry and Ecosystem Research).

The main scientific objectives of the GEOVIDE project are: (i) to better know and quantify the MOC and the carbon cycle in a decadal variability context, adding new key tracers; (ii) to map the distribution of the trace elements with their physical and chemical speciation; (iii) to investigate the link between the trace elements and the production, export and remineralisation of particulate organic matter; (iv) to identify the trace element sources and sinks and quantify their fluxes at the ocean boundaries; and (v) to better understand and quantify the paleoproxies  $^{231}\text{Pa}/^{230}\text{Th}$ ,  $\text{eNd}$  and  $\text{d}^{30}\text{Si}$ . The GEOVIDE project is part of the GEOTRACES international program, and also contributes to other international programmes, such as SOLAS (Surface Ocean Lower Atmosphere Study), IMBER, CARBOCHANGE and CLIVAR. The project was led by LEMAR (Laboratoire des sciences de l'Environnement MARin), CNRS (Centre National de la Recherche Scientifique), UBO (Université de Bretagne Occidentale), IRD (Institut de Recherche pour le Développement) and IFREMER.

The biennial repetition of the WOCE A25 section, with measurements of hydrographic and biogeochemical properties, allow to study the low-frequency fluctuations of the water masses, their circulation and transports, the MOC and the tracer transports; and also to estimate the  $C_{ANT}$  inventory (Lherminier et al., 2007, 2010; Thierry et al., 2008; Pérez et al., 2008).

### 3.1.1. - Measurements

At each station, continuous profiles of temperature, salinity (S) and dissolved oxygen ( $\text{O}_2$ ) were acquired from the surface to 15 m from the sea floor by using a Conductivity–Temperature–Depth (CTD) instrument incorporated to a rosette equipped with 24–28 Niskin bottles and

acoustic current meters. Measurements of geo-chemical variables were also performed from the sampling of the rosette Niskin bottles closed at different depths in the water column during the way up of the rosette. The depths at which the Niskin bottles were closed were distributed throughout the water column ensuring that all the water masses were sampled, which also allowed a better calibration of the CTD sensors. These measurements were supplemented by the velocity profiles performed with Acoustic Doppler Current Profilers (ADCPs).

Following the sampling procedures proposed during WOCE, the sequence of seawater samples was: O<sub>2</sub>, pH, total dissolved inorganic carbon (C<sub>T</sub>), total alkalinity (A<sub>T</sub>), nutrients and S.

#### **3.1.1.1.- CTD measurements**

During the cruises, the temperature, S and O<sub>2</sub> were continuously recorded from the full water column at each station by using a CTD instrument. In the cruises prior to 2008 a Neil Brown Mark III CTD probe was used, while in the subsequent cruises a SBE911plus (Sea-Bird Electronics) CTD probe was used. The CTD unit was equipped with dual temperature and conductivity sensors, a Digiquartz with TC pressure sensor, a SBE-43 oxygen probe, a SeaPoint fluorometer, a SeaPoint turbidimeter and an altimeter. The pressure sensor was calibrated in a metrology laboratory using 3 cycles of increasing–decreasing pressure between 0 and 6000 dbar. The static and dynamic effects of temperature on the pressure sensor were also estimated and corrected (Branellec and Thierry, 2013). The conductivity and O<sub>2</sub> sensors were calibrated using seawater S and O<sub>2</sub> samples. Overall, the CTD measurement accuracies were 1 dbar for pressure, 0.002°C for temperature, 0.003 for S and 1 μmol·kg<sup>-1</sup> for O<sub>2</sub> (Billant et al., 2004; Branellec and Thierry, 2013).

#### **3.1.1.2.- Oxygen (O<sub>2</sub>) sampling and measurement**

To calibrate the O<sub>2</sub> sensor, a minimum of 16 seawater samples at each station were used whose O<sub>2</sub> concentration was determined on board. The samples were drawn through short pieces of silicon tubing into clear, precalibrated, 120 mL glass bottles with plunger stopper. Sampling bottles were rinsed three times before taking the sample by filling the flask from the bottom, overflowing three times the equivalent volume of the vial, carefully avoiding the entry of bubbles. During the overflowing, the sample temperature was measured using a hand held electronic thermometer probe. Then, the sample was fixed (precipitation) with 0.6 mL of manganese chloride (MnCl<sub>2</sub> · 4H<sub>2</sub>O) and 0.6 mL of alkali-iodide solution (NaOH + NaI) iodide dispensed using precise repeat bottle top dispensers. Samples were then capped and shaken to ensure the complete chemical reaction. Samples were transferred to the analysis laboratory at a controlled temperature of 20°C (± 1°C), and then shaken again and stored in darkness for at least 24 hours until analysis to enable them to reach thermal equilibrium.

The O<sub>2</sub> concentration was determined by Winkler potentiometric titration following the WOCE standards (Culberson, 1991). Blank measurements were determined at the start of each run to account for the introduction of O<sub>2</sub> with the reagents and impurities in the MnCl<sub>2</sub>, as described in the WOCE Manual of Operations and Methods (Culberson, 1991). The samples were acidified prior to titration and stirred using a magnetic stir bar set at a constant spin. The titration was performed with a 0.02 N sodium thiosulphate solution, which normality was determined daily by comparison with a solution of potassium iodate with normality of 0.020013 N. Thiosulfate standardisation was carried out by adding the iodate after the other reagents and following on

directly from the blank measurements in the same flask. The dosing of the sodium thiosulfate solution was controlled by a titroprocessor associated with a platinum electrode, which measures the potential of the reaction. The volume of thiosulfate required for reduction of iodine was determined by the automatic determination of the inflection point in the curve of equivalence potential.

The uncertainty of the methodology was determined through the analysis of sample duplicates, i.e., by analysing two independent samples of the same depth in the water column, along the sections. The standard deviation of the duplicate differences was  $0.014 \text{ ml}\cdot\text{L}^{-1}$ . The precision of the  $\text{O}_2$  determination was better than  $1 \mu\text{mol}\cdot\text{kg}^{-1}$ .

### 3.1.1.3.- Total dissolved inorganic carbon ( $C_T$ ) sampling and measurement

Seawater samples for  $C_T$  were collected at selected depths of specific stations. Samples for  $C_T$  were taken directly from the Niskin bottles into 600 mL borosilicate glass bottles. Sampling bottles were washed twice with sample before filling the bottle from the bottom using a silicone pipe, overflowing half the equivalent volume of the bottle, while carefully avoiding the entry of bubbles. Then 0.3 mL of saturated aqueous solution of mercuric chloride was added to the sample to prevent biological alterations. The bottle was sealed with glass stoppers covered with Apiezon-L grease, leaving a headspace of 1% of the bottle volume. The samples were stored in the dark at room temperature until their analysis on land.

$C_T$  measurements were performed using the SOMMA (Single-Operator Multiparameter Metabolic Analysers) system (Johnson et al., 1987, 1993; Johnson and Wallace, 1992) coupled with a CM101\_093 coulometer. Prior to analyses, the samples were stored in the dark and thermally equilibrated at  $25^\circ\text{C}$  within the thermostated SOMMA system. The seawater sample was drawn into a calibrated pipette and dispensed into a stripping chamber, where it was acidified with 8.5%  $\text{H}_3\text{PO}_4$ . The resulting  $\text{CO}_2$  gas was carried by a free- $\text{CO}_2$  gas ( $\text{N}_2$ ) into a coulometric cell, where the coulometrical titration with ethanalamine was performed with photometric endpoint detection (Johnson et al., 1993). Following standard procedure, Certified Reference Materials (CRMs, distributed by A.G. Dickson from the Scripps Institution of Oceanography) were routinely analysed according to Dickson and Goyet (1994). The overall precision of the  $C_T$  analyses was  $1.6 \mu\text{mol}\cdot\text{kg}^{-1}$ .

$C_T$  was also determined from  $A_T$  and pH, using the equilibrium constants of the carbonic system of Mehrbach et al. (1973) refitted by Dickson and Millero (1987). The maximum error of the estimated  $C_T$  was  $2 \mu\text{mol}\cdot\text{kg}^{-1}$ , considering the uncertainties of  $A_T$  ( $1 \mu\text{mol}\cdot\text{kg}^{-1}$ ) and pH (0.0014), which is within the error of the  $C_T$  analysis (Lamb et al., 2001).

### 3.1.1.4.- pH sampling and measurement

Seawater samples for pH were collected at every depth level of each station. pH samples were taken directly from the Niskin bottles into special optical glass spectrophotometric cells of 28 mL of volume and 100 mm of pathlength. The cells were filled to overflowing and immediately stopped. Then they were stored in a thermostatic bath at  $25.0^\circ\text{C}$  around one hour before the analysis to ensure their stabilization at  $25^\circ\text{C}$ .

Seawater pH was measured using a double-wavelength spectrophotometric procedure (Clayton and Byrne, 1993). This method consists on adding an indicator solution to the seawater sample, so that the ratio between two absorbances at two different wavelengths is proportional to the sample pH. The indicator was an m-cresol purple solution prepared in seawater. All the absorbance measurements were obtained in the thermostated ( $25 \pm 0.2^\circ\text{C}$ ) cell compartment of a double beam spectrophotometer (Beckman DU-730 in 1997; CECIL 3041 in 2002; SHIMADZU UV-2401PC in 2004, 2006, 2008, 2010 and 2014; Perkin Elmer Lambda 800 UV-VIS in 2012). After blanking with the seawater sample without dye, 75  $\mu\text{L}$  of the dye solution were added to each sample using an adjustable repeater pipette. The absorbance was measured at three different fixed wavelengths (434, 578 and 730 nm), and pH, on the total hydrogen ion concentration scale ( $\text{pH}_T$ ), was calculated using the formula of Clayton and Byrne (1993):

$$\text{pH}_T = 1245.69/T + 3.8275 + 2.11 \cdot 10^{-3}(35 - S) + \log((R - 0.0069)/(2.222 - R \cdot 0.133))$$

where R is the ratio of the absorbances of the acidic and basic forms of the indicator corrected for baseline absorbance at 730 nm ( $R = A_{578}/A_{434}$ ), T is temperature in Kelvin scale and S is salinity. pH values were given following the equations described in Dickson et al. (2007), which include a correction due to the difference between seawater and the acidity indicator.

The replicability of the method was evaluated between 0.0015 and 0.0024 by the measurement of replicate samples along the cruises. Based on the former series of analysis, the pH uncertainty was determined at 0.0014 pH units (the mean of the standard deviations obtained in the reproducibility analyses).

### 3.1.1.5.- Total alkalinity ( $A_T$ ) sampling and measurement

$A_T$  samples were usually taken every other station. Eighteen samples were taken at all the bottle levels from bottom up to 500 m depth, and every two levels from 500 m depth up to the surface. Samples for  $A_T$  were taken directly from the Niskin bottles into 600 mL borosilicate glass bottles. Sampling bottles were washed twice with sample before filling the bottle from the bottom using a silicone pipe, overflowing half the equivalent volume of the bottle, and immediately stoppered. The samples were stored for at least 24 hours before the analyses.

Measurements of  $A_T$  were done by using an automatic potentiometric Metrohm titrator (“titrino” in the cruises prior to 2006, and “titrando” in subsequent cruises) with a Metrohm 6.0233.100 combination glass electrode and a Pt-1000 probe to check the temperature (Pérez and Fraga, 1987). A Knudsen pipette (~195 mL) was used to transfer the samples into an open Erlenmeyer flask in which the potentiometric titration was carried out with hydrochloric acid ( $[\text{HCl}] = 0.1 \text{ M}$ ). Potentiometric titrations were carried out to a final pH of 4.40 (Pérez and Fraga, 1987). The electrodes were standardised using a buffer of pH 4.42 made in  $\text{CO}_2$  free seawater (Pérez et al., 2000). The final volume of titration was determined by means of two pH endpoints (Mintrop et al., 2000). The 0.1 N HCl was prepared by mixing 0.5 mol (18.231 g) of commercially HCl supplied by Riedel-deHaën® (Fixanal 38285) with milli-Q water into a graduated 5-L beaker at controlled temperature conditions. The HCl normality is referred to  $20^\circ\text{C}$ . The variation of salinity after the titration is lower than 0.1 units, which is taken into account in the final  $A_T$  calculation.

Usually, each sample was analysed twice to quality control purposes. The average standard deviation of the replicates was about  $1.0 \mu\text{mol}\cdot\text{kg}^{-1}$ . The reproducibility of the method was also

checked by measuring 24 samples taken at the same depth. The standard deviation of all the  $A_T$  determinations was  $0.8 \mu\text{mol}\cdot\text{kg}^{-1}$ . In order to estimate the accuracy of the  $A_T$  method, CRM (distributed by A.G. Dickson from the Scripps Institution of Oceanography) analysis were also performed. Accordingly, the final pH of every batch of analyses was corrected to obtain the closest mean  $A_T$  to the certified value of the CRM. Surface seawater was used as a “quasi-steady” seawater substandard (SB) to check the precision of the  $A_T$  measurements. It consists in surface seawater taken from the non-toxic supply and stored in the dark into a large container (25–75 L) during 2 days before use. This SB was analysed at the beginning and at the end of each batch of analyses. The reproducibility of these SB measurements was better than 0.05% and the estimated drift for each day was very low. From the former series of analyses the  $A_T$  uncertainty was determined at  $1 \mu\text{mol}\cdot\text{kg}^{-1}$ .

### 3.1.1.6.- Nutrients sampling and measurement

Seawater samples for nutrients (nitrate ( $\text{NO}_3$ ), phosphate ( $\text{PO}_4$ ) and silicate ( $\text{SiO}_2$ )) were collected at every depth level of each station. Samples for nutrients were taken directly from the Niskin bottles into 125 mL solid-polyethylene containers. Sampling containers were washed three times with sample before filling. Samples were preserved in the dark at  $4^\circ\text{C}$  when analyses started more than one hour after sampling, and they were analysed no more than 24 hours after collection.

The nutrients were simultaneously analysed using an SOC Chemlab AAI type Auto-Analyser coupled with a Digital-Analysis Microstream data capture and a reduction system, following the methods described by Aminot and Chaussepied (1983) and Hansen and Grasso (1983). At the beginning and at the end of the measurement of each set of samples, a series of standard solutions (daily prepared) were analysed to calibrate the system. The standard solutions consisted of two mixed solutions (one for  $\text{NO}_3$  and  $\text{SiO}_2$  and other for  $\text{PO}_4$  and nitrite), whose concentrations covered the range of the measured nutrient concentrations. The standards of nutrient salts were prepared from nutrient salt minerals dried at  $105^\circ\text{C}$  for 3 hours. Primary solutions were performed with deionized water in calibrated volumetric flasks. Determination procedure was settled as a cycle of 2-3 minutes of sample pumping followed by 1-2 minutes of milli-Q water pumping. The precision for  $\text{NO}_3$ ,  $\text{PO}_4$  and  $\text{SiO}_2$  was evaluated at 0.2, 0.02 and  $0.1 \mu\text{mol}\cdot\text{kg}^{-1}$ , respectively.

### 3.1.1.7.- Salinity (S) sampling and measurement

To calibrate the conductivity sensor, a minimum of 16 seawater samples at each station were sampled and the S content was determined on board. Seawater samples for S were taken directly from the Niskin bottles into 125 mL glass bottles closed by a rubber seal. Sampling bottles were washed three times with sample before filling. The samples were placed in the analysis laboratory at a controlled temperature of  $20 \pm 1^\circ\text{C}$ , from 20 to 30 hours to enable them to reach thermal equilibrium.

Seawater S samples were analysed via a Guildline 8400A salinometer following the WOCE standards (Culberson, 1991). The salinometer was standardised with IAPSO Standard Seawater at the start of each crate of 24 samples. Salinometer operating temperature was  $21^\circ\text{C}$ . S was determined from the equation PSS 78 (UNESCO, 1981). The standard deviation was 0.0018. The uncertainty of the methodology was determined through the analysis of sample replicates



from pressure greater than 980 dbar along the sections. The standard deviation of the replicates was 0.0017.

### 3.1.1.8.- Acoustic Doppler Current Profiler (ADCP) measurements

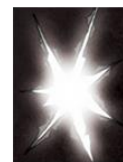
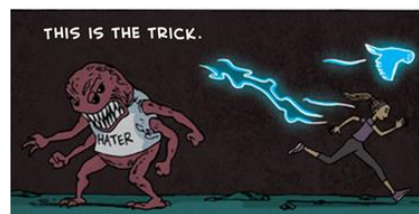
ADCP measurements were compiled along the cruise track in order to determine the velocity field of the sections. Velocity measurements between 32 m and 600 m were obtained using four-beam Shipboard ADCP (SADCP). The four beams of the instruments pinged every 2 or 3 seconds, and velocity profiles were calculated as ensemble averages of 20 values, after removing the ship velocities. A high level of quality was obtained by using combined navigation data from a differential GPS and two gyrocompasses. The correlation between the ship velocity and the current component along the trajectory during acceleration phases was then minimized by correcting the ADCP alignment. The estimated errors on the ensemble mean velocity are of the order of  $0.03 \text{ m}\cdot\text{s}^{-1}$ .

The rosette was also equipped with a downward-looking and an upward-looking Lowered ADCP (LADCP). Using the inverse method developed by Visbeck (2002), the two data sets were combined to estimate the horizontal velocity profiles at station locations. Velocity profiles were then studied one by one and compared with the SADCP station-averaged to check the quality of the data.

The velocity fields were obtained from the implementation of linear box inverse models (Lherminier et al., 2007, 2010; Gourcuff et al., 2011; Mercier et al., 2015). The inverse model was constrained by the SADCP measurements and by an overall mass balance of  $1 \pm 3 \text{ Sv}$  to the North (Lherminier et al., 2007, 2010).



PART III.- RESULTS AND DISCUSSION



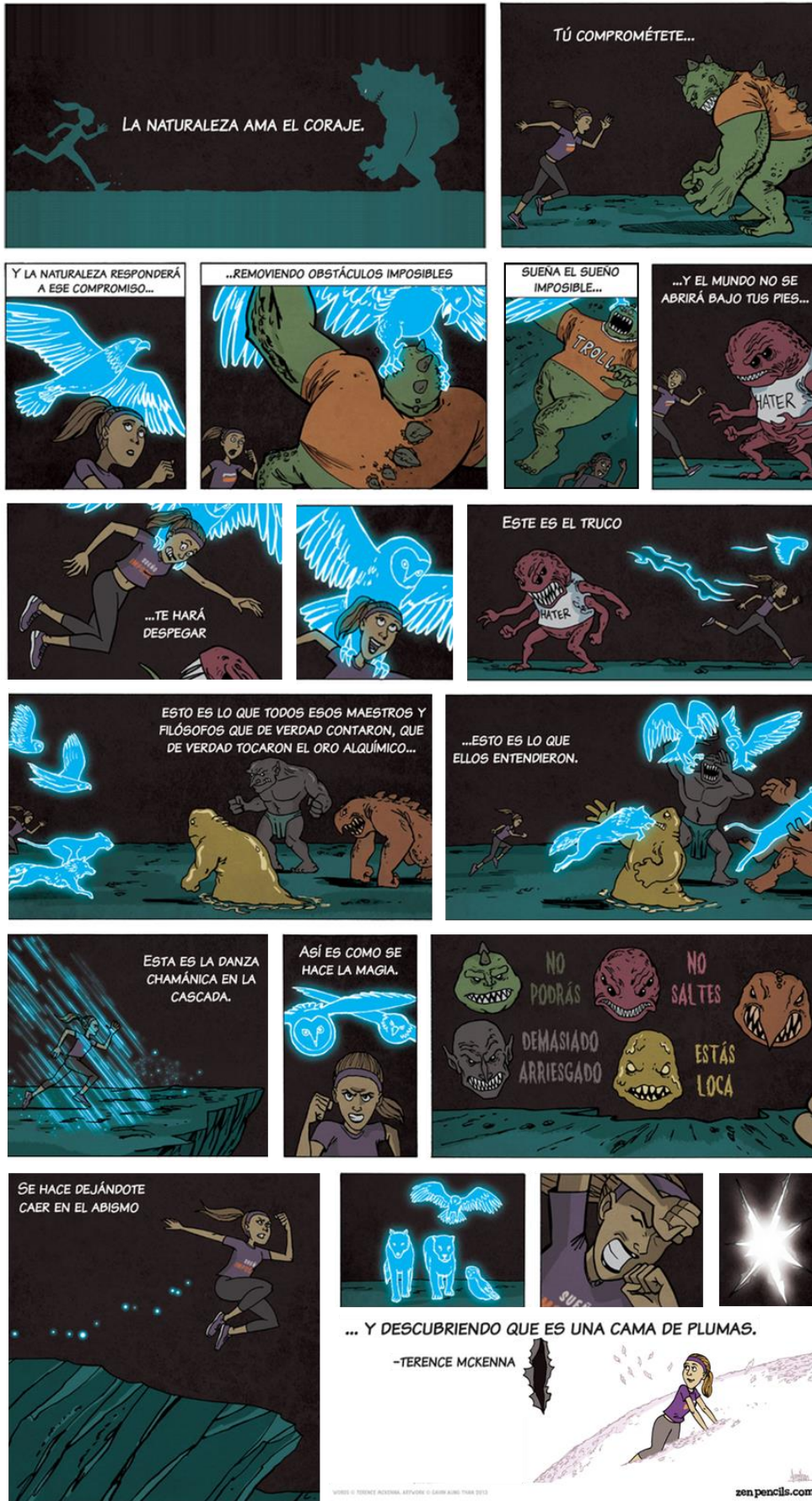
... AND DISCOVERING IT'S A FEATHER BED.

-TERENCE MCKENNA





# PARTE III.- RESULTADOS Y DISCUSIÓN



## Chapter 4.- Structure, transports and transformations of the water masses in the Atlantic Subpolar Gyre

### 4.1.- Resumen

En este capítulo se discuten las distribuciones y transportes de las principales masas de agua del Giro Subpolar del Atlántico Norte (GSPAN) durante el período 2002–2010 (secciones OVIDE 2002–2010 cada dos años), así como la variabilidad interanual de la estructura de las masas de agua entre 1997 (secciones 4x y METEOR) y 2010. La estructura de las masas de agua del GSPAN, cuantitativamente evaluada por medio de un análisis óptimo multiparamétrico (con 14 masas de agua), se combinó con los campos de velocidad resultantes de estudios anteriores utilizando modelos inversos para así obtener los transportes de volumen por masa de agua. También se evaluó la contribución relativa a la circulación termohalina del Atlántico (AMOC) de las principales masas de agua que caracterizan el GSPAN, identificando las masas de agua que contribuyen a la variabilidad de la AMOC. La reducción de la magnitud de la rama superior de la AMOC entre 1997 y la década de 2000 se asocia con la reducción en el transporte hacia el norte de las Aguas Centrales. Esta reducción del transporte hacia el norte de la AMOC está parcialmente compensada por la reducción del transporte hacia el sur de la rama inferior de la AMOC, asociada con la disminución del transporte del Agua Polar Intermedia y del Agua Modal Subpolar (SPMW) en la cuenca del Irminger. El flujo sobre el Reykjanes Ridge desde la cuenca Este del Atlántico Norte a la cuenca del Irminger ( $9,4 \pm 4,7$  Sv) se dividió en las contribuciones de Aguas Centrales ( $2,1 \pm 1,8$  Sv), Agua del Mar de Labrador (LSW;  $2,4 \pm 2,0$  Sv), Agua Intermedia Subártica (SAIW;  $4,0 \pm 0,5$  Sv) y Agua de desbordamiento de Islandia–Escocia (ISOW;  $0,9 \pm 0,9$  Sv). Una vez que LSW e ISOW cruzan sobre el Reykjanes Ridge, flujo favorecido por la fuerte mezcla alrededor de este accidente geográfico, salen de la cuenca del Irminger como aguas intermedias y de fondo. Los resultados también dan información acerca de las transformaciones que sufren las masas de agua dentro del GSPAN, como por ejemplo la contribución de las Aguas Centrales y SAIW en la formación de las diferentes variedades de SPMW gracias a la interacción océano–atmósfera.

### 4.2.- Abstract

In this chapter the distributions and transports of the main water masses in the North Atlantic Subpolar Gyre (NASPG) are discussed for the mean of the period 2002–2010 (OVIDE sections 2002 to 2010 every other year), as well as the inter-annual variability of the water mass structure from 1997 (4x and METEOR sections) to 2010. The water mass structure of the NASPG, quantitatively assessed by means of an Optimum MultiParameter analysis (with 14 water masses), was combined with the velocity fields resulting from previous studies using inverse models to obtain the water mass volume transports. The relative contribution to the Atlantic Meridional Overturning Circulation (AMOC) of the main water masses characterizing the NASPG is also evaluated, identifying the water masses that contribute to the AMOC variability. The reduction of

the magnitude of the upper limb of the AMOC between 1997 and the 2000s is associated with the reduction in the northward transport of the Central Waters. This reduction of the northward flow of the AMOC is partially compensated by the reduction of the southward flow of the lower limb of the AMOC, associated with the decrease in the transports of Polar Intermediate Water and Subpolar Mode Water (SPMW) in the Irminger Basin. The flow over the Reykjanes Ridge from the East North Atlantic Basin to the Irminger Basin ( $9.4 \pm 4.7$  Sv) is also decomposed into the contributions of the Central Waters ( $2.1 \pm 1.8$  Sv), Labrador Sea Water (LSW,  $2.4 \pm 2.0$  Sv), Subarctic Intermediate Water (SAIW,  $4.0 \pm 0.5$  Sv) and Iceland–Scotland Overflow Water (ISOW,  $0.9 \pm 0.9$  Sv). Once LSW and ISOW cross over the Reykjanes Ridge, favoured by the strong mixing around it, they leave the Irminger Basin through the deep-to-bottom levels. The results also give insights into the water mass transformations within the NASPG, such as the contribution of the Central Waters and SAIW to the formation of the different varieties of SPMW due to air–sea interaction.

### 4.3.- Introduction

The North Atlantic Subpolar Gyre (NASPG) is one of the key regions of the global ocean circulation, where interactions with the atmosphere contribute to warm-to-cold water mass transformations (e.g., Bersch et al., 2007; Yashayaev et al., 2007a; Sarafanov, 2009; Sarafanov et al., 2012). The North Atlantic Current (NAC) carries warm and salty waters from the subtropics towards the north-eastern Atlantic Ocean (Figure 18). East of the Charlie–Gibbs Fracture Zone (CGFZ) the NAC bifurcates into two branches, one flowing towards the Nordic Seas, and the other flowing towards the Iceland Basin (Read, 2000), where the Subpolar Mode Water (SPMW) is formed (McCartney and Talley, 1982; Tsuchiya et al., 1992; van Aken and Becker, 1996; Brambilla and Talley, 2008). The densest variety of SPMW is formed in the Labrador Sea (McCartney and Talley, 1982; Yashayaev, 2007), where intense winter heat loss leads to deep convection and formation of the Labrador Sea Water (LSW) (Tsuchiya et al., 1992; Bersch et al., 2007; Yashayaev, 2007). Afterwards, LSW joins the Deep Western Boundary Current (Bersch et al., 2007), where it flows over the Denmark Strait Overflow Water (DSOW) and the Iceland–Scotland Overflow Water (ISOW) (both derived from waters from the Arctic Ocean and the Nordic Seas; Rudels et al., 2002; Tanhua et al., 2008) and these altogether constitute the North Atlantic Deep Water (NADW) (Dickson and Brown, 1994).

The processes of water mass formation in the Subpolar North Atlantic, the Arctic Ocean and the Nordic Seas affect the Atlantic Meridional Overturning Circulation (AMOC) on long timescales (Böning et al., 1996; Willebrand et al., 2001; Marsh et al., 2005; Josey et al., 2009). The AMOC transports heat and anthropogenic carbon from the southern hemisphere of the Atlantic Ocean to the subtropics and the high northern latitudes, playing an active role in the climate variability. The North Atlantic Oscillation (NAO) is the dominant mode of the atmospheric variability in the NASPG (Hurrell, 1995), which influences both its strength and circulation (Curry and McCartney, 2001; Häkkinen and Rhines, 2004) and its shape (Bersch, 2002). Both direct observations (Flatau et al., 2003; Häkkinen and Rhines, 2004) and model results (Böning et al., 2006) confirm a spin down of the circulation of the NASPG between the mid-1990s and the 2000s due to the shift from high to low NAO indices, based on high-frequency time-series. The NAO also influences the AMOC strength (e.g., Eden and Willebrand, 2001; Marsh et al., 2005; Balmaseda et al., 2007; Böning et al., 2006), which has decreased over the last



decade (Balmaseda et al., 2007; Desbruyères et al., 2013; Xu et al., 2013; Mercier et al., 2015) and resulted in reductions in the poleward heat transport (Bryden et al., 2014; Mercier et al., 2015) and in the uptake of atmospheric carbon dioxide (Pérez et al., 2013).

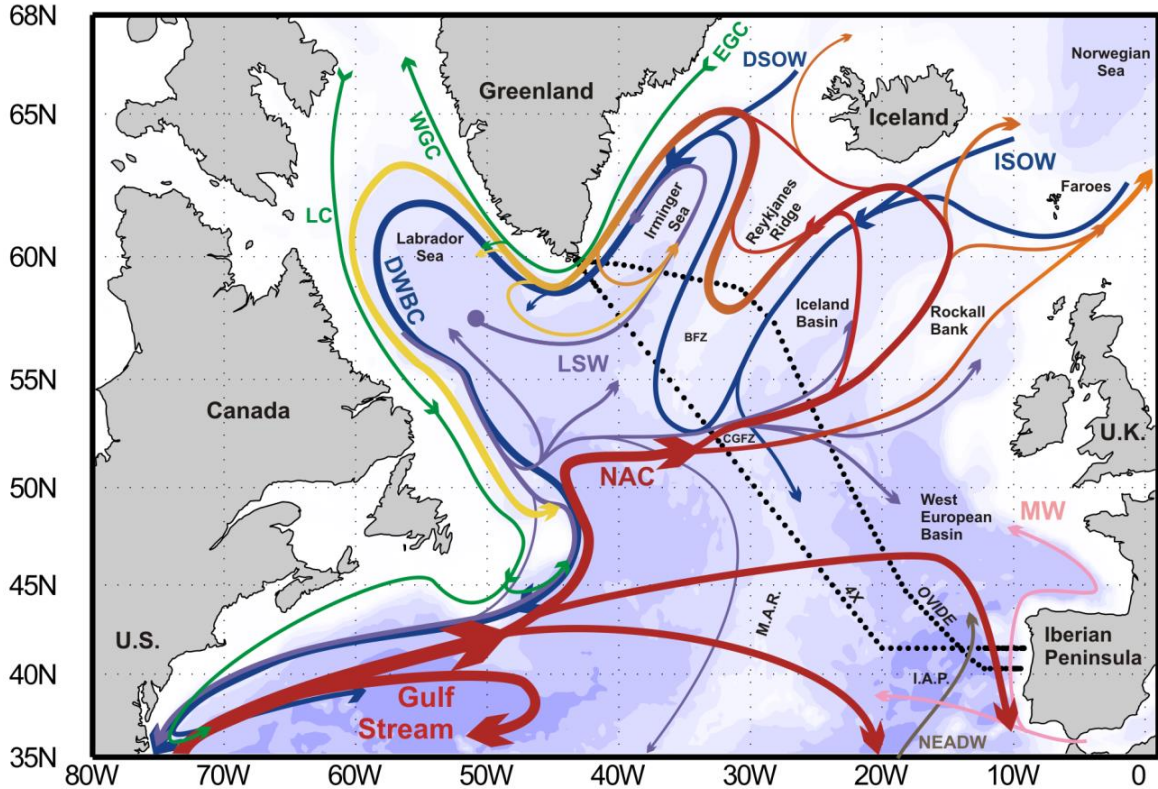


Figure 18.- Location of the 4x and OVIDE hydrographic stations plotted on bathymetry (500 m intervals). The North Atlantic circulation scheme, the major topographical features of the Subpolar North Atlantic, as well as the main water masses are also shown: East Greenland Current (EGC), West Greenland Current (WGC), Labrador Current (LC), Deep Western Boundary Current (DWBC), North Atlantic Current (NAC), Denmark Strait Overflow Water (DSOW), Iceland–Scotland Overflow Water (ISOW), Labrador Sea Water (LSW), Mediterranean Water (MW), North East Atlantic Deep Water (NEADW), Charlie–Gibbs Fracture Zone (CGFZ), Bight Fracture Zone (BFZ), Mid-Atlantic Ridge (M.A.R.) and Iberian Abyssal Plain (I.A.P.). Schematic diagram of the large-scale circulation compiled from Schmitz and McCartney (1993), Dengler et al. (2006), Schott and Brandt (2007, Plate 1), Sutherland and Pickart (2008, Figure 16), Lherminier et al. (2010, Fig. 1b) and Sarafanov et al. (2012).

The main objective of this chapter is to discuss the distributions and transports of the main water masses in the North Atlantic region for the first decade of the 2000s. The inter-annual variability of the water mass structure from 1997 to 2010 is also evaluated. For this purpose data from six repeats of the WOCE (World Ocean Circulation Experiment) A25 hydrographic section located at the southern boundary of the NASPG (Figure 18; Table 1) is used. The data include the 4x section taken in 1997 and the five repeats of the OVIDE (Observatoire de la variabilité interannuelle et décennale en Atlantique Nord) section taken every other year from 2002 to 2010. The distributions of the main water masses in each section were obtained by using an Optimum MultiParameter (OMP) analysis (Thompson and Edwards, 1981; Tomczak, 1981; Mackas et al., 1987; Tomczak and Large, 1989). Then they were combined with the velocity fields (from inverse models previously implemented (Lherminier et al., 2007, 2010; Gourcuff et al., 2011; Mercier et al., 2015)) in order to estimate the transport of each water mass across the sections. Although this



methodology has been applied before (Álvarez et al., 2004; Carracedo et al., 2014), this is the first time that it has been used to evaluate the inter-annual variability of the water mass distributions, specifically from 1997 to 2010. In addition, the water mass contributions to the AMOC and the water mass transformations that take place in the NASPG are also investigated.

Table 1.- Hydrographic cruises.

Cruise Name	Month/Year	Vessel	Reference
METEOR 1997	08–09/1997	R/V Meteor	Rhein et al. (2002)
4x 1997	08–09/1997	R/V Discovery	Álvarez et al. (2002)
OVIDE 2002	06–07/2002	N/O Thalassa	Lherminier et al. (2007)
OVIDE 2004	06–07/2004	N/O Thalassa	Lherminier et al. (2010)
OVIDE 2006	05–06/2006	R/V Maria S. Merian	Gourcuff et al. (2011)
OVIDE 2008	06–07/2008	N/O Thalassa	Mercier et al. (2015)
OVIDE 2010	06–07/2010	N/O Thalassa	Mercier et al. (2015)

The present chapter is organized as follows. In Section 4.4 it is described: the cruise data; the methodology followed in the OMP analysis, including a description of the 14 water masses considered; the velocity field obtained from earlier studies; and the methodology used to combine the velocity fields with the water mass distributions. The water mass distributions for the OVIDE period (2002–2010) are described and discussed in Section 4.5. In Section 4.6 the inter-annual variability of the water mass structure from 1997 to 2010 is described and discussed. The volume transports of the water masses are described and discussed in Section 4.7. This section also includes an estimation of the circulation and transformation of the water masses in the Subpolar North Atlantic as well as of the budget of water mass volume transports across the Reykjanes Ridge. The chapter is concluded in Section 4.8.

## 4.4.- Data and methods

### 4.4.1.- Biogeochemical data

The 4x and OVIDE sections were conducted across the southern boundary of the NASPG from the Iberian Peninsula to Cape Farewell (South Greenland), during the spring–summer periods of 1997 (4x section), 2002, 2004, 2006, 2008 and 2010 (OVIDE sections) (Figure 18; Table 1). Cruise data is available in the CCHDO (CLIVAR & Carbon Hydrographic Data Office) webpage (<http://cchdo.ucsd.edu>). These cruises are suitable for examining the inter-annual to decadal water mass variability because they were carried out at approximately the same time of the year –from June to August– and, except for the near-surface layers, the seasonal differences are expected to be smaller than the inter-annual changes. In addition, the monthly variability of the AMOC is weaker between June and August (Mercier et al., 2015).

During the cruises, the temperature and salinity (S) were continuously recorded at each station by using a Conductivity–Temperature–Depth (CTD) instrument. In the cruises prior to 2008 a Neil Brown Mark III CTD probe was used, while in the subsequent cruises a Sea-bird Electronics 911plus CTD probe was used. To calibrate the conductivity sensor, seawater S samples were analysed on board via a Guildline 8400A salinometer calibrated with IAPSO Standard Seawater following the WOCE standards (Culberson, 1991). The pressure sensor was calibrated in a metrology laboratory using 3 cycles of increasing–decreasing pressure between 0 and 6000 dbar. The static and dynamic effects of temperature on the pressure sensor were also estimated and corrected (Branellec and Thierry, 2013). Overall, the CTD measurement accuracies were 1 dbar for pressure, 0.002°C for temperature and 0.003 for S.

Seawater samples for nutrients (nitrate ( $\text{NO}_3$ ), phosphate ( $\text{PO}_4$ ) and silicate ( $\text{SiO}_2$ )) and oxygen ( $\text{O}_2$ ) were also taken and analysed on board. The nutrients were analysed using an SOC Chemlab AAI type Auto-Analyser coupled with a Digital-Analysis Microstream data capture and a reduction system, following the classic protocols and methods described by Aminot and Chaussepied (1983) and Hansen and Grasso (1983). The precision for  $\text{NO}_3$ ,  $\text{PO}_4$  and  $\text{SiO}_2$  was evaluated at 0.2, 0.02 and 0.1  $\mu\text{mol}\cdot\text{kg}^{-1}$ , respectively. The  $\text{O}_2$  was determined by Winkler potentiometric titration following the WOCE standards (Culberson, 1991), with a precision better than 1  $\mu\text{mol}\cdot\text{kg}^{-1}$ .

For further reference, the vertical sections of the mean properties (potential temperature ( $\theta$ ), S,  $\text{O}_2$ ,  $\text{NO}_3$ ,  $\text{SiO}_2$  and  $\text{PO}_4$ ) are shown in Figure 19.

#### 4.4.2.- *Optimum MultiParameter (OMP) analysis*

An Optimum MultiParameter (OMP) analysis (Thompson and Edwards, 1981; Tomczak, 1981; Mackas et al., 1987; Tomczak and Large, 1989) was used to resolve the water mass structure along the sections. The water masses are described by the so-called Source Water Types (SWT), which are points in the  $n$ -dimensional parameter space ( $n$  is the number of properties that characterize SWTs) (Tomczak, 1999). In this work, the SWTs are characterized by  $\theta$ , S,  $\text{O}_2^0$ ,  $\text{NO}_3^0$ ,  $\text{PO}_4^0$  and  $\text{SiO}_2^0$  (where the superscript 0 means preformed variables) (Table 2). Given a number of SWTs, the goal of an OMP analysis is to find the fractions of each SWT ( $X_i$ ) in each water sample. The  $X_i$ s strongly depend on the characterization of the SWTs (Tomczak, 1981), the choice of which is a key step of the analysis. In the following subsection the SWTs included in the analysis and their properties are described.

##### 4.4.2.1.- Water mass characterization

The Subpolar North Atlantic presents a large variety of water masses. In this study, 14 SWTs were considered as the main water masses explaining the physicochemical variability of this area and which encompass all the water samples of the sections (Figure 20a, b).

The saltiest waters of the sections are influenced by the Mediterranean Water (MW), which enters the North Atlantic from the Mediterranean Sea. MW is detected as a maximum in S ( $> 36.1$ ) and  $\theta$  (9–11°C) between 600 and 1700 m depth in the eastern North Atlantic (Harvey, 1982; Tsuchiya et al., 1992; van Aken and Becker, 1996; Álvarez et al., 2004). Following Castro et al. (1998) and Álvarez et al. (2004), I used the  $\theta$ /S properties of MW reported by Wüst and Defant

(1936) near Cape St. Vicente (Figure 20a; Table 2). In this way I avoid solving the mixing processes between the Mediterranean Outflow Water (overflowing from the Mediterranean Sea) and the central and intermediate waters of the East North Atlantic, which lead to the formation of MW (Ambar and Howe, 1979; Baringer and Price, 1997).

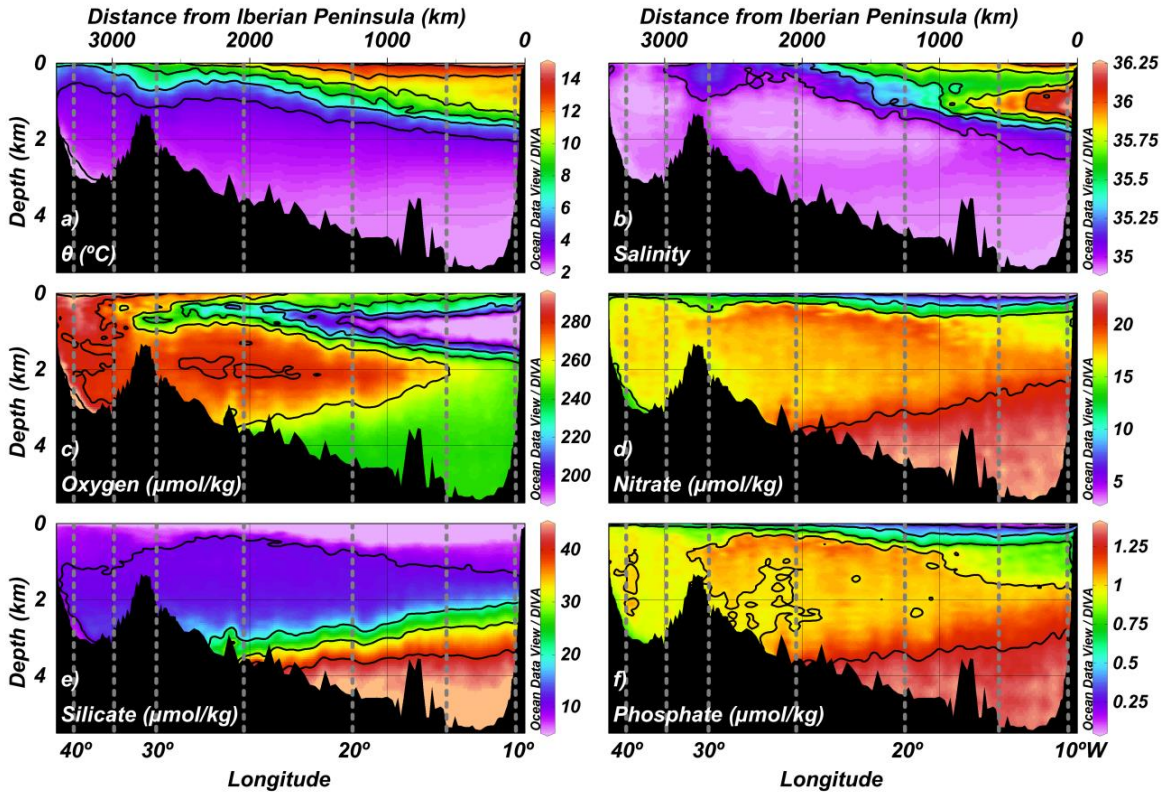


Figure 19.- Mean (a) potential temperature ( $\theta$ ), (b) salinity, (c) oxygen, (d) nitrate, (e) silicate and (f) phosphate along the OVIDE section, from the Iberian Peninsula (right) to Greenland (left).

The warmer waters are influenced by the North Atlantic Central Waters (Iselin, 1936). East of the Mid-Atlantic Ridge in the North Atlantic, the predominant variety of these waters is the East North Atlantic Central Water (ENACW) (Harvey, 1982; Pollard et al., 1996; Read, 2000), which is formed by winter convection in the intergyre region (Pollard et al., 1996). The  $\theta/S$  characteristics of ENACW can be fitted to a straight line from 12 to 16°C (Pollard et al., 1996). The end points from this line are defined by: ENACW<sub>16</sub>, whose  $\theta/S$  characteristics match those from the warmer central waters of Pollard et al. (1996); and ENACW<sub>12</sub>, which represents the upper limit of ENACW defined by Harvey (1982) (Figure 20a; Table 2). Here, I considered these two SWTs together as the Central Waters.

Part of the Central Waters carried by the NAC recirculates in the West European Basin (Figure 18), and part of them spreads towards the Iceland Basin, leading to the formation of SPMW (McCartney and Talley, 1982; Tsuchiya et al., 1992; van Aken and Becker, 1996; Brambilla and Talley, 2008). The hydrographic properties of SPMW change due to air-sea interaction processes (McCartney and Talley, 1982; Brambilla and Talley, 2008). Since this variability cannot be accounted by the OMP analysis, three SWTs were defined to characterize SPMW: two corresponding to SPMW present in the Iceland Basin (SPMW<sub>8</sub> and SPMW<sub>7</sub>), and

another one that accounts for the variety found in the Irminger Basin (IrSPMW, sometimes denoted as Irminger Sea Water (Krauss, 1995)). SPMW<sub>8</sub> and SPMW<sub>7</sub> were selected to characterize the thermohaline range of SPMW in the Iceland Basin (6–9°C and 35.1–35.25) (Stoll et al., 1996; van Aken and Becker, 1996) and are going to be considered together as IcSPMW. The  $\theta/S$  properties of SPMW<sub>7</sub> (Figure 20a; Table 2) were chosen close to the mean properties of SPMW over the eastern flank of the Reykjanes Ridge found by Thierry et al. (2008) in a box including the OVIDE section, while the  $\theta/S$  properties of SPMW<sub>8</sub> correspond to the SPMW variety formed within the Iceland Basin (Brambilla and Talley, 2008). Since the 8°C limit between the Central Waters and SPMW<sub>8</sub> (Brambilla and Talley, 2008; Brambilla et al., 2008) cannot be directly obtained by the OMP analysis, the OMP analysis was constrained by not allowing the presence of Central Waters east of the western branch of the NAC (Figure 18). In the northern part of the Irminger Basin, SPMW is characterized by  $\theta$  and S usually lower than 7°C and 35.1, respectively (Thierry et al., 2008). To characterize the SWT for IrSPMW, its  $\theta/S$  properties were chosen close to those of the Irminger Sea Water described by Krauss (1995) (Figure 20a; Table 2). These properties were also found by Brambilla and Talley (2008) in the NW Irminger Basin, which could indicate that this is the region of formation of IrSPMW.

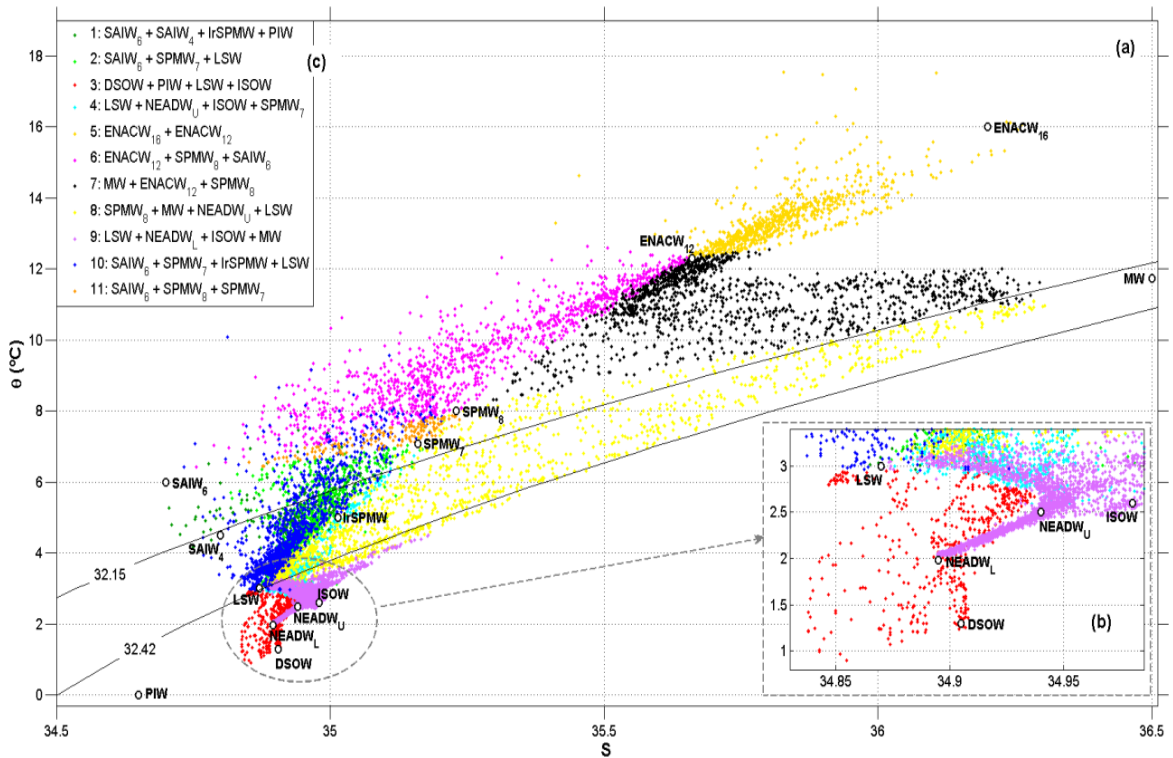


Figure 20.- (A) Potential temperature ( $\theta$ )/Salinity (S)-diagram including the Source Water Types (Table 2) used in the analysis and (B) zoomed for bottom waters. The mixing figures are shown in the (C) legend (see Table 2 for the acronyms of the source water types). The isopycnals referenced in the chapter are also plotted, i.e.,  $\sigma_1 = 32.15$  and  $\sigma_1 = 32.42$  (where is  $\sigma_1$  potential density referenced to 1000 dbar).

Table 2.- Main properties of each of the Source Water Types (SWTs, see footnote <sup>a</sup>) considered in the study with their corresponding standard deviation. The weights of each equation are also given, together with the square of correlation coefficients ( $r^2$ ) between the observed and estimated properties, the Standard Deviation of the Residuals (SDR) and the SDR/ $\varepsilon$  ratios from the data below 400 dbar. The  $\varepsilon$  used to compute the SDR/ $\varepsilon$  ratios are the

accuracies of the measured properties listed in section 4.4.2.2. The last column accounts for the uncertainties in the SWTs contributions. Values expressed on a per one basis.

	Potential temperature ( $\theta^{SWT}$ ) °C	Salinity ( $S^{SWT}$ )	Silicate ( $SiO_2^{0,SWT}$ ) <sup>b</sup> $\mu\text{mol}\cdot\text{kg}^{-1}$	Nitrate ( $NO_3^{0,SWT}$ ) <sup>b</sup>	Phosphate ( $PO_4^{0,SWT}$ ) <sup>b</sup>	Oxygen ( $O_2^{0,SWT}$ ) <sup>b</sup>	Uncertainty
ENACW <sub>16</sub>	16.00±0.13	36.20±0.02	0.85±0.12	0.00±0.16	0.00±0.01	241±7	0.04
ENACW <sub>12</sub>	12.30±0.18	35.66±0.03	1.6±0.8	7±1	0.31±0.07	251±8	0.04
MW	11.7±0.2	36.500±0.011	4.88±0.15	10.9±0.2	0.70±0.03	210±8	0.015
SAIW <sub>6</sub>	6.0±0.2	34.70±0.03	6.3±2.2	13±1	0.86±0.07	287±9	0.04
SAIW <sub>4</sub>	4.5±0.2	34.80±0.03	1.4±2.2	0±1	0.05±0.07	290±9	0.05
SPMW <sub>8</sub>	8.00±0.11	35.230±0.016	3.2±2.2	11±1	0.68±0.01	289±6	0.07
SPMW <sub>7</sub>	7.07±0.07	35.160±0.006	5.38±0.16	13.70±0.16	1.06±0.01	280±9	0.08
IrSPMW	5.00±0.02	35.014±0.013	7.1±0.4	15.0±0.4	0.98±0.02	300±9	0.13
LSW	3.00±0.19	34.87±0.02	10.0±0.8	16.5±0.8	1.05±0.12	287±10	0.10
ISOW	2.60±0.08	34.980±0.003	10±1	15.5±0.6	1.20±0.04	289±10	0.08
DSOW	1.30±0.06	34.905±0.006	7.8±0.5	14.1±0.8	1.10±0.06	309±10	0.05
PIW	0.0±0.2	34.65±0.03	8.4±2.2	9±1	0.25±0.07	310±11	0.06
NEADW <sub>U</sub>	2.50±0.08	34.940±0.007	29.2±0.6	19.2±0.6	1.32±0.05	269±10	– <sup>c</sup>
NEADW <sub>L</sub>	1.98±0.03	34.895±0.003	48.0±0.4	22.6±0.5	1.50±0.04	252±10	0.02
Weights	20	10	2	3 <sup>d</sup>	2 <sup>d</sup>	2	
r <sup>2</sup>	0.9991	0.9891	0.9975	0.9784	0.9477	0.9926	
SDR	0.02	0.006	0.5	0.5	0.07	2	
SDR/ε	2	1	2	3	3	2	

<sup>a</sup> ENACW<sub>16</sub> and ENACW<sub>12</sub> = Eastern North Atlantic Central Waters; MW = Mediterranean Water; SAIW<sub>6</sub> and SAIW<sub>4</sub> = Subarctic Intermediate Waters; SPMW<sub>8</sub> and SPMW<sub>7</sub> = Subpolar Mode Waters of the Iceland Basin and IrSPMW = of the Irminger Basin; LSW = Labrador Sea Water; ISOW = Iceland–Scotland Overflow Water; DSOW = Denmark Strait Overflow Waters; PIW = Polar Intermediate Water; and NEADW<sub>U</sub> = North East Atlantic Deep Water upper and NEADW<sub>L</sub> = lower.

<sup>b</sup> O<sub>2</sub> and nutrients represent preformed values; note that O<sub>2</sub> values are close to saturation and nutrient values are low.

<sup>c</sup> NEADW<sub>U</sub> has no uncertainty value since it is considered as a composed SWT (MW + LSW + ISOW + NEADW<sub>L</sub>, see section 4.5).

<sup>d</sup> The weights for NO and PO are the same as for NO<sub>3</sub><sup>0</sup> and PO<sub>4</sub><sup>0</sup>, respectively.

Once SPMW reaches the Labrador Sea, it is involved in deep convection processes which lead to the formation of LSW (Talley and McCartney, 1982). These episodes of deep convection are forced by the extreme winter heat loss combined with the cyclonic circulation in the Labrador Sea (Lazier et al., 2002). LSW is traceable by its low potential vorticity, relatively low S and high O<sub>2</sub> content (Figure 19) (Talley and McCartney, 1982; Harvey and Arhan, 1988; Pickart, 1992; Tsuchiya et al., 1992). The classical LSW (Bersch et al., 2007; Yashayaev et al., 2008) is built by intense winter convection, when the mixing layer reaches ~2000 m depth. Deep winter convection at these latitudes is controlled by the phase of the NAO and its persistence (Dickson et al., 1996; Bersch et al., 2007). Indeed, it is favoured during persistent phases of the high NAO index, such as the period 1987–1994, when the winter convection reached 2400 m depth (Lazier et al., 2002; Yashayaev, 2007), where the LSW properties reached extremal values of 2.9°C and 34.84 (Álvarez et al., 2004; Yashayaev, 2007). The thermohaline properties of the corresponding

SWT are consistent with the characteristic values for the classical LSW as a long-term average (Lazier, 1973; Dickson et al., 1996) (Figure 20a, b; Table 2).

The left limit of the  $\theta/S$ -diagram is characterized by the Subarctic Intermediate Water (SAIW), which originates in the western boundary of the NASPG (Arhan, 1990) from the mixture of the warm and salty waters of the NAC with the cold and low-salinity waters of the Labrador Current (Iselin, 1936; Read, 2000). The thermohaline properties of SAIW ( $4-7^{\circ}\text{C}$  and  $S < 34.9$ ) vary due to its spreading and subduction in a region characterized by a complex circulation, with horizontal and vertical mixing, recirculation processes and mesoscale variability, among other processes (Bubnov, 1968; Arhan, 1990). Similarly to what was done in the case of SPMW and in order to better depict SAIW, I defined two SWTs: SAIW<sub>6</sub>, which represents the fresher and relatively warm variety resulting from the progressive warming of the fresher Arctic waters while mixing with central waters (Figure 20a; Table 2); and SAIW<sub>4</sub>, which represents the saltier and relatively cold variety resulting from the cooling of the saltier central waters while mixing with the Arctic waters. The thermohaline properties of both SWTs follow the descriptions of Bubnov (1968) and Harvey and Arhan (1988).

The bottom part of the  $\theta/S$ -diagram shows DSOW and ISOW, which are complex mixtures of several water masses. The Norwegian Sea waters overflow and entrain the overlying warm saline Atlantic waters (SPMW and LSW) forming ISOW (van Aken and de Boer, 1995; Dickson et al., 2002; Fogelqvist et al., 2003). To avoid the parameterization of this mixing process (as in the case of MW), the ISOW thermohaline properties were defined by considering this overflow as the final result of those mixing processes, and according to the definition of van Aken and Becker (1996) (Figure 20a, b; Table 2). As for DSOW, it is formed after the Nordic Seas deep waters overflow and entrain Atlantic waters (SPMW and LSW) (Read, 2000; Yashayaev and Dickson, 2008). In addition, some authors have reported dense Greenland shelf water cascading down to the DSOW layer in the Irminger Sea (Olsson et al., 2005; Tanhua et al., 2005, 2008; Falina et al., 2012). According to this and following van Aken and de Jong (2012), DSOW was modelled by two SWTs: a relatively saline one (DSOW) and a relatively fresh one (the Polar Intermediate Water; PIW) (Figure 20a, b; Table 2). The  $\theta/S$  characteristics chosen for DSOW are in agreement with the characteristics of the saline variety of van Aken and de Jong (2012) and with the characteristics of DSOW after crossing the sill found by Tanhua et al. (2005). PIW is an SWT with characteristics close to the low-salinity variety of the overflow (Tanhua et al., 2005). I substituted the relatively fresh end-member proposed by van Aken and de Jong (2012) by PIW to take into account the dense shelf water intrusions, since these intrusions lie on a mixing line between PIW and the Irminger Current Water (Rudels et al., 2002; Falina et al., 2012). The  $\theta/S$  characteristics selected for PIW are in agreement with those proposed by Malmberg (1972) and Rudels et al. (2002).

The North East Atlantic Deep Water (NEADW) is formed as a result of different entrainments that occur along the journey of ISOW through the Iceland Basin (van Aken, 2000b). NEADW recirculates in the Iberian Basin and mixes with the surrounding waters, including the bottom waters coming from the Southern Ocean (Antarctic Bottom Water; van Aken and Becker, 1996). The  $\theta/S$  properties of NEADW below 2500 m depth in this basin can be approximated as a line (Saunders, 1986; Mantyla, 1994) whose end points define the SWTs here used representing the upper (NEADW<sub>u</sub>) and lower (NEADW<sub>l</sub>) varieties of NEADW (Figure 20a,



b; Table 2). The  $\theta/S$  properties of these two SWTs are close to those defined by Castro et al. (1998).

Having selected the  $\theta/S$  properties for each SWT from the literature, the OMP analysis was run taking the remaining chemical properties ( $NO_3^0$ ,  $PO_4^0$  and  $SiO_2^0$ ) from the work of Álvarez et al. (2004) and the  $O_2^0$  equal to saturation as a first guess. For those SWTs not defined in Álvarez et al. (2004), their first-guess chemical properties were taken as equal to those properties of the nearest SWT in Álvarez et al. (2004) ( $O_2^0$  equal to saturation). The final chemical properties for each SWT (those that best fit the measured data) were obtained from an iterative procedure (section 4.4.2.2). Some of the values of  $O_2^0$  were adjusted so as not to get negative values for either respiration or nutrients, and to account for the disequilibrium between the  $O_2$  content in the atmosphere and in the water mass at its time of formation (in the surface ocean) (Najjar and Keeling, 2000; Ito et al., 2004). The uncertainties in the properties were obtained as explained in section 4.4.2.2.

#### 4.4.2.2.- Methodology of the analysis

An OMP analysis is a simple mathematical approach based on measured data that solves the mixing between SWTs by a least square method constrained to be positive definite. The OMP analyses consider the properties (physical and/or chemical) of a given water sample to be the result of linear combinations of a finite number of water masses represented by the SWTs. They compute the fractions of each SWT ( $X_i$ ) in each water sample. In the OMP analyses, the SWT properties are assumed to be independent and equally affected by mixing. In addition, SWTs are considered to be time invariant; hence, changes in the properties of the water masses over time are reflected through water mass redistributions.

The methodology of the analysis here applied consists of two OMP steps (Pardo et al., 2012). In the first step a classical OMP (cOMP) was solved for each water sample. The cOMP analysis is based on conservative variables; in particular, in this study I used  $\theta$ ,  $S$ ,  $SiO_2$ , “NO” and “PO” (where “NO” =  $10.5 * NO_3 + O_2$ , “PO” =  $175 * PO_4 + O_2$ ; Broecker, 1974; Takahashi et al., 1985; Anderson and Sarmiento, 1994):

$$\begin{aligned}
 \sum_{i=1}^n X_i * \theta_i^{SWT} &= \theta^{sample} + R_{\theta} \\
 \sum_{i=1}^n X_i * S_i^{SWT} &= S^{sample} + R_S \\
 \sum_{i=1}^n X_i * SiO_{2i}^{SWT} &= SiO_2^{sample} + R_{SiO_2} \\
 \sum_{i=1}^n X_i * NO_i^{SWT} &= NO^{sample} + R_{NO} \\
 \sum_{i=1}^n X_i * PO_i^{SWT} &= PO^{sample} + R_{PO} \\
 \sum_{i=1}^n X_i &= 1 + R_{mass}
 \end{aligned} \quad (Eq. 4.1)$$

where  $R_p$  is the residual of each property  $p$  ( $\theta$ ,  $S$ ,  $SiO_2$ ,  $NO$  and  $PO$ ) measured ( $p^{sample}$ ) that the OMP tries to minimize and  $p_i^{SWT}$  is the property of each SWT  $i$ . The last equation accounts for the mass conservation. Before solving the system (minimization through a non-negative least square method), the equations were normalized (Tomczak and Large, 1989) and weighted (Pardo et al., 2012) (Table 2). The assignment of weights was, as a first step, directly related to the accuracy of the property and/or to the variability in the region of study. Weights were also adjusted so that the ratios between the Standard Deviations of the Residuals and the analytical error ( $\epsilon$ , accuracy of the measured properties) were almost the same for all the SWT properties (Table 2).



The weights of  $\theta$  and  $S$  are higher than those of the other properties because both have the lowest  $\epsilon$ . The mass equation has the highest weight to ensure its conservation.

The cOMP analysis was solved for each water sample in each one of the 11 mixing figures (Figure 20c). The mixing figures are groups of SWTs that are susceptible to mix together, and are set considering the characteristics and/or dynamics of the SWTs in the region of study. The term figure refers to the geometrical space in the  $\theta/S$  plane formed by 2 SWTs (line segment), 3 SWTs (triangle), 4 SWTs (square), etc. Actually, the mixing figures are  $n$ -dimensional spaces. Each mixing figure is constituted by a maximum of four SWTs in order to solve the system of 6 equations (Eq. 4.1) with at least two degrees of freedom. The mixing figures are vertically and horizontally sequenced, sharing at least one SWT with the adjacent mixing figures. The cOMP analysis is applied to assign the mixing figure where the water sample is best included (lowest residuals).

In the second step an extended OMP (eOMP) analysis was solved with the same set-up as the cOMP except that the eOMP considers conservative and non-conservative variables. I used  $\theta$  and  $S$  as conservative variables and  $\text{SiO}_2$ ,  $\text{NO}_3$ ,  $\text{PO}_4$  and  $\text{O}_2$  as non-conservative variables. A new unknown has to be considered,  $\Delta\text{O}$ , in order to account for the biogeochemical process of remineralisation of the organic matter. By taking into account the biogeochemical process of remineralisation of the organic matter, non-conservative variables can be included. The system of equations remains as follows:

$$\begin{aligned}
 \sum_{i=1}^n X_i * \theta_i^{\text{SWT}} &= \theta^{\text{sample}} + R_{\theta} \\
 \sum_{i=1}^n X_i * S_i^{\text{SWT}} &= S^{\text{sample}} + R_S \\
 \sum_{i=1}^n X_i * \text{SiO}_{2i}^{\text{SWT}} + \Delta\text{O}/r_{\text{Si}} &= \text{SiO}_2^{\text{sample}} + R_{\text{SiO}_2} \\
 \sum_{i=1}^n X_i * \text{O}_{2i}^{\text{SWT}} - \Delta\text{O} &= \text{O}_2^{\text{sample}} + R_{\text{O}_2} \\
 \sum_{i=1}^n X_i * \text{NO}_{3i}^{\text{SWT}} + \Delta\text{O}/r_{\text{N}} &= \text{NO}_3^{\text{sample}} + R_{\text{NO}_3} \\
 \sum_{i=1}^n X_i * \text{PO}_{4i}^{\text{SWT}} + \Delta\text{O}/r_{\text{P}} &= \text{PO}_4^{\text{sample}} + R_{\text{PO}_4} \\
 \sum_{i=1}^n X_i &= 1 + R_{\text{mass}}
 \end{aligned} \tag{Eq. 4.2}$$

where  $r_{\text{Si}}$  is 12,  $r_{\text{N}}$  is 10.5 and  $r_{\text{P}}$  is 175 (Takahashi et al., 1985; Anderson and Sarmiento, 1994).

The final result from the eOMP analysis is the  $X_i$ s in each water sample in the corresponding mixing figure selected through the cOMP analysis.

The cOMP analysis selects the mixing figure based on conservative water mass tracers, avoiding the complexity added by the non-conservative variables. Even though this analysis does not consider the variability associated with biological processes, it is accurate enough to select the appropriate mixing figure. Once the mixing figures are selected, the estimates of the  $X_i$ s are given by the eOMP analysis, which does take into account the effect of the biology in the measured variables.

The whole OMP analysis (cOMP and eOMP) was restricted to the water samples with pressure  $\geq 50$  dbar, to avoid the non-conservative behaviour of  $\theta$  and  $S$  in the surface layer due to air–sea interactions after the last maximum of winter convection. Additionally, special SWTs for the regions of intense air–sea interactions were also included (section 4.4.2.1). To avoid the input

of high percentages of fresh water over the Greenland shelf in this region the analysis was restricted to water samples with  $S > 34.7$  (Daniault et al., 2011).

Some of the SWTs were geographically constrained (Álvarez et al., 2004) according to the spreading of the water masses: MW was restricted south of the NAC front; DSOW and IrSPMW were restricted to the Irminger Basin; PIW was restricted to stations over the Greenland slope (in mixing figure 1; Figure 20c) since it is part of the East Greenland Current (Pickart et al., 2005), and within the DSOW mixing figure (in mixing figure 3) since it is assumed to contribute to DSOW (Falina et al., 2012); and LSW was not allowed in the East Greenland Current (Falina et al., 2012; von Appen et al., 2014).

To reduce the error of the whole OMP analysis, an iterative process was performed for nutrients (Álvarez et al., 2004), since they accumulate the highest errors. At each iteration we obtained new values of the nutrients for each SWT from  $X_i$ s and the measured data (eOMP equations). These new estimated values were assigned to the SWTs and the methodology was re-run. The process finishes when an asymptote is found in the value of the total residual of the analysis (eOMP) (in this work five iterations were performed). The iterative process improves the definition of the SWTs, thereby also improving the accuracy of the methodology.

The robustness of the methodology was tested through a perturbation analysis of uncertainties (Lawson and Hanson, 1974), where the physicochemical properties of each SWT (Álvarez et al., 2004; Pardo et al., 2012) and of each water sample (Álvarez et al., 2014) were modified by introducing normally distributed random numbers. This allows to check the sensitivity of the model to variations in the SWTs, due to environmental variability, and in the water samples, due to measurement errors (Leffanue and Tomczak, 2004). To apply this procedure, it is assumed that the property distributions follow a normal distribution constructed with the mean equal to the property value at each point and a standard deviation (STD) (Álvarez et al., 2004; Pardo et al., 2012). The perturbation process lies in varying the property values within the normal distribution. All the STDs used in perturbing the SWTs are shown in Table 2. The STDs of the water sample properties ( $\epsilon$  in Table 2) were obtained by considering  $\epsilon$  almost equal to the accuracy of each water sample property ( $\epsilon_\theta$  0.01,  $\epsilon_S$  0.01,  $\epsilon_{SiO_2}$  0.3,  $\epsilon_{NO_3}$  0.2,  $\epsilon_{PO_4}$  0.02 and  $\epsilon_{O_2}$  1). The STDs of the properties of the SWTs were obtained within the realm of the SWT ( $X_i > 75-95\%$ ) by one of the following methods:

- a) Following Karstensen and Tomczak (1998), the water samples with more than 95% of contribution of a certain SWT ( $X_i$ ) were selected and the STD calculated for each property. This method was only used when the number of water samples that could be selected for a certain SWT was more than 50. This procedure was applied to LSW, ISOW and NEADW<sub>L</sub>.
- b) For the water masses that were modelled by various SWTs (multi-SWTs), as the Central Waters, DSOW and SPMW, the multi-SWT contributions were obtained by adding the contributions of their respective components. Then the water samples with  $X_i$  of the multi-SWT greater than 95% were selected. The property values of each component of the multi-SWT were then subtracted from the values of the water samples and linear regressions between  $\theta$  and the rest of the resulting properties were performed. The STDs of the multi-SWT properties were assumed to be equal to the error of the intercept. The

properties of each component of the multi-SWT had the same STDs as the corresponding ones in the multi-SWT. With this methodology the variability due to the  $\theta$  variability was removed.

- c) A modification of the methodology in (b) was applied to MW, where samples with  $X_i > 75\%$  were selected and used for the linear regressions.

The STDs of the properties of SAIW were assigned equal to those of the Central Waters, because not enough water samples presented  $X_i > 95\%$  of this water mass. The STD of NEADW<sub>U</sub> was computed using the errors of the SWTs in which it is assumed to decompose (section 4.5).

The STDs for the O<sub>2</sub> were set as a value equal to 3% of the saturation value, since when a water mass is formed the content of O<sub>2</sub> is not exactly the saturation value (Najjar and Keeling, 2000; Ito et al., 2004).

100 perturbations were performed and the OMP analysis was solved for each perturbed system. Uncertainties in the  $X_i$ s are computed from the results of the perturbations. Then, the STD of the 100 SWT distribution matrixes was calculated. The mean of the STD matrix is shown in Table 2. The resulting uncertainties in the  $X_i$ s range were between 0.015 and 0.13, indicating that the methodology is robust. The SWTs with higher mean STD values are those that belong to a mixing figure that covers a small property range, where the variability of the SWTs has a greater effect.

The least square method constrained to non-negative solutions returns the total residual, i.e., the squared largest singular value for the set of residuals resulting from the eOMP equation system (Eq. 4.2). These residuals give insights about the reliability of the proposed mixing model, and indicate the quality of the solution for each depth range. The total and individual residuals for the water samples are shown in Figure 21.

The total residual of the eOMP analysis is almost zero from 500 m depth to the bottom (Figure 21a). The individual residuals present the same pattern (Figure 21b, c, d). In the surface layer, the assumption of conservativeness is not justified because this layer is subject to seasonal variability. Nevertheless, as  $\theta$  and S have the highest weights in the analysis (Table 2), the majority of the positive residuals of  $\theta$  in the surface–subsurface layer are compensated by the corresponding negative residuals of S.

Therefore, the model is consistent since its residuals lack a tendency with depth (Figure 21) and the Standard Deviations of the Residuals remain low, slightly higher than the corresponding measurement error (Table 2). Besides, the model's ability to reproduce the measured values is given as the correlation coefficient ( $r^2$ ) between the measured (water samples) and the expected values for the SWTs properties (values of the properties of each water sample obtained by substituting  $X_i$ s in the system of equations). The model is proved to be reliable since it explains almost 99% of the variability of the conservative tracers, and more than 97% of all the non-conservative tracers except PO<sub>4</sub> (94%) (Table 2). The Standard Deviations of the Residuals provide an estimation of the goodness of the proposed mixing model.

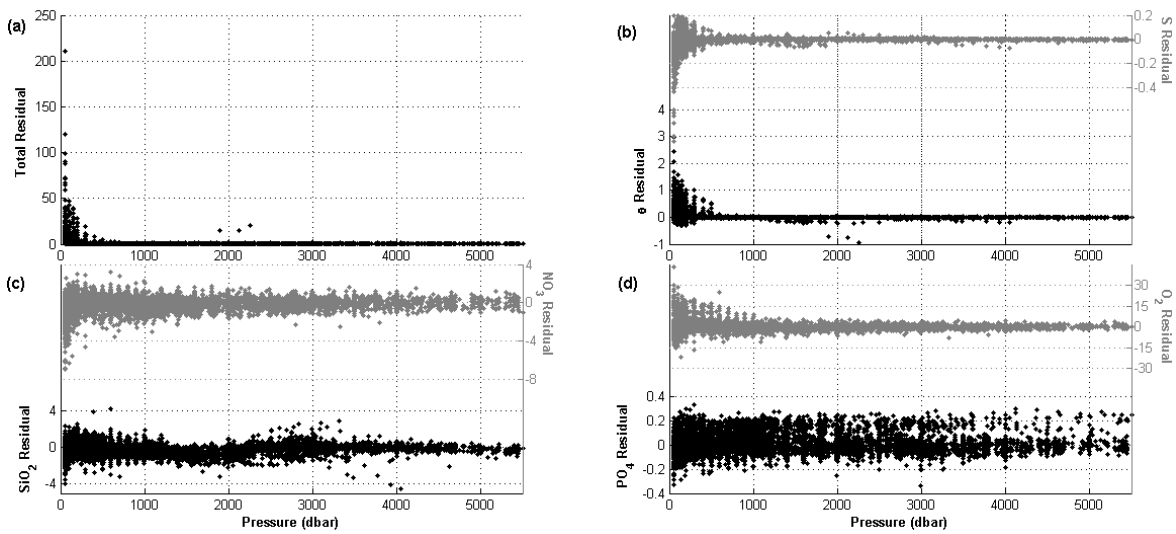


Figure 21.- Total residual from the extended Optimum MultiParameter (eOMP) analysis (a) and individual residuals from each eOMP equation (see Eq. 4.2): (b) potential temperature ( $\theta$ , in  $^{\circ}\text{C}$ ) and salinity (S); (c) silicate ( $\text{SiO}_2$ ) and nitrate ( $\text{NO}_3$ ) (both in  $\mu\text{mol}\cdot\text{kg}^{-1}$ ); and (d) phosphate ( $\text{PO}_4$ ) and oxygen ( $\text{O}_2$ ) (both in  $\mu\text{mol}\cdot\text{kg}^{-1}$ ).

When evaluating the water mass distributions derived from an OMP analysis, it should be taken into account that the properties that define the SWTs are time invariant; hence, changes in the properties of the water masses over time are reflected through water mass redistributions. Therefore, it is possible that some of the changes in the distribution of the SWTs may actually reflect inter-annual variations in the water mass properties not taken into account in the OMP set-up, and not only an increase/reduction of its extension. This affects water masses such as LSW and SPMW, whose properties vary from year to year due to formation processes and air–sea interaction differences.

#### 4.4.3.- Velocity field

The velocity fields in the sections are required to compute the volume transports by water mass. The velocity fields were obtained from the results of previous studies realized over the same sections using linear box inverse models. The inverse model configurations for 4x and OVIDE 2002 have been described by Lherminier et al. (2007), for OVIDE 2004 by Lherminier et al. (2010), for OVIDE 2006 by Gourcuff et al. (2011), and for OVIDE 2008 and 2010 by Mercier et al. (2015).

The inverse model is based on the least-squares formalism, which provides errors on the velocities and associated quantities such as the magnitude of AMOC (estimated in density coordinate) and the heat flux (Lherminier et al., 2010). The inverse model was constrained by direct Acoustic Doppler Current Profiler velocity measurements and by an overall mass balance of  $1 \pm 3$  Sv to the North (Lherminier et al., 2007, 2010).

The inverse model computes the absolute geostrophic transports orthogonal to the section. The Ekman transport is deduced from the wind fields averaged over the cruise period and added homogeneously in the first 40 metres (Mercier et al., 2015). The transport estimates of the inverse

model across OVIDE have been validated by favourable comparisons with independent measurements (Daniault et al., 2011; Gourcuff et al., 2011; Mercier et al., 2015).

#### 4.4.4.- *Combining the water mass distributions with the velocity fields*

The combination of the  $X_i$ s ( $i = 1-14$ ) obtained using the OMP analysis with the velocity fields allowed obtaining the volume transport of each SWT in the whole water column (Álvarez et al., 2004).

The  $X_i$ s were obtained at each measured point (i.e., bottle depth) for each hydrographic station, whereas the geostrophic and Ekman components of the flow were estimated at mid-distance between two hydrographic stations (defining a station pair) with a vertical resolution of 1 dbar. To match the velocity field, the SWT distributions were linearly interpolated at each dbar, and averaged in station pairs. The velocity field was obtained from the CTD downcast and the biogeochemical measurements (leading to the  $X_i$ s) were performed during the CTD upcast. To better match up both fields and compensate for vertical displacements of the water masses between the CTD downcast and upcast, I used density coordinates instead of pressure coordinates to interpolate the  $X_i$ s. To obtain  $X_i$ s until the bottom depth of each station pair, the shallower station profile in each station pair was extended until the maximum depth of the station pair by copying down the  $X_i$  values of the deepest measured point available.

Data of the upper layer (pressure  $\leq 50$  dbar) and of the Greenland shelf waters with  $S < 34.7$ , excluded from the OMP analysis, were appropriately reconstructed. The shallowest mixing contributions at each station of the upper layer were extrapolated up to the surface by keeping the same  $X_i$  values. In areas close to the Greenland shelf, water samples with  $S < 34.7$  were substituted by the nearest water sample included in the analysis.

#### 4.5.- **Water mass distributions for the first decade of the 2000s**

The water mass distributions were obtained for each repeat of the OVIDE section by means of an OMP analysis (section 4.4.2). It is important to remember that the water mass distributions here presented should be regarded as a best estimate and serve to illustrate the relative importance of the water masses, since the definitions of the SWTs in the OMP analysis mostly condition the distribution and the maximum contribution achieved by each SWT. Additionally, NEADW<sub>u</sub> is not shown because it was considered as a composite SWT (Álvarez et al., 2004; Carracedo et al., 2012) that can be derived from the mixing of 1.5% of MW, 18.4% of LSW, 29.5% of ISOW and 50.5% of NEADW<sub>l</sub> (decomposition based on  $\theta$ ,  $S$  and  $SiO_2$  content in the different water masses and on the work of van Aken (2000b)). In this section, the relevant features of the distributions of each SWT for the mean result of the OVIDE period (2002–2010) are described and discussed (Figure 22).

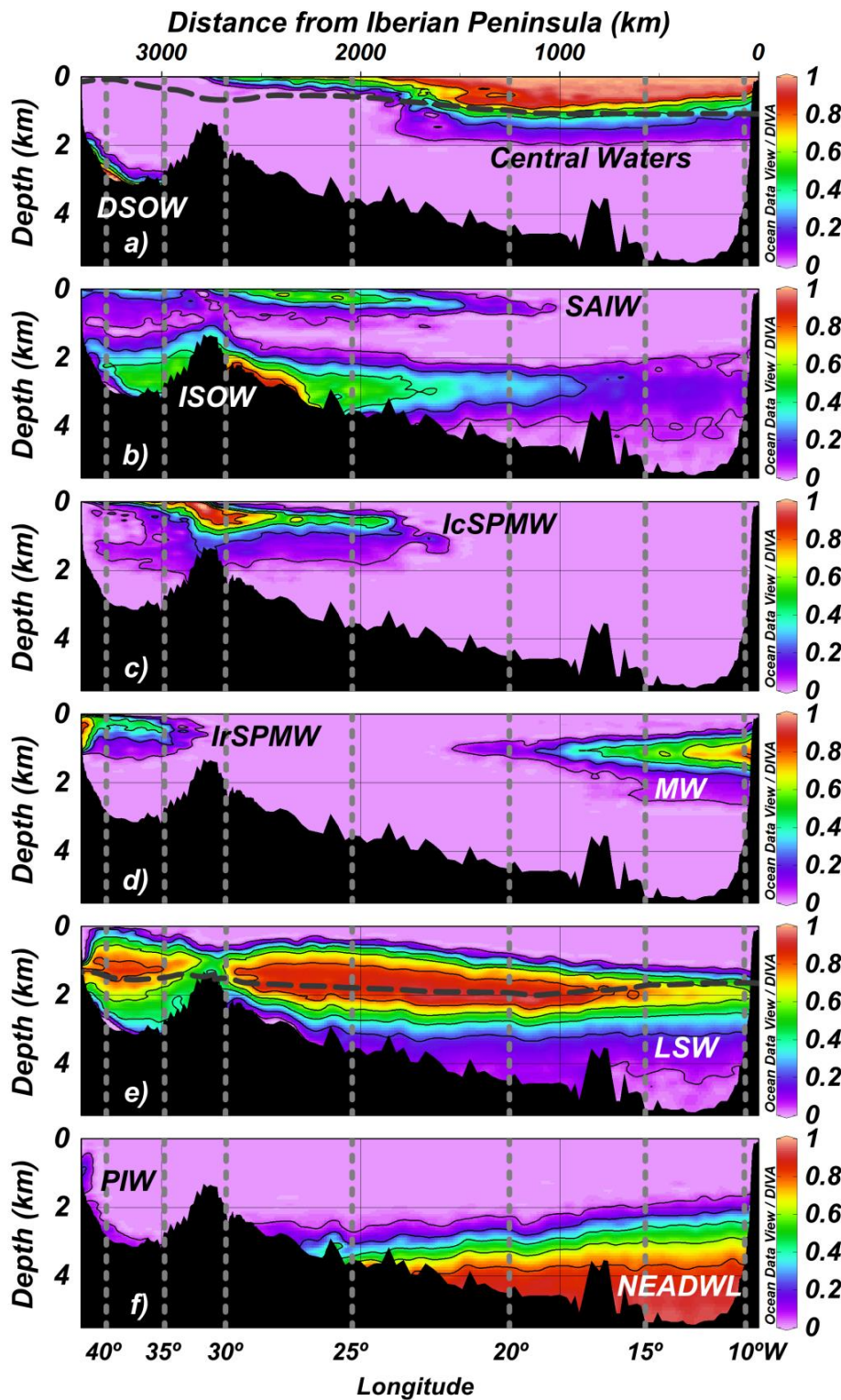


Figure 22.- Water mass distributions of the mean result for the OVIDE sections (2002–2010), from the Iberian Peninsula (right) to Greenland (left). The water mass contributions are expressed on a per unit basis (see Table 2 for the acronyms of the source water types). The dashed horizontal lines represent isopycnals:  $\sigma_1 = 32.15$  (plot a), which marks the limit between the upper and lower limb of the Atlantic Meridional Overturning Circulation; and  $\sigma_1 = 32.42$  (very similar to  $\sigma_0 = 27.8$ ; plot e), which marks the lower limit of Labrador Sea Water (LSW) on the classic works and approximately crosses the potential temperature/salinity definition of the source water type for LSW (Figure 20a).  $\sigma_1 = 32.42$  has the advantage of not varying rapidly in the eastern half of the sections.

### 4.5.1.- Upper waters

The Central Waters ( $ENACW_{16} + ENACW_{12}$ ) occupy the upper eastern part of the OVIDE section from the Iberian Peninsula until the Reykjanes Ridge (Figure 22a), representing an average of  $14.58 \pm 0.14\%$  of the total volume of the five sections. They follow the  $\theta$  maximum and the  $SiO_2$  minimum over the Iberian Basin (Figure 19a, e). Their distribution is associated with the circulation of the NAC, being the  $\theta/S$  front caused by the northern branch of the NAC (located at  $25^\circ W$  in the OVIDE sections, Figure 19a, b) the western limit of the Central Waters distribution. The Central Waters main core extends westwards, reflecting the cyclonic circulation of the Central Waters in the Iceland Basin and their southward flow over the eastern flank of the Reykjanes Ridge (Read, 2000; Pollard et al., 2004).

The main core of IcSPMW ( $SPMW_8 + SPMW_7$ ) is over the Reykjanes Ridge (Figure 22c). IcSPMW reaches the surface in the Irminger Basin, although it is formed in the Iceland Basin by the transformation (air–sea interactions) of the Central Waters (Thierry et al., 2008). This indicates that, at the time of OVIDE sections (summer), the surface waters in the Iceland Basin were warmer than  $8^\circ C$ . Furthermore, SAIW is also present in the surface waters of this basin, where it mixes with IcSPMW and the Central Waters. The distribution of IcSPMW also shows the transport of SPMW from the Iceland Basin to the Irminger Basin by the NAC (Irminger Current) (Brambilla and Talley, 2008).

IrSPMW extends from the Greenland slope until the Reykjanes Ridge (Figure 22d), with its main core over the Greenland slope. This distribution could indicate that the major region of formation of IrSPMW could be the NW of the Irminger Basin (Brambilla and Talley, 2008), from where the East Greenland Irminger Current would transport it until the OVIDE section. This SWT can be treated as a precursor of the upper LSW (Pickart et al., 2003). The continuity of the distributions of the Central Waters, IcSPMW and IrSPMW indicates that IrSPMW is the final product of the transformation of the Central Waters due to air–sea interaction processes (McCartney and Talley, 1982; Brambilla and Talley, 2008), IcSPMW being the intermediate point of the transformation.

### 4.5.2.- Intermediate waters

SAIW ( $SAIW_6 + SAIW_4$ ) is present in the upper layers of the northern half of the OVIDE sections (Figure 22b). The distribution of SAIW shows a maximum in the Iceland Basin associated with its advection from the Labrador Sea within the NAC and its subduction beneath the Central Waters (Bubnov, 1968; Arhan, 1990; Read, 2000). SAIW suffers a sharp decline once it encounters the NAC, but its contribution is significant until 600 m depth, where it still represents percentages greater than 25%. East of the Rockall Bank (Figure 18), SAIW deepens until intermediate water depths, where it overlies MW (Pollard et al., 1996). In fact, SAIW and MW contribute together to their surrounding waters in the region southeast of the NAC (Figure 18 and Figure 22b, d) (Harvey and Arhan, 1988).

The main core of MW is located around 1200 m depth off the shelf of the Iberian Basin (Figure 22d, see the tongue of maximum S and minimum  $O_2$  in Figure 19b, c), with a maximum of  $83.4 \pm 0.9\%$  coinciding with the S maximum of  $36.28 \pm 0.01$  ( $n = 5$ ; where  $n$  is the number of cruises). This main core is associated with the northward flow of MW (Reid, 1979) and its



westwards extension could be associated with its transport by meddies (Mazé et al., 1997) and by the Azores countercurrent (Carracedo et al., 2014).

LSW is the dominant SWT in the sections ( $35.0 \pm 0.6\%$  of the section volume,  $n = 5$ ; Figure 22e). It mainly extends from 1000 to 2500 m depth, coinciding with the S minimum ( $34.91 \pm 0.02$ ) and a relative  $O_2$  maximum ( $285 \pm 2 \mu\text{mol}\cdot\text{kg}^{-1}$ ) found in all the three basins (Figure 19b, c). LSW presents two main cores separated by the Reykjanes Ridge, which correspond to the different pathways of its circulation (Pickart et al., 2003; Álvarez et al., 2004). This “gap” separating the two LSW cores suggests a relatively strong mixing around and over the Reykjanes Ridge (Ferron et al., 2014), where the presence of fractions greater than 20% of ISOW and IcSPMW induces a decrease in LSW. This erosion of the LSW core is also reflected by a reduction of the S minimum over the Reykjanes Ridge (Figure 19b). Moreover, this is the location of the water mass described as the Icelandic Slope Water by Yashayaev et al. (2007a), which is defined as a result of the direct mixing of ISOW with Atlantic waters, mixing represented in our work by the mixing figure 4 (Figure 20c). In agreement with the work of Read (2000), the depth of the LSW core in the Irminger Basin is shallower than the one spreading across the Iceland and Iberian Basins, although they stay at the same density (see isopycnal  $\sigma_1 = 32.42$ , dashed line on Figure 22e; where  $\sigma_1$  is potential density referenced to 1000 dbar). The contribution of LSW in the south-eastern part of the sections is high (reaching maximum values of  $76 \pm 1\%$ ,  $n = 5$ ), emphasizing the influence of LSW until areas close to the Iberian Peninsula (Tsuchiya et al., 1992; Arhan et al., 1994a; Paillet et al., 1998). Moreover, the volume occupied by LSW gradually decreases from the Irminger Basin to the Iberian Basin. It represents  $45 \pm 1\%$  ( $n = 5$ ) of the volume of the Irminger Basin (defined between the Greenland slope and the Reykjanes Ridge),  $45 \pm 1\%$  of the volume of the Iceland Basin (defined from the Reykjanes Ridge until  $25.5^\circ\text{W}$ ) and  $30.3 \pm 0.5\%$  of the volume of the Iberian Basin (note that the volumes of the basins refer to the volumes at the section location, and the volumes per water mass are computed by weighting the volume of the basin by the SWT contribution).

### 4.5.3.- Overflows and deep waters

ISOW comes from the Iceland–Scotland sills and flows southwards along the eastern flank of the Reykjanes Ridge, where its main core is found (Figure 22b). This main core is located at depths greater than 2300 m, with maximum percentages of  $90 \pm 2\%$  ( $n = 5$ ), where the  $\theta/S$  properties are  $2.59 \pm 0.03^\circ\text{C}$  and  $34.979 \pm 0.002$ , respectively. From this region the core extends eastwards between  $\sim 2000$  and 4000 m depth, reaching values of 10% in the Iberian Abyssal Plain (Figure 18). This eastward extension could reveal that some ISOW must bypass the CGFZ and flow into the West European Basin. This feature is captured by the OMP analysis, since it is capable of capturing the significant fractions of the water masses better than the classical water mass descriptions. ISOW is also detected at the bottom in the central and eastern regions of the Irminger Basin, associated with its northward spreading after crossing the CGFZ (Dickson and Brown, 1994; Saunders, 2001). These findings could also be related to the northward flow of ISOW mainly in the interior part of the Irminger Basin (Sarfanov et al., 2012).

The deepest part of the Greenland continental slope is occupied by DSOW (Figure 22a). The distribution of this water mass can be traced in the vertical sections of the OVIDE mean properties (Figure 19) as a minimum of  $\theta$  ( $< 2^\circ\text{C}$ ), a maximum of  $O_2$  ( $> 280 \mu\text{mol}\cdot\text{kg}^{-1}$ ) and a relative minimum of nutrients. The inclusion of PIW in the analysis is an attempt to model the

entrainment of shelf waters into the deep waters of the Irminger Basin (Tanhua et al., 2008; Falina et al., 2012; von Appen et al., 2014). The presence of PIW (Figure 22f), even though in a very narrow area, supports the statement of the existence of certain dynamical processes that link the East Greenland shelf waters with the deep overflows.

NEADW<sub>L</sub> is the dominant water mass in the Iberian Basin from 2000 m depth to the bottom, with the main core below ~3500 m depth (Figure 22f). The distribution of this water mass follows the high SiO<sub>2</sub> concentrations at the bottom of the Iberian Basin (> 20 μmol·kg<sup>-1</sup>; Figure 19e), which are coupled with high concentrations of NO<sub>3</sub> and PO<sub>4</sub> (Figure 19d, f, respectively). The high SiO<sub>2</sub> levels reflect the influence of Antarctic Bottom Water (van Aken and Becker, 1996). The NEADW<sub>L</sub> isolines shallow eastwards due to the general deep eastern boundary upwelling of this water mass along the coast of the Iberian Peninsula (Arhan et al., 1994b). The northern part of the distribution of NEADW<sub>L</sub> is affected by the influences of LSW and ISOW.

#### 4.6.- Time variability of the water mass distributions between 1997 and 2010

In this section, the variability from 1997 to 2010 of SPMW (IcSPMW + IrSPMW), LSW and the deep overflows (DSOW and ISOW) is described and discussed (Figure 23). It should be mentioned that the different section pathways (Figure 18) could generate differences in the SWT distribution patterns between the 4x and OVIDE sections. The overlapping of the METEOR and OVIDE sections allows distinguishing between the differences in the SWTs distributions due to the different section pathways, and the inter-annual variability.

From the comparison of the LSW distributions in both cruises of 1997, it can be concluded that for the Irminger Basin the difference in the section pathway between the 4x and OVIDE sections is negligible, whereas for the Iceland Basin and around the Reykjanes Ridge it is an important component of the variability of the LSW distributions (Figure 23). In the Irminger Basin, from 1997 to 2010 the contribution of LSW gradually decreases, which is in agreement with the almost complete disappearance of the LSW signal found in 2007 by de Jong et al. (2012). LSW represents 58% of the volume of the Irminger Basin in 1997, then its importance decreases over time, representing 50% for 2002, with a sharp decrease in 2006 when it drops to 43%, a percentage that remains until 2010. The LSW maximum in the Iceland Basin decreases more slowly than the one in the Irminger Basin, meaning that in 2004 the fractions of the core in the Iceland Basin are higher (> 95%) than those of the core in the Irminger Basin (< 90%). This contrast is most noticeable in 2006 due to the sharp decrease in the fractions of LSW in the Irminger Basin. In the West European Basin (Figure 18) the greatest change in the fractions of LSW takes place in 2008, when the extension of the core is reduced in both the Iceland and the West European Basins, a reduction that continues in 2010. However, the volume occupied by LSW in the Iberian Basin is almost constant over time ( $30.3 \pm 0.5\%$  for the period 2002–2010), which indicates that the large inter-annual variability of the properties in its formation region attenuates due to mixing over the length and timescales of the transit from the Labrador Sea (Cunningham and Haine, 1995; Paillet et al., 1998). The difference in years between the deepening and total extension of LSW could be related to the changes in the volume of LSW formed. Between 1987 and 1995 the change in the NAO index led to the diminution in volume

and also the warming and salinization of LSW over time (Lazier et al., 2002; Yashayaev, 2007). These changes in the LSW properties are solved by the OMP analysis by adding more SPMW.

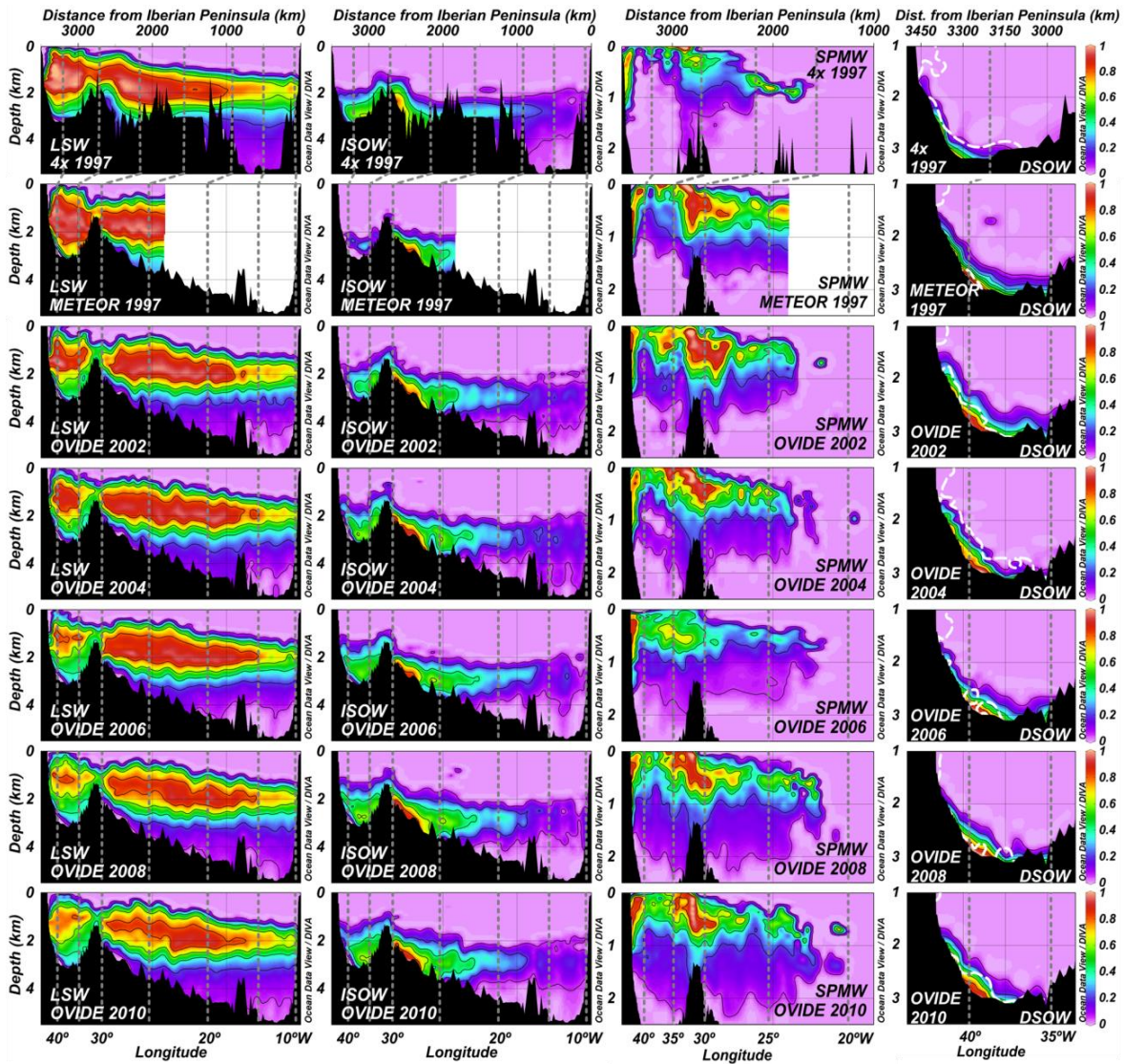


Figure 23.- Water mass distributions along the WOCE A25 sections, from 1997 (4x section, upper plots) to 2010 (OVIDE section, lower plots), from the Iberian Peninsula (right) to Greenland (left). The water mass contributions are expressed on a per unit basis. Note that  $SPMW = IrSPMW + IcSPMW$ . The dashed white line on the DSOW plots represents the limit of the PIW contributions (5% isoline) (see Table 2 for the acronyms of the source water types).

The SPMW ( $IcSPMW + IrSPMW$ ) distribution presents the greatest change between the two sections carried out in 1997 (Figure 23), which indicates that the section pathway influences the SPMW distribution since both cruises took place in the same time frame. The main path of the NAC around the Reykjanes Ridge is located north of the 4x section location (Figure 18) so that the fractions of SPMW observed at the 4x location are lower than at the OVIDE location. Meanwhile, the METEOR section presents an SPMW distribution similar to those of the OVIDE sections. Between 1997 (METEOR) and 2010, the importance of SPMW increases, rising from 24% to 30% of the volume of the Irminger Basin, with a rate of increase of 0.5% per year ( $r^2 =$

0.93), driven mainly by the increase in the upper 1000 m over the Reykjanes Ridge (0.7% per year,  $r^2 = 0.95$ ). This change may be related to the difference in the properties of the water masses at their formation regions. Since the end of the 1990s, the upper-ocean and upper intermediate waters of the NASPG have been getting saltier and warmer due to the redistribution of subpolar and subtropical waters caused by the NAO-induced slowdown and contraction of the NASPG (Bersch, 2002; Hátún et al., 2005; Sarafanov, 2009; de Boissésón et al., 2012). Thus, the 1997 section presents fresher waters than the 2000s sections, and the OMP replaces there less SPMW and more LSW. Moreover, the increasing amount of SPMW in the centre of the Irminger Basin could be associated with the reduction of the deep convection in the Labrador Sea, which resulted in a shallower variety of LSW (Pickart et al., 1996; Stramma et al., 2004; Bersch et al., 2007). The thickening observed in the SPMW distributions could indicate a salinization of LSW, solved by the OMP by adding greater fractions of SPMW.

The inter-annual variability of the depth, location and importance of LSW and SPMW seems to be connected. These results are in agreement with the interplay that exists between these water masses (Bersch et al., 1999). The upper parts of the Irminger Basin gain SPMW and lose LSW over time, demonstrating the ability of our OMP methodology to capture the different vintages of LSW formed over time (Yashayaev et al., 2008).

The distribution of ISOW is also influenced by the section pathway that is reflected by the differences in its distribution between the two 1997 cruises. For the 4x section the percentages of the ISOW core located over the eastern flank of the Reykjanes Ridge fall below 70%, whereas for the METEOR section it reaches percentages greater than 80% (Figure 23). This difference could be explained by the flow of part of ISOW through gaps in the Reykjanes Ridge located north of the CGFZ, between the METEOR and 4x sections, as found by Xu et al. (2010). The existence of various deep passages between the locations of the sections (Figure 18) may reduce the arrival of ISOW to the 4x section. The distribution of ISOW in the Irminger Basin also differs between the 4x and METEOR sections. The 4x section is located just after the CGFZ, so that the ISOW distributions on both sides of the ridge are similar. Meanwhile, in the METEOR section, the great distance between the fracture zone and the section causes ISOW to arrive more diluted at the section location after flowing anticyclonically around the ridge. For the same section pathway (METEOR-OVIDE), slight inter-annual changes in the distributions of ISOW are found on both sides of the Reykjanes Ridge. The core over the eastern flank of the ridge expands and contracts between cruises, which could reflect the inter-annual variability of the properties and sources of ISOW (Sarafanov et al., 2010). For the Irminger Basin, the ISOW influence increases over time, with the greatest change between 1997 (2% of volume) and 2002 (10%), increasing in importance until 2010 (15%), although with some inter-annual variability. The great difference between the ISOW distributions of the Irminger Basin in 1997 (METEOR) and 2002 could be related to the different LSW distribution on the two cruises. In 1997, after a period of high NAO index when large amounts of LSW were formed (Lazier et al., 2002; Yashayaev, 2007), LSW occupied almost the whole Irminger Basin, leaving little space for ISOW. In 2002, the reduction of the percentages of LSW allowed more ISOW to enter the Irminger Basin. These results are also supported by the increase of S in the Irminger Basin in the density range of ISOW found by Sarafanov et al. (2010). Since the properties that define an SWT are time invariant, the OMP analysis solves this increase of S by giving more presence to ISOW and less to LSW. This is also consistent with the increase of S in LSW (Lazier et al., 2002; Pickart et al., 2003; Kieke et al., 2007).

For 1997, DSOW seems to be colder at the 4x location than at the OVIDE location, which is reflected by lower percentages of DSOW and higher of PIW (Figure 23). This could indicate that (i) at 4x location the spill jet, represented by PIW, is not completely mixed with DSOW and the two SWTs can be more easily distinguished; and (ii) the existence of strong mixing between the two section locations led to a well-defined DSOW at the OVIDE location. Between METEOR and 2010, the DSOW distributions present no apparent trend at inter-annual timescales. In 2002 and 2004 the PIW influence in the DSOW layer is greater than in the other years, which is in agreement with the entrainment events observed by Falina et al. (2012). Adding the PIW contributions of mixing figure 3 (Figure 20c) to those of DSOW, this increase in the overflow volume can be observed. In both years, the DSOW contributions are greater, reaching more than 5.0% of the volume of the Irminger Basin, while in the other cruises its percentages do not exceed 4.5%. Probably, these changes could be associated with inter-annual variability in the water sources and transports of the overflows (Falina et al., 2012), which could ultimately be related to changes in the atmospheric forcing (Macrander et al., 2005), but the data here used is insufficient to relate these changes to a given timescale.

#### 4.7.- Water mass volume transports, recirculation and transformations in the Subpolar North Atlantic

For each OVIDE cruise the  $X_i$ s were combined with the absolute geostrophic velocity field (section 4.4.4) to obtain the water mass volume transports. Then the mean water mass volume transports were computed for the period 2002–2010 and integrated them along the section to obtain the net water mass volume transports (represented in Sverdrup;  $1 \text{ Sv} = 10^6 \text{ m}^3 \cdot \text{s}^{-1}$ ) (Figure 24). The water mass volume transports were calculated perpendicular to the sections and are positive northwards. Errors were computed by weighting the velocity errors by the  $X_i$ s. The velocity errors were computed at the reference level using the error covariance matrix of the inversion (Mercier, 1986; Lherminier et al., 2007, 2010). It is important to note that the water mass volume transport estimates are sensitive to the distribution of the SWTs.

The water masses that contribute to the northward transport in the section are the Central Waters ( $11.6 \pm 1.2 \text{ Sv}$ ), IcSPMW ( $2.6 \pm 1.5 \text{ Sv}$ ), SAIW ( $2.2 \pm 0.4 \text{ Sv}$ ) and MW ( $0.2 \pm 0.4 \text{ Sv}$ ) (Figure 24). These are the first estimates of the transports of the Central Waters, SPMW and SAIW in the Subpolar North Atlantic apart from the transports of the Central Waters and SAIW reported for the 4x section by Álvarez et al. (2004) (10.3 and 2.9 Sv, respectively). The MW transport here obtained is lower than that reported by Álvarez et al. (2004) and Schmitz (1996). This may be due to the variability derived from its transport by meddies (Arhan and King, 1995; Mazé et al., 1997).

The transformation of the above-cited water masses leads to the formation of IrSPMW, which transport ( $-8.8 \pm 0.9 \text{ Sv}$ ; Figure 24) is concentrated in the East Greenland Irminger Current. This water mass represents an important fraction of the  $-22.1 \pm 3.2 \text{ Sv}$  of the East Greenland Irminger Current estimated for the OVIDE sections of 2002 and 2004 by Lherminier et al. (2010). IrSPMW is the precursor of LSW, whose net transport across the OVIDE section is southwards ( $-0.9 \pm 1.8 \text{ Sv}$ ). This net southward transport of LSW, in agreement with a moderate formation of LSW in the Irminger Basin (Pickart et al., 2003), is explained by the strong southward transports found in the East Greenland Irminger Current, where small amounts of LSW

lead to great southward transports. Lherminier et al. (2007) reported a net northward export of LSW in the OVIDE section, while Bacon (1997) found a net transport of -1 Sv of LSW in a section close to the OVIDE section. The most likely explanation for the difference between the results here obtained and the two previous ones could lie in the specificities of the distributions obtained from the OMP analysis. The SWTs distributions are not defined by isopycnal ranges but as dilution from a “pure” SWT, so the OMP methodology assesses all the water mass contributions, even those outside the core of the water mass. This feature together with the inter-relation between LSW, SPMW and ISOW in the Irminger Basin (sections 4.4 and 4.5) could result in this kind of difference in the transport estimates.

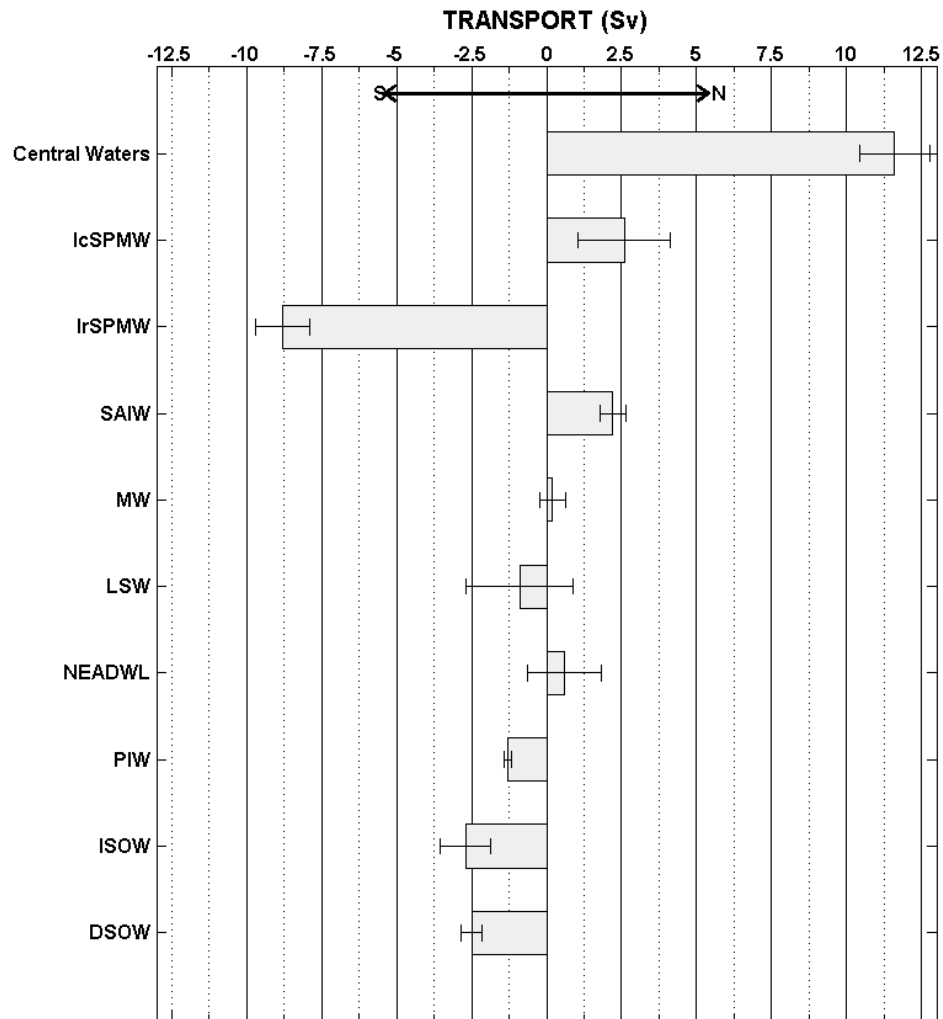


Figure 24.- Net water mass volume transports perpendicular to the OVIDE section for the mean result of the period (2002–2010). Transports (in Sv;  $1 \text{ Sv} = 10^6 \text{ m}^3 \cdot \text{s}^{-1}$ ) are positive northwards (see Table 2 for the acronyms of the source water types).

The water masses coming from the sills are PIW, DSOW and ISOW. The PIW transports were split into two main cores: a shallow one associated with mixing figure 1, and a deep one associated with mixing figure 3 (Figure 20c; section 4.4.2.2). For the shallow core of PIW the net transport is  $-1.3 \pm 0.1 \text{ Sv}$  (Figure 24). This transport is slightly lower than those reported by Pickart et al. (2005) (barely -2 Sv) and Falina et al. (2012) ( $-2.4 \pm 0.3 \text{ Sv}$  as mean transport for

2002–2004). This could be because the transports associated with the deep core of PIW were added to those of DSOW. Nevertheless, it is in agreement with the  $-1.3$  Sv of upper waters estimated to enter the Irminger Basin from the Nordic Seas (Hansen and Österhus, 2000). The transport of DSOW across the OVIDE section is  $-2.5 \pm 0.3$  Sv, which is in good agreement with the estimates of Ross (1984) (from  $-2$  to  $-3$  Sv), Eden and Willebrand (2001) ( $-2.5$  Sv), and Lherminier et al. (2010) ( $-2$  Sv, for the OVIDE sections of 2002 and 2004). However, this estimate is slightly lower than the  $-3$  Sv found by Dickson and Brown (1994), the  $-3.5 \pm 1.6$  Sv found by Macrander et al. (2005) and the  $-3.4 \pm 1.4$  Sv found by Jochumsen et al. (2012). Since in this study the assessment of the water mass volume transports is based on dilutions of a “pure” SWT, it would be expected to have lower volume transports than those estimated by isopycnals. These underestimates are compensated by the mixing with other SWTs (ISOW and LSW). The net transport of ISOW is  $-2.7 \pm 0.8$  Sv, a result supported by the  $-3.2 \pm 0.5$  Sv reported by Saunders (1996), the  $-3.6 \pm 0.5$  Sv reported by van Aken and Becker (1996), the  $-2.5 \pm 0.9$  Sv reported by Lherminier et al. (2007) and the  $-3.7 \pm 0.8$  Sv reported by Sarafanov et al. (2012). Finally, NEADW<sub>L</sub> also contributes to the net pull of the deep waters in the NASPG. The net transport of this water mass ( $0.6 \pm 1.2$  Sv) is comparable with the  $1.1$  Sv reported by van Aken and Becker (1996).

In a recent study, Mercier et al. (2015) estimated the magnitude of the upper and lower limbs of the AMOC (in density coordinates) for the OVIDE sections. These authors reported a magnitude of the upper limb of the AMOC of  $16.2 \pm 2.4$  Sv; and of  $-15.5 \pm 2.4$  Sv for the AMOC lower limb for the OVIDE period (2002–2010). Considering the isopycnal that separates the upper and lower limbs in Mercier et al. (2015) ( $\sigma_1 = 32.15$ ), the upper limb of the AMOC in the present study is represented by the Central Waters, IcSPMW and SAIW. The net northward transport of MW (Figure 24) was also included in the AMOC upper limb. These flows altogether result in an AMOC upper limb of  $16.6 \pm 1.5$  Sv for the OVIDE period. These upper AMOC contributors resemble the subtropical (Central Waters) and subpolar (SAIW and IcSPMW) components of the AMOC at the OVIDE sections described by Desbruyères et al. (2013). The lower limb of the AMOC is constituted by IrSPMW, PIW, LSW, ISOW, DSOW and NEADW<sub>L</sub>, resulting in a southward transport of  $-15.6 \pm 2.5$  Sv. Although in the present study the water masses that contribute to the upper and lower limbs of the AMOC may overlap both limbs, the resulting approach is in good agreement with the findings of Mercier et al. (2015). Combining the  $X_i$ s of the 4x section, obtained using the OMP methodology, with the velocity field of the section (Lherminier et al., 2007), the water mass volume transports of the 4x section reported by Álvarez et al. (2004) were reevaluated. For this section, the magnitudes of the upper and lower limbs of the AMOC obtained from the water masses contributing to each limb are  $23.3 \pm 1.2$  Sv and  $-21.1 \pm 1.8$  Sv, respectively. The difference with respect to the magnitude of the AMOC for the OVIDE period is explained by the greater transports in 1997 of the Central Waters ( $17.4 \pm 1.2$  Sv), IrSPMW ( $-12.0 \pm 0.3$  Sv) and PIW ( $-3.1 \pm 0.1$  Sv). The results of the present study support the findings of Mercier et al. (2015), who concluded that the decrease in the northward subsurface transport of the AMOC from 1993 to 2010 was balanced, at least partially, by a decrease in the southward export of the intermediate waters in the western Irminger Basin. These changes could be linked to a change in the circulation in response to a transition from previously high to low NAO indices over this time span (1997–2000s).



Taking advantage of the estimated water mass volume transports, the water mass circulation and transformation in the Subpolar North Atlantic was inferred based on four boxes defined following Lherminier et al. (2010) and limited to the south by the OVIDE section and to the north by the Greenland–Iceland–Scotland sills (Figure 25). The region east of the Reykjanes Ridge will be referred to as the East North Atlantic (ENA) Basin and the region west of the Reykjanes Ridge as the Irminger Basin. The final four boxes were obtained by dividing both basins vertically by the isopycnal  $\sigma_2 = 36.94$ , which traditionally defines the upper bound of the deep waters. Considering that no passages deeper than this isopycnal exist in the ridge between Iceland and the OVIDE section, this isopycnal also separates the water masses that can cross the Reykjanes Ridge (upper boxes) from those that cannot (lower boxes), which sets an additional constraint on the volume budgets. The water mass volume transports are considered positive when entering the boxes.

In order to obtain the volume budgets of the boxes, I considered the volume transports estimates through the Greenland–Iceland–Scotland sills available in the literature (Figure 25, grey numbers). In the ENA Basin, -7 Sv of relatively warm water ( $> 7^\circ\text{C}$ ) flow north-eastwards past the Faroes (Figure 18) (Schmitz and McCartney, 1993; van Aken and Becker, 1996; Hansen and Österhus, 2000), while 3 Sv enter the basin via the overflow waters (Olsen et al., 2008). In the Irminger Basin, 1.3 Sv of upper waters (Hansen and Österhus, 2000) and 3 Sv of overflow waters (Olsen et al., 2008) enter this basin from the Nordic Seas, whereas -1 Sv of Atlantic water exits this basin toward the Nordic Seas (Hansen and Österhus, 2000). The volume transports at the southern limit of the boxes (OVIDE section) are the mean volume transports across the OVIDE sections (section 4.5.3).

The net volume transport in the ENA Basin across the OVIDE section is  $13.4 \pm 4.7$  Sv and across the Iceland–Scotland sills is -4 Sv (Figure 25a, c). As a result,  $9.4 \pm 4.7$  Sv should flow from the ENA Basin to the Irminger Basin over the Reykjanes Ridge. This is corroborated by the volume budget of the Irminger Basin, where the difference between the net volume transport across the OVIDE section ( $-12.6 \pm 4.7$  Sv) and that across the Greenland–Scotland sills (3.3 Sv) is  $-9.5 \pm 4.7$  Sv. These estimates are very similar to the  $11.7 \pm 2.1$  Sv estimated by Lherminier et al. (2010) for the mean of the 2002–2004 OVIDE sections and to the  $9.1 \pm 1.8$  Sv estimated by Sarafanov et al. (2012) for the region between  $59.5^\circ\text{N}$  and the Greenland–Iceland–Scotland sills.

Of the 3 Sv of overflow waters entering the lower ENA box, only  $-1.3 \pm 2.6$  Sv exit this box across the OVIDE section (Figure 25c). This implies that  $1.7 \pm 2.6$  Sv should upwell and become part of the upper ENA box. In fact, these  $1.7 \pm 3.9$  Sv are necessary in the upper ENA box to balance the volume transports (Figure 25a). For the upper Irminger box, 0.3 Sv enter via the Greenland–Iceland sills and  $9.4 \pm 4.7$  Sv enter over the Reykjanes Ridge. Only  $-6.2 \pm 4.2$  Sv exit the box across the OVIDE section, thus implying that  $3.5 \pm 6.3$  Sv should sink and become part of the lower Irminger box. In this lower Irminger box, 3 Sv enter via the overflow waters and  $-6.4 \pm 2.2$  Sv exit across the OVIDE section, thereby  $3.4 \pm 2.2$  Sv are missing, and would be those from the upper Irminger box (Figure 25c). This is in agreement with the mean results for the 2002–2004 OVIDE sections of Lherminier et al. (2010), who estimated that  $3.9 \pm 1.8$  Sv cross from the upper to the lower box of the Irminger Basin.

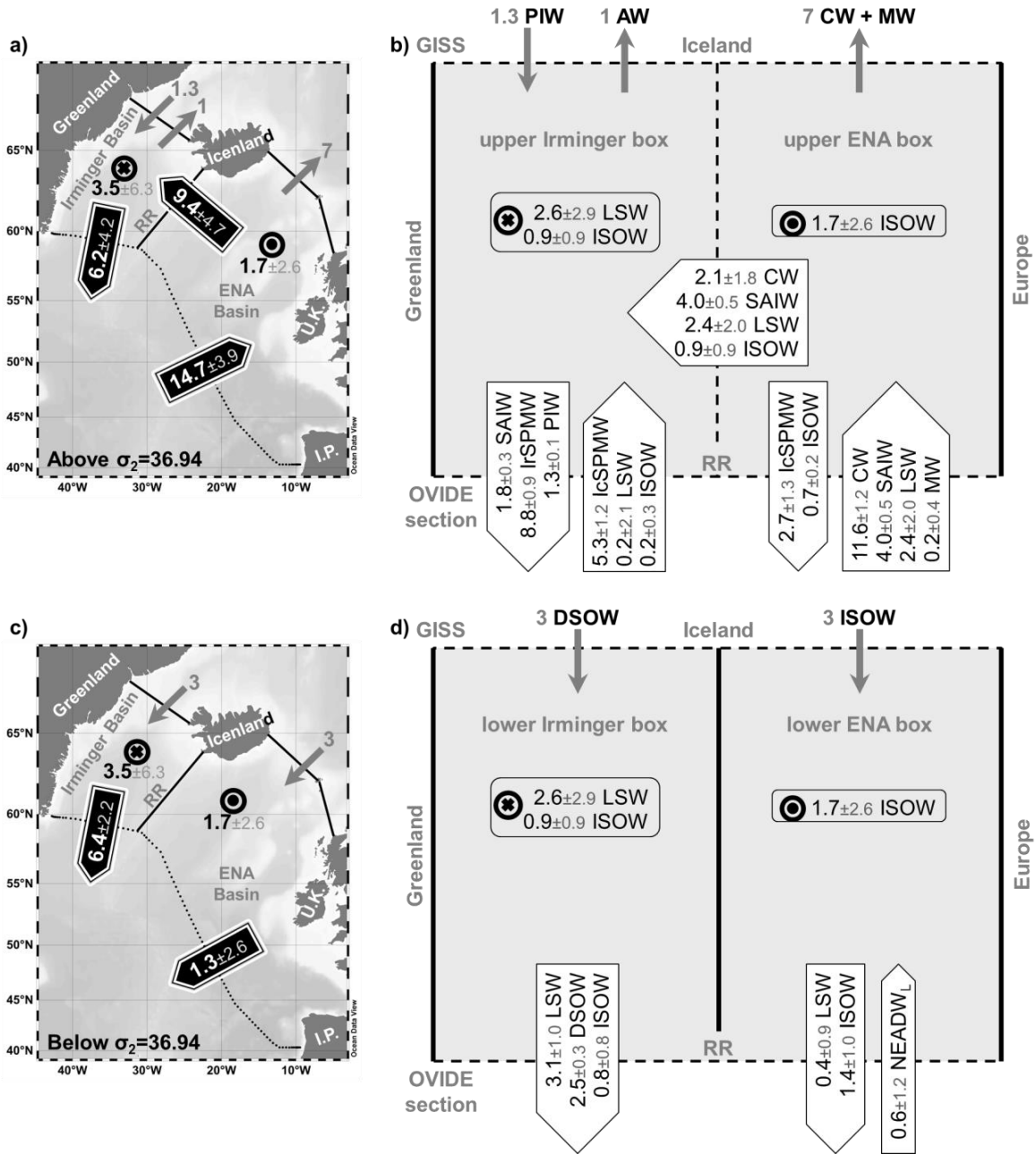


Figure 25.- Schematic diagram of the water mass circulation, transformation and transports in the North Atlantic Subpolar Gyre, based on a two-layer box model in between the OVIDE section and the Greenland–Iceland–Scotland sills (GISS). The transports (in Sv;  $1 \text{ Sv} = 10^6 \text{ m}^3 \cdot \text{s}^{-1}$ ) at the southern boundary are the mean transports across the OVIDE sections as obtained in the present study. The transports at the northern boundary (GISS) are defined as explained in section 4.7. The boundary between the western (East North Atlantic (ENA) Basin) and eastern (Irminger Basin) boxes is the Reykjanes Ridge (RR). RR is closed (open) for the deep (upper-ocean and mid-depth) circulation. The diapycnal volume fluxes (crossed and point circles) and the transports across the RR are inferred from the condition of volume conservation. The uncertainties are shown in grey. Note that CW accounts for Central Waters, AW for Atlantic waters (see Table 2 for the acronyms of the source water types) and I.P. for Iberian Peninsula.

The OMP-based water mass distributions allow disaggregating the water masses that are involved in each of those volume transports. The  $1.7 \pm 2.6 \text{ Sv}$  upwelling from the lower to the

upper ENA box should be ISOW, since from the 3 Sv of overflow waters entering the lower ENA box, only  $-1.4 \pm 1.0$  Sv leave the box across the OVIDE section. Thus, the remaining  $1.6 \pm 1.0$  Sv should upwell to the upper ENA box, which is proved by the net southward transport of  $-0.7 \pm 0.2$  Sv of ISOW in the upper ENA box across the OVIDE section (Figure 25b). The remaining  $0.9 \pm 0.9$  Sv should cross over the Reykjanes Ridge, which is consistent with the net southward export of  $-0.6 \pm 0.9$  Sv of ISOW in the Irminger Basin across the OVIDE section.

In order to estimate the other water mass components of the  $9.4 \pm 4.7$  Sv crossing over the Reykjanes Ridge the composition of the  $-7$  Sv crossing the Iceland–Scotland sills northwards should be determined. Since this flow has temperatures over  $7^{\circ}\text{C}$  (Schmitz and McCartney, 1993; van Aken and Becker, 1996), only the Central Waters, IcSPMW and MW (New et al., 2001) are possible sources. IcSPMW is excluded from this group because it is formed in the Iceland Basin close to the Reykjanes Ridge (McCartney and Talley, 1982; Tsuchiya et al., 1992; van Aken and Becker, 1996). Considering that the Central Waters and MW account for  $11.8 \pm 1.3$  Sv in the ENA Basin across the OVIDE section and that  $-7$  Sv cross the Iceland–Scotland sills northwards,  $4.8 \pm 1.3$  Sv are available to flow over the Reykjanes Ridge. MW flows northwards through the Rockall trough due to mixing with the Central Waters (Pollard et al., 1996; McCartney and Mauritzen, 2001; New et al., 2001) and does not reach the Reykjanes Ridge, thus the  $4.8 \pm 1.3$  Sv are attributed to the Central Waters. Once the Central Waters reach the Iceland Basin they transform into IcSPMW ( $-2.7 \pm 1.3$  Sv), leaving only  $2.1 \pm 1.8$  Sv of Central Waters available for crossing over the Reykjanes Ridge. The rest of the flow over the ridge corresponds to those waters colder than  $7^{\circ}\text{C}$  entering the upper ENA box through the OVIDE section, i.e.,  $4.0 \pm 0.5$  Sv of SAIW,  $2.4 \pm 2.0$  Sv of LSW and the  $0.9 \pm 0.9$  Sv of ISOW above estimated. Intensified vertical mixing at the Reykjanes Ridge (Ferron et al., 2014) could explain the appearance and transports of LSW and ISOW over the ridge.

After crossing the Reykjanes Ridge, LSW and ISOW intrude in the deep-to-bottom levels of the Irminger Basin, being the main components of the 3.5 Sv downwelling from the upper to the lower Irminger box. In fact, the net flows of LSW and ISOW in the Irminger Basin are almost compensated by their corresponding flows over the Reykjanes Ridge (Figure 25b). In the lower Irminger box, the  $-2.5 \pm 0.3$  Sv of DSOW leaving this box are slightly lower than the 3 Sv of overflow waters entering this box. The deficit in the DSOW volume transport, as explained before, is compensated by the excess of LSW and ISOW. This disagreement in the volume transports could be explained by two facts. First, the mixing between IrSPMW and PIW leads to waters with properties similar to those of LSW, which the OMP analysis assigned as LSW. Second, the contributions of the spill jet are very difficult to separate from those of LSW (von Appen et al., 2014), so that part of the spill jet that should be contributing to the DSOW volume transport would be attributed to the LSW volume transport.

In the upper Irminger box, the transport of PIW across the OVIDE section matches the 1.3 Sv entering this box from the Nordic Seas. The remaining water masses present in this box undergo significant transformations. From the  $4.0 \pm 0.5$  Sv of SAIW entering the Irminger Basin over the Reykjanes Ridge,  $-1.8 \pm 0.3$  Sv exit this basin through the OVIDE section. Besides, considering that  $-1$  Sv of Atlantic waters leaves the Irminger Basin towards the Nordic Seas,  $3.2 \pm 1.8$  Sv of Central Waters and SAIW should have been lost or transformed into other water masses. Considering that IrSPMW derives from IcSPMW, and that the inputs from the latter only account for  $5.3 \pm 1.2$  Sv in the Irminger Basin (Figure 25b), the  $3.2 \pm 1.8$  Sv of Central Waters and SAIW

should have contributed to the IrSPMW volume transport. The net southward export of  $-8.8 \pm 0.8$  Sv of IrSPMW across the OVIDE section is most probably the further precursor of LSW in the Labrador Sea (Talley and McCartney, 1982).

The high variability of the water mass transports around Cape Farewell (Daniault et al., 2011) hinders a consensus on the estimation of the formation of NADW (Clarke, 1984; Dickson and Brown, 1994; Bacon, 1997). The classical study of Dickson and Brown (1994) states that NADW is formed by the merger of ISOW, DSOW, Lower Deep Water (here represented by NEADW<sub>L</sub>) and minor contributions of LSW. Dickson and Brown (1994) state that the ISOW transport would increase due to the contribution of the Lower Deep Water and that LSW would contribute to the increase of the transport of DSOW from the sills until Cape Farewell, which is corroborated in the present study by the net southward transport of LSW in the Irminger lower box (Figure 25d). If the transports of all the contributors of NADW (net transport of DSOW, ISOW, NEADWL across the OVIDE section, and the net transport of LSW in the Irminger lower box across the OVIDE section) are added, I obtain a production of  $9.0 \pm 0.9$  Sv, a result slightly lower than the  $\sim 10$  Sv reported by Bacon (1997) at Cape Farewell.

Although the water mass volume transports given by the water mass distributions are sensitive to the distribution of the SWTs, which are subject to the definition of the SWTs, the volume transports estimated through the water mass distributions are more realistic than those obtained between density layers. In the studies performed between density layers, the volume transports between certain isopycnals are assigned entirely to a water mass, while the methodology described here allows this volume transport to be split between the different water masses found in this density range, which could lead to water mass volume transports lower than those estimated through the isopycnal method.

## 4.8.- Conclusions

---

In this study I show an application of the OMP analysis to identify temporal variations and transformations of the water masses along the WOCE A25 hydrographic sections (southern boundary of the NASPG). The choice of SWTs and mixing figures here performed is appropriate to describe all the cruise samples, as evidenced by the low residuals of the model. Water mass transformation through air–sea interactions is taken into account in the OMP set-up by specifying several varieties of SPMW. This novelty leads to realistic water mass distributions, confirming generally accepted knowledge of the Subpolar North Atlantic circulation. In particular, our water mass distributions evidence the subduction of SAIW below the NAC and the PIW cascading to the density of the Deep Western Boundary Current. The relative contribution from each water mass to the transports across the sections is also provided by combining the results from the OMP analysis with the velocity fields of the sections. The assessment of the water mass volume transports based on dilutions of a “pure” SWT (OMP-based) is particularly useful for areas of complex currents and relevant processes of water mass transformation, where this combined methodology can provide robust insights on the circulation features, improving the understanding of the regional oceanography.

The transport estimates by water mass are in good agreement with previous studies and match the main features of the northern North Atlantic Circulation. Considering the isopycnal

that separates the upper and lower limbs of the AMOC ( $\sigma_1 = 32.15$ ), each SWT is associated with the corresponding AMOC limb. In the present study, the upper limb of the AMOC is represented by the Central Waters, IcSPMW, SAIW and MW; and the lower limb of the AMOC is constituted by IrSPMW, PIW, LSW, ISOW, DSOW and NEADW<sub>L</sub>. This allows associating the reduction of the magnitude of the upper limb of the AMOC between 1997 and the 2000s (from  $23.3 \pm 1.2$  Sv to  $16.5 \pm 1.5$  Sv) with the reduction in the northward transport of the Central Waters. This reduction of the northward flow of the upper limb of the AMOC is partially compensated by the reduction of the southward flow of the lower limb of the AMOC, associated with the decrease in the transports of IrSPMW and PIW.

The assessment of the box model budgets allows disentangling the transformation pathway of the Central Waters. In the ENA Basin, 2.7 Sv of Central Waters are transformed into IcSPMW. This flow recirculates around the Reykjanes Ridge and joins IcSPMW advected from the south (possibly through a branch of the NAC as suggested by Pollard et al. (2004)), leading to a northward transport of 5.3 Sv of IcSPMW in the Irminger Sea. These 5.3 Sv combine with 1.1 Sv of Central Waters and 2.2 SAIW (crossing over the Reykjanes Ridge) to give 8.8 Sv of IrSPMW through air–sea interaction.

LSW is the main water mass across the sections ( $35.0 \pm 0.6\%$  of the section volume). The inter-annual variability observed in the upper layers of the Irminger Basin reflects the interplay between LSW and SPMW, the mixing of which emulates the presence of the upper LSW. In the lower layers at both sides of the Reykjanes Ridge it is possible to notice an interaction between LSW and ISOW, with an increasing presence of ISOW responding to the progressive dilution of LSW. The OMP results also reveal that LSW is strongly mixed with the surrounding waters mainly in two regions: (i) at and upstream of the Reykjanes Ridge, and (ii) in the Deep Western Boundary Current, where the contribution of LSW is significant ( $\sigma_0 > 27.80$ ). The slightly negative net transport of LSW across the OVIDE section is in agreement with a moderate formation of LSW in the Irminger Basin.

Waters from the ENA Basin cross over the Reykjanes Ridge and enter the Irminger Basin, where they are transformed and/or densified, passing from the upper and intermediate water domains to the deep water domain. The OMP analysis allowed decomposing the 9.4 Sv of flow across the Reykjanes Ridge into Central Waters, SAIW, LSW and ISOW; SAIW being the main contributor.

The distributions and transports of ISOW allow inferring that in the course of the ISOW's journey from the Iceland–Scotland sills to the CGFZ, part of it upwells and flows through gaps in the Reykjanes Ridge between the OVIDE and 4x sections. Once ISOW arrives at the CGFZ some fractions continue to flow into the West European Basin while the main stream crosses the fracture to the Irminger Basin, flowing northwards and joining the fractions that previously crossed the ridge.

The extension of this methodology to wide areas of the ocean could provide a useful basis for this kind of study or more ambitious ones dealing with the cycle of biogeochemical components in the ocean.



## Chapter 5.- Observed trends of the stressors of the CO<sub>2</sub> system in the Irminger and Iceland Basins

### 5.1.- Resumen

La repetición de secciones hidrográficas proporciona datos y conocimiento acerca de los cambios en la química del CO<sub>2</sub> en agua de mar a nivel de cuenca oceánica para escalas de tiempo multidecenales. En este capítulo se utilizan datos de mediciones de carbono inorgánico de alta calidad de doce campañas que siguen el mismo trayecto para analizar las consecuencias a largo plazo de la absorción del CO<sub>2</sub> antropogénico ( $C_{ANT}$ ) en las cuencas del Irminger e Islandia para el período 1981–2014. Los cambios en el  $C_{ANT}$ , pH, alcalinidad total ( $A_T$ ) y la saturación de CaCO<sub>3</sub>, este último en términos saturación de aragonito ( $\Omega_{Arag}$ ), fueron evaluados en las principales masas de agua de las cuencas y discutidos en el contexto de la circulación oceánica. Todas las masas de agua de las cuencas del Irminger e Islandia están ganando  $C_{ANT}$ , lo que da lugar a tasas de acidificación significativas. Las altas tasas de aumento de la concentración de  $C_{ANT}$  que se encuentran en las capas superiores de ambas cuencas ( $0,66 \pm 0,06 \mu\text{mol}\cdot\text{kg}^{-1}\cdot\text{yr}^{-1}$  en la cuenca del Irminger y  $0,50 \pm 0,06 \mu\text{mol}\cdot\text{kg}^{-1}\cdot\text{yr}^{-1}$  en la cuenca de Islandia) responden al aumento del CO<sub>2</sub> en la atmósfera, lo que se traduce en unas tendencias de acidificación de  $-0,011 \pm 0,002$  unidades de pH por década en ambas cuencas. Las aguas profundas de la cuenca del Irminger presentan unas tasas de acidificación muy similares a las de las capas superficiales, resultado de su reciente contacto con la atmósfera. La columna de agua de la cuenca del Irminger presenta unas tasas de aumento de la concentración de  $C_{ANT}$  mayores que las encontradas en la cuenca de Islandia, lo que refleja la mayor proximidad de la cuenca del Irminger a las zonas de formación de masas de agua. Estas mayores tasas dan lugar a unos descensos de pH mayores en la cuenca del Irminger que en la cuenca de Islandia. Para averiguar las causas de los cambios de pH, éstos se dividieron en dos componentes: uno derivado de la captación de  $C_{ANT}$  ( $\Delta\text{pH}_{C_{ANT}}$ ) y otro no directamente relacionado con la captación de  $C_{ANT}$  ( $\Delta\text{pH}_{Var}$ ). En las capas superiores de ambas cuencas, la acción del  $\Delta\text{pH}_{Var}$  (debida a la advección de aguas subtropicales) contrarresta el efecto del  $\Delta\text{pH}_{C_{ANT}}$ , dando lugar a que las tasas de acidificación observadas sólo representan un 72–87% de las tasas esperadas por la captación de  $C_{ANT}$ . En cambio, en las capas intermedias de la cuenca del Irminger, el efecto del  $\Delta\text{pH}_{Var}$  (producido por el envejecimiento de las aguas) refuerza la acidificación derivada de la captación de  $C_{ANT}$ , lo que da lugar a que la tasa de acidificación de estas aguas sea un 34% mayor que la esperada por la acción del  $\Delta\text{pH}_{C_{ANT}}$ . Los descensos de pH observados causan que la  $\Omega_{Arag}$  muestre tendencias de descenso significativas en todas las masas de agua de ambas cuencas. Las aguas intermedias de ambas cuencas presentan unas tasas de descenso de la  $\Omega_{Arag}$  de entre  $-2,4$  y  $-3,8\cdot 10^{-3}$  año<sup>-1</sup>, lo que da lugar a un ascenso del horizonte de saturación con una tasa de  $\sim 10$  m·año<sup>-1</sup>. En base a los cambios de pH y  $\Omega_{Arag}$  observados durante el periodo 1981–2014, se infirieron los cambios esperados para el final del siglo. Se espera un descenso del pH de las capas superiores de  $\sim 0,31$  unidades de pH respecto a los valores de la era preindustrial cuando la concentración de CO<sub>2</sub> atmosférico alcance los 800 ppm, lo cual es consistente con las predicciones del RCP8.5 del IPCC. La capa profunda de la cuenca del Irminger sufrirá un descenso de pH similar al de la capa superficial ( $\sim 0,27$  unidades de pH). Estos descensos de pH alcanzados cuando la concentración de CO<sub>2</sub> atmosférico sea de 800 ppm darán lugar a que toda la columna de



agua de las cuencas del Irminger e Islandia este sub-saturada en aragonito, tal como ya lo indicaron los modelos. Sin embargo, las aguas intermedias alcanzarán el estado de subsaturación mucho antes, llegando a este estado cuando la concentración de CO<sub>2</sub> atmosférico alcance los ~500–560 ppm. Los datos aquí recopilados también muestran la influencia del aumento de la descarga de los ríos árticos en la A<sub>T</sub> de las aguas profundas de la cuenca del Irminger, que presentan unas tendencias significativas de aumento de la A<sub>T</sub>.

## 5.2.- Abstract

Repeated hydrographic sections provide critically needed data and understanding about changes in the basin-wide seawater CO<sub>2</sub> chemistry over multi-decadal timescales. In this chapter high-quality data of inorganic carbon measurements from twelve cruises along the same track are used to discuss the long-term impacts of the uptake of anthropogenic CO<sub>2</sub> (C<sub>ANT</sub>) in the Irminger and Iceland Basins for the period 1981–2014. The changes in C<sub>ANT</sub>, pH, total alkalinity (A<sub>T</sub>) and CaCO<sub>3</sub> saturation, the latter in terms of aragonite ( $\Omega_{Arag}$ ), were evaluated in the main water masses of the basins and discussed in the context of the basin-wide circulation. All the water masses from both the Irminger and Iceland Basins are gaining C<sub>ANT</sub>, which results in significant acidification rates. The highest rates of increase in the C<sub>ANT</sub> concentration found in the upper layer of both basins ( $0.66 \pm 0.06 \mu\text{mol}\cdot\text{kg}^{-1}\cdot\text{yr}^{-1}$  in the Irminger Basin and  $0.50 \pm 0.06 \mu\text{mol}\cdot\text{kg}^{-1}\cdot\text{yr}^{-1}$  in the Iceland Basin) respond to the atmospheric CO<sub>2</sub> increase, resulting in acidification trends of  $-0.011 \pm 0.002$  pH units per decade in both basins. The acidification rates of the deep waters of the Irminger Basin are close to those found in the upper layers, which is indicative of their recent contact with the atmosphere. The entire water column of the Irminger Basin presents higher rates of increase of the C<sub>ANT</sub> concentration than those found in the Iceland Basin, reflecting the greater proximity of the former to the areas of water mass formation. These higher rates lead to greater pH drops in the Irminger Basin than in the Iceland Basin. In order to disentangle the drivers of the pH changes, they were decomposed into two components: one derived from the C<sub>ANT</sub> uptake ( $\Delta\text{pH}_{C_{ANT}}$ ) and another not directly related to the C<sub>ANT</sub> uptake ( $\Delta\text{pH}_{Var}$ ). In the upper layer of both basins, the  $\Delta\text{pH}_{Var}$  action (driven by the advection of subtropical waters) counteracts the effect of the  $\Delta\text{pH}_{C_{ANT}}$ , causing the observed acidification rates only represent a 72–87% of the expected rates due to the C<sub>ANT</sub> uptake. By contrast, in the intermediate layers of the Irminger Basin, the effect of the  $\Delta\text{pH}_{Var}$  (derived from the aging of the waters) reinforces the acidification derived from C<sub>ANT</sub> sequestration, being the observed acidification rates a 34% higher than those expected only by the  $\Delta\text{pH}_{C_{ANT}}$ . The decreases in pH cause that the  $\Omega_{Arag}$  shows significant decrease trends in all the water masses of both basins. The decreasing trends of  $\Omega_{Arag}$  between  $-2.4$  to  $-3.8\cdot 10^{-3} \text{ yr}^{-1}$  observed in the intermediate waters of both basins correspond with an upward migration of  $\sim 10 \text{ m}\cdot\text{yr}^{-1}$  in the saturation horizon. Taking advantage of the observed pH and  $\Omega_{Arag}$  changes for the period 1981–2014, the future changes for the end of the century were inferred. The upper layer will suffer a pH drop of  $\sim 0.31$  pH units with respect to the pre-industrial era by the time atmospheric CO<sub>2</sub> reaches 800 ppm, which is consistent with the predictions for the IPCC RCP8.5. A similar pH decrease is expected for the deep layer of the Irminger Basin ( $\sim 0.27$  pH units). These pH drops derived from the 800 ppm of atmospheric CO<sub>2</sub> cause that the whole water column of the Irminger and Iceland Basins becomes undersaturated in aragonite in agreement with the results of numerical models. However, the intermediate waters would become undersaturated in aragonite faster, reaching that state by the time the atmospheric CO<sub>2</sub> reaches  $\sim 500$ – $560$  ppm.

The data here compiled also show the influence of the increase of the arrival of Arctic fresh waters in the  $A_T$  content of the deep waters of the Irminger Basin, which present significant increases in  $A_T$ .

### 5.3.- Introduction

The oceanic uptake of a large fraction of the anthropogenic CO<sub>2</sub> ( $C_{ANT}$ ; CO<sub>2</sub> released from humankind's combined industrial and agricultural activities) has produced the well-known ocean acidification (e.g., Raven et al., 2005; Doney et al., 2009; Feely et al., 2009). This phenomenon includes seawater chemical changes such as reduction in pH and saturation states for calcium carbonate (CaCO<sub>3</sub>) minerals. It has the potential to dramatically affect marine organisms and ecosystems (e.g., Langdon et al., 2000; Riebesell et al., 2000; Pörtner et al., 2004; Gattuso et al., 2014) and to modify the major marine biogeochemical cycles (Gehlen et al., 2011; Matear and Lenton, 2014). The average pH ( $-\log_{10}[H^+]$ ) of ocean surface waters has decreased by about 0.1 pH units since the beginning of the industrial revolution (1750), with model projections showing an additional 0.1–0.4 drop by the end of the century, even under optimistic scenarios (Caldeira and Wickett, 2005; Orr, 2011; Ciais et al., 2013). This rate of change is probably one hundred times higher than at any time since the last Ice Age (Feely et al., 2004; Raven et al., 2005). These changes are so rapid that they can significantly reduce the buffering capacity of the natural processes that have moderated changes in ocean chemistry over most of geological time (Raven et al., 2005). Also, this rapid rate of change could cause certain calcifying species do not adapt fast enough to survive, thus altering the marine food webs (e.g., Orr et al., 2005; Doney et al., 2009).

Oceans have absorbed ~30% of the  $C_{ANT}$  emitted to the atmosphere between 1750 and 2013 (DeVries, 2014; Le Quéré et al., 2014). However, this  $C_{ANT}$  is not evenly distributed throughout the oceans (Sabine et al., 2004), entering preferentially in regions of upwelling and convective overturn (Maier-Reimer and Hasselmann, 1987; Sarmiento et al., 1992; Lazier et al., 2002). The Meridional Overturning Circulation (MOC) makes the North Atlantic one of the most important  $C_{ANT}$  sinks of the global ocean, storing 25% of the global oceanic  $C_{ANT}$  despite covering only 15% of the global ocean area (Sabine et al., 2004). The MOC transports CO<sub>2</sub>-laden waters from the Equator to the northern North Atlantic (e.g., Watson et al., 1995; Wallace, 2001; Álvarez et al., 2003; Quay et al., 2007), where the water mass formation processes provide the pathway for the  $C_{ANT}$  to pass from the surface mixed layer to the deep ocean (Lazier et al., 2002; Pérez et al., 2008; Steinfeldt et al., 2009). The Irminger and Iceland Basins are very appropriate places to monitor temporal changes in the Atlantic MOC, since the overflows from the Arctic Ocean and the Nordic Seas, and the Labrador Sea Water from the Labrador Sea flow into these basins. These newly formed waters are laden with  $C_{ANT}$  and other anthropogenic tracers (Azetsu-Scott et al., 2003; Kieke et al., 2007; Rhein et al., 2007, 2015). Moreover, the intense heat loss occurring in these basins makes them areas of water mass transformation, where surface and intermediate waters sink into the deep layers, particularly in the Irminger Basin (García-Ibáñez et al., In Press; see also Chapter 4 of this thesis), thus homogenizing the properties of the water column. Therefore, these basins are good locations to (1) follow the  $C_{ANT}$  penetration to the deep ocean and its consequences; and (2) detect changes in the formation rates of the water masses related to changes in the North Atlantic Oscillation (NAO), which can modify the expected rates of oceanic  $C_{ANT}$  uptake (Pérez et al., 2008).

The assessment of rates of ocean CO<sub>2</sub> uptake over multi-decadal timescales across ocean basins provides observational tests for ocean-atmosphere models. Repeated hydrographic sections provide a mean of quantifying basin-wide ocean uptake of C<sub>ANT</sub> (e.g., Friis et al., 2005; Brown et al., 2010; Wanninkhof et al., 2010; Guallart et al., 2015b). In the present work high-quality direct observations of the seawater CO<sub>2</sub> system variables taken from twelve cruises along the Irminger and Iceland Basins are examined. Previous studies have focused on the C<sub>ANT</sub> uptake and its effects in the Irminger and Iceland Basins (e.g., Pérez et al., 2008; Olafsson et al., 2009; Bates et al., 2012; Vázquez-Rodríguez et al., 2012). Nevertheless, the study here presented tries to give a more detailed view of the stressors of the CO<sub>2</sub> system in the water masses of the Irminger and Iceland Basins for the last three decades, concretely for the period 1981–2014, based on direct observations.

The present chapter is organized as follows. In Section 5.4 the dataset and the methodology followed, including the pH changes deconvolution into anthropogenic and non-anthropogenic components are described. The temperature, salinity and oxygen fields and trends are described and discussed in Section 5.5. Then, the changes in alkalinity (Section 5.6), C<sub>ANT</sub> concentration (Section 5.7), pH (Section 5.8) and saturation state for the aragonite form of CaCO<sub>3</sub> ( $\Omega_{Arag}$ ) (Section 5.9) are described and discussed. The reason of choosing the aragonite form of CaCO<sub>3</sub> is twofold. First, aragonite is approximately 50% more soluble than calcite (Mucci, 1983), so its saturation horizon is more susceptible to pH changes. And second, the aragonite is the main constituent of the skeletons of the cold-water corals *Lophelia pertusa* and *Madrepora oculata*, which are important hotspots of biodiversity in the Atlantic Ocean (Movilla et al., 2013; Lunden et al., 2014), many of them proposed as sites of marine protected areas. Predictions of the future changes in pH and  $\Omega_{Arag}$  are given in Section 5.10. The chapter is concluded in Section 5.11.

## 5.4.- Material and Methods

### 5.4.1.- Dataset

A total of twelve cruises along the same track were selected, spanning over 33 years (1981–2014), to study the temporal evolution of C<sub>ANT</sub>, pH, total alkalinity (A<sub>T</sub>) and  $\Omega_{Arag}$  in the Irminger and Iceland Basins (Figure 26; Table 3). The data was accessed from the Global Data Analysis Project (GLODAP) v2 website (<http://cdiac.ornl.gov/oceans/GLODAPv2>), except for the data of the OVIDE 2012 and 2014 cruises, which are not publicly available yet. The data of the 1991 cruises were merged to obtain more robust data for that year. All cruise data here used are compliant with the latest carbon system analytical recommendations for seawater. Only bottle data including CO<sub>2</sub> system analysis were used in this study.

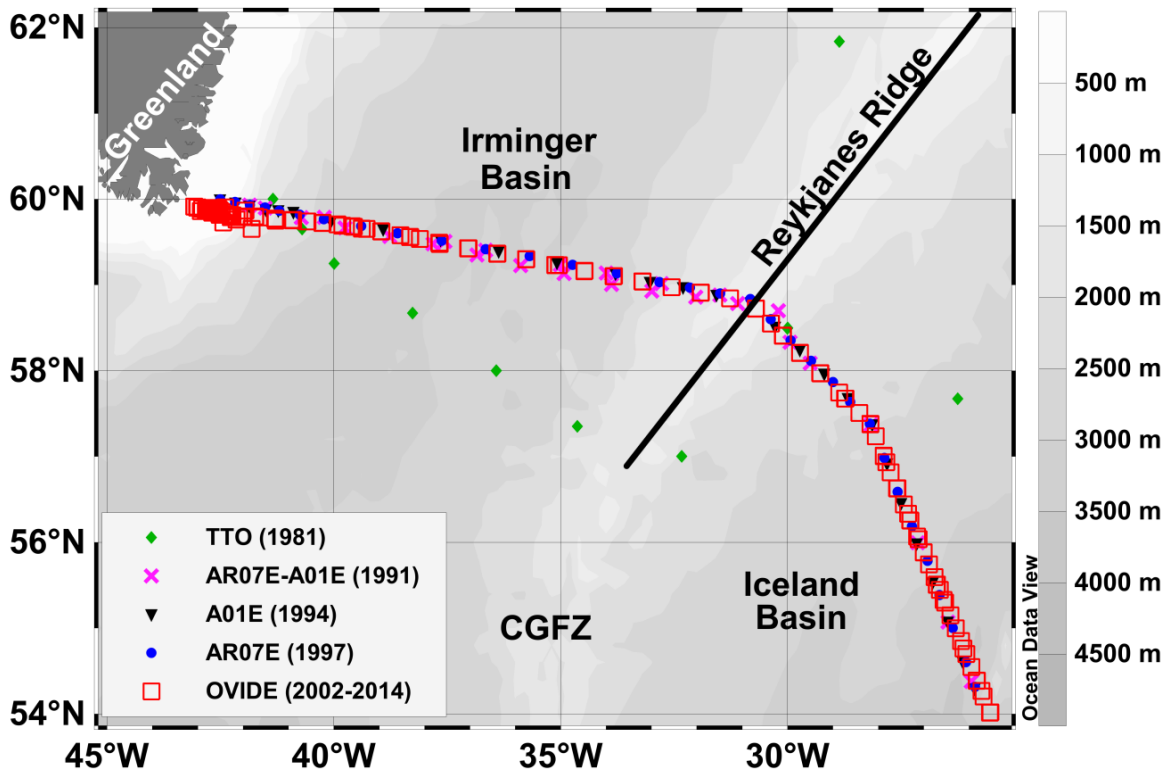


Figure 26.- Tracks of the twelve cruises of seawater CO<sub>2</sub> system measurements used in this study (1981–2014). The black line represents the boundary between the Irminger and the Iceland Basins constituted by the Reykjanes Ridge. CGFZ = Charlie-Gibbs Fracture Zone.

Table 3.- List of selected hydrographic cruises (Figure 26). P.I. denotes principal investigator, and #St the number of stations selected.

Cruise Name	Expocode	Month/Year	Vessel	P.I.	#St	Reference
TTO-NAS L6	316N19810821	08-09/1981	Knorr	W.J. Jenkins	11	Takahashi and Brewer (1986)
AR07E	64TR91_1	04-05/1991	Tyro	H.M. van Aken	12	
A01E	06MT18_1	09/1991	Meteor	J. Meincke	15	
A01E	06MT30_3	11-12/1994	Meteor	J. Meincke	27	
AR07E	06MT39_5	08/09-1997	Meteor	A. Sy	32	Rhein et al. (2002)
OVIDE 2002	35TH20020610	06/07-2012	Thalassa	H. Mercier	38	Lherminier et al. (2007)
OVIDE 2004	35TH20040604	06-07/2004	Thalassa	T. Huck	56	Lherminier et al. (2010)
OVIDE 2006	06MM20060523	05-06/2006	Maria S. Merian	P. Lherminier	44	Gourcuff et al. (2011)
OVIDE 2008	35TH20080610	06-07/2008	Thalassa	H. Mercier	45	Mercier et al. (2015)
OVIDE 2010	35TH20100610	06/2010	Thalassa	T. Huck; H. Mercier	46	Mercier et al. (2015)
CATARINA*	29AH20120623	06-07/2012	Sarmiento de Gamboa	A.F. Ríos	44	This work
GEOVIDE*	35PQ20140517	05-06/2014	Pourquoi Pas?	G. Sarthou	31	This work

\* Both the CATARINA (<http://catarina.iim.csic.es/en>) and GEOVIDE (<http://www.geovide.obs-vlfr.fr>) cruises contain the OVIDE section (<http://wwz.ifremer.fr/lpo/La-recherche/Projets-en-cours/OVIDE>), and are referred in the chapter as OVIDE 2012 and 2014, respectively.

At least two variables of the seawater CO<sub>2</sub> system were measured on all the cruises, but the measured pairs varied between cruises. The A<sub>T</sub> samples were analysed by potentiometric titration and determined by developing either a full titration curve (Millero et al., 1993; Dickson and Goyet, 1994; Ono et al., 1998) or from single point titration (Pérez and Fraga, 1987; Mintrop et al., 2000), with an overall accuracy of 4 μmol·kg<sup>-1</sup>. The total dissolved inorganic carbon (C<sub>T</sub>) samples were analysed with Single Operator Multiparameter Metabolic Analysers (SOMMA) based on coulometric titration techniques (Johnson et al., 1993) and were calibrated with Certified Reference Materials (CRMs), achieving an overall accuracy of 2 μmol·kg<sup>-1</sup>. The exception to the latter is the 1981 TTO-NAS cruise, where C<sub>T</sub> was determined potentiometrically (Bradshaw et al., 1981) and no CRMs were used, which led to an accuracy of 4 μmol·kg<sup>-1</sup>. The pH was determined either potentiometrically (Dickson, 1993a, b) using pH electrodes or, more commonly, with a spectrophotometric method (Clayton and Byrne, 1993) adding m-cresol purple as indicator in either scanning or diode array spectrophotometers. The spectrophotometric pH determination has a typical precision range of 0.0002–0.0004 pH units (Clayton and Byrne, 1993; Liu et al., 2011). However, Carter et al. (2013) reported an accuracy of the spectrophotometric pH determination of 0.0055 pH units. When direct pH measurements were not performed, it was computed from A<sub>T</sub> and C<sub>T</sub> using the thermodynamic equations of the seawater CO<sub>2</sub> system (Dickson et al., 2007) and the CO<sub>2</sub> dissociation constants of Mehrbach et al. (1973) refitted by Dickson and Millero (1987). An uncertainty of 0.006 pH units was estimated for these calculated pH by random propagation of the reported A<sub>T</sub> and C<sub>T</sub> accuracies. The exception to the latter is the 1981 TTO-NAS cruise, whose C<sub>T</sub> accuracy caused the estimated uncertainty for calculated pH to be slightly higher (0.008 pH units). The pH values here reported are at 25°C and on the Seawater Scale (pH<sub>SWS<sub>25</sub></sub>). Some of the data from the older cruises were adjusted to overcome the effects on the precision due to differences in the analytical procedures (Pérez et al., 2008, 2010; Vázquez-Rodríguez et al., 2012).

The C<sub>ANT</sub> concentrations were estimated applying the φC<sub>T</sub><sup>0</sup> method (Pérez et al., 2008; Vázquez-Rodríguez, 2009a), which produces good estimations over the whole latitudinal range of the Atlantic Ocean (Vázquez-Rodríguez et al., 2009b). The φC<sub>T</sub><sup>0</sup> method is a process-oriented geochemical approach that considers the processes controlling the C<sub>ANT</sub> uptake by the ocean: from the biogeochemistry of the seawater CO<sub>2</sub> system to the mixing and air-sea exchanges. It also considers the spatiotemporal variability of the preformed A<sub>T</sub> (A<sub>T</sub><sup>0</sup>) and air-sea CO<sub>2</sub> disequilibrium (ΔC<sub>dis</sub>) since the pre-industrial era. The subsurface layer reference for water mass formation conditions produces parameterizations of A<sub>T</sub><sup>0</sup> and ΔC<sub>dis</sub> that serve to estimate C<sub>ANT</sub> without the need for any additional zero-C<sub>ANT</sub> reference (Vázquez-Rodríguez et al., 2012a). The procedure requires as input parameters C<sub>T</sub> and A<sub>T</sub>. The overall uncertainty of the method has been estimated in 5.2 μmol·kg<sup>-1</sup> (Pérez et al., 2008; Vázquez-Rodríguez, 2009a). The trends of C<sub>ANT</sub> estimated by the φC<sub>T</sub><sup>0</sup> method were contrasted with those of the parameter C\* obtained with the ΔC\* method (Gruber et al., 1996), whose main difference with the φC<sub>T</sub><sup>0</sup> method is the assumption of constant ΔC<sub>dis</sub> (Matsumoto and Gruber, 2005).

The Ω<sub>Arag</sub> was also calculated as function of A<sub>T</sub> and C<sub>T</sub>, using the equation of Mucci (1983). The CaCO<sub>3</sub> saturation state is defined as the ratio between the observed and the expected ion product of the concentrations of calcium and carbonate ions when the solution is in equilibrium with a particular CaCO<sub>3</sub> mineral. Since in the open ocean the variations in the calcium ion concentration are rather small and closely related to variations in salinity, the

carbonate ion concentration mainly determines the  $\Omega_{\text{Arag}}$ . This characteristic makes the  $\Omega_{\text{Arag}}$  an optimum indicator of the environmental availability of dissolved carbonate ions. Seawater is in equilibrium with a CaCO<sub>3</sub> mineral when  $\Omega = 1$ , supersaturated when  $\Omega > 1$ , and undersaturated when  $\Omega < 1$ . The saturation horizon refers to the depth at which the saturation is 1, and separates supersaturated waters (above) from undersaturated waters (below).

#### ***5.4.2.- pH change deconvolution: anthropogenic and non-anthropogenic components***

To estimate how much of the change in pH is due to the uptake of  $C_{\text{ANT}}$  from gas exchange with the atmosphere, pH changes were decomposed into those related to the  $C_{\text{ANT}}$  uptake ( $\Delta\text{pH}_{C_{\text{ANT}}}$ ) and those not directly related to the  $C_{\text{ANT}}$  uptake ( $\Delta\text{pH}_{\text{Var}}$ ), as in Byrne et al. (2010), Guallart et al. (2015a) and Ríos et al. (Submitted).

To compute both components of the pH change, first the  $C_{\text{T}}$  that the water masses would have without the presence of  $C_{\text{ANT}}$  was estimated subtracting the  $C_{\text{ANT}}$  values estimated by the  $\varphi C_{\text{T}}^0$  method (Pérez et al., 2008; Vázquez-Rodríguez, 2009a) from the measured  $C_{\text{T}}$ . Then the associated pH change ( $\Delta\text{pH}_{\text{Var}}$ ) was calculated based on the resulting  $C_{\text{T}}$  ( $C_{\text{T}} - C_{\text{ANT}}$ ) using the thermodynamic equations of the seawater CO<sub>2</sub> system (Dickson et al., 2007) and the CO<sub>2</sub> dissociation constants of Mehrbach et al. (1973) refitted by Dickson and Millero (1987). Finally, the  $\Delta\text{pH}_{C_{\text{ANT}}}$  resulted from the subtraction of the  $\Delta\text{pH}_{\text{Var}}$  to the measured  $\text{pH}_{\text{SWS}_{25}}$ .

The uncertainties related with the reproducibility or the precision of the pH measurements and the  $C_{\text{ANT}}$  estimates are the ones that directly affect the accuracy of the estimates of the  $\Delta\text{pH}_{C_{\text{ANT}}}$  and the  $\Delta\text{pH}_{\text{Var}}$ , or even of the rates of change of  $C_{\text{ANT}}$  and  $\text{pH}_{\text{SWS}_{25}}$ . Most of the more relevant terms for the accuracy of spectrophotometric determination of pH are related to the accuracy in the determination of the equilibrium constant of the m-cresol and not to the accuracy of the absorbance measurements (Carter et al., 2013). Besides, an important part of the uncertainty of the  $C_{\text{ANT}}$  estimation is related to the accuracy of the constant terms (performed variables and Redfield ratios). However, when the changes in pH and  $C_{\text{ANT}}$  are determined, the uncertainties in the constants terms are cancelled out. Therefore, the real precision in the determination of the  $\Delta\text{pH}_{\text{SWS}_{25}}$  and their components can be determined by determining the standard deviation (STD) of the values in the almost  $C_{\text{ANT}}$ -free deep waters that present negligible CO<sub>2</sub> variability. Sampling of deep waters in the Iberian Abyssal Plain during the seven repeats of the OVIDE line enables the determination of the reproducibility and uncertainty of the main variables (Table 4). The uncertainties of the Apparent Oxygen Utilization (AOU; the difference between the saturated concentrations of oxygen calculated using the equations of Benson and Krause (1984) and the measured concentrations of oxygen),  $A_{\text{T}}$  and  $\text{pH}_{\text{SWS}_{25}}$  in the seven OVIDE cruises are very similar and the reproducibility between cruises is even better. The uncertainty of the  $\varphi C_{\text{T}}^0$  estimates ( $5.2 \mu\text{mol}\cdot\text{kg}^{-1}$ ) and the accuracy of the spectrophotometric pH measurements (0.0055 pH units) are larger than the STDs of the values of  $C_{\text{ANT}}$  ( $1.2\text{--}1.6 \mu\text{mol}\cdot\text{kg}^{-1}$ ) and  $\text{pH}_{\text{SWS}_{25}}$  (0.002–0.003 pH units), so the STDs may be the errors for the  $C_{\text{ANT}}$  and the  $\Delta\text{pH}_{\text{SWS}_{25}}$ . It is corroborated by the observed uncertainties of the  $\Delta\text{pH}_{C_{\text{ANT}}}$  and the  $\Delta\text{pH}_{\text{Var}}$ , whose uncertainties are very similar in the seven OVIDE cruises. The STDs of the  $C_{\text{ANT}}$  values in Table 4 are lower than the  $2.4 \mu\text{mol}\cdot\text{kg}^{-1}$  reported by Ríos et al. (2003) in the South Atlantic (meridional transect

from 4°N to 23°N along 9°W), the 2.7  $\mu\text{mol}\cdot\text{kg}^{-1}$  reported by Guallart et al. (2015a) from a transect across the Equatorial Atlantic (24°N), and the 2.7  $\mu\text{mol}\cdot\text{kg}^{-1}$  reported by Ríos et al. (Submitted) from a transect along the Atlantic Ocean (50°S–36°N), all based in the same back-calculation technique. Based on the STDs of the  $C_{\text{ANT}}$  estimates in these almost  $C_{\text{ANT}}$ -free abyssal waters, these authors estimate an uncertainty of 0.005 in pH, which is estimated as the maximum error for the  $\Delta\text{pH}_{C_{\text{ANT}}}$  and the  $\Delta\text{pH}_{\text{Var}}$  in this work.

Table 4.- Mean values  $\pm$  standard deviation of pressure (in dbar), potential temperature ( $\theta$ , in °C), salinity, Apparent Oxygen Utilization (AOU, in  $\mu\text{mol}\cdot\text{kg}^{-1}$ ), total alkalinity ( $A_{\text{T}}$ , in  $\mu\text{mol}\cdot\text{kg}^{-1}$ ), anthropogenic CO<sub>2</sub> estimated with the  $\phi C_{\text{T}}^0$  method ( $C_{\text{ANT}}$ , in  $\mu\text{mol}\cdot\text{kg}^{-1}$ ), pH in seawater scale at 25°C ( $\text{pH}_{\text{SWS}_{25}}$ ), pH change not derived from the  $C_{\text{ANT}}$  uptake ( $\Delta\text{pH}_{\text{Var}}$ ) and concentration of carbonate ions ( $[\text{CO}_3^{2-}]$ , in  $\mu\text{mol}\cdot\text{kg}^{-1}$ ) for the bottom waters of the Iberian Abyssal Plain sampled during the OVIDE cruises. “n” represents the number of data considered in each cruise.

Year (n)	Pressure	$\theta$	Salinity	AOU	$A_{\text{T}}$	$C_{\text{ANT}}$	$\text{pH}_{\text{SWS}_{25}}$	$\Delta\text{pH}_{\text{Var}}$	$[\text{CO}_3^{2-}]$
2002 (144)	4205 $\pm$ 526	2.182 $\pm$ 0.080	34.913 $\pm$ 0.008	86.1 $\pm$ 2.0	2351 $\pm$ 3	6.4 $\pm$ 1.3	7.731 $\pm$ 0.003	7.716 $\pm$ 0.005	104.0 $\pm$ 1.0
2004 (158)	4263 $\pm$ 499	2.162 $\pm$ 0.075	34.908 $\pm$ 0.007	87.1 $\pm$ 1.4	2352 $\pm$ 3	6.2 $\pm$ 1.2	7.731 $\pm$ 0.003	7.717 $\pm$ 0.006	104.0 $\pm$ 0.9
2006 (132)	4252 $\pm$ 529	2.170 $\pm$ 0.082	34.913 $\pm$ 0.008	85.4 $\pm$ 1.6	2350 $\pm$ 3	6.2 $\pm$ 1.3	7.732 $\pm$ 0.003	7.717 $\pm$ 0.005	104.1 $\pm$ 1.0
2008 (125)	4206 $\pm$ 511	2.179 $\pm$ 0.075	34.911 $\pm$ 0.007	84.9 $\pm$ 1.8	2353 $\pm$ 4	7.0 $\pm$ 1.6	7.734 $\pm$ 0.003	7.718 $\pm$ 0.006	104.9 $\pm$ 1.1
2010 (131)	4312 $\pm$ 524	2.163 $\pm$ 0.077	34.908 $\pm$ 0.008	85.9 $\pm$ 1.6	2351 $\pm$ 3	7.0 $\pm$ 1.2	7.730 $\pm$ 0.002	7.714 $\pm$ 0.004	103.8 $\pm$ 0.8
2012 (102)	4397 $\pm$ 526	2.149 $\pm$ 0.077	34.909 $\pm$ 0.008	87.9 $\pm$ 1.6	2352 $\pm$ 3	5.1 $\pm$ 1.2	7.733 $\pm$ 0.002	7.721 $\pm$ 0.004	104.1 $\pm$ 0.8
2014 (54)	4441 $\pm$ 477	2.141 $\pm$ 0.069	34.904 $\pm$ 0.007	87.4 $\pm$ 1.3	2353 $\pm$ 3	5.5 $\pm$ 1.5	7.733 $\pm$ 0.003	7.720 $\pm$ 0.006	104.2 $\pm$ 0.8

### 5.4.3.- Water mass characterization

The changes in the variables of the seawater CO<sub>2</sub> system were assessed in the main water masses of the Irminger and Iceland Basins, so that the variability of the properties within each defined layer is kept to a minimum. The predominant water masses in the study region are Subpolar Mode Water (SPMW), upper and classical Labrador Sea Water (uLSW and cLSW, respectively), Iceland–Scotland Overflow Water (ISOW) and Denmark Strait Overflow Water (DSOW) (Figure 27). The water masses were defined by potential density following the limits suggested by Azetsu-Scott et al. (2003), Kieke et al. (2007), Pérez et al. (2008) and Yashayaev et al. (2008).

To achieve more robust and consistent mean property values for each water mass, the cruise data was linearly interpolated at each dbar, an improvement with respect to the works of Pérez et al. (2008, 2010) and Vázquez-Rodríguez et al. (2012b). To obtain property values until the bottom depth of each station, the station profiles were extended until the bottom by copying down the values of the deepest measured depth. Data of the upper layer (pressure  $\leq$  100 dbar) was homogenized with the mean value of the pressure range 50–100 dbar to reduce the seasonal influence on the inter-annual trends (Vázquez-Rodríguez et al., 2012a). Then, the interpolated station profiles of each cruise were divided into the different water mass density intervals for each basin (Figure 27). The data assigned to each water mass density range at each station was finally averaged for each cruise and weighted by the area of the corresponding layer. The mean values of the properties for each water mass and their STDs are listed in Table 5.



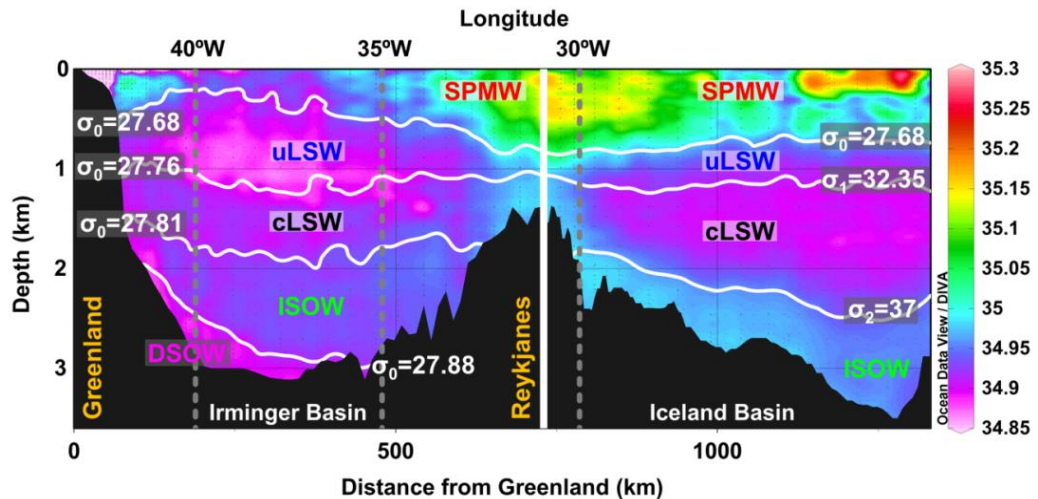


Figure 27.- Limits of the layers and basins considered in this study plotted on the mean salinity of the sections. The boundary isopycnals are represented in potential density ( $\sigma$ , in  $\text{kg}\cdot\text{m}^{-3}$ ), and the vertical white line represents the limit (Reykjanes Ridge) between the Irminger (left) and Iceland Basins (right). The acronyms of the layers account for: Subpolar Mode Water (SPMW), upper and classical Labrador Sea Water (uLSW and cLSW, respectively), Iceland–Scotland Overflow Water (ISOW) and Denmark Strait Overflow Water (DSOW).

For further reference, the vertical sections of the mean properties (potential temperature ( $\theta$ ), salinity, AOU,  $A_T$ ,  $\text{pH}_{\text{SW}S_{25}}$ ,  $C_{\text{ANT}}$ ,  $\Delta\text{pH}_{\text{Var}}$  and  $\Omega_{\text{Avg}}$ ) for the period 1981–2014 are shown in Figure 28. The AOU was used instead of oxygen because it accounts for the changes in water mass ventilation and the organic matter remineralization, which are linked to the decrease of the  $\Delta\text{pH}_{\text{Var}}$  (Brewer, 1978; Guallart et al., 2015a).

## 5.5.- Temperature, Salinity and AOU fields

The vertical section mean profiles of  $\theta$  and salinity ( $S$ ) show the relatively warm ( $\theta > 5^\circ\text{C}$ ) and saline ( $S > 35$ ) central waters (here represented as SPMW) occupying the first 1000 m of the water column (Figure 28a,b). The SPMW is warmer and saltier in the Iceland Basin than in the Irminger Basin, which reflects the circulation of this water mass from the former to the latter transported by the North Atlantic Current (NAC) (Brambilla and Talley, 2008). The mixing of SPMW with the surrounding waters around the Reykjanes Ridge, in conjunction with the air-sea interaction, results in a colder and fresher SPMW in the Irminger Basin.

The  $S$  values in the SPMW layer present no significant long-term trend, neither in the Irminger Basin nor in the Iceland Basin, but high inter-annual variability (Figure 29a,b). Especially significant is the sharp increase in  $S$  of this water mass in the Iceland Basin between 1994 and 1997, from average  $S$  values of  $34.981 \pm 0.108$  ( $n = 96$ ) to  $35.093 \pm 0.095$  ( $n = 98$ ) (Table 5). This  $S$  change could be generated by a greater arrival of subtropical waters due to the contraction of the North Atlantic Subpolar Gyre related to the shift in the winter NAO index from positive to neutral/negative values between both cruises (Bersch, 2002; Hátún et al., 2005; Sarafanov et al., 2008; de Boisséson et al., 2012). In the Irminger Basin, it stands out the  $S$  decrease between 1991 and 1994 (Figure 4a), from  $34.984 \pm 0.055$  ( $n = 45$ ) to  $34.881 \pm 0.365$  ( $n = 84$ ), and the subsequent recovery in 1997 to the intermediate value of  $34.950 \pm 0.133$  ( $n = 104$ ). From 1997 onwards, the influence of the subtropical waters arriving from the Iceland Basin can be

also detected although less pronounced, with a slight increase from 1997 to 2006. The maximum *S* found in 2006 could be indicative of the maximum contraction of the Subpolar Gyre. From 2006 onwards, the *S* values present a decreasing trend of  $-0.010 \pm 0.004 \text{ yr}^{-1}$  ( $r^2 = 0.84$ ,  $p\text{-value} < 0.05$ ). It may be the result of the recovery of the extension of the gyre in the subsequent years that would lead to the ventilation of SPMW (Sarfanov, 2009; de Boissésou et al., 2012), reaching the uLSW layer in the region closest to Greenland (Pickart et al., 2003). The changes in AOU of SPMW are less clear (Figure 29c,d), but in the Irminger Basin its AOU changes follow those of the uLSW layer, which may indicate a possible ventilation of the latter in the Irminger Basin (Pickart et al., 2003; Kieke et al., 2006).

Below SPMW is LSW (uLSW and cLSW), which is characterized by  $\theta$  between 3 and 4°C and *S* between 34.85 and 35 (Figure 28a,b). The waters of both the uLSW and the cLSW layers present higher  $\theta$ , *S* and AOU in the Iceland Basin than in the Irminger Basin, due to their mixing with the surrounding waters during their flow from the Labrador Sea (their formation region) to the Iceland Basin (Bersch et al., 1999; García-Ibáñez et al., In Press; see also Chapter 4 of this thesis). The mixing around the Reykjanes Ridge is clearly evident in the *S* fields of uLSW and cLSW, where relatively high *S* values can be found (Figure 28b).

In the Irminger Basin, the *S* values in the uLSW layer show a significant long-term trend of  $0.0010 \pm 0.0003 \text{ yr}^{-1}$  ( $r^2 = 0.53$ ,  $p\text{-value} < 0.01$ ), influenced by inter-annual variability (Figure 29a). Whereas the cLSW layer presents no significant long-term trend due to the high *S* values encountered in 1981 and 1991. If these cruises are excluded, a significant increasing trend of  $0.0039 \pm 0.0004 \text{ yr}^{-1}$  ( $r^2 = 0.94$ ,  $p\text{-value} < 0.01$ ) is found. This *S* increase is in agreement with the progressive salinization of cLSW due to lateral mixing coinciding with a period of weak winter convection at the Labrador Sea (e.g., Lazier et al., 2002; Kieke et al., 2006; Rhein et al., 2007; Yashayaev et al., 2008). This is also evident in the increasing AOU values from 1994 (when AOU values are at its minimum,  $28 \pm 7 \mu\text{mol}\cdot\text{kg}^{-1}$ ) to 2014 (when AOU values are at its maximum,  $45 \pm 3 \mu\text{mol}\cdot\text{kg}^{-1}$ ) (Figure 29c), result of the re-stratification of the water column that leads to an aging of the water masses due to isopycnal mixing. The *S* and AOU minimum found in the cLSW layer of the Irminger Basin in 1994–1997 is coherent with the *S* minimum found in 1994 in the Labrador Sea (Yashayaev et al., 2008). The salinization of cLSW is the responsible of the increase in *S* of uLSW from 1997 onwards, although the formation of uLSW during that period (e.g., Rhein et al., 2015) keeps its *S* values lower than those of cLSW. However, the aging of cLSW is not patent in uLSW because uLSW has been ventilated during the OVIDE period (2002–2014). Interestingly, from 2010 onwards the *S* values of cLSW are higher than those of the layers above (uLSW) and below (ISOW) it. Hence, this salinization should be the result of the mixing of cLSW and SPMW in the Labrador Sea (Lazier et al., 2002; Yashayaev, 2007).

In the Iceland Basin, no significant long-term trends in the *S* values of uLSW and cLSW are found (Figure 29b) due to the attenuation of the variability caused by the mixing occurred from the Irminger Basin to the Iceland Basin (Cunningham and Haine, 1995; Paillet et al., 1998). However, the pattern of AOU of uLSW clearly reflects the formation history of this water mass. uLSW loses oxygen from 1981 to 1997, and gains oxygen thereafter, reaching its maximum ventilation in 2010 (Figure 29d). This AOU minimum is in agreement with the enhanced production of LSW in the Labrador Sea in 2008 (Yashayaev and Loder, 2009). The deep convection in 2008 could explain why uLSW and cLSW present similar *S* and AOU values from 2010 onwards.

Table 5.- Temporal evolution (1981–2014) of the values (average ± standard deviation) of potential temperature ( $\theta$ , in °C), salinity, Apparent Oxygen Utilization (AOU, in  $\mu\text{mol}\cdot\text{kg}^{-1}$ ), salinity normalized total alkalinity ( $\text{NA}_T$ , in  $\mu\text{mol}\cdot\text{kg}^{-1}$ ), anthropogenic CO<sub>2</sub> estimated with the  $\phi\text{C}_T^0$  method ( $\text{C}_{\text{ANT}}$ , in  $\mu\text{mol}\cdot\text{kg}^{-1}$ ), pH in seawater scale at 25°C ( $\text{pH}_{\text{SWS}_{25}}$ ), pH change not derived from the  $\text{C}_{\text{ANT}}$  uptake ( $\Delta\text{pH}_{\text{Var}}$ ) and saturation state of aragonite ( $\Omega_{\text{Arag}}$ ) for the water masses considered in the Iceland Basin (Table 5a) and the Irminger Basin (Table 5b). All values listed here were obtained by vertically and horizontally integrating each property within each water mass.  $\text{xCO}_2$  represents the atmospheric CO<sub>2</sub> excess (in ppm) with respect to the preindustrial atmospheric CO<sub>2</sub> concentration (278.5 ppm). See water mass acronyms in Figure 27.

Year	$\text{xCO}_2$	$\theta$	Salinity	AOU	$\text{NA}_T$	$\text{C}_{\text{ANT}}$	$\text{pH}_{\text{SWS}_{25}}$	$\Delta\text{pH}_{\text{Var}}$	$\Omega_{\text{Arag}}$
SPMW ( $\sigma_0 < 27.68 \text{ kg}\cdot\text{m}^{-3}$ )									
1981	62	6.231 ± 1.655	35.003 ± 0.064	32.3 ± 18.3	2308 ± 4	30.3 ± 3.1	7.772 ± 0.057	7.839 ± 0.057	1.7 ± 0.3
1991	77	6.420 ± 1.067	35.004 ± 0.083	40.8 ± 20.3	2309 ± 2	33.3 ± 7.0	7.756 ± 0.032	7.830 ± 0.043	1.7 ± 0.2
1994	80	6.553 ± 1.380	34.981 ± 0.108	42.1 ± 21.9	2310 ± 2	34.7 ± 6.9	7.757 ± 0.048	7.833 ± 0.055	1.7 ± 0.3
1997	85	7.376 ± 2.506	35.093 ± 0.095	44.9 ± 23.6	2308 ± 2	35.8 ± 9.3	7.797 ± 0.083	7.872 ± 0.092	1.9 ± 0.5
2002	95	7.217 ± 1.577	35.083 ± 0.083	39.6 ± 29.9	2307 ± 2	37.4 ± 10.5	7.764 ± 0.064	7.844 ± 0.077	1.7 ± 0.3
2004	99	7.173 ± 1.882	35.068 ± 0.113	45.6 ± 31.5	2307 ± 3	38.4 ± 10.4	7.751 ± 0.064	7.835 ± 0.077	1.7 ± 0.3
2006	103	7.359 ± 1.774	35.058 ± 0.090	45.4 ± 32.8	2307 ± 2	39.5 ± 10.3	7.752 ± 0.067	7.838 ± 0.080	1.7 ± 0.3
2008	107	7.069 ± 2.019	35.079 ± 0.113	38.8 ± 26.5	2310 ± 2	44.3 ± 10.0	7.749 ± 0.066	7.845 ± 0.076	1.7 ± 0.4
2010	111	6.920 ± 1.999	35.029 ± 0.113	42.9 ± 28.0	2310 ± 2	43.2 ± 10.1	7.740 ± 0.066	7.836 ± 0.076	1.6 ± 0.3
2012	115	6.892 ± 2.298	35.025 ± 0.088	43.1 ± 28.2	2308 ± 2	44.4 ± 10.9	7.735 ± 0.070	7.834 ± 0.080	1.6 ± 0.4
2014	120	6.811 ± 1.560	35.051 ± 0.079	38.2 ± 29.9	2310 ± 2	47.2 ± 10.7	7.739 ± 0.059	7.843 ± 0.071	1.6 ± 0.3
uLSW ( $27.68 < \sigma_0 < 27.76 \text{ kg}\cdot\text{m}^{-3}$ )									
1981	62	4.010 ± 0.233	34.916 ± 0.015	39.5 ± 12.6	2308 ± 4	25.3 ± 3.1	7.738 ± 0.018	7.796 ± 0.023	1.4 ± 0.1
1991	77	4.132 ± 0.341	34.934 ± 0.031	51.3 ± 4.3	2309 ± 0	23.4 ± 1.9	7.726 ± 0.007	7.780 ± 0.005	1.4 ± 0.0
1994	80	4.119 ± 0.306	34.933 ± 0.021	54.6 ± 5.5	2310 ± 0	24.5 ± 1.9	7.721 ± 0.006	7.778 ± 0.005	1.4 ± 0.0
1997	85	4.181 ± 0.267	34.942 ± 0.017	55.1 ± 4.6	2310 ± 0	24.7 ± 1.5	7.757 ± 0.005	7.811 ± 0.004	1.5 ± 0.0
2002	95	4.198 ± 0.348	34.944 ± 0.032	53.0 ± 4.2	2307 ± 1	25.9 ± 1.6	7.716 ± 0.005	7.777 ± 0.004	1.3 ± 0.0
2004	99	4.075 ± 0.327	34.927 ± 0.028	51.2 ± 5.8	2308 ± 2	28.0 ± 1.6	7.711 ± 0.004	7.777 ± 0.005	1.3 ± 0.0
2006	103	4.135 ± 0.385	34.936 ± 0.033	49.3 ± 6.2	2307 ± 3	30.2 ± 2.4	7.710 ± 0.007	7.781 ± 0.007	1.3 ± 0.0
2008	107	4.084 ± 0.365	34.928 ± 0.036	45.5 ± 5.4	2311 ± 2	33.4 ± 2.0	7.711 ± 0.004	7.789 ± 0.005	1.3 ± 0.0
2010	111	4.093 ± 0.347	34.929 ± 0.034	43.9 ± 5.0	2310 ± 2	34.8 ± 1.7	7.709 ± 0.005	7.790 ± 0.004	1.3 ± 0.0
2012	115	4.135 ± 0.313	34.934 ± 0.025	47.9 ± 4.3	2308 ± 1	33.4 ± 1.3	7.704 ± 0.004	7.783 ± 0.003	1.3 ± 0.0
2014	120	4.138 ± 0.296	34.934 ± 0.023	45.5 ± 4.2	2310 ± 1	36.3 ± 2.0	7.704 ± 0.004	7.789 ± 0.004	1.3 ± 0.0
cLSW ( $27.76 < \sigma_0 < 27.81 \text{ kg}\cdot\text{m}^{-3}$ )									
1981	62	3.548 ± 0.259	34.939 ± 0.054	43.7 ± 1.9	2309 ± 3	19.8 ± 3.0	7.742 ± 0.010	7.787 ± 0.007	1.2 ± 0.4
1991	77	3.333 ± 0.231	34.924 ± 0.071	44.7 ± 4.0	2310 ± 1	20.4 ± 3.4	7.735 ± 0.009	7.783 ± 0.007	1.2 ± 0.3
1994	80	3.277 ± 0.187	34.916 ± 0.070	44.5 ± 3.4	2310 ± 1	21.1 ± 3.0	7.730 ± 0.006	7.779 ± 0.005	1.2 ± 0.4
1997	85	3.249 ± 0.214	34.913 ± 0.115	42.4 ± 3.5	2310 ± 1	25.1 ± 2.5	7.775 ± 0.005	7.828 ± 0.004	1.4 ± 0.6
2002	95	3.241 ± 0.251	34.915 ± 0.098	43.2 ± 3.4	2308 ± 1	23.4 ± 2.7	7.727 ± 0.005	7.782 ± 0.004	1.1 ± 0.4
2004	99	3.218 ± 0.234	34.908 ± 0.112	44.2 ± 2.6	2309 ± 2	24.4 ± 2.5	7.723 ± 0.004	7.780 ± 0.003	1.1 ± 0.4
2006	103	3.280 ± 0.248	34.917 ± 0.087	42.5 ± 2.0	2308 ± 2	25.8 ± 3.4	7.722 ± 0.005	7.783 ± 0.004	1.1 ± 0.4
2008	107	3.289 ± 0.248	34.920 ± 0.119	41.9 ± 2.3	2312 ± 2	28.1 ± 2.8	7.722 ± 0.004	7.787 ± 0.004	1.1 ± 0.4
2010	111	3.310 ± 0.270	34.923 ± 0.089	43.0 ± 2.2	2311 ± 1	27.9 ± 3.2	7.720 ± 0.004	7.785 ± 0.005	1.1 ± 0.4
2012	115	3.376 ± 0.247	34.934 ± 0.073	46.9 ± 1.4	2309 ± 1	26.3 ± 2.9	7.716 ± 0.004	7.778 ± 0.004	1.1 ± 0.4
2014	120	3.369 ± 0.264	34.934 ± 0.085	46.8 ± 1.7	2312 ± 2	27.6 ± 3.2	7.716 ± 0.004	7.781 ± 0.004	1.1 ± 0.4
ISOW ( $27.81 < \sigma_0 < 27.88 \text{ kg}\cdot\text{m}^{-3}$ )									
1981	62	2.738 ± 0.205	34.968 ± 0.035	52.9 ± 2.8	2312 ± 2	13.5 ± 1.3	7.737 ± 0.006	7.769 ± 0.005	1.0 ± 0.0
1991	77	2.726 ± 0.169	34.962 ± 0.064	56.6 ± 6.2	2317 ± 6	14.5 ± 2.7	7.733 ± 0.005	7.767 ± 0.007	1.0 ± 0.1
1994	80	2.705 ± 0.146	34.958 ± 0.067	56.0 ± 5.5	2317 ± 6	15.4 ± 5.5	7.732 ± 0.011	7.768 ± 0.006	1.0 ± 0.1
1997	85	2.712 ± 0.158	34.958 ± 0.117	52.6 ± 5.0	2316 ± 5	22.2 ± 1.6	7.784 ± 0.003	7.830 ± 0.006	1.4 ± 0.1
2002	95	2.690 ± 0.152	34.960 ± 0.097	54.0 ± 5.4	2315 ± 6	17.3 ± 2.2	7.728 ± 0.004	7.768 ± 0.005	1.0 ± 0.1
2004	99	2.669 ± 0.155	34.952 ± 0.111	55.0 ± 7.7	2315 ± 9	17.7 ± 3.7	7.724 ± 0.004	7.766 ± 0.008	1.0 ± 0.1
2006	103	2.700 ± 0.153	34.960 ± 0.086	54.0 ± 5.9	2314 ± 7	18.2 ± 3.0	7.724 ± 0.004	7.766 ± 0.006	0.9 ± 0.1
2008	107	2.723 ± 0.122	34.961 ± 0.117	51.8 ± 5.4	2319 ± 4	22.0 ± 3.5	7.723 ± 0.005	7.774 ± 0.007	0.9 ± 0.1
2010	111	2.726 ± 0.158	34.960 ± 0.087	52.0 ± 6.3	2317 ± 5	21.9 ± 4.3	7.720 ± 0.004	7.772 ± 0.009	0.9 ± 0.1
2012	115	2.757 ± 0.160	34.968 ± 0.069	54.7 ± 4.7	2315 ± 5	20.7 ± 2.7	7.718 ± 0.004	7.767 ± 0.006	0.9 ± 0.1
2014	120	2.720 ± 0.149	34.964 ± 0.086	56.2 ± 6.7	2320 ± 8	21.6 ± 3.1	7.718 ± 0.004	7.769 ± 0.006	0.9 ± 0.1

Table 5b.- The same as Table 5a for the Irminger Basin.

Year	xCO <sub>2</sub>	θ	Salinity	AOU	NA <sub>T</sub>	C <sub>ANT</sub>	pH <sub>SWS25</sub>	ΔpH <sub>Var</sub>	Ω <sub>Ang</sub>
SPMW (σ <sub>θ</sub> < 27.68 kg·m <sup>-3</sup> )									
1981	62	5.842 ± 1.674	34.957 ± 0.095	24.8 ± 18.1	2306 ± 3	30.0 ± 3.1	7.771 ± 0.051	7.837 ± 0.051	1.7 ± 0.3
1991	77	5.510 ± 0.668	34.984 ± 0.055	24.6 ± 10.6	2308 ± 1	34.4 ± 4.2	7.763 ± 0.015	7.839 ± 0.020	1.7 ± 0.1
1994	80	5.488 ± 1.290	34.881 ± 0.365	24.8 ± 12.0	2311 ± 8	33.9 ± 4.4	7.771 ± 0.025	7.845 ± 0.028	1.7 ± 0.1
1997	85	5.841 ± 2.111	34.950 ± 0.133	27.5 ± 17.2	2310 ± 3	35.9 ± 7.2	7.771 ± 0.071	7.868 ± 0.076	1.8 ± 0.4
2002	95	5.843 ± 1.732	34.981 ± 0.319	25.9 ± 21.3	2309 ± 8	40.2 ± 5.6	7.756 ± 0.050	7.844 ± 0.052	1.7 ± 0.3
2004	99	5.834 ± 1.926	34.964 ± 0.533	25.1 ± 18.9	2309 ± 6	43.0 ± 6.1	7.751 ± 0.038	7.847 ± 0.043	1.7 ± 0.2
2006	103	6.072 ± 1.531	35.003 ± 0.268	25.3 ± 19.0	2306 ± 5	42.4 ± 6.3	7.753 ± 0.048	7.847 ± 0.052	1.7 ± 0.2
2008	107	5.913 ± 2.530	34.991 ± 0.748	18.6 ± 22.0	2310 ± 13	48.2 ± 6.1	7.751 ± 0.053	7.857 ± 0.053	1.7 ± 0.3
2010	111	5.943 ± 2.235	34.972 ± 0.689	23.9 ± 19.6	2310 ± 12	47.1 ± 7.1	7.747 ± 0.048	7.851 ± 0.050	1.7 ± 0.2
2012	115	5.476 ± 2.840	34.920 ± 0.827	21.7 ± 24.7	2311 ± 15	49.5 ± 7.0	7.737 ± 0.053	7.847 ± 0.055	1.6 ± 0.3
2014	120	5.419 ± 1.933	34.935 ± 0.542	21.3 ± 21.3	2311 ± 11	49.7 ± 5.5	7.736 ± 0.048	7.847 ± 0.049	1.6 ± 0.2
uLSW (27.68 < σ <sub>θ</sub> < 27.76 kg·m <sup>-3</sup> )									
1981	62	3.690 ± 0.505	34.887 ± 0.059	32.6 ± 12.5	2307 ± 2	24.9 ± 4.0	7.743 ± 0.013	7.800 ± 0.015	1.4 ± 0.1
1991	77	3.830 ± 0.397	34.910 ± 0.030	32.2 ± 8.5	2309 ± 1	29.1 ± 4.0	7.740 ± 0.009	7.807 ± 0.011	1.5 ± 0.1
1994	80	3.685 ± 0.378	34.891 ± 0.034	36.0 ± 7.0	2310 ± 0	29.4 ± 4.7	7.733 ± 0.007	7.801 ± 0.008	1.5 ± 0.1
1997	85	3.655 ± 0.390	34.884 ± 0.036	35.1 ± 8.5	2310 ± 0	32.1 ± 5.4	7.743 ± 0.014	7.841 ± 0.010	1.6 ± 0.1
2002	95	3.839 ± 0.356	34.903 ± 0.031	36.7 ± 9.0	2309 ± 1	31.9 ± 4.0	7.725 ± 0.007	7.799 ± 0.014	1.4 ± 0.1
2004	99	3.791 ± 0.403	34.898 ± 0.037	38.8 ± 7.5	2310 ± 2	33.6 ± 3.2	7.716 ± 0.006	7.794 ± 0.008	1.3 ± 0.1
2006	103	3.909 ± 0.358	34.913 ± 0.030	36.1 ± 6.8	2307 ± 1	33.5 ± 3.4	7.720 ± 0.005	7.798 ± 0.009	1.4 ± 0.1
2008	107	3.956 ± 0.324	34.915 ± 0.027	29.4 ± 8.8	2310 ± 2	39.7 ± 4.8	7.720 ± 0.006	7.812 ± 0.015	1.4 ± 0.1
2010	111	3.963 ± 0.357	34.919 ± 0.033	34.6 ± 7.2	2310 ± 1	38.4 ± 3.8	7.715 ± 0.005	7.804 ± 0.010	1.4 ± 0.1
2012	115	4.010 ± 0.331	34.925 ± 0.027	29.5 ± 8.5	2309 ± 1	42.3 ± 4.8	7.714 ± 0.005	7.811 ± 0.014	1.4 ± 0.1
2014	120	3.917 ± 0.276	34.909 ± 0.026	30.1 ± 9.0	2310 ± 1	42.3 ± 5.5	7.712 ± 0.003	7.809 ± 0.013	1.4 ± 0.1
cLSW (27.76 < σ <sub>θ</sub> < 27.81 kg·m <sup>-3</sup> )									
1981	62	3.432 ± 0.208	34.934 ± 0.026	40.5 ± 3.0	2306 ± 1	19.6 ± 3.7	7.744 ± 0.010	7.789 ± 0.005	1.2 ± 0.1
1991	77	3.272 ± 0.259	34.900 ± 0.036	34.2 ± 5.9	2309 ± 1	25.6 ± 4.0	7.738 ± 0.007	7.797 ± 0.006	1.3 ± 0.1
1994	80	3.008 ± 0.291	34.871 ± 0.034	28.5 ± 7.3	2309 ± 1	26.5 ± 6.0	7.737 ± 0.009	7.798 ± 0.008	1.3 ± 0.1
1997	85	3.041 ± 0.304	34.875 ± 0.032	31.3 ± 6.7	2309 ± 0	29.1 ± 5.2	7.746 ± 0.008	7.819 ± 0.007	1.3 ± 0.1
2002	95	3.269 ± 0.324	34.907 ± 0.033	39.9 ± 3.9	2309 ± 1	26.0 ± 1.7	7.727 ± 0.004	7.788 ± 0.003	1.2 ± 0.1
2004	99	3.328 ± 0.277	34.914 ± 0.028	42.0 ± 3.6	2310 ± 2	27.7 ± 1.5	7.721 ± 0.004	7.786 ± 0.002	1.2 ± 0.1
2006	103	3.446 ± 0.232	34.931 ± 0.028	41.4 ± 2.5	2307 ± 1	27.0 ± 1.4	7.723 ± 0.002	7.786 ± 0.003	1.2 ± 0.1
2008	107	3.444 ± 0.198	34.929 ± 0.016	40.1 ± 2.8	2310 ± 2	30.1 ± 1.9	7.721 ± 0.002	7.791 ± 0.004	1.2 ± 0.0
2010	111	3.502 ± 0.280	34.935 ± 0.028	41.7 ± 2.4	2311 ± 2	29.9 ± 1.8	7.720 ± 0.003	7.790 ± 0.003	1.2 ± 0.0
2012	115	3.527 ± 0.183	34.940 ± 0.020	44.2 ± 1.9	2310 ± 1	30.2 ± 1.8	7.714 ± 0.002	7.785 ± 0.003	1.2 ± 0.0
2014	120	3.551 ± 0.195	34.943 ± 0.017	44.7 ± 3.1	2310 ± 1	29.8 ± 2.3	7.715 ± 0.003	7.785 ± 0.004	1.2 ± 0.1
ISOW (27.81 < σ <sub>θ</sub> < 27.88 kg·m <sup>-3</sup> )									
1981	62	3.044 ± 0.392	34.952 ± 0.031	43.9 ± 3.7	2306 ± 1	14.8 ± 3.4	7.747 ± 0.007	7.781 ± 0.004	1.1 ± 0.1
1991	77	2.933 ± 0.245	34.938 ± 0.016	46.1 ± 3.4	2310 ± 2	16.1 ± 3.0	7.741 ± 0.008	7.779 ± 0.005	1.1 ± 0.1
1994	80	2.747 ± 0.327	34.917 ± 0.020	44.8 ± 4.5	2310 ± 1	19.1 ± 7.0	7.738 ± 0.015	7.782 ± 0.004	1.0 ± 0.1
1997	85	2.724 ± 0.226	34.910 ± 0.014	41.0 ± 3.7	2311 ± 1	22.2 ± 3.4	7.749 ± 0.007	7.799 ± 0.005	1.1 ± 0.1
2002	95	2.770 ± 0.305	34.918 ± 0.021	43.9 ± 3.5	2309 ± 1	19.5 ± 2.4	7.733 ± 0.002	7.778 ± 0.005	1.0 ± 0.1
2004	99	2.754 ± 0.386	34.916 ± 0.030	44.4 ± 4.8	2311 ± 2	22.6 ± 2.4	7.726 ± 0.002	7.778 ± 0.004	1.0 ± 0.1
2006	103	2.863 ± 0.289	34.930 ± 0.015	43.3 ± 4.7	2309 ± 2	22.1 ± 2.6	7.728 ± 0.002	7.779 ± 0.006	1.0 ± 0.1
2008	107	2.889 ± 0.248	34.932 ± 0.012	41.7 ± 2.9	2311 ± 1	24.9 ± 2.2	7.726 ± 0.002	7.784 ± 0.004	1.0 ± 0.1
2010	111	2.861 ± 0.277	34.930 ± 0.016	43.3 ± 3.4	2312 ± 2	24.8 ± 2.2	7.724 ± 0.002	7.782 ± 0.004	1.0 ± 0.1
2012	115	2.901 ± 0.269	34.935 ± 0.014	46.1 ± 3.1	2311 ± 1	24.6 ± 2.2	7.720 ± 0.002	7.777 ± 0.004	1.0 ± 0.1
2014	120	2.911 ± 0.280	34.937 ± 0.017	46.7 ± 4.9	2311 ± 1	24.2 ± 3.6	7.720 ± 0.004	7.777 ± 0.005	1.0 ± 0.1
DSOW (σ <sub>θ</sub> > 27.88 kg·m <sup>-3</sup> )									
1981	62	1.788 ± 0.323	34.892 ± 0.012	36.6 ± 2.4	2305 ± 1	13.3 ± 2.5	7.746 ± 0.006	7.777 ± 0.002	1.0 ± 0.1
1991	77	1.872 ± 0.347	34.899 ± 0.011	38.4 ± 3.4	2309 ± 2	15.0 ± 2.2	7.743 ± 0.008	7.778 ± 0.004	0.9 ± 0.1
1994	80	1.712 ± 0.350	34.876 ± 0.008	37.0 ± 2.3	2308 ± 1	17.8 ± 3.8	7.736 ± 0.008	7.778 ± 0.002	0.9 ± 0.1
1997	85	1.838 ± 0.352	34.890 ± 0.009	36.7 ± 1.8	2309 ± 1	25.3 ± 2.3	7.767 ± 0.008	7.822 ± 0.003	1.2 ± 0.0
2002	95	1.704 ± 0.330	34.886 ± 0.014	39.4 ± 3.7	2308 ± 1	17.7 ± 1.6	7.731 ± 0.003	7.773 ± 0.004	0.9 ± 0.1
2004	99	1.508 ± 0.374	34.868 ± 0.023	36.2 ± 4.8	2309 ± 2	21.9 ± 1.1	7.723 ± 0.003	7.774 ± 0.003	0.9 ± 0.1
2006	103	1.972 ± 0.293	34.907 ± 0.004	38.6 ± 3.6	2309 ± 1	21.2 ± 1.6	7.727 ± 0.002	7.776 ± 0.004	0.9 ± 0.0
2008	107	1.992 ± 0.354	34.913 ± 0.005	37.3 ± 3.4	2311 ± 2	25.0 ± 1.8	7.723 ± 0.003	7.781 ± 0.003	0.9 ± 0.0
2010	111	1.876 ± 0.344	34.896 ± 0.011	34.6 ± 4.3	2311 ± 1	25.7 ± 1.6	7.723 ± 0.003	7.783 ± 0.004	0.9 ± 0.1
2012	115	1.964 ± 0.357	34.909 ± 0.008	39.5 ± 4.3	2311 ± 1	25.9 ± 2.1	7.715 ± 0.003	7.776 ± 0.003	0.9 ± 0.1
2014	120	1.823 ± 0.415	34.905 ± 0.015	37.9 ± 4.9	2310 ± 1	26.7 ± 2.5	7.713 ± 0.004	7.776 ± 0.004	0.9 ± 0.1

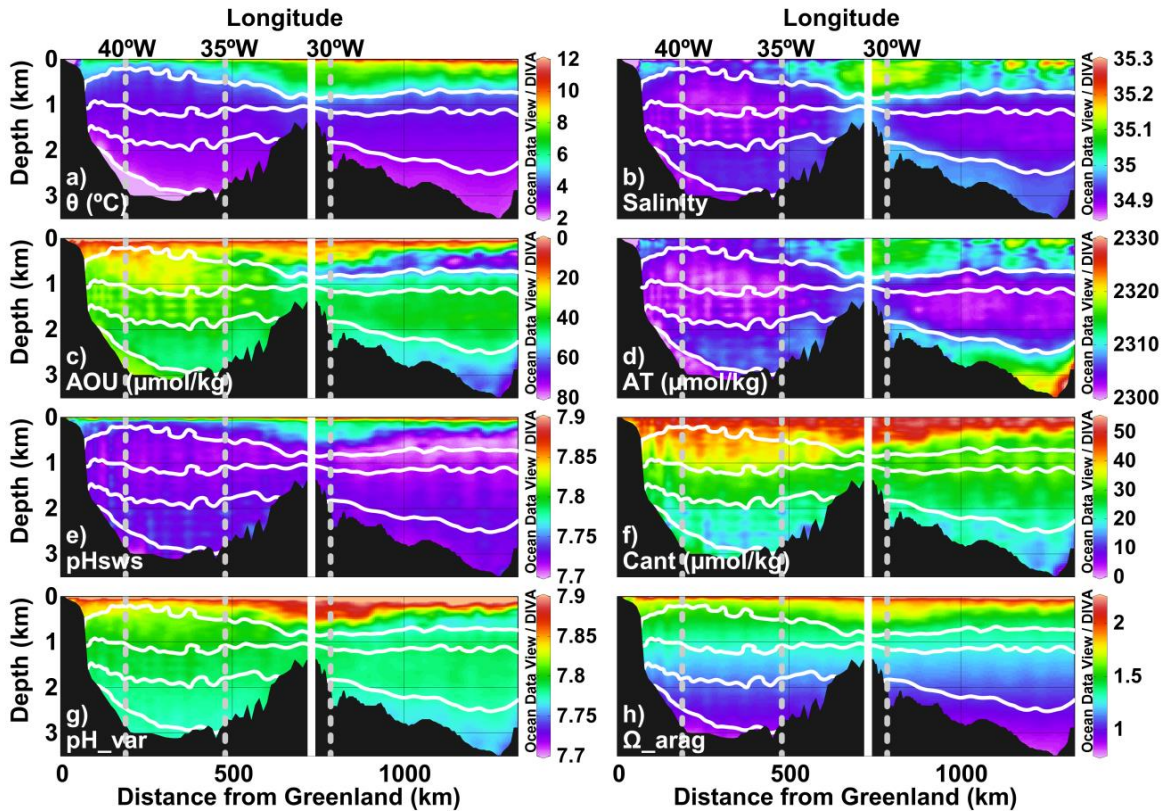


Figure 28.- Mean properties for the studied period (1981–2014) along the cruise track, from Greenland (left) to the Iceland Basin (right): (a) Potential temperature ( $\theta$ , in  $^{\circ}\text{C}$ ), (b) salinity, (c) Apparent Oxygen Utilization (AOU, in  $\mu\text{mol}\cdot\text{kg}^{-1}$ ), (d) total alkalinity (AT, in  $\mu\text{mol}\cdot\text{kg}^{-1}$ ), (e) pH in seawater scale at  $25^{\circ}\text{C}$  (pHsws), (f) anthropogenic  $\text{CO}_2$  estimated with the  $\varphi C_T^0$  method (Cant, in  $\mu\text{mol}\cdot\text{kg}^{-1}$ ), (g) pH change not derived from the Cant uptake (pH\_var) and (h) saturation of  $\text{CaCO}_3$  in terms of aragonite ( $\Omega_{\text{arag}}$ ).

With  $\theta < 3^{\circ}\text{C}$  and S between 34.9 and 35, ISOW is located beneath cLSW (Figure 28a,b). ISOW presents higher  $\theta$ , S and AOU values in the Iceland Basin than in the Irminger Basin (Figure 29a,b,c), which reflects the circulation of this water mass. ISOW comes from the Iceland–Scotland sill and flows southwards into the Iceland Basin. Then, it crosses the Reykjanes Ridge across the Charlie-Gibbs Fracture Zone, where it mixes with the recently ventilated cLSW and DSOW, becoming colder, fresher and more oxygenated.

The influence of cLSW over ISOW is evident in the Irminger Basin, where their S and AOU values show similar patterns (Figure 29a,c). The salinization and aging of cLSW from 1994 onwards is transmitted to ISOW from 1997 onwards. In the Iceland Basin, ISOW is influenced by the lower North Atlantic Deep Water, which causes the attenuation of the ISOW signal. Therefore, the mean values of S and AOU of the ISOW layer of the Iceland Basin are higher than those found in the Irminger Basin (Figure 29).

In the bottom of the Irminger Basin, a fifth water mass can be distinguished, DSOW. DSOW is the coldest and freshest water mass of the sections, with  $\theta < 2^{\circ}\text{C}$  and  $S < 34.9$  (Figure 28a,b). It is also traceable by its relative AOU minimum at the bottom of the western part of the Irminger Basin (Figure 28c). The variability of the S and AOU of DSOW (Figure 29a,c) is linked



to that of the entrainment downhill of the sills (Rudels et al., 2002; Tanhua et al., 2005; Pérez et al., 2008; Falina et al., 2012).

The AOU decrease observed in SPMW, uLSW, cLSW and ISOW in the Irminger Basin in 2008 (Figure 29a,c) may indicate that the enhanced convection episode occurred in the Labrador Sea that year could also have had its replicate in the Irminger Basin.

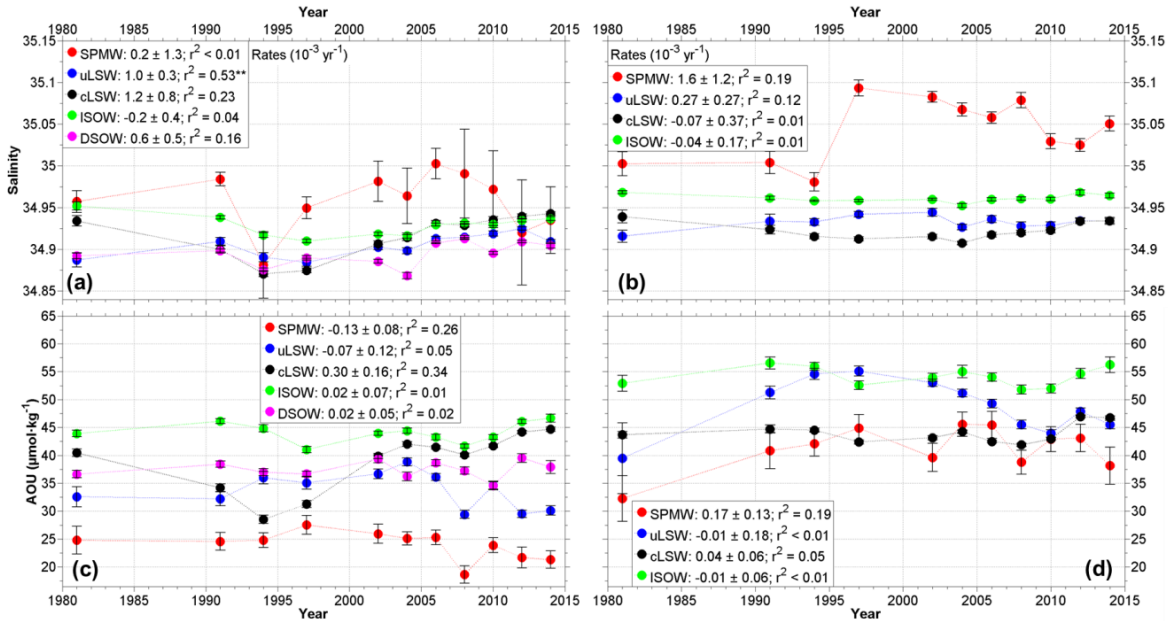


Figure 29.- Temporal evolution between 1981 and 2014 of the average values of (a and b) Salinity and (c and d) Apparent Oxygen Utilization (AOU, in  $\mu\text{mol}\cdot\text{kg}^{-1}$ ) in main water masses of the Irminger (a and c) and Iceland (b and d) Basins. Each point represents the average property of a particular water mass (SPMW (red dots), uLSW (blue dots), cLSW (black dots), ISOW (green dots) and DSOW (magenta dots)) at the time of each cruise (Table 5). The error bars represent the error of the mean. The inset boxes give the trends  $\pm$  standard error of the estimate and the correlation coefficients ( $r^2$ ). \*\* denotes that the trend is statistically significant at the 95% level (p-value < 0.05). See water mass acronyms in Figure 27.

## 5.6.- Alkalinity trends

The waters of the Irminger and Iceland Basins present an almost homogeneous value of  $A_T$  between 2300 and 2310  $\mu\text{mol}\cdot\text{kg}^{-1}$  (Figure 28d). However, SPMW and ISOW in the Iceland Basin present values of  $A_T$  higher than 2310  $\mu\text{mol}\cdot\text{kg}^{-1}$ . The high  $A_T$  values of ISOW come from the influence of the lower North Atlantic Deep Water, which is also reflected by the high silicate values found in the ISOW layer in the Iceland Basin (not shown). The high  $A_T$  values of SPMW are the result of the high S of this water mass (Figure 28b).

The mean  $A_T$  values for each layer were normalized ( $NA_T$ ) to an S value of 35 to eliminate the influence of the S on the  $A_T$ . There are other methods to normalize  $A_T$  that take into account other factors that affect this variable, especially in surface waters (Friis et al., 2003; Carter et al., 2014), however we used the normalization method most widely applied to analyse the variability of the whole water column and that is still used nowadays (e.g., Millero et al., 2010). The  $NA_T$  values of the Irminger waters in 2006 seem to be negatively biased (Figure 30a). From the data of the deep waters of the Iberian Abyssal Plain, the bias seems to be -2.3  $\mu\text{mol}\cdot\text{kg}^{-1}$  (Table 4). This

value is within the range of no correction accepted by the CARINA data base (Key et al., 2010), so the 2006 data was not corrected.

In the Irminger Basin, cLSW, ISOW and DSOW show significant long-term trends of increase in  $NA_T$  (Figure 30a). The  $NA_T$  trends were also calculated excluding the cruises of 1981 and 2006, which are outliers. The faster  $NA_T$  increase observed in the DSOW layer with respect to the other layers is consistent with its Arctic origin, since the Arctic Ocean is gaining  $NA_T$  due to the increase in river discharge (Anderson et al., 2004; Smith et al., 2007; Cooper et al., 2008; Haine et al., 2015). The ISOW layer presents similar rates of increase in  $NA_T$  in both basins (Figure 30a,b). The cLSW layer only presents significant trends of  $NA_T$  increase in the Irminger Basin, which could be related to the fact that this layer includes waters resulting from the mixing between SPMW and Arctic waters (Polar Intermediate Water) (von Appen et al., 2014; García-Ibáñez et al., In Press; see also Chapter 4 of this thesis). Consequently, the  $NA_T$  increases in the Irminger Basin here observed may be related to the arrival of waters of Arctic origin (Anderson et al., 2004; Smith et al., 2007; Cooper et al., 2008; Haine et al., 2015).

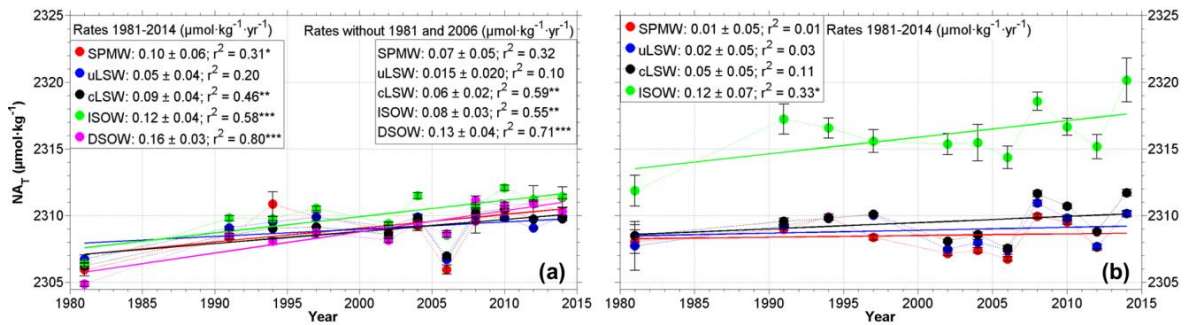


Figure 30.- Temporal evolution between 1981 and 2014 of the average salinity normalized total alkalinity ( $NA_T$ , in  $\mu\text{mol}\cdot\text{kg}^{-1}$ ) values in main water masses of the Irminger (a) and Iceland (b) Basins. Each point represents the average  $NA_T$  of a particular water mass (SPMW (red dots), uLSW (blue dots), cLSW (black dots), ISOW (green dots) and DSOW (magenta dots)) at the time of each cruise (Table 5). The error bars represent the error of the mean. The inset boxes give the trends  $\pm$  standard error of the estimate and the correlation coefficients ( $r^2$ ). \* denotes that the trend is statistically significant at the 90% level (p-value < 0.1), \*\* at the 95% level (p-value < 0.05), and \*\*\* at the 99% level (p-value < 0.01). See water mass acronyms in Figure 27.

In the Iceland Basin, the inter-annual variability of the  $NA_T$  values of uLSW and cLSW is very similar throughout the entire studied period (Figure 30b). During the OVIDE period (2002–2014) the inter-annual variability of the  $NA_T$  values of SPMW is similar to that of uLSW and cLSW. The  $NA_T$  values of ISOW show an increasing trend statistically significant at 90% level, whose rate is similar to that found in DSOW, which suggests that the cause of these increasing  $NA_T$  trends may be the increased runoff of the Siberian rivers with high  $A_T$  content (Anderson et al., 2004; Smith et al., 2007; Cooper et al., 2008; Haine et al., 2015).

## 5.7.- $C_{ANT}$ trends

The waters from both the Irminger and Iceland Basins are gaining  $C_{ANT}$  in response to the increasing  $C_{ANT}$  concentrations in the atmosphere (Figure 28f, and Figure 31a,b). The convection processes occurred in these basins (Pickart et al., 2003; García-Ibáñez et al., In Press; see also Chapter 4 of this thesis) and in the surrounding ones (i.e., Labrador and Nordic Seas) provides an



important pathway for the C<sub>ANT</sub> to pass from the surface mixed layer to the intermediate and deep layers. The C<sub>ANT</sub> concentrations follow an opposite similar pattern to that of the AOU (Figure 28c): high values, close to saturation (80% of saturation), near the surface that decrease when increasing depth (Figure 28f).

The SPMW layer shows the greatest rates of C<sub>ANT</sub> increase, owned to its direct contact with the atmosphere (Figure 31a,b; Table 6). In the Irminger Basin, the C<sub>ANT</sub> levels of SPMW keep rising in response to the atmospheric CO<sub>2</sub> increase at about 85% of the expected rate if saturation with the atmospheric CO<sub>2</sub> is assumed ( $\sim 0.45 \mu\text{mol}\cdot\text{C}\cdot\text{kg}^{-1}\cdot(\text{ppm}\cdot\text{CO}_2^{\text{atm}})^{-1}$ ). This could be explained by the fact that surface waters reach balance with the atmosphere within  $\sim 5$  years (Biaostoch et al., 2007). Besides, the rate of C<sub>ANT</sub> increase in the SPMW layer in the Irminger Basin here reported ( $0.66 \pm 0.03 \mu\text{mol}\cdot\text{kg}^{-1}\cdot\text{yr}^{-1}$ ; Figure 31a) is very similar to that found by Pérez et al. (2010) ( $0.62 \pm 0.03 \mu\text{mol}\cdot\text{kg}^{-1}\cdot\text{yr}^{-1}$ ), even though the present study has a larger time range (8 years more), meaning that the rate of C<sub>ANT</sub> uptake observed until 2006 was maintained until 2014. In the Iceland Basin, the rate of C<sub>ANT</sub> increase is about 64% of the expected rate if saturation with the atmospheric CO<sub>2</sub> is assumed, which is in concordance with the higher AOU values found in SPMW in this basin (Figure 28c). This difference is derived from the thicker SPMW layer found in the Iceland Basin, which includes poorly ventilated waters with low content in oxygen and C<sub>ANT</sub> (Figure 28c). The rate of C<sub>ANT</sub> increase of SPMW in the Iceland Basin ( $0.50 \pm 0.06 \mu\text{mol}\cdot\text{kg}^{-1}\cdot\text{yr}^{-1}$ ; Figure 31a) is lower than that reported by Perez et al. (2010) ( $0.70 \pm 0.08 \mu\text{mol}\cdot\text{kg}^{-1}\cdot\text{yr}^{-1}$ ), because these authors delimited the surface layer by  $\sigma_0 = 27.60$ , thus not including the poorly ventilated waters between  $\sigma_0 = 27.60$  and  $\sigma_0 = 27.68$ . The expected decrease in the rate of increase of the C<sub>ANT</sub> concentration due to the reduction in the convection processes related with the shift of the NAO index is not observed. The rate of C<sub>ANT</sub> increase is maintained during the OVIDE period (2002–2014) due to the increase in the atmospheric xCO<sub>2</sub>. During the OVIDE period the atmospheric C<sub>ANT</sub> anomaly (i.e., the CO<sub>2</sub> increase in the atmosphere since the industrial revolution) is 33% higher than during the high NAO index period (the mean xCO<sub>2</sub> for the period 1991–1997 was 359 ppm, while for the period 2002–2014 it was 386 ppm). This is in agreement with the prediction of Byrne et al. (2010), who expected a steadily increase of the C<sub>ANT</sub> concentration in seawater as atmospheric levels keep rising.

The uLSW and cLSW layers behave similarly in both basins (Figure 31a,b), although the C<sub>ANT</sub> values are higher in the Irminger Basin than in the Iceland Basin (Figure 28f). However, uLSW gains C<sub>ANT</sub> faster than cLSW from 2006 onwards in the Irminger Basin, being its tendency more similar to that of its upper bound SPMW layer. This change in tendency is also detected in the Iceland Basin. This is in agreement with the enhancement of the formation of uLSW due to the shift in the NAO index between the late 1990s and the 2000s (Pickart et al., 2003; Yashayaev, 2007; Rhein et al., 2015). The sharp increase in the C<sub>ANT</sub> concentration in uLSW in 2008 may be related the enhanced convection in the Labrador Sea in 2008 (Yashayaev and Loder, 2009), but may also indicate that uLSW was renewed in the Irminger Basin. The rate of C<sub>ANT</sub> increase of uLSW in the Iceland Basin ( $0.39 \pm 0.09 \mu\text{mol}\cdot\text{kg}^{-1}\cdot\text{yr}^{-1}$ ; Figure 31a) is in agreement with that reported by Perez et al. (2010) ( $0.40 \pm 0.06 \mu\text{mol}\cdot\text{kg}^{-1}\cdot\text{yr}^{-1}$ ).

In the Irminger Basin, the cLSW layer gains C<sub>ANT</sub> rapidly from 1981 to 1997 ( $0.58 \pm 0.09 \mu\text{mol}\cdot\text{kg}^{-1}\cdot\text{yr}^{-1}$ ;  $r^2 = 0.99$ ;  $p\text{-value} < 0.01$ ), reaching its maximum concentration in 1997 (Figure 31a; Table 5). Between 1997 and 2002 the C<sub>ANT</sub> concentration of cLSW in the Irminger Basin decreases significantly. From 2002 onwards, this layers gains again C<sub>ANT</sub>, although at a lower rate

$(0.35 \pm 0.12 \mu\text{mol}\cdot\text{kg}^{-1}\cdot\text{yr}^{-1}; r^2 = 0.74; p\text{-value} = 0.01)$  than that observed between 1981 and 1997. All these changes may be linked to the circulation changes occurred in the North Atlantic Subpolar Gyre related to the changes in the NAO index. The period 1987–1994 was characterized by a persistent phases of high NAO index, that lead to deep winter convection in the Labrador Sea and the formation of a large volume of cLSW (e.g., Lazier et al., 2002; Azetsu-Scott et al., 2003; Kieke et al., 2007; Yashayaev, 2007). The change in the NAO index in 1995 hindered the ventilation of cLSW, which led to the dilution of the  $C_{\text{ANT}}$  in the cLSW layer. During the period of weak convection that followed, cLSW was slowly enriched in  $C_{\text{ANT}}$  due to the permanently active isopycnal mixing with the recently ventilated uLSW. These tendencies are less clear in the Iceland Basin since the large inter-annual variability in its formation region attenuates due to mixing over the length and timescales of the transit from the Labrador Sea (Cunningham and Haine, 1995; Paillet et al., 1998).

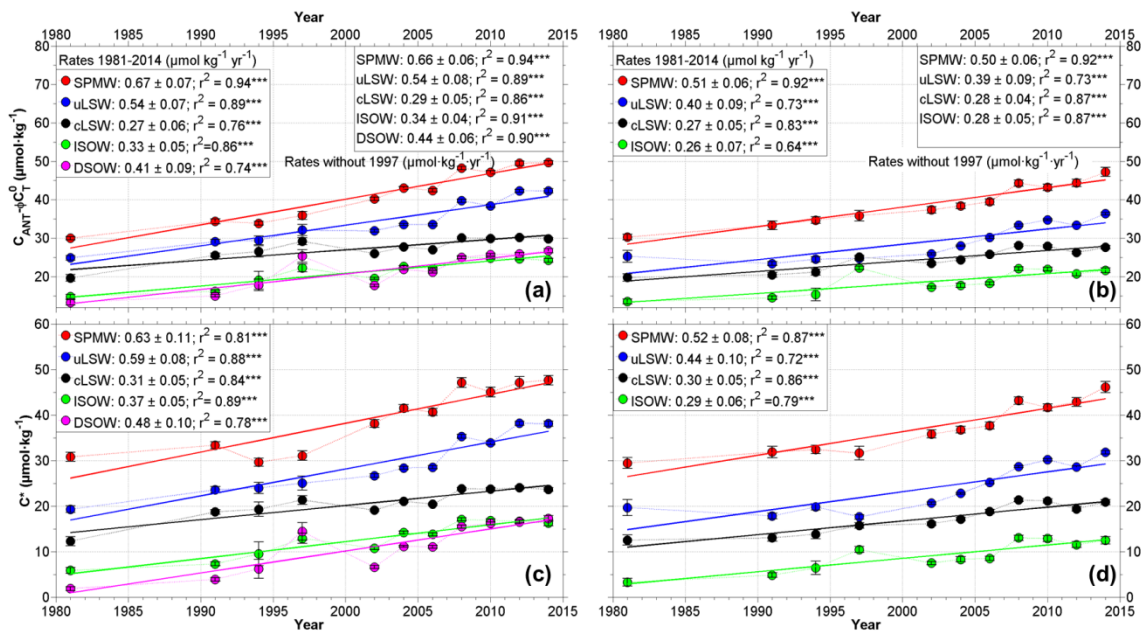


Figure 31.- Temporal evolution between 1981 and 2014 of the average values of (a and b) anthropogenic CO<sub>2</sub> estimated with the  $\phi C_T^0$  method ( $C_{\text{ANT}} - \phi C_T^0$ , in  $\mu\text{mol}\cdot\text{kg}^{-1}$ ) and (c and d) the parameter  $C^*$  obtained with the  $\Delta C^*$  method (in  $\mu\text{mol}\cdot\text{kg}^{-1}$ ) in main water masses of the Irmingier (a and c) and Iceland (b and c) Basins. Each point represents the average property of a particular water mass (SPMW (red dots), uLSW (blue dots), cLSW (black dots), ISOW (green dots) and DSOW (magenta dots)) at the time of each cruise (Table 5). The error bars represent the error of the mean. The inset boxes give the trends  $\pm$  standard error of the estimate and the correlation coefficients ( $r^2$ ). \*\*\* denotes that the trend is statistically significant at the 99% level ( $p\text{-value} < 0.01$ ). See water mass acronyms in Figure 27.

The  $C_{\text{ANT}}$  concentration in the ISOW layer increases continuously in both basins (Figure 31a,b) suggesting incorporation of young water by entrainment downhill of the Iceland–Scotland sills. The mean  $C_{\text{ANT}}$  concentration observed in the ISOW layer is lower in the Iceland Basin than the Irmingier Basin (Figure 31a,b), which is related with the dilution of the ISOW signal with important portions of the almost  $C_{\text{ANT}}$ -free lower North Atlantic Deep Water (Figure 28f). The rapid increase in the  $C_{\text{ANT}}$  concentrations observed in ISOW in 1997 was already observed by Perez et al. (2008), who related it with the combination of the effects of the increase in the  $C_{\text{ANT}}$

storage associated with the strong ventilation occurred during the large period of high NAO indices (late 1980s-mid 1990s) and the low AOU values.

Table 6.- Long-term trends (1981–2014) of anthropogenic CO<sub>2</sub> estimated with the  $\phi C_T^0$  method ( $C_{ANT}$ , in  $\mu\text{mol}\cdot\text{kg}^{-1}$ ), parameter  $C^*$  obtained with the  $\Delta C^*$  method (in  $\mu\text{mol}\cdot\text{kg}^{-1}$ ), saturation state of aragonite ( $\Omega_{Arag}$ ), pH in seawater scale at 25°C ( $\text{pH}_{\text{SWS}_{25}}$ ), pH change related to the  $C_{ANT}$  penetration ( $\Delta\text{pH}_{C_{ANT}}$ ) and pH change not derived from the  $C_{ANT}$  uptake ( $\Delta\text{pH}_{\text{Var}}$ ) versus atmospheric  $x\text{CO}_2$  excess (in ppm; difference between the atmospheric CO<sub>2</sub> concentration at the time of the cruise and the preindustrial atmospheric CO<sub>2</sub> concentration (278.5 ppm)) for the water masses considered in the Irminger and Iceland Basins. The column “Preindustrial” compiles the intercepts of the trends. See layer acronyms in Figure 27.

Variable	Layer	Irminger Basin			Iceland Basin		
		Preindustrial $\pm$ Standard Error	Slope $\pm$ Standard Error	$r^2$	Preindustrial $\pm$ Standard Error	Slope $\pm$ Standard Error	$r^2$
		$\mu\text{mol}\cdot\text{kg}^{-1}$	$\mu\text{mol}\cdot\text{kg}^{-1}\cdot\text{ppm}^{-1}$		$\mu\text{mol}\cdot\text{kg}^{-1}$	$\mu\text{mol}\cdot\text{kg}^{-1}\cdot\text{ppm}^{-1}$	
$^1C_{ANT}$	SPMW	5.7 $\pm$ 2.9	0.37 $\pm$ 0.03	0.96***	11.5 $\pm$ 2.7	0.29 $\pm$ 0.03	0.95***
	uLSW	4.8 $\pm$ 3.7	0.31 $\pm$ 0.04	0.92***	7.7 $\pm$ 4.7	0.22 $\pm$ 0.05	0.79***
	cLSW	11.9 $\pm$ 2.8	0.16 $\pm$ 0.03	0.84***	8.9 $\pm$ 2.2	0.16 $\pm$ 0.02	0.89***
	ISOW	2.9 $\pm$ 2.4	0.19 $\pm$ 0.02	0.91***	2.7 $\pm$ 2.3	0.16 $\pm$ 0.02	0.89***
	DSOW	3.2 $\pm$ 2.9	0.25 $\pm$ 0.03	0.92***			
$C^*$	SPMW	4.4 $\pm$ 5.4	0.36 $\pm$ 0.06	0.86***	8.9 $\pm$ 3.4	0.30 $\pm$ 0.04	0.91***
	uLSW	-3.0 $\pm$ 3.8	0.34 $\pm$ 0.04	0.91***	-0.5 $\pm$ 5.0	0.25 $\pm$ 0.05	0.78***
	cLSW	4.2 $\pm$ 3.1	0.17 $\pm$ 0.03	0.81***	0.9 $\pm$ 2.3	0.17 $\pm$ 0.02	0.88***
	ISOW	-7.0 $\pm$ 2.8	0.21 $\pm$ 0.03	0.88***	-6.6 $\pm$ 3.2	0.16 $\pm$ 0.03	0.78***
	DSOW	-14.8 $\pm$ 5.3	0.27 $\pm$ 0.05	0.78***			
		ppm <sup>-1</sup>			ppm <sup>-1</sup>		
$^1\Omega_{Arag}$	SPMW	1.84 $\pm$ 0.04	-0.0018 $\pm$ 0.0004	0.78***	1.83 $\pm$ 0.05	-0.0017 $\pm$ 0.0005	0.66***
	uLSW	1.59 $\pm$ 0.07	-0.0020 $\pm$ 0.0008	0.53**	1.52 $\pm$ 0.01	-0.0021 $\pm$ 0.0001	0.98***
	cLSW	1.36 $\pm$ 0.05	-0.0014 $\pm$ 0.0005	0.57**	1.33 $\pm$ 0.01	-0.0019 $\pm$ 0.0001	0.99***
	ISOW	1.15 $\pm$ 0.03	-0.0011 $\pm$ 0.0003	0.64***	1.07 $\pm$ 0.01	-0.0012 $\pm$ 0.0001	0.97***
	DSOW	1.03 $\pm$ 0.02	-0.0011 $\pm$ 0.0002	0.86***			
		pH units·ppm <sup>-1</sup>			pH units·ppm <sup>-1</sup>		
$^1\text{pH}_{\text{SWS}_{25}}$	SPMW	7.814 $\pm$ 0.009	-0.0006 <sub>1</sub> $\pm$ 0.0000 <sub>9</sub>	0.88***	7.805 $\pm$ 0.011	-0.0005 <sub>5</sub> $\pm$ 0.0001 <sub>1</sub>	0.80***
	uLSW	7.781 $\pm$ 0.006	-0.0005 <sub>9</sub> $\pm$ 0.0000 <sub>6</sub>	0.93***	7.769 $\pm$ 0.005	-0.0005 <sub>6</sub> $\pm$ 0.0000 <sub>5</sub>	0.96***
	cLSW	7.778 $\pm$ 0.004	-0.0005 <sub>3</sub> $\pm$ 0.0000 <sub>4</sub>	0.97***	7.767 $\pm$ 0.003	-0.0004 <sub>3</sub> $\pm$ 0.0000 <sub>3</sub>	0.97***
	ISOW	7.777 $\pm$ 0.004	-0.0004 <sub>8</sub> $\pm$ 0.0000 <sub>4</sub>	0.97***	7.760 $\pm$ 0.002	-0.0003 <sub>5</sub> $\pm$ 0.0000 <sub>2</sub>	0.99***
	DSOW	7.784 $\pm$ 0.006	-0.0005 <sub>7</sub> $\pm$ 0.0000 <sub>6</sub>	0.94***			
$^1\Delta\text{pH}_{C_{ANT}}$	SPMW	-0.011 $\pm$ 0.007	-0.0008 <sub>4</sub> $\pm$ 0.0000 <sub>7</sub>	0.96***	-0.025 $\pm$ 0.007	-0.0006 <sub>4</sub> $\pm$ 0.0000 <sub>7</sub>	0.94***
	uLSW	-0.010 $\pm$ 0.008	-0.0007 <sub>2</sub> $\pm$ 0.0000 <sub>8</sub>	0.93***	-0.016 $\pm$ 0.010	-0.0005 <sub>5</sub> $\pm$ 0.0001 <sub>0</sub>	0.82***
	cLSW	-0.026 $\pm$ 0.006	-0.0003 <sub>9</sub> $\pm$ 0.0000 <sub>6</sub>	0.87***	-0.020 $\pm$ 0.005	-0.0003 <sub>9</sub> $\pm$ 0.0000 <sub>5</sub>	0.91***
	ISOW	-0.006 $\pm$ 0.006	-0.0004 <sub>5</sub> $\pm$ 0.0000 <sub>6</sub>	0.92***	-0.006 $\pm$ 0.005	-0.0003 <sub>8</sub> $\pm$ 0.0000 <sub>5</sub>	0.90***
	DSOW	0.009 $\pm$ 0.007	-0.0005 <sub>9</sub> $\pm$ 0.0000 <sub>7</sub>	0.92***			
$^1\Delta\text{pH}_{\text{Var}}$	SPMW	7.035 $\pm$ 0.288	0.0004 <sub>1</sub> $\pm$ 0.0001 <sub>4</sub>	0.57**	7.547 $\pm$ 0.377	0.0001 <sub>5</sub> $\pm$ 0.0001 <sub>9</sub>	0.09
	uLSW	7.361 $\pm$ 0.441	0.0002 <sub>2</sub> $\pm$ 0.0002 <sub>2</sub>	0.14	7.922 $\pm$ 0.513	-0.0000 <sub>7</sub> $\pm$ 0.0002 <sub>6</sub>	0.01
	cLSW	8.282 $\pm$ 0.303	-0.0002 <sub>5</sub> $\pm$ 0.0001 <sub>5</sub>	0.31*	7.966 $\pm$ 0.241	-0.0000 <sub>9</sub> $\pm$ 0.0001 <sub>2</sub>	0.09
	ISOW	7.883 $\pm$ 0.176	-0.00005 $\pm$ 0.00009	0.05	7.660 $\pm$ 0.199	0.0000 <sub>5</sub> $\pm$ 0.0001 <sub>0</sub>	0.05
	DSOW	7.710 $\pm$ 0.230	-0.00003 $\pm$ 0.00011	0.01			

\* Statistically significant at the 90% level (p-value < 0.10); \*\* statistically significant at the 95% level (p-value < 0.05); \*\*\* statistically significant at the 99% level (p-value < 0.01).

<sup>1</sup> Trends without considering the 1997 cruise.

The  $C_{ANT}$  concentration of DSOW shows a similar pattern than that of ISOW in the Irminger Basin (Figure 31a). This similar behaviour likely derive from vigorous mixing processes, but it may also reflect the common origin of the water masses present in these layers, which in last instance traces the  $C_{ANT}$  increase in their Arctic source waters. In fact, Azetsu-Scott et al. (2003) reported CFC concentrations for the ISOW layer lower than for the DSOW layer in the Labrador Sea, being the CFC concentration increased at a rate 25% lower in the ISOW layer for the period 1991–2000.

The  $C_{ANT}$  rates estimated using the conservative tracer  $C^*$  show similar rates to those obtained from the  $\varphi C_T^0$  method (Figure 31; Table 6), thus corroborating the results here obtained. The absolute difference between both methods ( $\Delta C^*$  and  $\varphi C_T^0$ ) is the  $\Delta C_{dis}$  term, which is water mass dependent and should be nearly constant in each water mass unless there are long-term changes in the disequilibrium (Matsumoto and Gruber, 2005; Khatiwala et al., 2009). In the Iceland Basin both sets of trends are not significantly different at 95% level. In the Irminger Basin the trends resulting from the  $\varphi C_T^0$  method are significantly lower than those from  $\Delta C^*$  method in the uLSW and ISOW layers. This difference is explained by the fact that the  $\varphi C_T^0$  method considers a term proportional to the  $C_{ANT}$  concentration of the water mass, while the  $\Delta C^*$  method considers a constant  $\Delta C_{dis}$  term (Matsumoto and Gruber, 2005). Since the  $\Delta C_{dis}$  term used by the  $\varphi C_T^0$  method increases slightly with time, the rate of change of  $C_{ANT}$  determined by the  $\varphi C_T^0$  method is slightly lower than that determined by the  $\Delta C^*$  method.

## 5.8.- Acidification trends

The general pattern of  $pH_{SWS_{25}}$  follows the expected distribution, with high-surface values higher than 7.85, which rapidly decrease with increasing depth until a pH minimum zone at ~500 m depth (Figure 28e). The high values of  $pH_{SWS_{25}}$  above the uppermost ~200 m respond to the photosynthetic activity of primary producers that withdraw dissolved CO<sub>2</sub> from seawater. The prominent pH decrease in the first 500 m is largely associated with remineralization of sinking organic matter by microorganisms (Millero, 2007), which is corroborated by the gradient found in the  $\Delta pH_{var}$  (Figure 28g). The  $pH_{SWS_{25}}$  minimum (< 7.7), which coincides with a maximum of AOU, is associated to an area of slower circulation (Pérez et al., 1993) where the products of the remineralization of the organic matter accumulate. Below 500 m depth, the whole section shows relatively homogeneous low  $pH_{SWS_{25}}$  values of about 7.70–7.75. However, the ISOW layer in the Iceland Basin shows slightly lower  $pH_{SWS_{25}}$  values than in the Irminger Basin. These lower values may derive from the fact that ISOW is more “pure” in the Iceland Basin than in the Irminger Basin, thus being its anthropogenic signal higher in the Iceland Basin.

The net effect of the absorption of  $C_{ANT}$  by the oceans is the increase in the concentrations of H<sup>+</sup> in seawater, i.e., the decrease in seawater pH. This decrease in  $pH_{SWS_{25}}$  is observed in all the layers and in both basins (Figure 32a,b; Table 6), being more pronounced in all the layers of the Irminger Basin due to the presence of younger waters. The general pattern seems to be a decrease of the acidification rates with increasing depth, except in the DSOW layer that presents acidification rates similar to those found in the upper layers. This indicates that DSOW is a newly formed water that has been recently in contact with the atmosphere. The general trends of decreasing  $pH_{SWS_{25}}$  are disrupted by the data of the 1997 cruise, which are outliers.

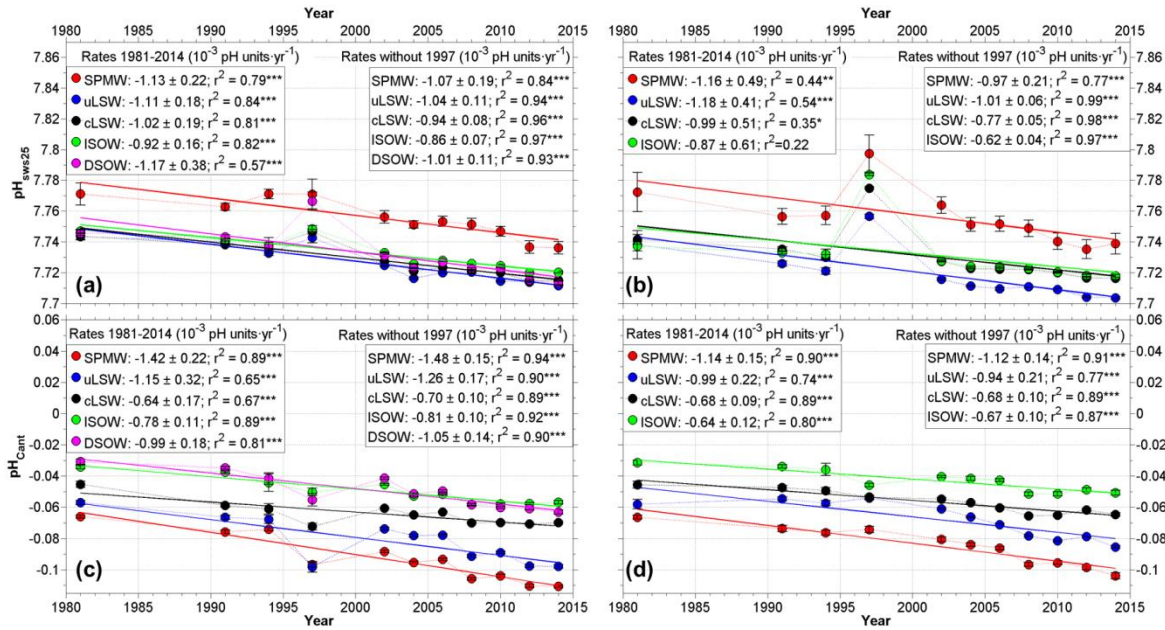


Figure 32.- Temporal evolution between 1981 and 2014 of the average values of (a and b) pH in seawater scale at 25°C ( $\text{pH}_{\text{sws}_{25}}$ ) and (c and d) pH change derived from the uptake of anthropogenic CO<sub>2</sub> ( $\text{pH}_{\text{Cant}}$ ) in main water masses of the Irminger (a and c) and Iceland (b and c) Basins. Each point represents the average property of a particular water mass (SPMW (red dots), uLSW (blue dots), cLSW (black dots), ISOW (green dots) and DSOW (magenta dots)) at the time of each cruise (Table 5). The error bars represent the error of the mean. The inset boxes give the trends  $\pm$  standard error of the estimate and the correlation coefficients ( $r^2$ ). \*\* denotes that the trend is statistically significant at the 95% level ( $p$ -value < 0.05), and \*\*\* at the 99% level ( $p$ -value < 0.01). See water mass acronyms in Figure 27.

The observed rate of  $\text{pH}_{\text{sws}_{25}}$  decrease in SPMW of the Iceland Basin ( $-0.0010 \pm 0.0002$  pH units  $\text{yr}^{-1}$ ; Figure 32b) is in agreement with that observed in the Iceland Sea time-series (68°N, 12.66°W; Olafsson et al. (2009, 2010)) for the period 1983–2014 ( $-0.0014 \pm 0.0005$  pH units  $\text{yr}^{-1}$ ; Bates et al. (2014)). the rates of  $\text{pH}_{\text{sws}_{25}}$  decrease here observed in SPMW in the Irminger Basin ( $-0.0011 \pm 0.0002$  pH units  $\text{yr}^{-1}$ ) is half that observed in the sea surface waters of the Irminger Sea time-series (64.3°N, 28°W; Olafsson et al. (2010)) for the period 1983–2014 ( $-0.0026 \pm 0.0006$  pH units  $\text{yr}^{-1}$ ; Bates et al. (2014)). Our rates in SPMW of both basins are slightly lower than those observed in the Subtropical Atlantic time-series stations ESTOC (29.04°N, 15.50°W; Santana-Casiano et al. (2007), González-Dávila et al. (2010)) for the period 1995–2014 ( $-0.0018 \pm 0.0002$  pH units  $\text{yr}^{-1}$ ; Bates et al. (2014)) and BATS (32°N, 64°W; Bates et al. (2014)) for the period 1983–2014 ( $-0.0017 \pm 0.0001$  pH units  $\text{yr}^{-1}$ ; Bates et al. (2014)). The difference between the acidification rates here estimated for SPMW and those reported for the Irminger Sea and the Subtropical North Atlantic may rely on the fact that our acidification rates are based on  $\text{pH}_{\text{sws}_{25}}$  data, whereas the others are based on pH reported at *in situ* temperature. Consequently, some of the  $\text{pH}_{\text{sws}_{25}}$  changes reported by the time-series stations may be associated with changes in temperature rather than changes in  $A_T$  and  $C_T$ . Comparing with the acidification rates observed in the Pacific Ocean, the results here obtained are slightly lower than those reported in the Central North Pacific by the time-series station HOT (22.45°N, 158°W; Dore et al. (2009)) for the period 1988–2014 ( $-0.0016 \pm 0.0001$  pH units  $\text{yr}^{-1}$ ; Bates et al. (2014)). However, the acidification rates here reported are in agreement with those found by Wakita et al. (2013) in the winter mixed of the Subarctic Western North Pacific (time-series stations K2 and KNOT) for the period 1997–

2011 ( $-0.0010 \pm 0.0004$  pH units·yr<sup>-1</sup>). Those authors argued that the lower acidification rates found in their study region were due to an increase in  $A_T$ .

The decomposition of the pH changes into the  $\Delta pH_{C_{ANT}}$  and the  $\Delta pH_{Var}$  allows inferring the possible causes of the acidification trends here reported. The  $\Delta pH_{Var}$  field shows a similar pattern to that of the  $pH_{SWS_{25}}$  (Figure 28g). However, the  $\Delta pH_{Var}$  values are slightly higher than those of the  $pH_{SWS_{25}}$ , meaning that the water masses of the sections are clearly exposed to the acidification caused by the  $C_{ANT}$  uptake.

In a steady state ocean, the  $\Delta pH_{Var}$  would be constant and all the pH decrease would be explained by the  $\Delta pH_{C_{ANT}}$ . However, the  $\Delta pH_{Var}$  shows long-term trends, some of them statistically significant (Figure 33; Table 6). The observed acidification rates of SPMW represents only 72–87% of the expected pH change due to the  $C_{ANT}$  uptake ( $\Delta pH_{C_{ANT}}$ ). This is explained by the positive trends of the  $\Delta pH_{Var}$  observed in this layer that counteract the effect of the  $\Delta pH_{C_{ANT}}$ , resulting in a net dampening of the acidification signal. This would contribute to explain the difference between the  $pH_{SWS_{25}}$  trends for the upper layer here reported and those observed in the time-series stations above mentioned. The buffering of the acidification is caused by the arrival of salty and alkaline subtropical waters transported by the NAC to the study region. Wakita et al. (2013) reported similar results for the Western Subarctic Gyre in the North Pacific Ocean where the increasing trend of  $A_T$  for the period 1997–2011 inhibited 50% of the acidification.

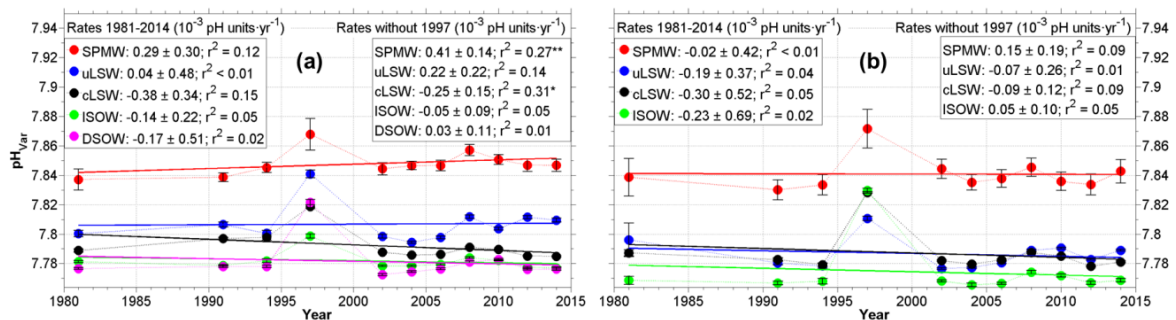


Figure 33.- Temporal evolution between 1981 and 2014 of the average pH change not derived from the uptake of anthropogenic CO<sub>2</sub> ( $pH_{Var}$ ) values in main water masses of the Irminger (a) and Iceland (b) Basins. Each point represents the average  $pH_{Var}$  of a particular water mass (SPMW (red dots), uLSW (blue dots), cLSW (black dots), ISOW (green dots) and DSOW (magenta dots)) at the time of each cruise (Table 5). The error bars represent the error of the mean. The inset boxes give the trends  $\pm$  standard error of the estimate and the correlation coefficients ( $r^2$ ). \* denotes that the trend is statistically significant at the 90% level (p-value < 0.1), \*\* at the 95% level (p-value < 0.05), and \*\*\* at the 99% level (p-value < 0.01). See water mass acronyms in Figure 27.

The cLSW layer in the Irminger Basin present a reduction in pH 34% higher than that directly related to the  $C_{ANT}$  uptake ( $\Delta pH_{C_{ANT}}$ ; Figure 32a,c; Table 6). This is explained by the reinforcement of the negative  $\Delta pH_{C_{ANT}}$  trend due to the negative  $\Delta pH_{Var}$  trend (Figure 33). The decreasing trend of  $\Delta pH_{Var}$  is related to the aging of this water mass corroborated by the increasing trends of S and AOU. The reinforcement of the acidification trends by natural processes was also found in the North Pacific Ocean (Wakita et al., 2013).

In the same region, Vázquez-Rodríguez et al. (2012b) studied the  $pH_{SWS_{25}}$  changes in the different water masses of the basins. These authors normalized the average  $pH_{SWS_{25}}$  values of each



layer taking into account the climatological values compiled in WOA05 ([http://www.nodc.noaa.gov/OC5/WOA05/pr\\_woa05.html](http://www.nodc.noaa.gov/OC5/WOA05/pr_woa05.html)). The steps for their normalization were: (1) to calculate for each layer the differences between the mean values of  $\theta$ , S, silicate and AOU from the cruise data and those derived from the WOA05 data; (2) to calculate the atmospheric CO<sub>2</sub> concentration at the time of each cruise; (3) to perform for each layer a multiple linear regression between the observed average pH<sub>SWS<sub>25</sub></sub> value and the variables resulting from steps 1 and 2; (4) finally, the normalized pH<sub>SWS<sub>25</sub></sub> (pH<sub>N</sub>) was obtained by subtracting the result of step 3 (using only those variables statistically significant in the regression) from the observed average pH<sub>SWS<sub>25</sub></sub> value in each layer. The rates of pH<sub>N</sub> would closely reflect those of the  $\Delta\text{pH}_{\text{C}_{\text{ANT}}}$  here obtained, because the normalization probably remove an important part of the natural variability (if any). The  $\Delta\text{pH}_{\text{C}_{\text{ANT}}}$  trends here obtained (Figure 32) are in agreement with the pH<sub>N</sub> trends reported by Vázquez-Rodríguez et al. (2012b), except in SPMW and uLSW in the Irminger Basin, and cLSW in the Iceland Basin. In the cLSW layer in the Iceland Basin the pH<sub>N</sub> rate is  $(-1.57 \pm 0.20) \cdot 10^{-3}$  pH units·yr<sup>-1</sup>, which is nearly twice the rates of  $\Delta\text{pH}_{\text{C}_{\text{ANT}}}$  or pH<sub>SWS<sub>25</sub></sub> here observed. This high rate may be the result of the timeframe used to estimate the pH<sub>N</sub> rate (1991–2008) that is nearly half of the period of time here used, which also coincides with the timeframe where rapid changes in the convection processes leading to the formation of cLSW took place (transition from high to low NAO periods). These facts could drove to a very high rate of acidification in cLSW estimated by Vázquez-Rodríguez et al. (2012b). In the Irminger Basin, the pH<sub>N</sub> rates of  $(-1.85 \pm 0.09) \cdot 10^{-3}$  pH units·yr<sup>-1</sup> estimated for SPMW and  $(-1.71 \pm 0.05) \cdot 10^{-3}$  pH units·yr<sup>-1</sup> for uLSW (Vázquez-Rodríguez et al., 2012b) are slightly higher than the  $\Delta\text{pH}_{\text{C}_{\text{ANT}}}$  rates of  $(-1.48 \pm 0.15) \cdot 10^{-3}$  pH units·yr<sup>-1</sup> and of  $(-1.26 \pm 0.17) \cdot 10^{-3}$  pH units·yr<sup>-1</sup>, respectively. These discrepancies may result from the different cruises used for the decade of 1990s in combination with the interpolation procedure here used and the different timeframe of both studies.

The differences in the C<sub>ANT</sub> estimates due to different treatment of the  $\Delta\text{C}_{\text{dis}}$  term in the  $\Delta\text{C}^*$  and  $\varphi\text{C}_{\text{T}}^0$  methods could generate an extra acidification up to 0.04 pH units·yr<sup>-1</sup> if the  $\Delta\text{pH}_{\text{C}_{\text{ANT}}}$  is calculated in base of the C\* estimates. This would suggest that using an  $\Delta\text{C}_{\text{dis}}$  term that varies over time, like the proposed in the  $\varphi\text{C}_{\text{T}}^0$  method, produces  $\Delta\text{pH}_{\text{V}_{\text{ar}}}$  closer to the steady-state than the resulting from the application of the C\* parameter. It is especially important for the SPMW layer, where a higher rate of increase in the C<sub>ANT</sub> estimates would lead to a greater contribution of the  $\Delta\text{pH}_{\text{V}_{\text{ar}}}$  to the observed acidification rates.

## 5.9.- Changes in the CaCO<sub>3</sub> saturation horizon

Spatial and temporal changes in the saturation estate of CaCO<sub>3</sub> are important for understanding how ocean acidification might impact future ecosystems. The  $\Omega_{\text{Arag}}$  decreases with increasing depth, being the surface and intermediate waters supersaturated ( $\Omega_{\text{Arag}} > 1$ ) and the waters of the ISOW and DSOW layers below 2500 dbar undersaturated in the aragonite form of CaCO<sub>3</sub> ( $\Omega_{\text{Arag}} < 1$ ) (Figure 28h). Despite the differences in the pH<sub>SWS<sub>25</sub></sub> fields between the Irminger and Iceland Basins (Figure 28e,g), there are no appreciable differences in the  $\Omega_{\text{Arag}}$  fields of both basins. This is due to the important influence of the pressure field in the  $\Omega_{\text{Arag}}$  that causes similar profiles in both basins. The study region is an area of low vertical  $\Omega_{\text{Arag}}$  gradient compared to the tropics and subtropics (Chung et al., 2004). The  $\Omega_{\text{Arag}}$  values in the winter mixed layer depth here observed are lower than those observed in subtropical and tropical areas ( $\Omega_{\text{Arag}} \approx 4$ ).



The  $\Omega_{\text{Arag}}$  shows significant decreasing trends in all the water masses when excluding the data of the 1997 cruise (Figure 34). The greatest rate of  $\Omega_{\text{Arag}}$  decrease is located in the uLSW layer with a mean value for both basins of  $-0.0036 \pm 0.0007 \text{ yr}^{-1}$ . The rates of  $\Omega_{\text{Arag}}$  decrease of the SPMW layer in the Iceland Basin here reported ( $-0.0030 \pm 0.0009 \text{ yr}^{-1}$ ; Figure 34) is higher than that observed in the Iceland Sea time-series for the period 1983–2014 ( $-0.0018 \pm 0.0027 \text{ yr}^{-1}$ ; Bates et al. (2014)). However, the rate of  $\Omega_{\text{Arag}}$  decrease in SPMW in the Irminger Basin here reported ( $-0.0030 \pm 0.0007 \text{ yr}^{-1}$ ) is more than two times lower than that observed in the Irminger Sea time-series for the period 1983–2014 ( $-0.0080 \pm 0.0040 \text{ yr}^{-1}$ ; Bates et al. (2014)). Comparing the rates here reported with those in other time-series stations, they are also lower than that reported in the ESTOC time-series stations for the period 1995–2014 ( $-0.0115 \pm 0.0023 \text{ yr}^{-1}$ ; Bates et al. (2014)), in the BATS time-series stations for the period 1983–2014 ( $-0.0095 \pm 0.0007 \text{ yr}^{-1}$ ; Bates et al. (2014)), and in the HOT time-series station for the period 1988–2014 ( $-0.0084 \pm 0.0011 \text{ yr}^{-1}$ ; Bates et al. (2014)). The rates of  $\Omega_{\text{Arag}}$  decrease found in the upper waters of the Atlantic Ocean are one order of magnitude lower than those found in the subtropical South Pacific at 400 dbar horizon between 1994 and 2009 by Murata et al. (2015). These authors associate the rapid decreasing rates with the increase in the organic matter remineralization and the weakening of the water mass ventilation.

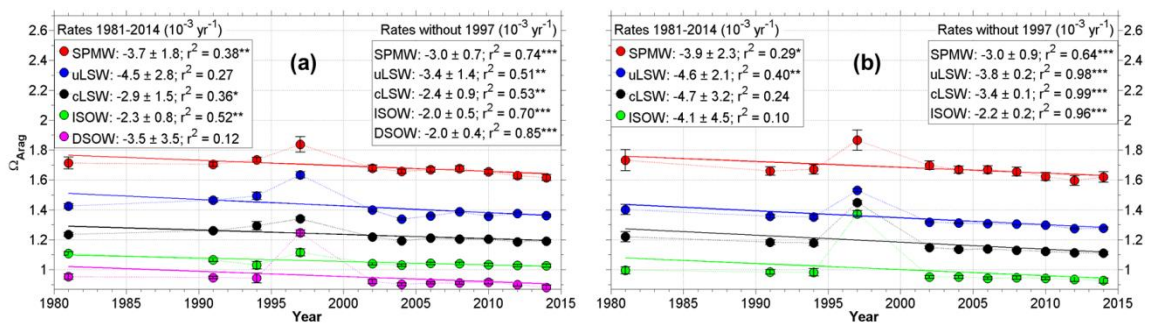


Figure 34.- Temporal evolution between 1981 and 2014 of the average saturation of CaCO<sub>3</sub> in terms of aragonite ( $\Omega_{\text{Arag}}$ ) values in main water masses of the Irminger (a) and Iceland (b) Basins. Each point represents the average  $\Omega_{\text{Arag}}$  of a particular water mass (SPMW (red dots), uLSW (blue dots), cLSW (black dots), ISOW (green dots) and DSOW (magenta dots)) at the time of each cruise (Table 5). The error bars represent the error of the mean. The inset boxes give the trends  $\pm$  standard error of the estimate and the correlation coefficients ( $r^2$ ). \* denotes that the trend is statistically significant at the 90% level (p-value < 0.1), \*\* at the 95% level (p-value < 0.05), and \*\*\* at the 99% level (p-value < 0.01). See water mass acronyms in Figure 27.

The decreasing trends between  $-2.4$  and  $-3.8 \cdot 10^{-3} \text{ yr}^{-1}$  observed in intermediate waters (uLSW and cLSW; Figure 34) correspond with a shoaling of the saturation horizon (isopleth where  $\Omega_{\text{Arag}} = 1$ ) at a rate of  $\sim 10 \text{ m} \cdot \text{yr}^{-1}$ , which is more than twice the shoaling trend found in the Iceland Sea time-series station for the period 1985–2008 (Olafsson et al., 2009), and almost twice the shoaling trend found in the subtropical South Pacific between 1994 and 2009 (Murata et al., 2015) at 400 dbar horizon. The shoaling of the saturation horizon may affect aragonitic cold-water corals (e.g., Langdon et al., 2000), although some authors argued that the calcification rates of these corals are unaffected by the shoaling of the aragonite saturation horizon (Guinotte et al., 2006; Jackson et al., 2014; Rodolfo-Metalpa et al., 2015).

## 5.10.- Future changes in the variables of the seawater CO<sub>2</sub> system

From the set of observations here used, projections of future changes in pH<sub>SW<sub>S</sub>25</sub> and  $\Omega_{\text{Arag}}$  levels were estimated. The projections were calculated under the assumption that the general circulation of the ocean and the observed trends for the period 1981–2014 here reported (Table 6) will behave similarly for the rest of the 21st century, which is rather tentative. Such linear extrapolation is not constrained, but several works have demonstrated that the decline in the parameters of the seawater CO<sub>2</sub> system, like bicarbonate ions, is almost linear for predictions made between 2000 and 2050 (e.g., Zeebe et al., 1999; Hauck et al., 2010). The buffering effect of the CaCO<sub>3</sub> dissolution in deep waters can be disregarded since it tends to occur over timescales at least one order of magnitude larger than the one here considered. Therefore it can be assumed that on decadal timescales pH and  $\Omega_{\text{Arag}}$  will evolve in the future analogously to what it is observed in the present study.

The expected increasing stratification of the surface layers (Friedlingstein and Prentice, 2010) could possibly hamper the processes of water mass ventilation and reduce the effectiveness in the transport of C<sub>ANT</sub> towards the ocean interior via deep convection (Pérez et al., 2010). Therefore, assuming a steady state for the general circulation can potentially cause overestimates in the projected pH values for surface and intermediate waters. Nevertheless, this slowdown in the acidification process due to the decrease in the C<sub>ANT</sub> uptake could be counterbalanced by the enhanced remineralization of the organic matter precipitated by the increase in the stratification.

According to the projections here obtained, the pH<sub>SW<sub>S</sub>25</sub> of SPMW could drop ~0.31 pH units with respect to the pre-industrial era (from ~7.81 to ~7.50) by the time atmospheric CO<sub>2</sub> reaches 800 ppm (about twice the present atmospheric CO<sub>2</sub> concentration), which is consistent with the predictions for the IPCC representative concentration pathway 8.5 (RCP.5) (Ciais et al., 2013), which is the worst scenario within the predicted. According to RCP8.5, the atmospheric CO<sub>2</sub> reaches 800 ppm by the year ~2065 (van Vuuren et al., 2011). The projected pH drop for uLSW (~0.30 pH units, from ~7.78 to ~7.48) is similar to that in the SPMW layer. In the case of cLSW, the linear projection predicts a pH decrease of ~0.25 pH units with respect to the pre-industrial pH by the time atmospheric CO<sub>2</sub> reaches 800 ppm (from ~7.77 to ~7.57). The expected pH drop for ISOW is ~0.20 pH units (from ~7.77 to ~7.52), whereas the pH decrease projected for DSOW (~0.27 pH units, from ~7.78 to ~7.51) is similar to that of the upper layers. It is noteworthy that the projected acidification rates for the waters of the Irminger Basin are between 0.06 (ISOW) and 0.10 (SPMW) pH units higher than for the Iceland Basin.

Nowadays, the overflow waters ISOW and DSOW are already undersaturated in aragonite ( $\Omega_{\text{Arag}} < 1$ ), albeit their preindustrial values of  $\Omega_{\text{Arag}}$  were 1.11 and 1.03, respectively (Table 6). The projections of the  $\Omega_{\text{Arag}}$  levels here obtained suggest that the whole water column will be undersaturated in aragonite by the time atmospheric CO<sub>2</sub> reaches 800 ppm (~2065), which is in agreement with numerical models results (Feely et al., 2009; Matear and Lenton, 2014). The  $\Omega_{\text{Arag}}$  of SPMW in both basins would change from its preindustrial value of 1.83 to 0.93. However, the uLSW and cLSW layers would reach aragonite undersaturation faster. The uLSW layer would reach the undersaturation state by the time the atmospheric CO<sub>2</sub> reaches ~560 ppm, and cLSW by

the time atmospheric CO<sub>2</sub> reaches ~500 ppm and not 900 ppm as previously suggested by numerical models (Orr et al., 2005). Those atmospheric CO<sub>2</sub> concentrations would be achieved between ~2035 and ~2045 according to RCP8.5 (van Vuuren et al., 2011). The preindustrial  $\Omega_{\text{Arag}}$  value of 1.56 estimated for uLSW is higher than that of cLSW (1.34); however uLSW would reach undersaturation levels at a similar atmospheric CO<sub>2</sub> concentration at which cLSW would reach it due to the greater influence of the anthropogenic acidification on uLSW. The rapid decrease of the  $\Omega_{\text{Arag}}$  levels in cLSW is explained by its formation history. The high-NAO enhanced ventilation occurred towards the mid-late 1980s fostered the fast formation of a massive vintage of cLSW that transported C<sub>ANT</sub> from the surface into intermediate waters. The shutdown of the cLSW production due to the shift of the NAO index in the late 1990s (e.g., Lazier et al., 2002; Kieke et al., 2006; Rhein et al., 2007; Yashayaev et al., 2008) cause the aging of this water mass, fostering the acidification of this layer (34% faster as found in Section 5.8), and thus lowering its  $\Omega_{\text{Arag}}$  values. The early undersaturations in aragonite of uLSW and cLSW could produce negative impacts for the cold-water corals that inhabit the depths at which these water masses are located (Strömgen, 1971; Zibrowius, 1980; Freiwald et al., 2004).

## 5.11.- Conclusions

The net effect of the C<sub>ANT</sub> uptake by the oceans is the decrease in its pH and carbonate ion concentration, thus lowering the buffering capacity of seawater. The progressive acidification of the North Atlantic waters has been assessed from direct observations spanning the last three decades (1981–2014). By separating the observed pH changes into an anthropogenic and a non-anthropogenic component, an attribution to the underlying drivers is provided. The increasing atmospheric CO<sub>2</sub> concentrations have significantly decreased the pH of the whole water column of the Irminger and Iceland Basins, with the greatest pH changes observed in surface and intermediate waters. The C<sub>ANT</sub> concentration of the upper layer increases roughly keeping pace with rising atmospheric CO<sub>2</sub>, whereas the pH drop does not follow this trend. The salty and alkaline subtropical waters transported by the NAC to the study region buffer the acidification caused by the C<sub>ANT</sub> increase in the upper layer. Intermediate waters exhibit acidification rates similar to those found in the surface waters, which are caused by a combination of anthropogenic and non-anthropogenic components. In the Irminger Basin, the acidification rate of cLSW due to the C<sub>ANT</sub> uptake is reinforced by the aging of this water mass from the end of the 1990s onwards. The deep waters of the Irminger Basin present a clear evidence of significant acidification from anthropogenic forcing.

Calcification or dissolution of both planktonic and benthic calcifying organisms commonly depends on the carbonate ion concentration, often expressed by the degree of saturation of the biominerals aragonite and calcite. The addition of C<sub>ANT</sub> during the last 33 years has caused the aragonite saturation horizons to shoal towards the surface in the Irminger and Iceland Basins at a rate of ~10 m·yr<sup>-1</sup>, which is more than twice the shoaling trend previously found in the Iceland Sea.

Taking advantage of the observed pH and  $\Omega_{\text{Arag}}$  changes for the period 1981–2014, the future changes of these variables are inferred. SPMW would experience a pH drop of ~0.31 pH units with respect to the pre-industrial value by the time atmospheric CO<sub>2</sub> reaches 800 ppm (about twice the present atmospheric concentration of CO<sub>2</sub>), which is in agreement with the projections

of the RCP8.5. Similar pH decrease is projected for DSOW (~0.27 pH units). The estimated projections also suggest that the whole water column of both basins will be undersaturated in aragonite by the time atmospheric CO<sub>2</sub> reaches 800 ppm (~2065), which is in agreement with the results of numerical models. However, uLSW and cLSW would reach aragonite undersaturation levels more rapidly, by the time atmospheric CO<sub>2</sub> reaches ~560 ppm (~2045) and ~500 ppm (~2035), respectively.

The data here compiled also show significant long-term trends of increasing alkalinity in the deep waters of the Irminger Basin, which may be related to increase in river discharge in the Arctic Ocean.

Ocean acidification has emerged as a key topic of concern regarding the potential of the changes in the seawater CO<sub>2</sub> system to create feedbacks to global climate in a myriad of ways. Studies of full-depth data of the variables of the seawater CO<sub>2</sub> system across ocean basins, as this study, are necessary to put any future change in the context of the changes that have already occurred.

## Chapter 6.- Variability of the transport of anthropogenic CO<sub>2</sub> at the Greenland–Portugal OVIDE section: controlling mechanisms

### 6.1.- Resumen

En este capítulo se investiga la variabilidad interanual a decenal en el transporte de CO<sub>2</sub> antropogénico ( $C_{ANT}$ ) a través del Atlántico Norte Subpolar (ANSP). Para ello se utilizan datos de alta resolución de las secciones transoceánicas 4x y OVIDE, llevadas a cabo entre Groenlandia y Portugal durante seis veranos entre 1997 y 2010. El transporte de  $C_{ANT}$  a través de estas secciones ( $T_{C_{ANT}}$ ) es hacia el norte, con un valor medio de  $254 \pm 29 \text{ kmol}\cdot\text{s}^{-1}$  para el período 1997–2010. No existe una tendencia temporal de  $T_{C_{ANT}}$  para este período debido a su variabilidad interanual. A fin de comprender los mecanismos que controlan la variabilidad del  $T_{C_{ANT}}$  a través del ANSP, se propone un nuevo método para cuantificar el  $T_{C_{ANT}}$  causado por las circulaciones diapícnica e isopícnica. El componente diapícnico produce un alto  $T_{C_{ANT}}$  hacia el norte ( $400 \pm 29 \text{ kmol}\cdot\text{s}^{-1}$ ) que es parcialmente compensado por un  $T_{C_{ANT}}$  hacia el sur causado por el componente isopícnico ( $-171 \pm 11 \text{ kmol}\cdot\text{s}^{-1}$ ), localizado principalmente en el Mar de Irminger. Gracias a esta descomposición se concluye que el componente diapícnico es el principal responsable de la variabilidad del  $T_{C_{ANT}}$  a través del ANSP. Tanto la circulación termohalina (calculada en coordenadas de densidad,  $MOC\sigma$ ) como el aumento de  $C_{ANT}$  en la columna de agua tienen un efecto importante en la variabilidad del componente diapícnico y del  $T_{C_{ANT}}$  en sí. En base a este análisis, se propone un estimador simplificado para la variabilidad del  $T_{C_{ANT}}$  basado en la intensidad de la  $MOC\sigma$  y en la diferencia en la concentración de  $C_{ANT}$  de las ramas superior e inferior de la  $MOC\sigma$  ( $\Delta C_{ANT}$ ). Este estimador es consistente con el componente diapícnico del  $T_{C_{ANT}}$  y ayuda a separar el efecto de la variabilidad de la circulación en la variabilidad del  $T_{C_{ANT}}$  del causado por el aumento de  $C_{ANT}$ . La  $\Delta C_{ANT}$  ha estado aumentando durante la última década, y es muy probable que el aumento continuo de  $C_{ANT}$  en las masas de agua provoque un aumento en el  $T_{C_{ANT}}$  a través del ANSP a largo plazo. Sin embargo, en la escala de tiempo analizada (1997–2010) es la  $MOC\sigma$  la que controla la variabilidad del  $T_{C_{ANT}}$ , enmascarando cualquier tendencia en el  $T_{C_{ANT}}$ . Extrapolando la tasa de aumento de la  $\Delta C_{ANT}$  observada y considerando la ralentización del 25% de la  $MOC\sigma$  predicha para finales de siglo, se espera que el  $T_{C_{ANT}}$  a través del ANSP aumente  $430 \text{ kmol}\cdot\text{s}^{-1}$  durante el siglo XXI. En consecuencia, podría preverse un aumento de la tasa de almacenamiento de  $C_{ANT}$  en el ANSP.

### 6.2.- Abstract

The inter-annual to decadal variability in the transport of anthropogenic CO<sub>2</sub> ( $C_{ANT}$ ) across the Subpolar North Atlantic (SPNA) is investigated in this chapter, using summer data of the 4x and OVIDE high-resolution transoceanic sections, from Greenland to Portugal, occupied

six times from 1997 to 2010. The transport of  $C_{ANT}$  across this section ( $T_{C_{ANT}}$ ) is northwards, with a mean value of  $254 \pm 29 \text{ kmol}\cdot\text{s}^{-1}$  over the 1997–2010 period. The  $T_{C_{ANT}}$  undergoes inter-annual variability, masking any trend different from 0 for this period. In order to understand the mechanisms controlling the variability of the  $T_{C_{ANT}}$  across the SPNA, a new method that quantifies the  $T_{C_{ANT}}$  caused by the diapycnal and isopycnal circulation is proposed. The diapycnal component yields a large northward  $T_{C_{ANT}}$  ( $400 \pm 29 \text{ kmol}\cdot\text{s}^{-1}$ ) that is partially compensated by a southward  $T_{C_{ANT}}$  caused by the isopycnal component ( $-171 \pm 11 \text{ kmol}\cdot\text{s}^{-1}$ ), mainly localised in the Irminger Sea. Most importantly, the diapycnal component is found to be the main driver of the variability of the  $T_{C_{ANT}}$  across the SPNA. Both the Meridional Overturning Circulation (computed in density coordinates,  $\text{MOC}\sigma$ ) and the  $C_{ANT}$  increase in the water column have an important effect on the variability of the diapycnal component and of the  $T_{C_{ANT}}$  itself. Based on this analysis, a simplified estimator for the variability of the  $T_{C_{ANT}}$  is proposed based on the intensity of the  $\text{MOC}\sigma$  and on the difference of  $C_{ANT}$  between the upper and lower limb of the  $\text{MOC}\sigma$  ( $\Delta C_{ANT}$ ). This estimator shows a good consistency with the diapycnal component of the  $T_{C_{ANT}}$  and helps to disentangle the effect of the variability of both the circulation and the  $C_{ANT}$  increase on the variability of the  $T_{C_{ANT}}$ . The  $\Delta C_{ANT}$  keeps increasing over the past decade, and it is very likely that the continuous  $C_{ANT}$  increase in the water masses will cause an increase in the  $T_{C_{ANT}}$  across the SPNA at long timescale. Nevertheless, at the timescale analysed here (1997–2010), the  $\text{MOC}\sigma$  controls the variability of the  $T_{C_{ANT}}$ , blurring any trend of the  $T_{C_{ANT}}$ . Extrapolating the observed  $\Delta C_{ANT}$  increase rate and considering the predicted slow-down of 25% of the  $\text{MOC}\sigma$ , the  $T_{C_{ANT}}$  across the SPNA is expected to increase by  $430 \text{ kmol}\cdot\text{s}^{-1}$  during the 21st century. Consequently, an increase in the storage rate of  $C_{ANT}$  in the SPNA could be envisaged.

### 6.3.- Introduction

The ocean acts as an important sink for the CO<sub>2</sub> emitted by human activities. It has stored approximately one third of the total anthropogenic CO<sub>2</sub> ( $C_{ANT}$ ) emissions since the beginning of the industrial era (Sabine et al., 2004). The  $C_{ANT}$  is uptaken by the air–sea interface and its distribution depends on mixing processes and transport into the ocean interior; this is the reason why the  $C_{ANT}$  concentration generally decreases with increasing depth. The storage of  $C_{ANT}$  in the deep ocean depends on the ventilation and formation of intermediate and deep waters (Tanhua et al., 2006; Rhein et al., 2007; Steinfeldt et al., 2009).

Among all oceans, the highest rate of  $C_{ANT}$  storage is found in the North Atlantic Ocean, mainly in the subpolar region (Sabine et al., 2004; Khatiwala et al., 2013). An increase in the  $C_{ANT}$  storage is associated with an increase in the  $C_{ANT}$  concentration of the water masses. The rate at which the  $C_{ANT}$  concentration increases in the different water masses depends on both their ages and their positions in the water column. In the Subpolar North Atlantic (SPNA), the upper layers that contain Subantarctic Intermediate Water (SAIW), Subpolar Mode Water (SPMW) and North Atlantic Central Water (NACW) present the highest  $C_{ANT}$  increase trends, changing from average values of  $35\text{--}40 \mu\text{mol}\cdot\text{kg}^{-1}$  in 1991–1993 to up to  $55 \mu\text{mol}\cdot\text{kg}^{-1}$  in 2006 (Pérez et al., 2010). Besides, the production of Labrador Sea Water (LSW) fosters a fast injection of  $C_{ANT}$  in the intermediate and deep waters, so that this water mass also presents a high trend of  $C_{ANT}$  increase.

Otherwise, the deeper water masses of the Eastern North Atlantic show no significant tendencies in their  $C_{ANT}$  content between 1991 and 2006 (Pérez et al., 2010).

In the North Atlantic Ocean the highest air–sea fluxes of  $C_{ANT}$  are detected at mid-latitude (Mikaloff-Fletcher et al., 2006). Besides, Pérez et al. (2013) have inferred that the  $C_{ANT}$  is the main component of the air–sea CO<sub>2</sub> fluxes at mid-latitude in the North Atlantic Ocean, while the natural component is the dominant one in the SPNA. They also detected a decrease in the storage rate of  $C_{ANT}$  between 1997 and 2006 in the SPNA that was related to the reduction in the intensity of the Meridional Overturning Circulation (computed in density coordinates,  $MOC\sigma$ ). Based on those findings, they elucidated the important contribution of the lateral advection of  $C_{ANT}$  from middle to high latitudes to the  $C_{ANT}$  storage in the SPNA. The other important element of the  $C_{ANT}$  storage in the SPNA is the advection of water masses recently ventilated such as the different vintages of LSW. Consequently, how the  $C_{ANT}$  is transported in the SPNA is a crucial issue for understanding how the ocean is storing  $C_{ANT}$  and for modelling the future role of the ocean damping the atmospheric CO<sub>2</sub> increase caused by humankind.

Nowadays, there is an important international effort in understanding how the ocean uptakes, distributes and stores  $C_{ANT}$ . There are estimations of CO<sub>2</sub> fluxes computed from sea surface pCO<sub>2</sub> measurements, ocean (model) inversions, atmospheric inversions and/or ocean biogeochemical models. Some of these methods also provide an estimation of the transport of  $C_{ANT}$  ( $T_{C_{ANT}}$ ) in the ocean (Mikaloff-Fletcher et al., 2006; Gruber et al., 2009; Tjiputra et al., 2010), but unfortunately, direct estimations of the  $T_{C_{ANT}}$  are not abundant and they are concentrated in the Atlantic Ocean. In the North Atlantic Ocean, the  $T_{C_{ANT}}$  has been estimated from observational data across 24°N and across a transversal section between 40°N and 60°N. The  $T_{C_{ANT}}$  is larger at mid-latitudes than in the northernmost latitudes (Table 7). The large differences between the uncertainties given for the  $T_{C_{ANT}}$  estimations (Table 7) are very likely due to the different methods used to compute the volume transport since most of the  $T_{C_{ANT}}$  errors come from the volume transport uncertainties. The observation-based  $T_{C_{ANT}}$  estimations are in general larger than the  $T_{C_{ANT}}$  estimated by ocean (model) inversions or by biogeochemical models (Table 7), but all of them present large errors. This shows that further improvements are necessary to provide more realistic  $T_{C_{ANT}}$  estimations. To bridge the gap between observations and models, it is necessary to understand better which circulation mechanisms control the  $T_{C_{ANT}}$  and its temporal variability. For example, following the results of Pérez et al. (2013), it seems crucial that models reproduce a realistic variability of the Atlantic Meridional Overturning Circulation.

In this work, data measured between 1997 and 2010 from Greenland to Portugal (4x and OVIDE sections; Figure 35) are used to analyse the  $T_{C_{ANT}}$  variability across the SPNA. The circulation across this section was described by Lherminier et al. (2007, 2010) and Mercier et al. (2015). Briefly, at gyre scale, the structures intersecting the section are a cyclonic circulation in the Irminger Sea, a cyclonic circulation in the Iceland Basin, the North Atlantic Current (NAC) flowing directly northwards east of Eriador Seamount (ESM), and lastly, an anticyclonic circulation dominating the Western European Basin (WEB). Beside this gyre-scale circulation, the  $MOC\sigma$  is an important feature of the circulation across the OVIDE section, which upper limb transports warm  $C_{ANT}$ -laden surface waters northwards, mainly by the NAC. North of the section, the waters are cooled, thus being depleted in  $C_{ANT}$ , and then flow southwards at depth (the lower



limb) mainly close to Greenland, in the Deep Western Boundary Current (DWBC). The limit between the upper and lower limbs of the MOC $\sigma$  is defined by  $\sigma_1$  (potential density referenced to 1000 dbar) equal to  $32.14 \pm 0.03 \text{ kg}\cdot\text{m}^{-3}$  (called  $\sigma_{\text{MOC}}$ ; Mercier et al., 2015).

Table 7.- Estimations of transport of anthropogenic CO<sub>2</sub> ( $T_{\text{C}_{\text{ANT}}}$ ; in  $\text{kmol}\cdot\text{s}^{-1}$ ) in the North Atlantic Ocean from literature. The  $T_{\text{C}_{\text{ANT}}}$  is often given in  $\text{PgC}\cdot\text{yr}^{-1}$  ( $1 \text{ Pg}\cdot\text{Cyr}^{-1} = 2642 \text{ kmol}\cdot\text{s}^{-1}$ ).

Reference	Latitude	Time	Method	$T_{\text{C}_{\text{ANT}}}$ ( $\text{kmol}\cdot\text{s}^{-1}$ )
Mikaloff-Fletcher et al. (2006)	18°N	1765–1995	Ocean (model) inversion	$317 \pm 26$
Gruber et al. (2009)	24.5°N	1765–1995	Ocean (model) inversion	211
Tjiputra et al. (2010)	24.5°N	1990s–2000s	Biogeochemical model	$396 \pm 106$
Rosón et al. (2003)	24.5°N	1992	Observations	$634 \pm 211$
Macdonald et al. (2003)	24.5°N	1992–1998	Observations	$502 \pm 211$
Pérez et al. (2013)	40–60°N	2002–2006 (referred to 2004)	Observations	$195 \pm 24$
Mikaloff-Fletcher et al. (2006)	49°N	1765–1995	Ocean (model) inversion	$53 \pm 26$
Tjiputra et al. (2010)	49°N	1990s–2000s	Biogeochemical model	~100

The MOC $\sigma$  has been identified as the element of the circulation mainly driving the heat transport across several transoceanic sections in the North Atlantic Ocean; meanwhile, the isopycnal heat transport has a minor impact (Ganachaud and Wunsch, 2003; Mercier et al., 2015). Recently, Pérez et al. (2013) evaluated the  $C_{\text{ANT}}$  storage rate and the variability of the  $T_{\text{C}_{\text{ANT}}}$  across the subpolar gyre, finding a significant impact of the MOC $\sigma$  on both of them.

Following Pérez et al. (2013) and using a longer time-series, this study goes further. First, the variability of the  $T_{\text{C}_{\text{ANT}}}$  across the SPNA at inter-annual to decadal timescales is evaluated for the first time. Second, a new method is proposed in order to evaluate the effect of the different elements of the ocean circulation on the variability of the  $T_{\text{C}_{\text{ANT}}}$ . Third, a simplified estimator for the  $T_{\text{C}_{\text{ANT}}}$  across the SPNA is proposed based on the factors chiefly responsible of its variability. Finally, the influence of the increase in  $C_{\text{ANT}}$  in the ocean in the variability of the  $T_{\text{C}_{\text{ANT}}}$  is analysed. The chapter is organized as follows: data and the main water masses circulating across the OVIDE section are detailed in Section 6.4; the  $T_{\text{C}_{\text{ANT}}}$  computation as well as the new method to clarify the effect of the different component of the circulation on the  $T_{\text{C}_{\text{ANT}}}$  are explained in Section 6.5; the main results of this study are exposed in Section 6.6; finally, results are discussed in Section 6.7.

## 6.4.- Data sets

The data used in the present study were acquired during the 4x and OVIDE cruises along the A25 line (Figure 35, Table 8), where full-depth hydrographic stations were carried out between Greenland and Portugal. An overview of the instruments and calibrations associated with the physical parameters is presented by Mercier et al. (2015) and summarized hereafter. The CTD-O<sub>2</sub> measurement accuracies are better than 1 dbar for pressure, 0.002°C for temperature, 0.003 for

salinity  $S$  and  $1 \mu\text{mol}\cdot\text{kg}^{-1}$  for dissolved oxygen  $\text{O}_2$  (Billant et al., 2004; Branellec and Thierry, 2013). The current velocities perpendicular to the section were estimated by combining the geostrophic currents and the velocities measured by the Shipboard Acoustic Doppler Current Profilers in an inverse model using the generalized least squares (Mercier, 1986; Lux et al., 2001). The specificities associated with the A25 section are detailed by Lherminier et al. (2007, 2010).

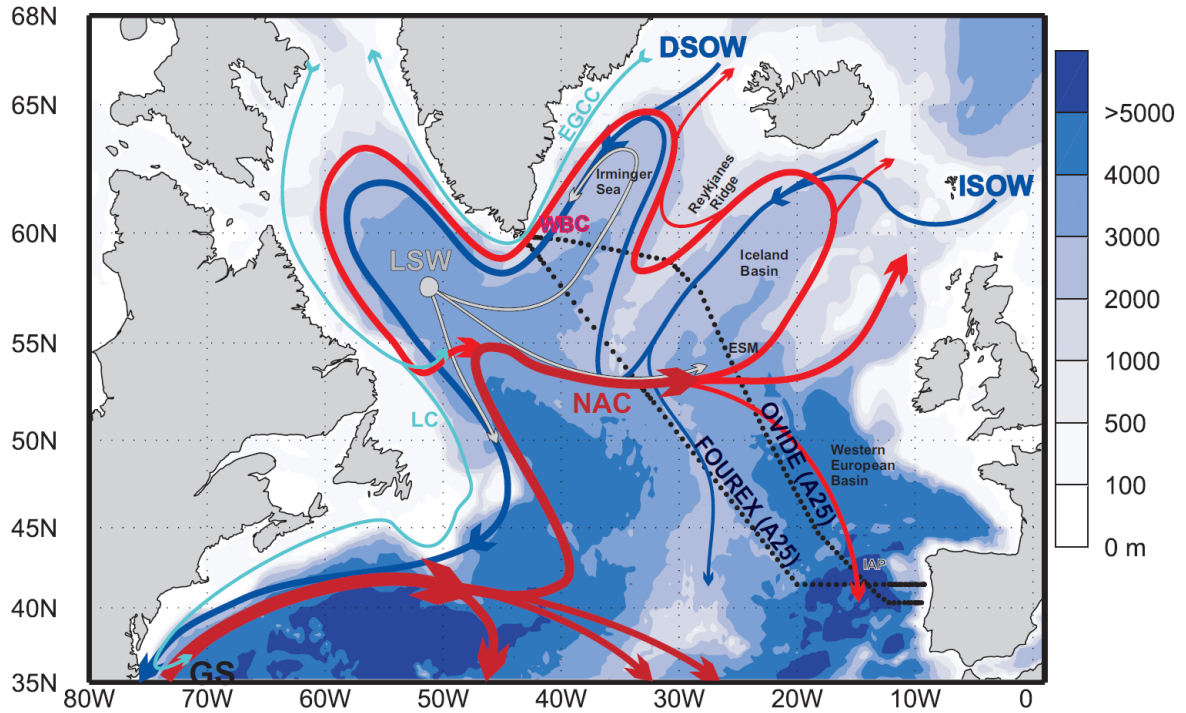


Figure 35.- Schematic circulation in the North Atlantic Ocean. The main pathways of warm and salty waters originating from the Subtropical Atlantic Ocean are shown in red lines while the deep currents are displayed in dark blue. The cyan lines represent the fresh and cold currents over the shelves (Eastern Greenland Coastal Current (EGCC) and Labrador Current (LC)). The grey lines indicate the spreading of the Labrador Sea Water (LSW). The hydrographic stations of the OVIDE and 4x (FOUREX) sections are represented with black dots. The other abbreviations are DSOW = Denmark Strait Overflow Water, ISOW = Iceland-Scotland Overflow Water, WBC = Western Boundary Current, NAC = North Atlantic Current, GS = Gulf Stream, ESM = Eriador Seamount, and IAP = Iberian Abyssal Plain.

The measurements relative to the CO<sub>2</sub> system were all obtained from bottle samples. The pH was determined with a spectrophotometric method (Clayton and Byrne, 1993), resulting in an accuracy of 0.003 pH units or better. The total alkalinity ( $A_T$ ) was analysed with potentiometric titration and determined by single point titration (Pérez and Fraga, 1987; Mintrop et al., 2000), with an accuracy of  $4 \mu\text{mol}\cdot\text{kg}^{-1}$ . The total dissolved inorganic carbon ( $C_T$ ) was calculated from pH and  $A_T$ . Then the concentration of  $C_{\text{ANT}}$  is determined from  $C_T$ ,  $A_T$ ,  $\text{O}_2$ , nutrients, temperature and  $S$ , applying the  $\phi C_T^0$  method (Pérez et al., 2008; Vázquez-Rodríguez et al., 2009a). A random propagation of the errors associated with the input variables yielded an overall uncertainty of  $5.2 \mu\text{mol}\cdot\text{kg}^{-1}$  in the  $C_{\text{ANT}}$  concentration.

Table 8.- Hydrographic cruises.

Cruise Name	Month/Year	Vessel	Reference
4x 1997	08–09/1997	R/V Discovery	Álvarez et al. (2002)
OVIDE 2002	06–07/2002	N/O Thalassa	Lherminier et al. (2007)
OVIDE 2004	06–07/2004	N/O Thalassa	Lherminier et al. (2010)
OVIDE 2006	05–06/2006	R/V Maria S. Merian	Gourcuff et al. (2011)
OVIDE 2008	06–07/2008	N/O Thalassa	Mercier et al. (2015)
OVIDE 2010	06–07/2010	N/O Thalassa	Mercier et al. (2015)

The vertical sections of properties (potential temperature ( $\theta$ ),  $S$ ,  $C_{ANT}$ ) are shown for 2002 and 2010 in Figure 36. They show the gradient of surface properties from cold and fresh waters in the Irminger Sea to warm, salty and  $C_{ANT}$ -rich waters towards Portugal. The strongest surface fronts east of the ESM mark the branches of the NAC (Lherminier et al., 2010). Note however that the penetration of  $C_{ANT}$  in the first 1000 m is comparable in the Irminger Sea and in the Iberian Abyssal Plain (IAP).

At intermediate depth, the minimum of  $S$  that marks LSW is observed from the Greenland slope to the Azores–Biscay Rise. Following Yashayaev et al. (2007b), two vintages of LSW can be distinguished: the upper LSW (uLSW;  $32.32 < \sigma_1 < 32.37$ ), and the classical LSW (cLSW;  $32.40 < \sigma_1 < 32.44$ ). Both varieties of LSW are marked by a relative maximum in  $C_{ANT}$  due to their recent ventilation in the Labrador Sea, although it is much less clear for cLSW in 2010, consistent with the fact that this water mass was not ventilated between 1994 and 2008 (Yashayaev and Loder, 2009).

Deep and bottom waters below LSW have very different properties in the SPNA and in the inter-gyre region. Northwest of the ESM, those waters are rich in overflow waters coming from the Nordic Seas: the Iceland–Scotland Overflow Water (ISOW, below cLSW) and the Denmark Strait Overflow Water (DSOW, below  $\sigma_1 = 32.53$ ; Tanhua et al., 2005). Southeast of the ESM, the deep and bottom waters are rich in Antarctic Bottom Water (AABW), which has not been in contact with the atmosphere for several decades and presents the lowest concentration of  $C_{ANT}$  in the whole section. This distribution creates a horizontal gradient of  $C_{ANT}$  at the bottom, from  $C_{ANT}$ -free waters in the southeast to intermediate  $C_{ANT}$  concentration in overflow waters in the northwest.

Between 2002 and 2010, the concentration of  $C_{ANT}$  increased dramatically over the whole section (Figure 36), except in the AABW-derived waters where the  $C_{ANT}$  concentration is very low. As it will be explained in the results, this increase has a big impact on the variability of the  $T_{C_{ANT}}$  across the section.

All the trends given in the present study were estimated fitting a straight line by means of least squares. Confidence intervals were calculated considering a  $T$  student distribution at the 95%

confidence level. The mean values estimated for a period of time are given with the standard error, i.e.,  $\pm \sigma/\sqrt{N}$ , where N is the number of cruises.

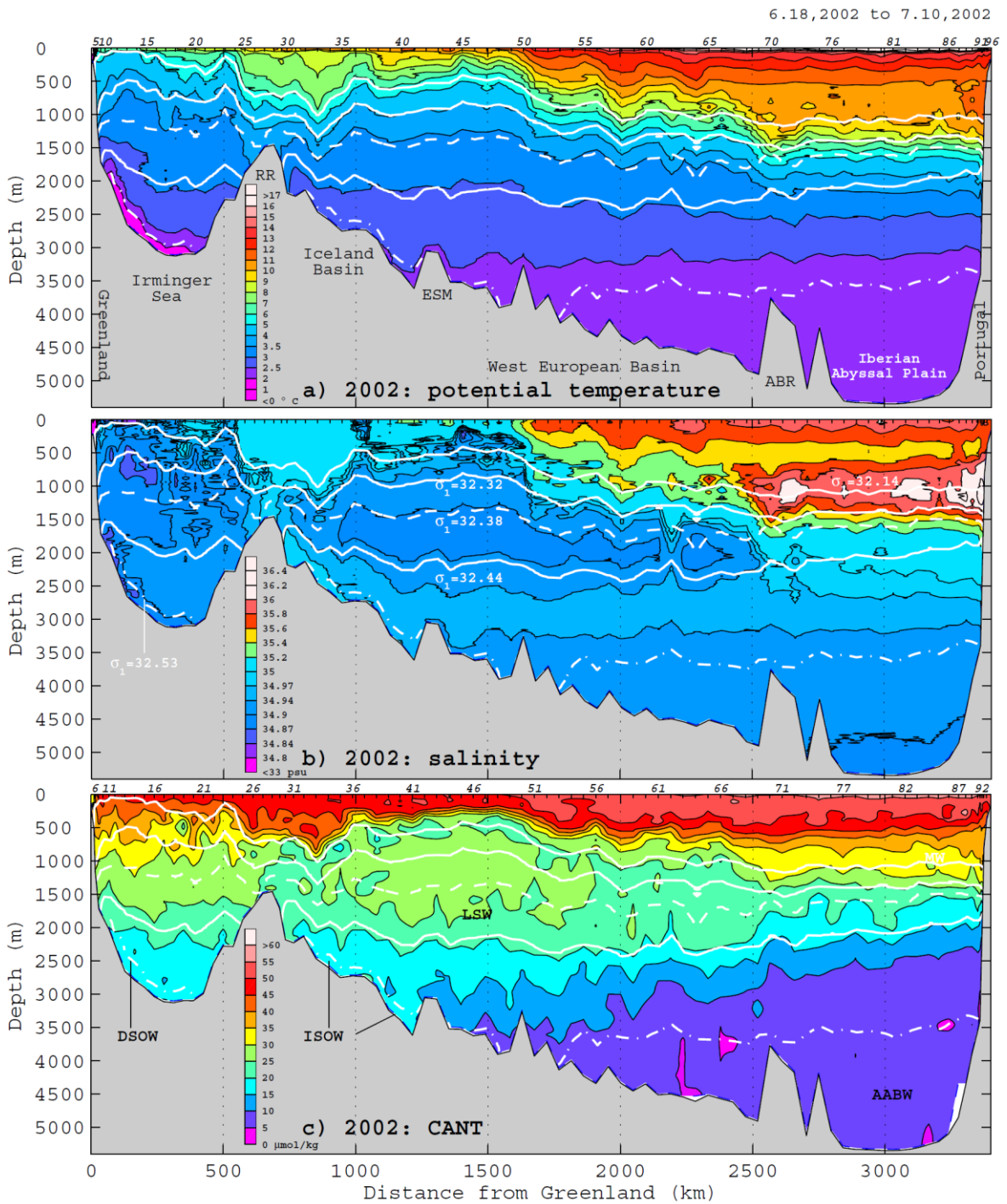


Figure 36.- OVIDE sections of 2002 and 2010 of (a, d) potential temperature in °C, (b, e) salinity and (c, f) anthropogenic CO<sub>2</sub> (CANT) in  $\mu\text{mol}\cdot\text{kg}^{-1}$ . The isopycnals referenced in the chapter are plotted in all the figures; their specific values are indicated in (b) and (e). All the water masses cited in the chapter are localized in the section in (c) and (f): DSOW = Demark Strait Overflow Water, ISOW = Iceland–Scotland Overflow Water, LSW = Labrador Sea Water, MW = Mediterranean Water, AABW = Antarctic Bottom Water. The other abbreviations in (a) and (d) are RR = Reykjanes Ridge, ESM = Eriador Sea Mount and ABR = Azores–Biscay Ridge. The numbers at the top of each plot indicate the station numbers.

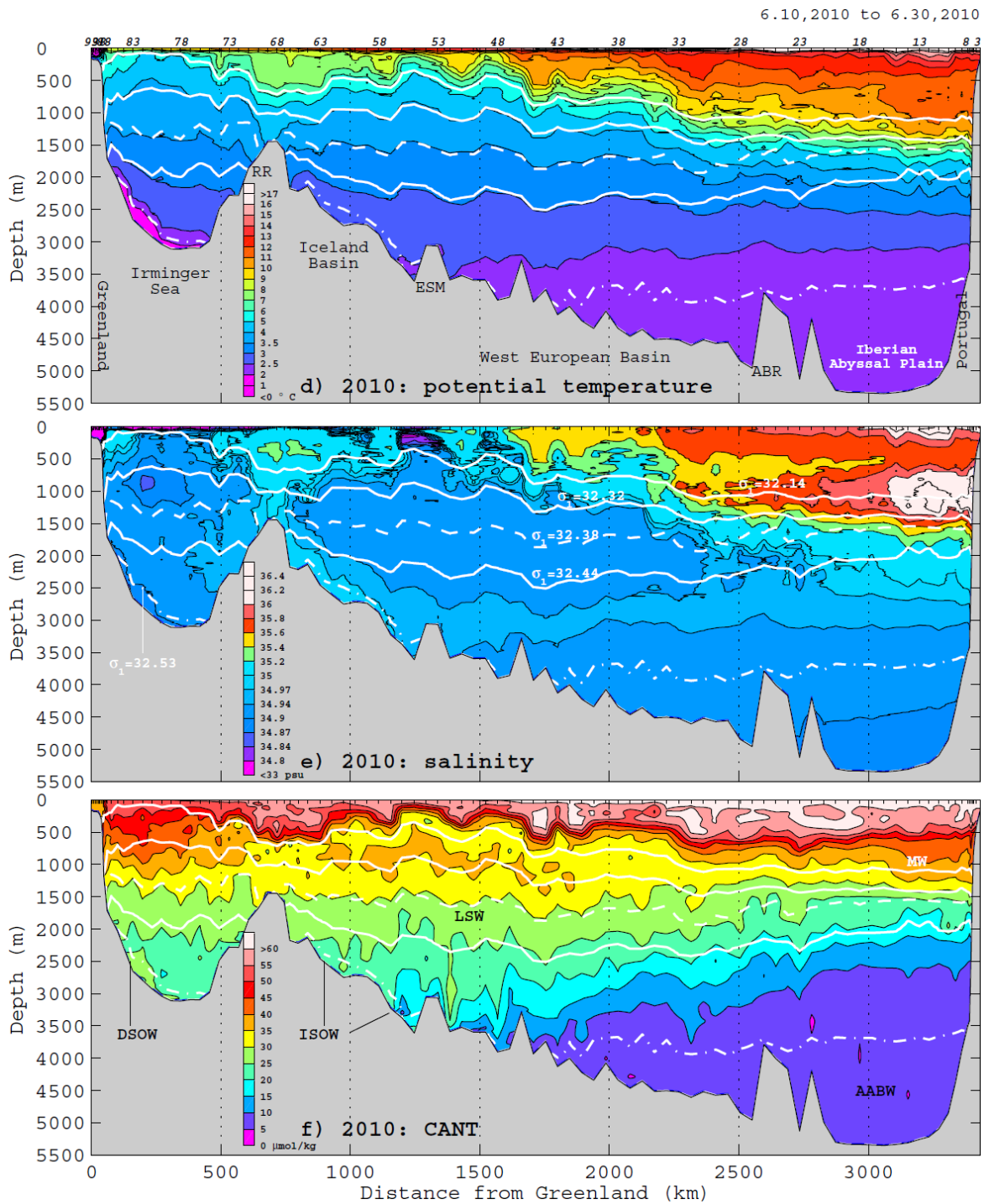


Figure 36.- Continued.

## 6.5.- Method: transport of anthropogenic CO<sub>2</sub> and its decomposition

The transport of any property across the Greenland to Portugal section can be computed as

$$T_{\text{PROP}} = \int_{\text{Greenland bottom}}^{\text{Portugal surface}} \int v \rho [\text{PROP}] dx dz \quad (\text{Eq. 6.1})$$

where  $v$  is the velocity orthogonal to the section,  $\rho$  is the in situ density and  $[\text{PROP}]$  is the concentration of any property. Note that  $x$  is the horizontal coordinate along the section and  $z$  is the vertical coordinate. The error of the transport of any property is calculated taking into account the co-variance matrix of errors of the volume transport obtained from the inverse model; therefore, the errors in the transport of any property come mainly from the volume transport uncertainties.

Understanding the processes by which the ocean transports heat, freshwater and  $C_{\text{ANT}}$  is an important issue in climate modelling. In order to evaluate the elements of the circulation that influence the heat transport across transoceanic sections, several authors, for example Böning and Herrman (1994) or Bryden and Imawaki (2001), suggested the decomposition of heat transport into three components. This methodology has been widely applied for both heat and salt fluxes in the majority of the oceans, but in the case of  $C_{\text{ANT}}$ , it has only been applied by Álvarez et al. (2003). Following the previous authors, for a transoceanic section velocity ( $V$ ), the  $C_{\text{ANT}}$  can be split into

$$V(x, z) = V_0 + \langle v \rangle(z) + v'(x, z) \quad (\text{Eq. 6.2})$$

$$C_{\text{ANT}}(x, z) = \langle C_{\text{ANT}} \rangle(z) + C_{\text{ANT}}'(x, z) \quad (\text{Eq. 6.3})$$

where  $v = V(x, z) - V_0$ ,  $V_0$  representing the section-averaged velocity corresponding to the net transport across the section.  $\langle v \rangle(z)$  is the mean vertical profile of velocity anomalies and  $\langle C_{\text{ANT}} \rangle(z)$  is the mean vertical profile of  $C_{\text{ANT}}$ .  $v'(x, z)$  and  $C_{\text{ANT}}'(x, z)$  are the deviations from the corresponding mean vertical profiles. In the same way the  $T_{C_{\text{ANT}}}$  computed following Eq. (6.1) can be decomposed into three components (Eq. 6.4):

$$T_{C_{\text{ANT}}} = \rho V_0 \overline{\langle C_{\text{ANT}} \rangle(z)} + \rho \overline{\langle v \rangle(z) \langle C_{\text{ANT}} \rangle(z)} + \rho \overline{v'(x, z) C_{\text{ANT}}(x, z)} \quad (\text{Eq. 6.4})$$

where the overbar denotes the area integration.

Álvarez et al. (2003) carried out the decomposition of the  $T_{C_{\text{ANT}}}$  across the 4x section using pressure as vertical coordinate, the same way as heat and salt transport decompositions are usually done. Because of the strong horizontal density gradient and the general circulation patterns across the section, it is preferable to do the decomposition in density coordinates ( $z = \sigma_1$ ). Indeed, along the OVIDE section, the upper and lower limbs of the Meridional Overturning Circulation, namely, the northward NAC and the southward Western Boundary Current (WBC), respectively, overlap in the depth coordinate, while they have nearly distinct density properties. Therefore, when the Meridional Overturning Circulation is computed in a pressure coordinate for the A25

section, its intensity is underestimated (Lherminier et al., 2010; Mercier et al., 2015). Thus, the  $T_{C_{ANT}}$  computation and decomposition should be done in a density coordinates.

It is the very first time that the  $T_{C_{ANT}}$  decomposition exposed in Eq. (6.4) is computed in density coordinates. Regarding the order of the different terms, Eq. (6.4) can be written as

$$T_{C_{ANT}} = T_{C_{ANT}}^{net} + T_{C_{ANT}}^{diap} + T_{C_{ANT}}^{isop} \quad (\text{Eq. 6.5})$$

where

$$T_{C_{ANT}}^{net} = \rho V_0 \overline{\langle C_{ANT} \rangle (\sigma_1)} \quad (\text{Eq. 6.6})$$

$$T_{C_{ANT}}^{diap} = \rho \overline{\langle v \rangle (\sigma_1) \langle C_{ANT} \rangle (\sigma_1)} \quad (\text{Eq. 6.7})$$

$$T_{C_{ANT}}^{isop} = \rho \overline{v'(x, \sigma_1) C_{ANT}'(x, \sigma_1)} \quad (\text{Eq. 6.8})$$

being  $T_{C_{ANT}}^{net}$  the net transport of  $C_{ANT}$  across the section related to a northward transport of about 1 Sv associated with the Arctic mass balance (Lherminier et al., 2007).  $T_{C_{ANT}}^{diap}$  is the transport of  $C_{ANT}$  linked to the diapycnal circulation that accounts for the light to dense water mass conversion north of the section (Grist et al., 2009) related to the overturning circulation. Lastly,  $T_{C_{ANT}}^{isop}$  quantifies the transport of  $C_{ANT}$  due to the isopycnal circulation, i.e., the integration of how  $C_{ANT}$  and transport co-vary in each layer. This term is usually called horizontal circulation when the decomposition is done in pressure coordinates (e.g., Böning and Herrmann, 1994); however, in the present study, it is not the horizontal circulation, since isopycnals present important slopes all along the section (Figure 36).

Using the same methodology as Álvarez et al. (2003) but changing the vertical coordinate from pressure to density, it is expected to find a larger contribution of the overturning component to the total  $T_{C_{ANT}}$  in the same way that the Meridional Overturning Circulation intensity across the section increases when it is computed in density coordinates.

## 6.6.- Results

### 6.6.1.- Transport of anthropogenic CO<sub>2</sub> across the Greenland–Portugal section

The  $T_{C_{ANT}}$  across the Greenland–Portugal section from 1997 to 2010 is shown in Figure 37 (black line). The mean value for the whole period is  $254 \pm 29 \text{ kmol}\cdot\text{s}^{-1}$ . The standard deviation is  $71 \text{ kmol}\cdot\text{s}^{-1}$  (while the errors in each estimate average to  $48 \text{ kmol}\cdot\text{s}^{-1}$ ). Note that a positive  $T_{C_{ANT}}$  value means a northward transport of  $C_{ANT}$  while a negative value points to a southward transport. At the beginning of the period, in 1997, the  $T_{C_{ANT}}$  was  $289 \pm 32 \text{ kmol}\cdot\text{s}^{-1}$ . This value is far off the one estimated by Álvarez et al. (2003;  $116 \pm 126 \text{ kmol}\cdot\text{s}^{-1}$ ). Because both results correspond to the same data, the difference between them comes from the methodology: on the one hand because of the constrains considered for computing the volume transport across the section in Álvarez et al. (2003) and in the present study are different (Lherminier et al., 2007); on the other hand because they did not use the  $\phi C_T^0$  approximation for calculating the  $C_{ANT}$ . Later, Pérez et al. (2013) computed the  $T_{C_{ANT}}$  across the OVIDE section between 2002 and 2006; their mean value for that



period is  $195 \pm 24 \text{ kmol}\cdot\text{s}^{-1}$ . For the same period, in the present study it is obtained a mean value of  $208 \pm 40 \text{ kmol}\cdot\text{s}^{-1}$ , a compatible result considering the error bars.

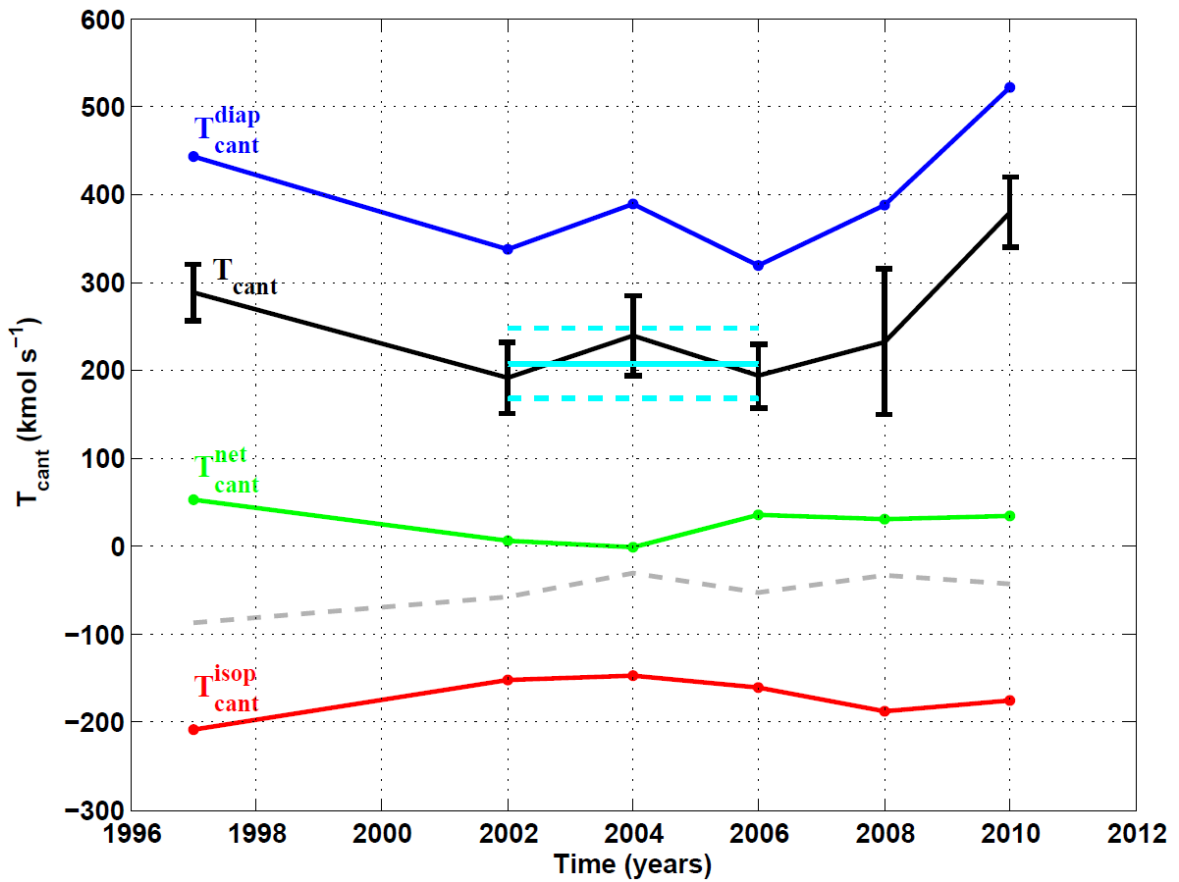


Figure 37.- Transport of anthropogenic CO<sub>2</sub> ( $T_{cant}$ ; in  $\text{kmol}\cdot\text{s}^{-1}$ ) (black) and its components (diapycnal in blue, isopycnal in red and net in green) across the A25 section as a function of time. The dashed grey line is the  $T_{cant}$  due to the Ekman transport, which is dispatched between the other three components. The cyan lines are the mean value (2002–2006) and the error bars of the  $T_{cant}$  representative of the mid-2000s.

The evolution of the  $T_{C_{ANT}}$  between 1997 and 2010 (black line in Figure 37) presents inter-annual variability, with a decrease from 1997 to the mid-2000s (see the mean value for 2002–2006 displayed in cyan in Figure 37) and a recovery thereafter. This  $T_{C_{ANT}}$  recovery and the significant highest value in 2010 ( $380 \pm 64 \text{ kmol}\cdot\text{s}^{-1}$ ) have never been reported before. The trend for the whole period of time is  $4.0 \pm 15.5 \text{ kmol}\cdot\text{s}^{-1}\cdot\text{yr}^{-1}$ . This result is statistically not different from 0 since the inter-annual variability blurs the longer timescale variability, at least over this 14-year period.

### 6.6.2.- Decomposition of the transport of anthropogenic CO<sub>2</sub> across the Greenland–Portugal section

The evolution of each of the  $T_{C_{ANT}}$  components ( $T_{C_{ANT}}^{diap}$ ,  $T_{C_{ANT}}^{isop}$  and  $T_{C_{ANT}}^{net}$ ) are also displayed in Figure 37. The sum of these three components is exactly the total  $C_{ANT}$  flowing across the A25 section. The 1997–2010 mean values of  $T_{C_{ANT}}^{diap}$ ,  $T_{C_{ANT}}^{isop}$  and  $T_{C_{ANT}}^{net}$  are  $400 \pm 29 \text{ kmol}\cdot\text{s}^{-1}$ ,

$-171 \pm 11 \text{ kmol}\cdot\text{s}^{-1}$  and  $26 \pm 9 \text{ kmol}\cdot\text{s}^{-1}$ , respectively. For all the years the  $T_{C_{ANT}}^{\text{diap}}$  is larger than the  $T_{C_{ANT}}$ ; meanwhile, the  $T_{C_{ANT}}^{\text{isop}}$  is always negative. Finally, the net transport is the smallest contribution to the  $T_{C_{ANT}}$  since the net transport of volume across the section is very low, less than 1 Sv, and because the section average  $C_{ANT}$  concentration is around  $26 \mu\text{mol}\cdot\text{kg}^{-1}$ .

By definition, the  $T_{C_{ANT}}^{\text{isop}}$  is the  $T_{C_{ANT}}$  along isopycnals. It is the area integration of the co-variance of the anomalies of volume transport and  $C_{ANT}$  at each station and density level across the section (Eq. 6.8). The  $T_{C_{ANT}}^{\text{isop}}$  shows a non-negligible southward  $T_{C_{ANT}}$  across the A25 section. The result contrasts with the isopycnal transport of heat (Mercier et al., 2015) that has a minor contribution to the total heat flux in the North Atlantic Ocean (Ganachaud and Wunsch, 2003). The spatial distribution of the  $T_{C_{ANT}}^{\text{isop}}$  is analysed to understand the origin of its southward resultant. Figure 38a displays the mean value of the  $T_{C_{ANT}}^{\text{isop}}$  over 1997–2010, accumulated from Greenland to Portugal and from the bottom to each density level. For water denser than  $\sigma_1 = 32.14$  the accumulated  $T_{C_{ANT}}^{\text{isop}}$  is  $-150 \text{ kmol}\cdot\text{s}^{-1}$ , which is the 87% of the total ( $-171 \text{ kmol}\cdot\text{s}^{-1}$ ). It shows that, for the whole section, the  $T_{C_{ANT}}^{\text{isop}}$  occurs mainly in the dense waters. To locate the main region contributing to the  $T_{C_{ANT}}^{\text{isop}}$ , the latter was vertically integrated and horizontally accumulated from Greenland to each station along the section (Figure 38b). The maximum negative value is reached approximately 200 km from Greenland, exactly where the maximum negative value of volume transport is found (Figure 38c). From that point eastwards, a northward  $T_{C_{ANT}}$  caused by the recirculation in the Irminger Sea diminished the total southward  $T_{C_{ANT}}^{\text{isop}}$  in this basin (Figure 38b). In the intermediate and deep waters ( $\sigma_1 > 32.14$ ) east of the Reykjanes Ridge, anomalies of  $C_{ANT}$  in isopycnal layers are quite small, resulting in a weak contribution to the  $T_{C_{ANT}}^{\text{isop}}$  (Figure 38b). Taking into account the whole water column, there is a southward  $T_{C_{ANT}}^{\text{isop}}$  in the WEB (Figure 38b) mainly explained by a northward advection of a negative anomaly of  $C_{ANT}$  in the intermediate layers (Figure 38c). Indeed, the shallow isopycnal layers in the Irminger Sea are richer in  $C_{ANT}$  than the same layers found deeper in the WEB and the IAP (Figure 36). It can then be concluded that southward  $T_{C_{ANT}}$  associated with the  $T_{C_{ANT}}^{\text{isop}}$  mainly occurs in the Irminger Sea. In order to identify the water masses mainly responsible for this transport, the  $T_{C_{ANT}}$  associated with the  $T_{C_{ANT}}^{\text{isop}}$  is horizontally but not vertically integrated (Figure 38d). Two different ranges of densities are identified as the major contributions to the  $T_{C_{ANT}}^{\text{isop}}$ . The lower lobe ( $32.48 < \sigma_1 < 32.55$ ) corresponds to the overflow waters (DSOW and ISOW), while the upper lobe corresponds to the intermediate and surface waters of the Irminger Sea (note the shallow position of  $\sigma_1 = 32.14$  in the Irminger Sea; Figure 36). In this basin, the waters corresponding to the density range of both lobes contain high concentrations of  $C_{ANT}$  (Figure 36) due to their recent formation and/or ventilation. To summarize, the southward resultant of the  $T_{C_{ANT}}^{\text{isop}}$  is mainly localized in the Irminger Sea where the southward  $T_{C_{ANT}}$  caused by the WBC is partially compensated by the northward transport caused by the inner recirculation in this basin. Concerning water masses, only LSW has a minor contribution to the  $T_{C_{ANT}}^{\text{isop}}$ ; it will be discussed further in Section 6.7.

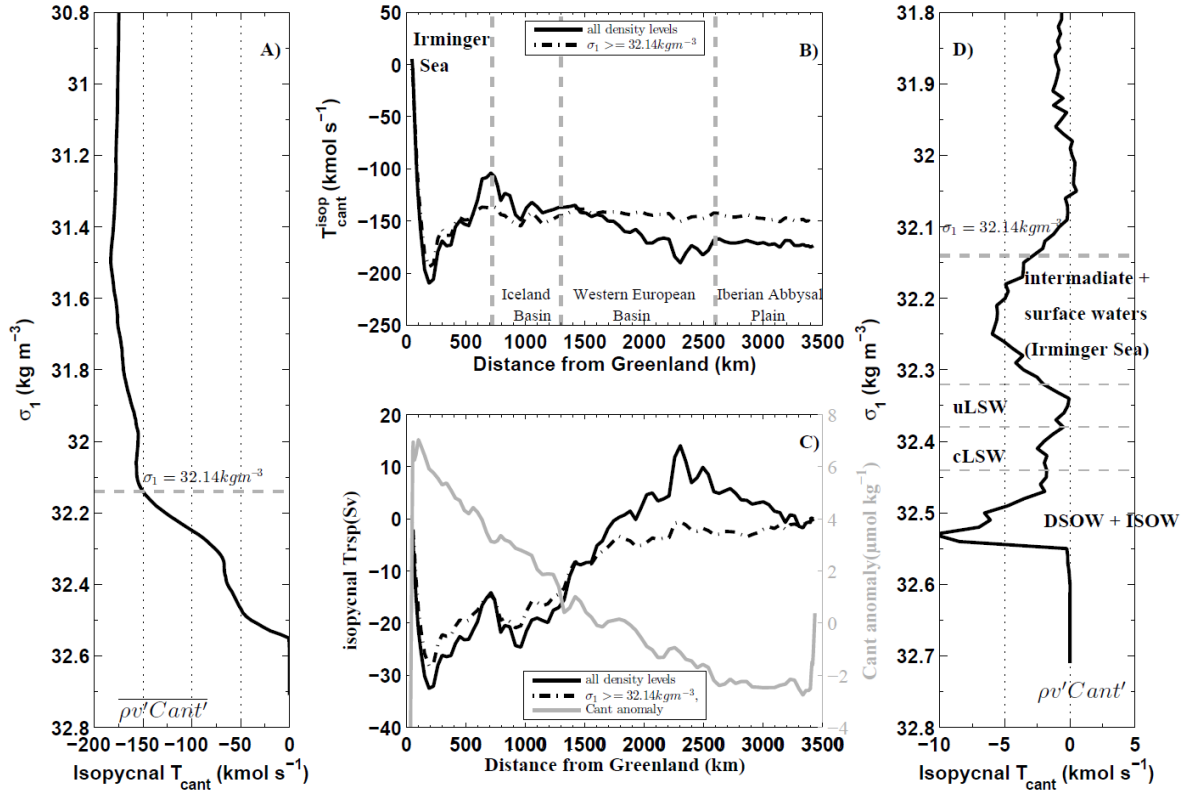


Figure 38.- Transport of anthropogenic CO<sub>2</sub> (Cant) caused by the isopycnal component ( $T_{cant}^{isop}$ ) averaged over time. (A) The  $T_{cant}^{isop}$  (in  $\text{kmol s}^{-1}$ ) accumulated from the bottom to each specific density level. (B) The  $T_{cant}^{isop}$  horizontally accumulated from Greenland to each station along the section, and vertically integrated for the whole water column (continuous line) and for waters denser than  $\sigma_1 = 32.14$  (dashed line). (C) On the left axis: isopycnal volume transport (in Sv; where  $1 \text{ Sv} = 10^6 \text{ m}^3 \cdot \text{s}^{-1}$ ) accumulated from Greenland to each station, and vertically integrated for the whole water column (continuous black line) and for waters denser than  $\sigma_1 = 32.14$  (dashed black line). On the right axis: mean value of Cant anomalies vertically averaged all along the section (grey line; in  $\mu\text{mol} \cdot \text{kg}^{-1}$ ). (D) The  $T_{cant}^{isop}$  horizontally but not vertically integrated (see Figure 35 for the abbreviations). Note that in plots (A) and (D) the vertical axes do not have the same scale.

The  $T_{CANT}$  across isopycnals, which is the  $T_{CANT}^{diap}$  (Eq. 6.7), is decomposed in terms of mean profiles of anomalies of volume transport (Figure 39a) and  $C_{ANT}$  concentration (Figure 39b) computed in isopycnal layers (with a resolution of  $0.01 \text{ kg} \cdot \text{m}^{-3}$ ). The upper and lower limbs of the MOC $\sigma$  can be identified in Figure 39a, with northward (southward) volume transports above (below)  $\sigma_{MOC}$ . The vertical profile of  $C_{ANT}$  concentration averaged in density layers (Figure 39b) shows, as expected, decreasing  $C_{ANT}$  concentration when increasing depth. The profile of  $T_{CANT}$  (Figure 39c) follows perfectly the vertical profile of volume transport. The vertical integration of the diapycnal component of the volume transport (Figure 39a) is equal to 0 Sv. However, because the  $C_{ANT}$  concentration is larger in the upper limb of the MOC $\sigma$  than in the lower one (Figure 39b), the  $T_{CANT}^{diap}$  results in a strong positive value once vertically integrated (Figure 37).

The Ekman transport has been estimated separately from wind stress data averaged over the months of the cruises (Mercier et al., 2015) and equally distributed in the first 30 m. After that, it has been added to the absolute geostrophic velocity across the section and analysed together. It has not been considered as the fourth element of the circulation because it is

dispatched between the  $T_{C_{ANT}}^{diap}$ ,  $T_{C_{ANT}}^{isop}$  and  $T_{C_{ANT}}^{net}$  components. Nevertheless, it is worth mentioning that the Ekman transport causes a southward  $T_{C_{ANT}}$  (dashed grey line in Figure 37), whose mean value is  $-50 \pm 8 \text{ kmol}\cdot\text{s}^{-1}$  and its standard deviation is  $21 \text{ kmol}\cdot\text{s}^{-1}$ .

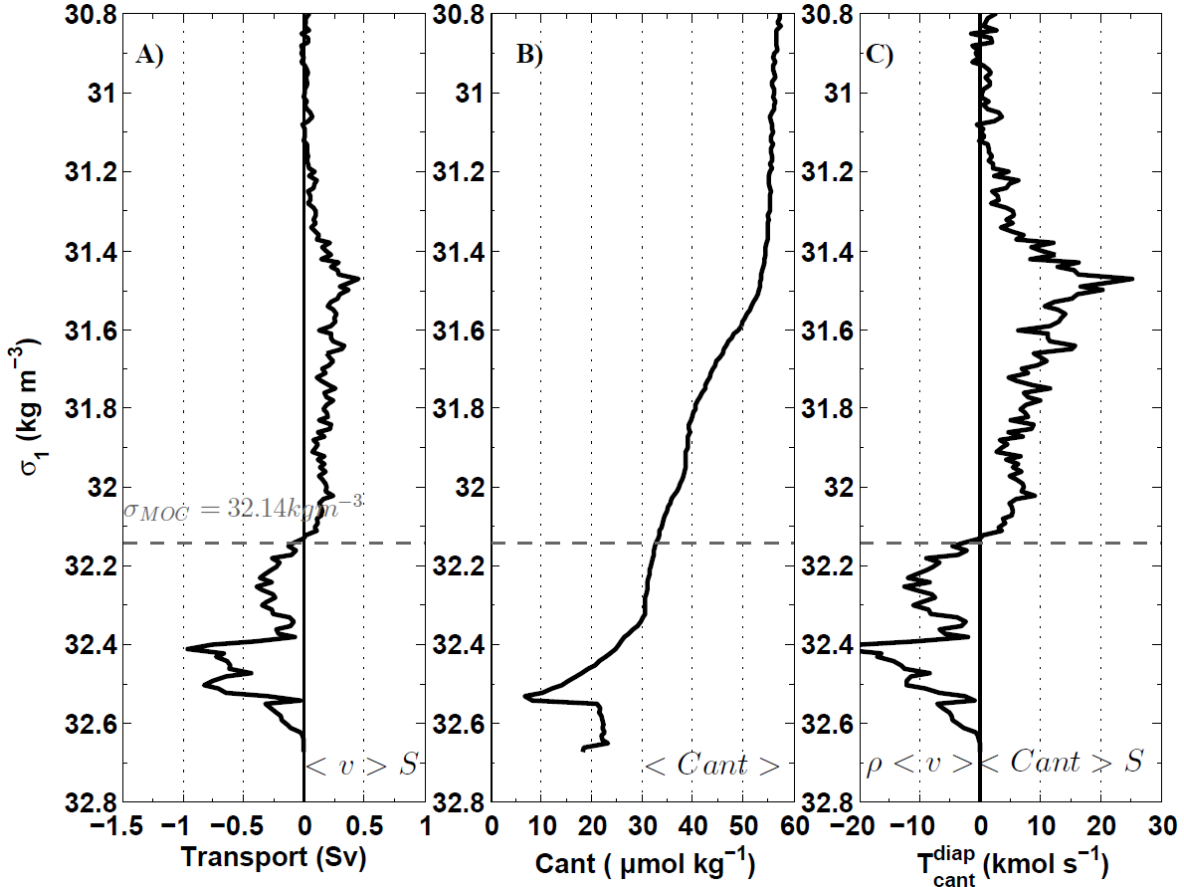


Figure 39.- The diapycnal component of the transport of anthropogenic CO<sub>2</sub> ( $T_{cant}^{diap}$ ) and the different elements by which it was computed (see Eq. 6.7). (A) Profile of anomalies of volume transport (in Sv) integrated into density ( $\sigma_1$ ) layers with a  $0.01 \text{ kg}\cdot\text{m}^{-3}$  resolution. (B) Mean profile of anthropogenic CO<sub>2</sub> (Cant; in  $\mu\text{mol}\cdot\text{kg}^{-1}$ ) averaged at each density layer. (C)  $T_{cant}^{diap}$  profile (in  $\text{kmol}\cdot\text{s}^{-1}$ ). All the data represented in this figure are the averages of the six surveys analysed in the present study. In the formulation, S means the area of each density layer along the section and replaces the overbar given in Eq. (6.7), since there is no vertical integration in the data displayed in the figure.

### 6.6.3.- Variability of the transport of anthropogenic CO<sub>2</sub>

In this part of the chapter, the variability of the  $T_{C_{ANT}}$  across the OVIDE section is analysed. It is expected that changes in both the circulation and the  $C_{ANT}$  concentration of water masses have a certain influence on the variability of the  $T_{C_{ANT}}$ . In the previous section the  $T_{C_{ANT}}$  was decomposed into three different elements of the ocean circulation. In this section it is going to be evaluated which elements of the circulation have a major influence on the variability of the  $T_{C_{ANT}}$  and whether the  $C_{ANT}$  increase in the water masses affects the variability of the  $T_{C_{ANT}}$ .

### 6.6.3.1.- Variability of the components of the $T_{C_{ANT}}$

The variability of the  $T_{C_{ANT}}$  and the  $T_{C_{ANT}}^{diap}$  (black and blue lines in Figure 37, respectively) is very well correlated ( $r^2 = 0.99$ ; p-value  $< 0.01$ ). By contrast, the  $T_{C_{ANT}}^{isop}$  presents a small variability that is not correlated with the  $T_{C_{ANT}}$  ( $r^2 = 0.44$ ; p-value = 0.38), and the same is true for the  $T_{C_{ANT}}^{net}$  ( $r^2 = 0.40$ ; p-value = 0.43). Therefore, the  $T_{C_{ANT}}^{diap}$  mainly drives the variability of the  $T_{C_{ANT}}$ .

In terms of volume transport, the  $T_{C_{ANT}}^{diap}$  is directly related to the  $MOC\sigma$ . Pérez et al. (2013) suggested that the weakening of the lateral advection of  $C_{ANT}$  between 1997 and 2006, caused by the slow-down of the  $MOC\sigma$ , is responsible for the decrease in the  $C_{ANT}$  storage rate during that period. However, during the period of time studied in this work (1997–2010), the  $MOC\sigma$  intensity (Figure 40a) is correlated neither with the  $T_{C_{ANT}}$  ( $r^2 = 0.58$ , p-value = 0.23) nor with the  $T_{C_{ANT}}^{diap}$  ( $r^2 = 0.68$ , p-value = 0.13). These results suggest that, although the diapycnal circulation is related to the  $MOC\sigma$ , in the case of the  $T_{C_{ANT}}$  there is another factor acting on the variability of the  $T_{C_{ANT}}^{diap}$ . It is very likely that the  $C_{ANT}$  concentration change is the other factor controlling the variability of the  $T_{C_{ANT}}^{diap}$ , and thus the variability of the  $T_{C_{ANT}}$ .

### 6.6.3.2.- A simplified estimator for the variability of the $T_{C_{ANT}}$

The overturning circulation has been identified as the component of the circulation mainly driving the heat flux variability across the subpolar gyre (Mercier et al., 2015). After defining the  $MOC\sigma$  as the maximum of the transport streamfunction computed in density coordinates, these authors approximated the heat transport variability across the OVIDE section, taking into account the temperature difference between the upper and lower limbs of the  $MOC\sigma$  and the intensity of the  $MOC\sigma$ . This method applied to the  $T_{C_{ANT}}$  could help to clarify the effect of both the circulation changes and the  $C_{ANT}$  increase on the variability of the  $T_{C_{ANT}}$ . Therefore the following estimator is proposed:

$$T_{C_{ANT}}^0 = \Delta C_{ANT} \cdot \rho \cdot MOC\sigma$$

where  $\Delta C_{ANT}$  is the difference between the mean value of  $C_{ANT}$  in the upper and lower limbs of the  $MOC\sigma$ ,  $\rho$  is the in situ density and  $MOC\sigma$  is the intensity of the Meridional Overturning Circulation computed in density coordinates (Mercier et al., 2015). The time evolution of  $MOC\sigma$  and  $\Delta C_{ANT}$  is shown in Figure 40a.

It is expected the estimator  $T_{C_{ANT}}^0$  to be a good approximation of the  $T_{C_{ANT}}^{diap}$  because it takes into account the diapycnal circulation via the  $MOC\sigma$  intensity and not the isopycnal component of the circulation. Furthermore, by using the difference in the  $C_{ANT}$  concentration between both limbs of the  $MOC\sigma$ , the  $C_{ANT}$  increase in the waters flowing through the A25 section is taken into account, which is expected to have an important role in the variability of the  $T_{C_{ANT}}^{diap}$ . As a matter of fact, the estimator  $T_{C_{ANT}}^0$  is quite similar to the  $T_{C_{ANT}}^{diap}$  (blue and cyan lines in Figure 40b) and they are well correlated ( $r^2 = 0.82$ , p-value = 0.04).

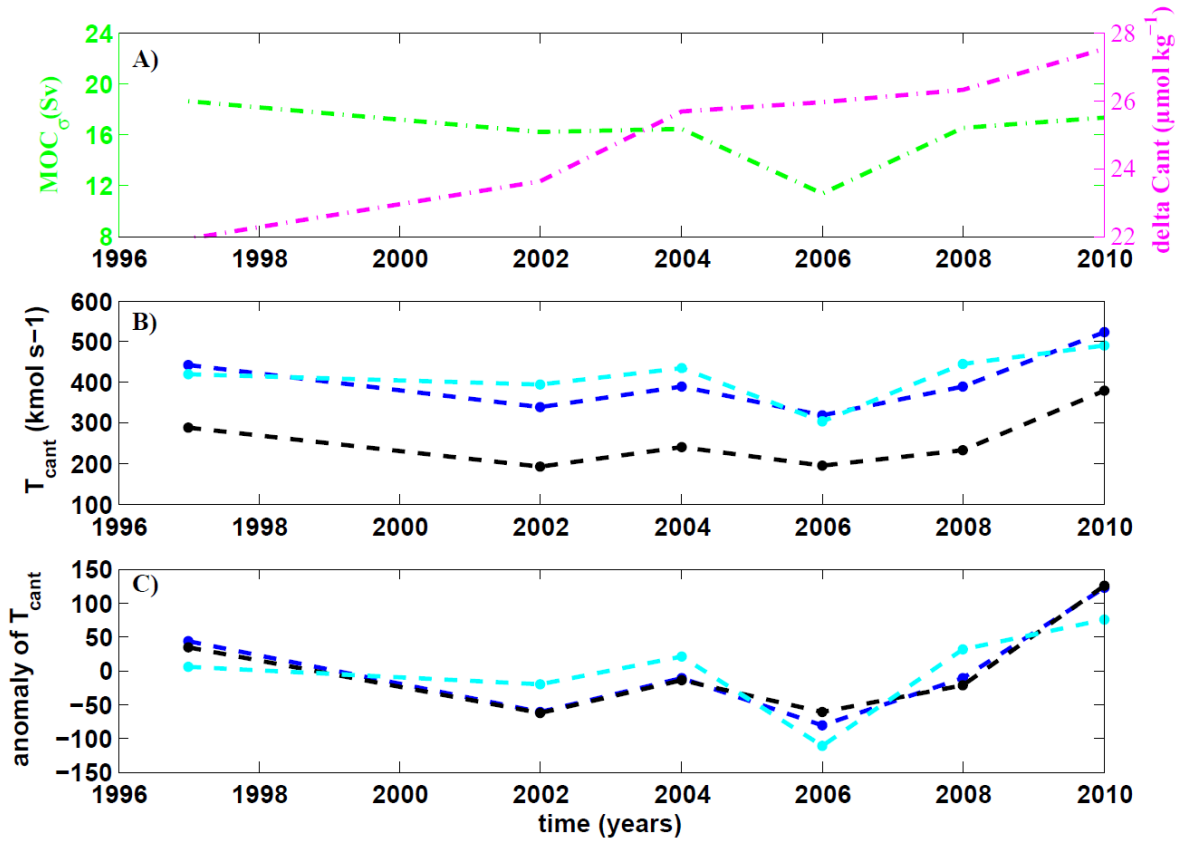


Figure 40.- (A) Time evolution of the intensity of the Meridional Overturning Circulation computed in density coordinates ( $MOC_{\sigma}$ , in green; in Sv) and the difference in anthropogenic CO<sub>2</sub> (Cant) between the upper and lower limbs of the  $MOC_{\sigma}$  (delta Cant, in pink; in  $\mu\text{mol}\cdot\text{kg}^{-1}$ ). (B) Time evolution of the transport of Cant ( $T_{\text{cant}}$ ; black line), the diapycnal transport of Cant ( $T_{\text{CANT}}^{\text{diap}}$ ; blue line) and the  $T_{\text{cant}}$  computed by the estimator ( $T_{\text{CANT}}^0$ ; cyan line) (all in  $\text{kmol}\cdot\text{s}^{-1}$ ). (C) Time evolution of anomalies of the  $T_{\text{cant}}$  (black line), the  $T_{\text{CANT}}^{\text{diap}}$  (blue line), the  $T_{\text{CANT}}^0$  (cyan line) in relation to the mean value computed over 1997–2010 (all in  $\text{kmol}\cdot\text{s}^{-1}$ ).

To compare their variability, the anomalies of the  $T_{\text{CANT}}$ , the  $T_{\text{CANT}}^{\text{diap}}$  and the  $T_{\text{CANT}}^0$  time series are plotted in Figure 40c. Although similar patterns between the  $T_{\text{CANT}}$  and the  $T_{\text{CANT}}^0$  anomalies can be distinguished by eye, their correlation ( $r^2 = 0.75$ ,  $p\text{-value} = 0.09$ ) is not as good as between the  $T_{\text{CANT}}^{\text{diap}}$  and the  $T_{\text{CANT}}^0$  since the estimator does not consider the isopycnal contribution.

In conclusion, the  $T_{\text{CANT}}$  cannot be totally inferred from the proposed estimator  $T_{\text{CANT}}^0$  since the isopycnal component has a non-negligible contribution, but it is a good estimation of the  $T_{\text{CANT}}^{\text{diap}}$ . As the  $T_{\text{CANT}}^{\text{diap}}$  mainly drives the variability of the  $T_{\text{CANT}}$  across the A25 section, the proposed estimator  $T_{\text{CANT}}^0$  is, at least, a fairly good indicator of the variability of the  $T_{\text{CANT}}$  across the section. Moreover, it will help to disentangle the relative contribution of the circulation and the  $C_{\text{ANT}}$  increase in the variability of the  $T_{\text{CANT}}$ .

### 6.6.3.3.- The effect of the anthropogenic CO<sub>2</sub> concentration changes on the variability of the $T_{C_{ANT}}$

In the A25 section during the period 1997–2010, the section-average  $C_{ANT}$  concentration increased at a rate of  $0.29 \pm 0.21 \mu\text{mol}\cdot\text{kg}^{-1}\cdot\text{yr}^{-1}$ , which means an increase of  $4 \mu\text{mol}\cdot\text{kg}^{-1}$  between 1997 and 2010. The  $C_{ANT}$  increase in the upper limb of the MOC $\sigma$ , which imports  $C_{ANT}$  into the subpolar region, is larger than the increase in the lower limb of the MOC $\sigma$ , which exports  $C_{ANT}$  from the subpolar region:  $0.63 \pm 0.27 \mu\text{mol}\cdot\text{kg}^{-1}\cdot\text{yr}^{-1}$  and  $0.20 \pm 0.25 \mu\text{mol}\cdot\text{kg}^{-1}\cdot\text{yr}^{-1}$ , respectively (Figure 41).

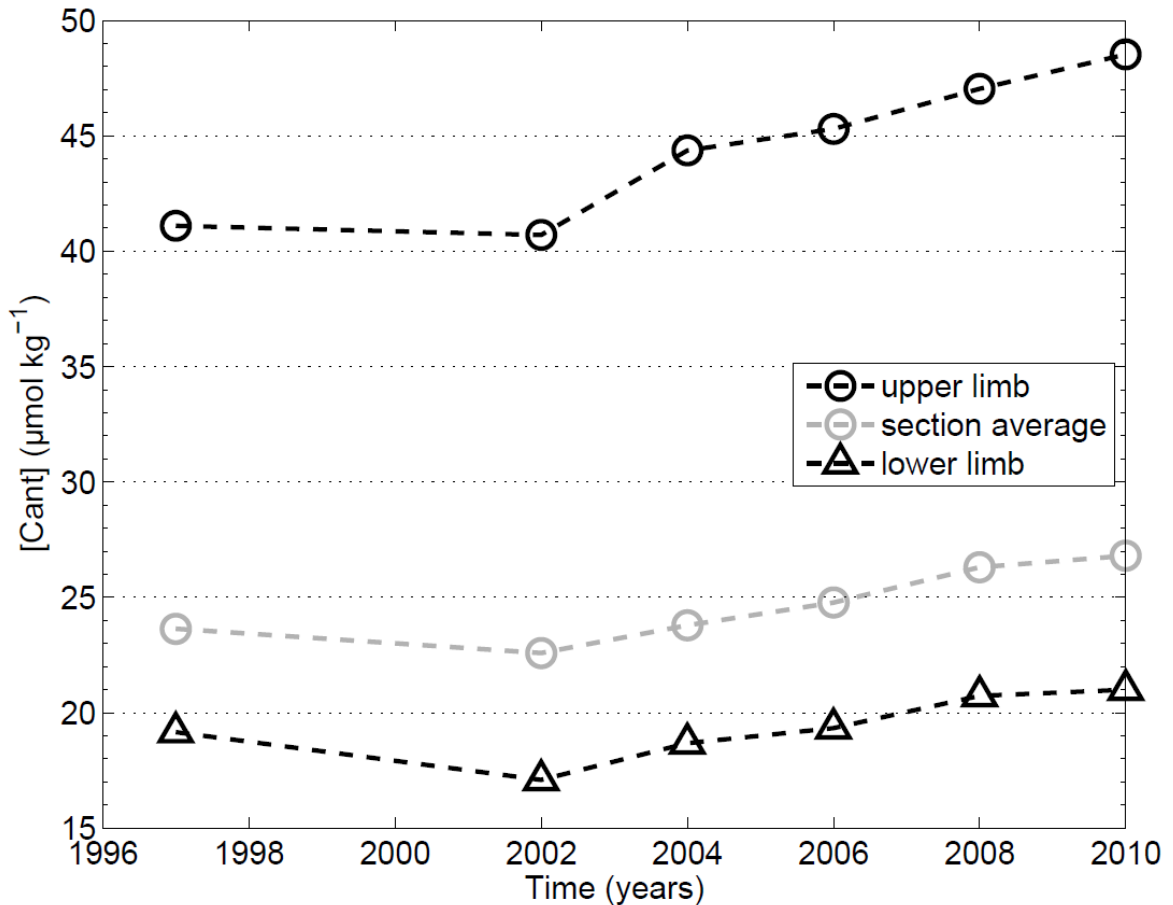


Figure 41.- Time evolution of anthropogenic CO<sub>2</sub> ( $C_{ANT}$ ) concentrations (in  $\mu\text{mol}\cdot\text{kg}^{-1}$ ): upper limb of the Meridional Overturning Circulation computed in density coordinates (MOC $\sigma$ ; black circles), section average value (grey circles), and lower limb of the MOC $\sigma$  (triangles).

In the previous section the estimator  $T_{C_{ANT}}^0$  was presented, which is a good indicator of the variability of the  $T_{C_{ANT}}$  across the A25 section. Using this estimator, if a steady circulation hypothesis is considered (MOC $\sigma$  constant, e.g., 16 Sv), the  $T_{C_{ANT}}^0$  increases at a rate of  $7.0 \pm 1.6 \text{ kmol}\cdot\text{s}^{-1}\cdot\text{yr}^{-1}$ . It means that the  $C_{ANT}$  increase in the ocean waters yields an increase in the northward  $T_{C_{ANT}}$  across the A25 section. However, the overturning circulation has an important role in the variability of the  $T_{C_{ANT}}$ , and it introduces a larger variability than the  $C_{ANT}$  increase at inter-annual timescale. This is why the “real” trend estimated for the  $T_{C_{ANT}}$  for the period 1997–2010 is positive but not statistically different from 0.



To assess the relative role of the  $C_{ANT}$  concentration and circulation in the  $T_{C_{ANT}}$  and to compare it with the analysis of Pérez et al. (2013), the period between 1997 and 2006 is studied. During that period, the  $MOC\sigma$  intensity across the OVIDE section decreased (Mercier et al., 2015) at a rate of  $0.68 \pm 0.65 \text{ Sv}\cdot\text{yr}^{-1}$ . Simultaneously, the  $T_{C_{ANT}}$  decreased at a rate of  $9.3 \pm 11.7 \text{ kmol}\cdot\text{s}^{-1}\cdot\text{yr}^{-1}$ , while the  $C_{ANT}$  concentration increased at a rate of  $0.48 \pm 0.56 \mu\text{mol}\cdot\text{kg}^{-1}\cdot\text{yr}^{-1}$  and  $0.01 \pm 0.42 \mu\text{mol}\cdot\text{kg}^{-1}\cdot\text{yr}^{-1}$  in the upper and lower limbs of the  $MOC\sigma$ , respectively. All these trends are not statistically different from 0, likely due to the low number of data, only 4, but they give insights that the  $C_{ANT}$  concentration increased in the upper limb of the  $MOC\sigma$ ; meanwhile it hardly changed in the lower limb. Taking into account these results it can be concluded that, in the period between 1997 and 2006, the  $MOC\sigma$  decrease prevailed on the variability of the  $T_{C_{ANT}}$ . Indeed, using the proposed estimator  $T_{C_{ANT}}^0$ , if a steady circulation was considered, the  $T_{C_{ANT}}$  would increase at a rate of  $7.8 \pm 3.2 \text{ kmol}\cdot\text{s}^{-1}\cdot\text{yr}^{-1}$  during the period 1997–2006. However, if the  $C_{ANT}$  concentration is maintained constant between 1997 and 2006, the  $T_{C_{ANT}}$  would decrease at a rate of  $15.3 \pm 14.6 \text{ kmol}\cdot\text{s}^{-1}\cdot\text{yr}^{-1}$ , that is, the slow-down of the  $MOC\sigma$  would cause a decrease in the  $T_{C_{ANT}}$  statistically different from 0.

Over the whole studied period, 1997–2010, the trends in the  $T_{C_{ANT}}$  and the  $T_{C_{ANT}}^0$  are not significant. In the hypothetical case of a steady circulation, the  $T_{C_{ANT}}^0$  increases at a rate of  $7.0 \pm 1.6 \text{ kmol}\cdot\text{s}^{-1}\cdot\text{yr}^{-1}$  since the  $\Delta C_{ANT}$  is continuously increasing. Conversely, if the  $\Delta C_{ANT}$  remains constant, the variability of the  $T_{C_{ANT}}^0$  follows the variability of the  $MOC\sigma$  with no trend.

All these results suggest that, at inter-annual to decadal timescales, the variability of the  $MOC\sigma$  mainly drives the variability of the  $T_{C_{ANT}}$  across the OVIDE section. Nonetheless, the  $C_{ANT}$  increase also causes a long-term increase in the  $T_{C_{ANT}}$  that, at the timescale analysed here, is blurred by the inter-annual variability caused by the variability of the  $MOC\sigma$ .

## 6.7.- Discussion and conclusions

The continuous increase in CO<sub>2</sub> concentration in the atmosphere due to human activities is softened by the oceanic CO<sub>2</sub> uptake. The question is how long the ocean will act as a sink for this greenhouse gas. Therefore, it is really important to quantify and understand the mechanisms acting in its transport and storage in the oceans. It is well-known that the North Atlantic Ocean presents the highest storage rate of  $C_{ANT}$  of the global oceans, mainly in the SPNA (Sabine et al., 2004). Recently, it has been demonstrated that the lateral advection provides the main supply of  $C_{ANT}$  to the SPNA (Pérez et al., 2013). In the last decade, the estimations of the  $T_{C_{ANT}}$  by observational data and models have yielded quite different results: models tend to show lower values than data (Table 7). The present study have been focused in the physical aspect of the  $T_{C_{ANT}}$  in order to understand the mechanisms driving the  $T_{C_{ANT}}$  across the SPNA and to describe for the first time its inter-annual to decadal variability.

In agreement with previous works (Álvarez et al., 2003; Pérez et al., 2013), a northward  $T_{C_{ANT}}$  across the section was obtained. The mean value for the period 1997–2010 is  $254 \pm 29 \text{ kmol}\cdot\text{s}^{-1}$ ; its standard deviation is  $71 \text{ kmol}\cdot\text{s}^{-1}$ . No significant long-term changes have been identified during this period, due to the clear decrease between 1997 and the mid-2000s (cyan

values in Figure 37) and the recover thereafter. The initial decrease was due to the slow-down of the MOC and the increase that follows was mainly due to the increase in the  $C_{ANT}$  concentration in the ocean waters.

Splitting the  $T_{C_{ANT}}$  into its different components, it has been observed that the  $T_{C_{ANT}}^{isop}$  causes a non-negligible southward transport (Figure 37), mainly localized in the Irminger Sea (Figure 38). It contrasts with the heat fluxes across the North Atlantic Ocean, for which the  $T_{C_{ANT}}^{isop}$  has a minor contribution to the total heat flux (Ganachaud and Wunsch, 2003); across the A25 section specifically, the isopycnal heat flux accounts for less than 10% of the total heat flux (Mercier et al., 2015). The different behaviour between the  $T_{C_{ANT}}$  and the heat fluxes across the A25 section is due to the differences in the horizontal gradient of  $C_{ANT}$  and temperature: the  $C_{ANT}$  markedly decreases eastwards due to the age of the water masses; meanwhile the temperature presents a subtle increase (Figure 36). As a result, high positive anomalies of  $C_{ANT}$  are found in the Irminger Sea, while the temperature anomalies are close to 0°C. Therefore, the isopycnal contribution is more important in the  $T_{C_{ANT}}$  than in the heat flux.

To go further in the analysis of the  $T_{C_{ANT}}^{isop}$  in the Irminger Sea, it is found that the overflow waters (DSOW and ISOW) and the intermediate and surface waters are mainly responsible for the southward transport (Figure 38d). The fact that intermediate and surface waters of the Irminger Sea have a high contribution to the  $T_{C_{ANT}}^{isop}$  is because their high  $C_{ANT}$  concentration as compared to the waters with the same density range in the WEB and the IAP as for example Mediterranean Water (Figure 36). The high  $C_{ANT}$  content in the intermediate waters of the Irminger Sea is likely due to the recent ventilation of these waters. Indeed, Våge et al. (2009) observed a 700 m-deep mixed layer in winter 2007–2008. In the case of the overflow waters, the relatively high  $C_{ANT}$  concentration is mainly due to the entrainment of  $C_{ANT}$ -rich thermocline water at the sills during the process of overflow (Sarafanov et al., 2010).

Once the water masses mainly responsible for the  $T_{C_{ANT}}^{isop}$  have been identified, the question is: why does LSW, both upper and classical, yield a minor contribution to the  $T_{C_{ANT}}^{isop}$  (Figure 38)? The answer is likely related to changes in the formation rate of these water masses and their spreading all along the A25 section. On the one hand, during the first half of the 1990s, cLSW was abundantly formed in the Labrador Sea (Rhein et al., 2002), so it was enriched in  $C_{ANT}$ . In the mid-1990s there was a shut-down in the formation of this water mass that was compensated by an enhanced production of uLSW in the Labrador Sea and possibly in the Irminger Sea (Kieke et al., 2007; Yashayaev et al., 2007b; Rhein et al., 2011). Thenceforth, cLSW was exported to the Irminger Sea and northeast Atlantic, taking between 6 months (Sy et al., 1997) to 2 years (Straneo et al., 2003) to reach the Irminger Sea and 3–6 years to get to the Mid-Atlantic Ridge (Kieke et al., 2009). Because of this spreading, cLSW was homogenized all along the A25 section, resulting in small  $C_{ANT}$  anomalies. On the other hand, the evolution of the  $T_{C_{ANT}}^{isop}$  in the uLSW density range during the period 1997–2010 displays more temporal variability (not shown), probably due to the intermittent ventilation of this water mass over the 2000s and to the advection timescales that are comparable to those of cLSW. However, the average of the  $T_{C_{ANT}}^{isop}$  in the density range of uLSW for the 1997–2010 period is close to zero; this is why a minor

contribution of uLSW to the  $T_{C_{ANT}}^{isop}$  is identified, and a more detailed analysis of its variability is out of the scope of this study.

The decomposition of the  $T_{C_{ANT}}$  also shows that the overturning component ( $T_{C_{ANT}}^{diap}$ ) is the major contribution to the  $T_{C_{ANT}}$ , whose mean value over the period 1997–2010 is  $400 \pm 29 \text{ kmol}\cdot\text{s}^{-1}$ . Moreover, as in the case of the heat flux, it drives the variability of the  $T_{C_{ANT}}$ . The  $T_{C_{ANT}}^{diap}$  is related to the MOC $\sigma$  that transports warm and  $C_{ANT}$ -enriched waters northwards in its upper limb and denser, colder and poorer in  $C_{ANT}$  waters southwards in its lower limb. The estimator  $T_{C_{ANT}}^0$  is a schematic representation of this mechanism and indeed a good correlation between the  $T_{C_{ANT}}^0$  and the  $T_{C_{ANT}}^{diap}$  is found. It also offers a simple proxy for testing numerical models. However, the  $T_{C_{ANT}}^0$  does not represent all the processes involved in the  $T_{C_{ANT}}$  in the SPNA.

It is well known that the MOC $\sigma$  presents a high seasonal variability. For example, Mercier et al. (2015) showed that it has a seasonal amplitude of 4.3 Sv. The data analysed in the present study were measured during summer months. Mercier et al. (2015) show that the MOC $\sigma$  at the A25 section presents its yearly minimum in summer, but their results also show that the inter-annual variability of the MOC $\sigma$  can be reliably represented by summer data. Therefore, it is expected that the inter-annual variability of the  $T_{C_{ANT}}$  will be well captured in the present study, although the magnitudes here given are likely to be weaker than the annual means.

The  $T_{C_{ANT}}^0$  was used to get an order of magnitude of the relative importance of the  $C_{ANT}$  content and the circulation on the  $T_{C_{ANT}}$  across the SPNA at long timescales. On the one hand, the  $C_{ANT}$  concentration is increasing faster in the upper limb of the MOC $\sigma$  than in the lower limb, showing trends of  $0.63 \pm 0.27 \text{ }\mu\text{mol}\cdot\text{kg}^{-1}\cdot\text{yr}^{-1}$  and  $0.20 \pm 0.25 \text{ }\mu\text{mol}\cdot\text{kg}^{-1}\cdot\text{yr}^{-1}$ , respectively, during the period 1997–2010. It means that, in the SPNA, there is more  $C_{ANT}$  being imported in the upper limb than being exported in the lower limb, resulting in an accumulation of  $C_{ANT}$ , in agreement with Sabine et al. (2004) and Pérez et al. (2010). The minor increase in the  $C_{ANT}$  concentration in the lower limb is due to the dilution of the convected and overflow waters rich in  $C_{ANT}$  with the deep waters poor in  $C_{ANT}$ . It is expected that the  $C_{ANT}$  concentration in both limbs will be linked to the variability of the MOC $\sigma$ , although at which timescale remains unknown. Indeed, it depends on the advection of waters from the subtropical areas in the upper limb, and on the processes of deep and intermediate water formation in the lower limb. However, it is striking that the  $\Delta C_{ANT}$  keeps increasing independently of the variability of the MOC $\sigma$  at a mean rate of  $0.43 \pm 0.10 \text{ }\mu\text{mol}\cdot\text{kg}^{-1}\cdot\text{yr}^{-1}$  (pink line in Figure 40a). This increasing rate is going to cause an augmentation in the  $T_{C_{ANT}}$  across the A25 section, and consequently, an increase in the storage rate in the SPNA. On the other hand, models have predicted a slow-down of 25% of the MOC $\sigma$  at the end of the present century (IPCC, 2007) independently of the inter-annual to decadal variability observed by Mercier et al. (2015). Taking into account the predicted slow-down of the MOC $\sigma$  and the positive trend of the  $\Delta C_{ANT}$  computed in this work, the  $T_{C_{ANT}}^0$  would increase at a rate of  $4.3 \pm 0.1 \text{ kmol}\cdot\text{s}^{-1}\cdot\text{yr}^{-1}$  during the 21st century. It means an increase of  $430 \text{ kmol}\cdot\text{s}^{-1}$  of the  $T_{C_{ANT}}$  in 100 years, despite the predicted slow-down of the MOC $\sigma$ . To conclude, the faster increase in  $C_{ANT}$  in the upper limb than in the lower limb will cause an augmentation of the northward  $T_{C_{ANT}}$  across the SPNA at long timescales. Nevertheless, at the timescale analysed in this work

(1997–2010), the inter-annual variability of the  $\text{MOC}\sigma$  blurs the long-term increase in the  $T_{\text{C}_{\text{ANT}}}$  caused by the  $\Delta\text{C}_{\text{ANT}}$  increase. Furthermore, this result is quite speculative since (i) it is supposed that the trend in the  $\Delta\text{C}_{\text{ANT}}$  will remain constant and (ii) the model-based decrease in the  $\text{MOC}\sigma$  is taken as true. However, it gives an interesting order of magnitude.

It is suspected that the long-term increase in the  $T_{\text{C}_{\text{ANT}}}$  would cause an increase in the storage rate of  $\text{C}_{\text{ANT}}$  in the SPNA. Pérez et al. (2013) observed a decrease in the storage rate of  $\text{C}_{\text{ANT}}$  in the SPNA between 1997 (high  $\text{MOC}\sigma$ ) and 2002–2006 (low  $\text{MOC}\sigma$ ). They reported a change in the storage rate from  $0.083 \pm 0.008 \text{ GtC}\cdot\text{yr}^{-1}$  to  $0.026 \pm 0.004 \text{ GtC}\cdot\text{yr}^{-1}$  between both periods. However, because of the short time span, the  $\Delta\text{C}_{\text{ANT}}$  increase was too small to compensate for the large intra-decadal decrease in the  $\text{MOC}\sigma$  that caused the decrease in the  $T_{\text{C}_{\text{ANT}}}$  across the A25 section and consequently the decrease in the  $\text{C}_{\text{ANT}}$  storage rate reported by Pérez et al. (2013). Calculating the storage rate for 1997–2010 is the subject of a future work.

To sum up, although the  $T_{\text{C}_{\text{ANT}}}^{\text{isop}}$  has a considerable contribution to the  $T_{\text{C}_{\text{ANT}}}$  across the A25 section, the major contribution to the  $T_{\text{C}_{\text{ANT}}}$  is the  $T_{\text{C}_{\text{ANT}}}^{\text{diap}}$ , which is also the main driver of its variability. In both components of the transport ( $T_{\text{C}_{\text{ANT}}}^{\text{isop}}$  and  $T_{\text{C}_{\text{ANT}}}^{\text{diap}}$ ), the  $\text{C}_{\text{ANT}}$  concentration plays an important role: the horizontal gradient of  $\text{C}_{\text{ANT}}$  across the section is responsible for the southward  $T_{\text{C}_{\text{ANT}}}$  by the  $T_{\text{C}_{\text{ANT}}}^{\text{isop}}$ , while the  $\text{C}_{\text{ANT}}$ -laden waters flowing northwards are responsible for the large positive values of the  $T_{\text{C}_{\text{ANT}}}^{\text{diap}}$ . Finally, it has been shown that the variability of the  $\text{MOC}\sigma$  dominates the variability of the  $T_{\text{C}_{\text{ANT}}}$  at inter-annual to decadal timescales, but that the  $\text{C}_{\text{ANT}}$  increase seems to control the  $T_{\text{C}_{\text{ANT}}}$  change at longer timescales. Therefore, in spite of the predicted slow-down of the  $\text{MOC}\sigma$  by 2100, an increase in the storage rate of  $\text{C}_{\text{ANT}}$  in the SPNA would be expected.



# PART IV.- SUMMARY AND CONCLUSIONS





# PARTE IV.- RESUMEN Y CONCLUSIONES





## Capítulo 7.- Resumen y conclusiones

Los resultados de la presente tesis doctoral se organizaron en tres grandes bloques. En el capítulo 4 se empleó un análisis óptimo multiparamétrico para evaluar la estructura de las masas de agua del Giro Subpolar del Atlántico Norte durante el período 2002–2010, así como su variación temporal entre 1997 y 2010. Mediante la combinación de esta estructura de masas de agua con los campos de velocidad se evaluaron los transportes de volumen de las principales masas de agua y su contribución a la circulación termohalina del Atlántico (AMOC). Por último se evaluaron las transformaciones que sufren las masas de agua dentro del Giro Subpolar del Atlántico Norte. En el capítulo 5 se evaluaron los cambios de pH y de saturación de  $\text{CaCO}_3$  resultado del incremento de la concentración de  $\text{CO}_2$  antropogénico ( $C_{\text{ANT}}$ ) en las principales masas de agua de las cuencas del Irminger e Islandia durante el periodo 1981–2014. Se investigaron los componentes antropogénico y no antropogénico de los cambios de pH para evaluar su importancia relativa en los cambios de pH observados. En base a las tendencias observadas de pH y saturación de  $\text{CaCO}_3$  durante el periodo de estudio se infirieron los cambios esperados de estas variables para el final del siglo. Por último se evaluaron los cambios en la alcalinidad total de las aguas de las cuencas del Irminger e Islandia. En el capítulo 6 se investigó la variabilidad interanual a decenal en el transporte del  $C_{\text{ANT}}$  a través del Atlántico Norte Subpolar entre 1997 y 2010. Los mecanismos que controlan la variabilidad del transporte de  $C_{\text{ANT}}$  ( $T_{\text{CANT}}$ ) se evaluaron mediante la partición del  $T_{\text{CANT}}$  en sus componentes diapícnico e isopícnico. En base a este análisis, se propuso un estimador simplificado para la variabilidad del  $T_{\text{CANT}}$ , basado en la intensidad de la AMOC y en la diferencia de  $C_{\text{ANT}}$  entre las ramas superior e inferior de la AMOC.

A continuación se resumen los principales resultados obtenidos en cada uno de los capítulos, que constituyen las conclusiones generales referentes a los tres bloques temáticos que fueron objeto de esta tesis doctoral.

### 7.1.- Capítulo 4: Estructura, transportes y transformaciones de las masas de agua del Giro Subpolar del Atlántico

En este capítulo se muestra una aplicación del análisis óptimo multiparamétrico (OMP) como base para identificar las variaciones temporales y las transformaciones de las masas de agua a lo largo de las secciones hidrográficas WOCE A25 (4x y OVIDE, en el límite sur del Giro Subpolar del Atlántico Norte). La selección de masas de agua y figuras de mezcla fue la apropiada ya que el OMP fue capaz de reproducir las características fisicoquímicas de todas las muestras, tal como lo demuestran los bajos residuos del modelo. En la configuración del OMP, la transformación de las masas de agua debida a la interacción océano-atmósfera se tuvo en cuenta mediante la selección de diversas variedades de Agua Modal Subpolar (SPMW). Esta novedad produce distribuciones de masas de agua realistas, que confirman los conocimientos generales de la circulación del Atlántico Norte Subpolar. Concretamente, las distribuciones de masas de agua obtenidas evidencian la subducción del Agua Intermedia Subártica (SAIW) bajo la corriente del Atlántico Norte (NAC) y la intrusión del Agua Polar Intermedia (PIW) en el rango de densidad de la corriente profunda del margen occidental (DWBC). La contribución relativa de cada masa

de agua a los transportes a través de las secciones hidrográficas se calculó mediante la combinación de los resultados del análisis OMP con los campos de velocidad de las secciones. La evaluación del transporte de volumen por masa de agua basada en diluciones de una masa de agua “pura” (resultado de un análisis OMP) es particularmente útil para zonas con distribuciones de corrientes complejas e importantes procesos de transformación de masas de agua, donde esta metodología combinada puede proporcionar información sobre las características de la circulación, mejorándose así la comprensión de la oceanografía regional.

Las estimaciones de los transportes por masa de agua son consistentes con los resultados de anteriores estudios y con las principales características de la circulación del Atlántico Norte. Teniendo en cuenta la isopícnica que separa las ramas superior e inferior de la AMOC ( $\sigma_1 = 32,15$ ; donde  $\sigma_1$  es la densidad potencial referenciada a 1000 metros), cada masa de agua se asoció con la correspondiente rama de la AMOC. En este estudio, la rama superior de la AMOC está compuesta por Aguas Centrales, SPMW de Islandia (IcSPMW), SAIW y Agua Mediterránea; mientras que la rama inferior de la AMOC está constituida por SPMW del Irminger (IrSPMW), PIW, Agua del Mar de Labrador (LSW), Agua de desbordamiento de Islandia–Escocia (ISOW), Agua de desbordamiento de Dinamarca y Agua Profunda del Atlántico Noreste. Este análisis permite asociar la reducción de la magnitud de la rama superior de la AMOC entre 1997 y la década de 2000 (de  $23,3 \pm 1,2$  Sv a  $16,5 \pm 1,5$  Sv; donde  $1 \text{ Sv} = 10^6 \text{ m}^3 \cdot \text{s}^{-1}$ ) con la reducción en el transporte hacia el norte de las Aguas Centrales. Esta reducción del flujo hacia el norte de la rama superior de la AMOC está parcialmente compensada por la reducción del flujo hacia el sur de la rama inferior, asociada con la disminución del transporte de IrSPMW y PIW.

La evaluación del modelo de cajas permitió comprender la transformación de las Aguas Centrales. En la cuenca Este del Atlántico Norte (ENA) 2,7 Sv de Aguas Centrales se transforman en IcSPMW. Este flujo recircula alrededor del Reykjanes Ridge y se une a la IcSPMW advectada desde el sur (posiblemente a través de una rama de la NAC como sugieren Pollard et al. (2004)), lo que da lugar a un transporte de 5,3 Sv hacia el norte de IcSPMW en la cuenca del Irminger. Estos 5,3 Sv se combinan con 1,1 Sv de Aguas Centrales y 2,2 Sv de SAIW (que cruzan sobre el Reykjanes Ridge) para dar lugar a 8,8 Sv de IrSPMW como resultado de la interacción océano-atmósfera.

La principal masa de agua de las secciones hidrográficas es LSW ( $35,0 \pm 0,6\%$  del volumen de la sección). La variabilidad interanual observada en las capas superiores de la cuenca del Irminger refleja la interacción entre LSW y SPMW, cuya mezcla emula la presencia de la variedad superior de LSW. En las capas inferiores a ambos lados del Reykjanes Ridge se observa la interacción entre LSW e ISOW, con un incremento de la presencia de ISOW con el tiempo como respuesta a la progresiva dilución de LSW. Los resultados del OMP también revelan que LSW se mezcla vigorosamente con las aguas que la rodean principalmente en dos regiones: (i) a lo largo del Reykjanes Ridge, y (ii) en la DWBC ( $\sigma_0 > 27,80$ ), donde la contribución de LSW es significativa. El transporte neto de LSW ligeramente negativo a través de la sección OVIDE corrobora la formación moderada de LSW en la cuenca del Irminger.

Las aguas de la cuenca ENA cruzan sobre el Reykjanes Ridge y entran en la cuenca del Irminger, donde se transforman y/o densifican, pasando de la zona de aguas superiores e intermedias a la zona de aguas profundas. El análisis OMP permite descomponer el flujo de 9,4 Sv

a través del Reykjanes Ridge en Aguas Centrales, SAIW, LSW e ISOW; siendo SAIW el principal contribuyente.

Las distribuciones y transportes de ISOW permiten inferir que a lo largo de su viaje entre el umbral de Islandia–Escocia y la Zona de Fractura de Charlie-Gibbs (CGFZ), parte de ella asciende y fluye a través de pequeñas fracturas en el Reykjanes Ridge situadas entre las secciones OVIDE y 4x. Una vez que ISOW llega a la CGFZ, una pequeña parte sigue hacia la cuenca occidental de Europa mientras que la corriente principal atraviesa la fractura llegando a la cuenca del Irminger, donde fluirá hacia el norte y se unirá a las fracciones que anteriormente cruzaron el Reykjanes Ridge.

La extensión de esta metodología a amplias zonas del océano podría proporcionar una base útil para otros estudios de este tipo o para otros más ambiciosos relacionados con los componentes de los ciclos biogeoquímicos del océano.

## 7.2.- Capítulo 5: Tendencias observadas en los factores de estrés del sistema del CO<sub>2</sub> en las cuencas del Irminger e Islandia

El efecto último de la absorción de  $C_{ANT}$  por el océano es la disminución del pH y concentración de iones carbonato del agua de mar, reduciendo así su capacidad tampón. En este capítulo se evaluó la progresiva acidificación de las masas de agua del Atlántico Norte en base a medidas directas del sistema del CO<sub>2</sub> oceánico que abarcan las últimas tres décadas (1981–2014). Para averiguar las causas de los cambios de pH se evaluaron sus componentes antropogénico (derivado de la captación de CO<sub>2</sub> antropogénico;  $\Delta pH_{C_{ANT}}$ ) y no antropogénico (no directamente relacionado con la captación de CO<sub>2</sub> antropogénico;  $\Delta pH_{VAR}$ ). Las crecientes concentraciones de CO<sub>2</sub> atmosférico han disminuido significativamente el pH de toda la columna de agua de las cuencas del Irminger e Islandia, observándose las mayores tasas de descenso de pH en las aguas superficiales e intermedias. El aumento del contenido en  $C_{ANT}$  de la capa superficial es consecuente con el aumento de la concentración de CO<sub>2</sub> en la atmósfera, pero el descenso de pH no sigue este patrón. La acidificación de las aguas superficiales es amortiguada por la llegada de aguas subtropicales más salinas y con un mayor contenido en alcalinidad. Las aguas intermedias presentan unas tasas de acidificación similares a las encontradas en las aguas superficiales, que son causadas por una combinación de los efectos de los componentes antropogénico y no antropogénico. En la cuenca del Irminger, la tasa de acidificación esperada en la capa ocupada por la variedad “clásica” de LSW debida a la absorción de  $C_{ANT}$  se ve reforzada por el envejecimiento de esta masa de agua desde el final de la década de 1990. Las aguas profundas de la cuenca del Irminger presentan una tasa de acidificación significativa con un marcado carácter antropogénico.

La calcificación y/o disolución de los organismos planctónicos y bentónicos formadores de estructuras calcáreas normalmente depende de la concentración de iones carbonato, a menudo expresada por el grado de saturación de los biominerales aragonito y calcita. La captación oceánica de  $C_{ANT}$  durante los últimos 33 años ha provocado que los horizontes de saturación de aragonito asciendan a una velocidad de  $\sim 10 \text{ m}\cdot\text{año}^{-1}$  en las cuencas del Irminger e Islandia, tasa que es más de dos veces mayor que las anteriormente observadas en la cuenca de Islandia.

En base a las tasas de cambio de pH y  $\Omega_{\text{Arag}}$  observadas durante el periodo 1981–2014, se infirieron los cambios esperados de estas variables para el final del siglo. En base a estas estimaciones, la capa superficial experimentará una caída de pH de  $\sim 0,31$  unidades con respecto a la era pre-industrial en el momento en que la concentración de  $\text{CO}_2$  atmosférico llegue a los 800 ppm (aproximadamente el doble de la concentración actual). La capa profunda de la cuenca del Irminger experimentará una disminución de pH similar a la de las aguas superficiales ( $\sim 0,27$  unidades de pH). Las proyecciones también muestran que toda la columna de agua de ambas cuencas estará subsaturada en aragonito en el momento en que el  $\text{CO}_2$  atmosférico alcance los 800 ppm ( $\sim 2065$ ). Sin embargo, las aguas intermedias alcanzarán los niveles subsaturación en aragonito más rápidamente, concretamente cuando la concentración de  $\text{CO}_2$  atmosférico alcance los  $\sim 500$ – $560$  ppm ( $\sim 2035$ – $2045$ ).

Los datos aquí recopilados también muestran tendencias significativas de incremento de la alcalinidad a largo plazo en las aguas profundas de la cuenca del Irminger, que pueden estar relacionadas con el aumento de la descarga de los ríos árticos.

La acidificación del océano se ha convertido en un tema clave debido a las posibles retroalimentaciones climáticas que puede provocar a nivel global. Los estudios de las variables del sistema del  $\text{CO}_2$  de oceánico en toda la columna de agua y a lo largo de las cuencas oceánicas (como el realizado en esta tesis) son necesarios para poder evaluar las consecuencias de los cambios futuros.

### **7.3.- Capítulo 6: Variabilidad del transporte de $\text{CO}_2$ antropogénico en las secciones OVIDE entre Groenlandia y Portugal: mecanismos controladores**

El continuo aumento de la concentración de  $\text{CO}_2$  en la atmósfera debido a las actividades humanas es suavizado por la absorción de  $\text{CO}_2$  por parte del océano. La pregunta es ¿cuánto tiempo el océano va a actuar como sumidero de este gas de efecto invernadero? Por lo tanto, es realmente importante cuantificar y comprender los mecanismos que actúan en el transporte y almacenamiento de  $\text{CO}_2$  en los océanos. Este capítulo se ha centrado en estudiar el aspecto físico del transporte de  $C_{\text{ANT}}$  ( $T_{\text{C}_{\text{ANT}}}$ ) con el fin de comprender los mecanismos que lo controlan en el Atlántico Norte Subpolar y describir por vez primera su variabilidad interanual a decenal.

Se obtuvo un  $T_{\text{C}_{\text{ANT}}}$  a través de la sección hacia el norte, con un valor promedio de  $254 \pm 29 \text{ kmol}\cdot\text{s}^{-1}$  para el período 1997–2010, con una desviación estándar de  $71 \text{ kmol}\cdot\text{s}^{-1}$ . No se identificaron cambios significativos a largo plazo en este período debido a la transición entre una clara disminución del  $T_{\text{C}_{\text{ANT}}}$  desde 1997 y mediados de la década de 2000 y su posterior recuperación. La disminución inicial se debe a la desaceleración de la AMOC y el posterior aumento se debe principalmente al aumento en la concentración  $C_{\text{ANT}}$ .

La división del  $T_{\text{C}_{\text{ANT}}}$  en sus diferentes componentes permitió observar que el componente isopícnico ( $T_{\text{C}_{\text{ANT}}}^{\text{isop}}$ ) da lugar a un importante  $T_{\text{C}_{\text{ANT}}}$  hacia el sur, localizado principalmente en la cuenca del Irminger. Las aguas de desbordamiento (ISOW y DSOW) y las aguas intermedias y de superficie son las principales responsables de este transporte hacia el sur. El hecho de que las aguas

intermedias y de superficie de la cuenca del Irminger tengan una alta contribución al  $T_{C_{ANT}}^{isop}$  se debe a su concentración de  $C_{ANT}$  relativamente alta en comparación con la de las aguas del mismo rango de densidad en la cuenta oeste europea. El alto contenido en  $C_{ANT}$  de las aguas intermedias de la cuenca del Irminger es probablemente debido a la reciente ventilación de estas aguas. En el caso de las aguas de desbordamiento, la concentración de  $C_{ANT}$  relativamente alta se debe principalmente a la entrada de aguas de la termoclina ricas en  $C_{ANT}$  durante el proceso de desbordamiento.

La descomposición del  $T_{C_{ANT}}$  en sus diferentes componentes también muestra que el componente de diapícnico ( $T_{C_{ANT}}^{diap}$ ) es el principal contribuyente del  $T_{C_{ANT}}$ , cuyo valor medio durante el período 1997–2010 es de  $400 \pm 29 \text{ kmol}\cdot\text{s}^{-1}$ . Además el  $T_{C_{ANT}}^{diap}$  es el responsable de la variabilidad del  $T_{C_{ANT}}$ . El  $T_{C_{ANT}}^{diap}$  está relacionado con la AMOC, cuya rama superior transporta aguas cálidas y enriquecidas en  $C_{ANT}$  hacia el norte, mientras que su rama inferior transporta aguas más densas, frías y pobres en  $C_{ANT}$  hacia el sur. El estimador del  $T_{C_{ANT}}$  aquí presentado ( $T_{C_{ANT}}^0$ ) es una representación esquemática de este mecanismo, lo que queda corroborado por la buena correlación entre el  $T_{C_{ANT}}^0$  y el  $T_{C_{ANT}}^{diap}$ . El  $T_{C_{ANT}}^0$  también sirve como una aproximación sencilla para probar los modelos numéricos. Sin embargo, el  $T_{C_{ANT}}^0$  no recoge todos los procesos que intervienen en el  $T_{C_{ANT}}$  en el Atlántico Norte Subpolar.

El  $T_{C_{ANT}}^0$  se utiliza para obtener la importancia relativa a largo plazo del contenido en  $C_{ANT}$  y la circulación en el  $T_{C_{ANT}}$  a través del Atlántico Norte Subpolar. Por un lado, la concentración de  $C_{ANT}$  está aumentando más rápidamente en la rama superior de la AMOC que en la rama inferior, con unas tendencias durante el período 1997–2010 de  $0,63 \pm 0,27 \text{ }\mu\text{mol}\cdot\text{kg}^{-1}\cdot\text{año}^{-1}$  y  $0,20 \pm 0,25 \text{ }\mu\text{mol}\cdot\text{kg}^{-1}\cdot\text{año}^{-1}$ , respectivamente. Esto significa que en el Atlántico Norte Subpolar hay más  $C_{ANT}$  siendo importado en la rama superior que siendo exportado en la rama inferior, lo que da lugar a una acumulación de  $C_{ANT}$ . Se espera que la concentración  $C_{ANT}$  en ambas ramas se vincule a la variabilidad de la AMOC, aunque sigue sin conocerse a qué escala temporal ocurrirá. Sin embargo, la diferencia de  $C_{ANT}$  entre ambas ramas de la AMOC ( $\Delta C_{ANT}$ ) aumenta independientemente de la variabilidad de la AMOC, con una tasa media de  $0,43 \pm 0,10 \text{ }\mu\text{mol}\cdot\text{kg}^{-1}\cdot\text{año}^{-1}$ . Esta tasa de incremento va a causar un aumento en el  $T_{C_{ANT}}$  a través de la sección OVIDE y, en consecuencia, un aumento en la tasa de almacenamiento de  $C_{ANT}$  en el Atlántico Norte Subpolar. Por otro lado, los modelos han pronosticado una desaceleración del 25% de la AMOC a finales de siglo. Teniendo esto en cuenta y con la tendencia positiva de la  $\Delta C_{ANT}$  calculada en este trabajo, el  $T_{C_{ANT}}^0$  aumentaría a un ritmo de  $4,3 \pm 0,1 \text{ kmol}\cdot\text{s}^{-1}\cdot\text{año}^{-1}$  durante el siglo XXI. Esto implica un aumento del  $T_{C_{ANT}}$  de  $430 \text{ kmol}\cdot\text{s}^{-1}$  en 100 años, a pesar de la predicha desaceleración de la AMOC. Sin embargo, en la escala de tiempo analizada (1997–2010) la variabilidad interanual de la AMOC enmascara el aumento a largo plazo del  $T_{C_{ANT}}$  causado por el aumento de la  $\Delta C_{ANT}$ . Este resultado es bastante especulativo ya que (i) supone que la tendencia en la  $\Delta C_{ANT}$  permanecerá constante y (ii) se asume como cierta la disminución de la AMOC predicha por los modelos. A pesar de esto, da una idea del orden de magnitud.

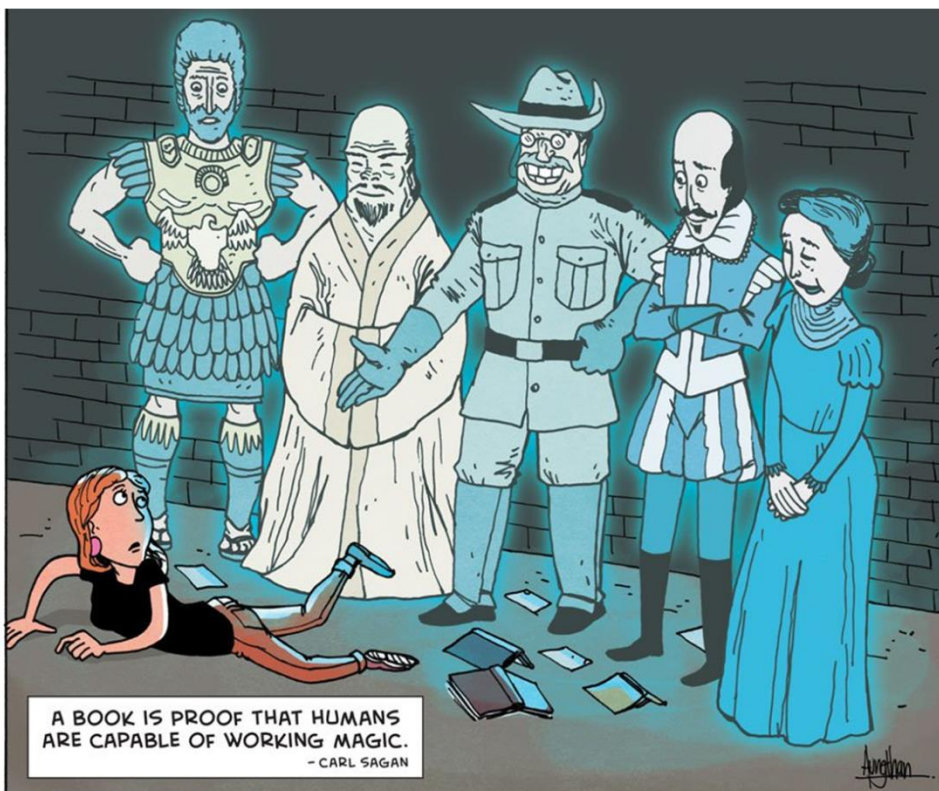
En resumen, aunque el  $T_{C_{ANT}}^{isop}$  tiene una contribución considerable al  $T_{C_{ANT}}$  a través de la sección OVIDE, el mayor contribuyente es el  $T_{C_{ANT}}^{diap}$ , que es también el principal responsable de la

variabilidad del  $T_{C_{ANT}}$ . La concentración de  $C_{ANT}$  juega un papel importante en ambos componentes del  $T_{C_{ANT}}$ : el gradiente horizontal de  $C_{ANT}$  través de la sección es responsable del  $T_{C_{ANT}}$  hacia el sur por el  $T_{C_{ANT}}^{isop}$ , mientras que las aguas cargadas de  $C_{ANT}$  que fluyen hacia el norte son las responsables del alto  $T_{C_{ANT}}$  hacia el norte del  $T_{C_{ANT}}^{diap}$ . Finalmente, se ha demostrado que la variabilidad de la AMOC domina la variabilidad del  $T_{C_{ANT}}$  a escalas de tiempo interanuales a decenales, pero que el aumento de  $C_{ANT}$  parece controlar los cambios en el  $T_{C_{ANT}}$  a escalas de tiempo mayores. Por lo tanto, a pesar de la desaceleración de la AMOC predicha para el 2100, se espera un aumento en la tasa de almacenamiento de  $C_{ANT}$  en el Atlántico Norte Subpolar.

# REFERENCES



MAYBE SOMEBODY DEAD FOR THOUSANDS OF YEARS.



WORDS © CARL SAGAN, ARTWORK © GAVIN AUNG THAN 2012

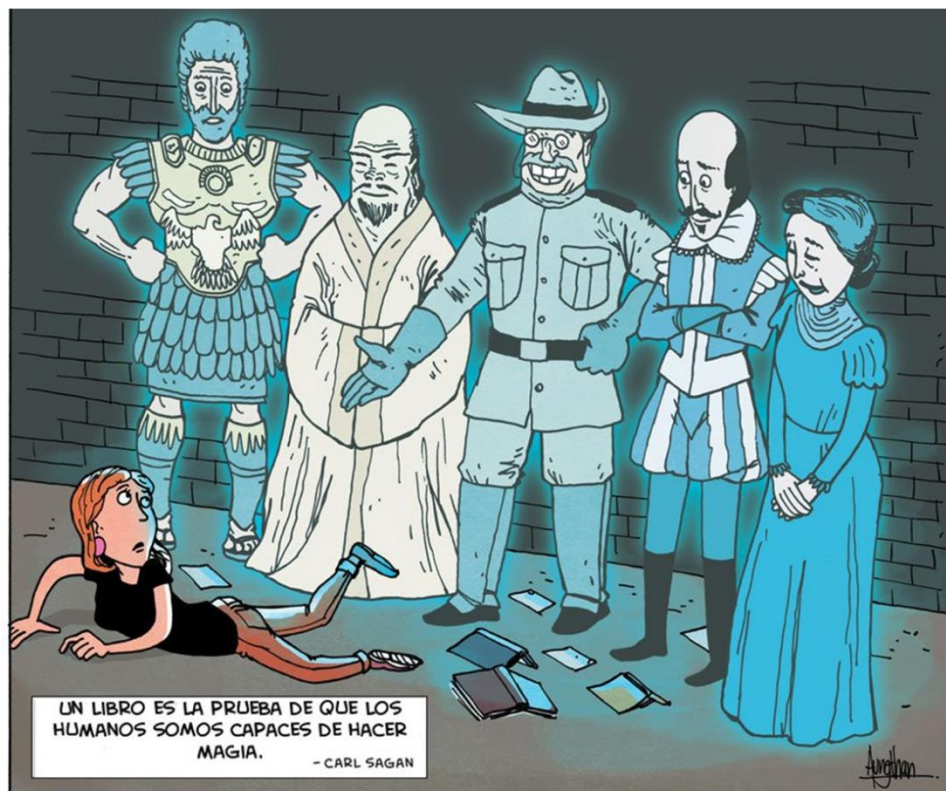
zenpencils.com



# BIBLIOGRAFÍA



ALGUIEN QUE QUIZÁ MURIÓ HACE MILES DE AÑOS.



- Álvarez, M., Brea, S., Mercier, H., Álvarez-Salgado, X.A., 2014. Mineralization of biogenic materials in the water masses of the South Atlantic Ocean. I: Assessment and results of an optimum multiparameter analysis. *Prog. Oceanogr.* 123, 1–23. doi:10.1016/j.pocean.2013.12.007
- Álvarez, M., Bryden, H.L., Pérez, F.F., Ríos, A.F., Rosón, G., 2002. Physical and biogeochemical fluxes and net budgets in the subpolar and temperate North Atlantic. *J. Mar. Res.* 60, 191–226. doi:10.1357/00222400260497462
- Álvarez, M., Pérez, F.F., Bryden, H., Ríos, A.F., 2004. Physical and biogeochemical transports structure in the North Atlantic subpolar gyre. *J. Geophys. Res.* 109. doi:10.1029/2003JC002015
- Álvarez, M., Ríos, A.F., Pérez, F.F., Bryden, H.L., Rosón, G., 2003. Transports and budgets of total inorganic carbon in the subpolar and temperate North Atlantic. *Glob. Biogeochem. Cycles* 17, 1002. doi:10.1029/2002GB001881
- Ambar, I., Howe, M.R., 1979. Observations of the Mediterranean outflow-I: Mixing in the Mediterranean outflow. *Deep Sea Res* 26, 535–554. doi:10.1016/0198-0149(79)90095-5
- Aminot, A., Chaussepied, M., 1983. Manuel des analyses chimiques en Milieu Marin. Publications du CNEXO, 395p.
- Anderson, L.A., Sarmiento, J.L., 1994. Redfield ratios of remineralization determined by nutrient data analysis. *Glob. Biogeochem Cycles* 8, 65–80. doi:10.1029/93GB03318
- Anderson, L.G., Jutterström, S., Kaltin, S., Jones, E.P., Björk, G., 2004. Variability in river runoff distribution in the Eurasian Basin of the Arctic Ocean. *J. Geophys. Res. Oceans* 109, C01016. doi:10.1029/2003JC001773
- Archer, D., 2005. Fate of fossil fuel CO<sub>2</sub> in geologic time. *J. Geophys. Res. Oceans* 110, C09S05. doi:10.1029/2004JC002625
- Archer, D., Eby, M., Brovkin, V., Ridgwell, A., Cao, L., Mikolajewicz, U., Caldeira, K., Matsumoto, K., Munhoven, G., Montenegro, A., Tokos, K., 2009. Atmospheric Lifetime of Fossil Fuel Carbon Dioxide. *Annu. Rev. Earth Planet. Sci.* 37, 117–134. doi:10.1146/annurev.earth.031208.100206
- Arhan, M., 1990. The North Atlantic Current and subarctic intermediate water. *J. Mar. Res.* 48, 109–144. doi:10.1357/002224090784984605
- Arhan, M., Colin de Verdière, A., Mémary, L., 1994a. The eastern boundary of the subtropical North Atlantic. *J. Phys. Oceanogr.* 24, 1295–1316. doi:10.1175/1520-0485(1994)024<1295:TEBOTS>2.0.CO;2
- Arhan, M., Colin De Verdière, A., Mémary, L., 1994b. The Eastern Boundary of the Subtropical North Atlantic. *J. Phys. Oceanogr.* 24, 1295–1316. doi:10.1175/1520-0485(1994)024<1295:TEBOTS>2.0.CO;2
- Arhan, M., King, B., 1995. Lateral mixing of the Mediterranean Water in the eastern North Atlantic. *J. Mar. Res.* 53, 865–895. doi:10.1357/0022240953212990
- Azetsu-Scott, K., Jones, E.P., Yashayaev, I., Gershay, R.M., 2003. Time series study of CFC concentrations in the Labrador Sea during deep and shallow convection regimes (1991–2000). *J. Geophys. Res.* 108, 3354. doi:10.1029/2002JC001317
- Bacon, S., 1997. Circulation and Fluxes in the North Atlantic between Greenland and Ireland. *J Phys Ocean.* 27, 1420–1435. doi:10.1175/1520-0485(1997)027<1420:CAFITN>2.0.CO;2
- Balmaseda, M.A., Smith, G.C., Haines, K., Anderson, D., Palmer, T.N., Vidard, A., 2007. Historical reconstruction of the Atlantic Meridional Overturning Circulation from the ECMWF operational ocean reanalysis. *Geophys Res Lett* 34, L23615. doi:10.1029/2007GL031645
- Barbero, L., González-Dávila, M., Santana-Casiano, J.M., Álvarez, M., 2010. Variability of the water mass transports and fluxes in the eastern North Atlantic during 2001. *J. Geophys. Res. Oceans* 115. doi:10.1029/2008JC005212
- Baringer, M.O., Price, J.F., 1997. Mixing and Spreading of the Mediterranean Outflow. *J Phys Ocean.* 27, 1654–1677. doi:10.1175/1520-0485(1997)027<1654:MASOTM>2.0.CO;2

- Barker, S., Ridgwell, A., 2012. Ocean Acidification. *Nat. Educ. Knowl.* 3, 21.
- Barnston, A.G., Livezey, R.E., 1987. Classification of seasonality and persistence of low-frequency atmospheric circulation patterns. *Mon Wea Rev* 115, 1083–1126. doi:10.1175/1520-0493(1987)115<1083:CSAPOL>2.0.CO;2
- Bates, N., Astor, Y., Church, M., Currie, K., Dore, J., Gonaález-Dávila, M., Lorenzoni, L., Muller-Karger, F., Olafsson, J., Santa-Casiano, M., 2014. A Time-Series View of Changing Ocean Chemistry Due to Ocean Uptake of Anthropogenic CO<sub>2</sub> and Ocean Acidification. *Oceanography* 27, 126–141. doi:10.5670/oceanog.2014.16
- Bates, N.R., Best, M.H.P., Neely, K., Garley, R., Dickson, A.G., Johnson, R.J., 2012. Detecting anthropogenic carbon dioxide uptake and ocean acidification in the North Atlantic Ocean. *Biogeosciences* 9, 2509–2522. doi:10.5194/bg-9-2509-2012
- Beining, P., Roether, W., 1996. Temporal evolution of CFC 11 and CFC 12 concentrations in the ocean interior. *J. Geophys. Res. Oceans* 101, 16455–16464. doi:10.1029/96JC00987
- Benson, B.B., Krause, D., 1984. The concentration and isotopic fractionation of oxygen dissolved in freshwater and seawater in equilibrium with the atmosphere. *Limnol. Oceanogr.* 29, 620–632. doi:10.4319/lo.1984.29.3.0620
- Bersch, M., 2002. North Atlantic Oscillation–induced changes of the upper layer circulation in the northern North Atlantic Ocean. *J Geophys Res* 107, 3156. doi:10.1029/2001JC000901
- Bersch, M., Meincke, J., Sy, A., 1999. Interannual thermohaline changes in the northern North Atlantic 1991–1996. *Deep Sea Res. Part II Top. Stud. Oceanogr.* 46, 55–75. doi:10.1016/S0967-0645(98)00114-3
- Bersch, M., Yashayaev, I., Koltermann, K.P., 2007. Recent changes of the thermohaline circulation in the subpolar North Atlantic. *Ocean Dyn.* 57, 223–235. doi:10.1007/s10236-007-0104-7
- Biastoch, A., Käse, R.H., Stammer, D.B., 2003. The sensitivity of the Greenland-Scotland overflow to forcing changes. *J Phys Ocean.* 33, 2307–2319. doi:10.1175/1520-0485(2003)033<2307:TSOTGR>2.0.CO;2
- Biastoch, A., Völker, C., Böning, C.W., 2007. Uptake and spreading of anthropogenic trace gases in an eddy-permitting model of the Atlantic Ocean. *J. Geophys. Res.* 112, C09017. doi:10.1029/2006JC003966
- Billant, A., Branellec, P., Mercier, H., 2004. Campagne OVIDE 2002 : rapport de données CTD-O2. <http://archimer.ifremer.fr/doc/00210/32082/>.
- Bollmann, M., Bosch, T., Colijn, F., Ebinghaus, R., Froese, R., Güssow, K., Khalilian, S., Krastel, S., Körtzinger, A., Langenbuch, M., Latif, M., Matthiessen, B., Melzner, F., Oschlies, A., Petersen, S., Proelß, A., Quaas, M., Reichenbach, J., Requate, T., Reusch, T., Rosenstiel, P., Schmidt, J.O., Schrottke, K., Sichelschmidt, H., Siebert, U., Soltwedel, R., Sommer, U., Stattegger, K., Sterr, H., Sturm, R., Treude, T., Vafeidis, A., van Bernem, C., van Beusekom, J., Voss, R., Visbeck, M., Wahl, M., Wallmann, K., Weinberger, F., 2010. World Ocean Review 1 - Living with the oceans. A report on the state of the world's oceans.
- Böning, C.W., Bryan, F.O., Holland, W.R., Döscher, R., 1996. Deep-Water Formation and Meridional Overturning in a High-Resolution Model of the North Atlantic. *J Phys Ocean.* 26, 1142–1164. doi:10.1175/1520-0485(1996)026<1142:DWFAMO>2.0.CO;2
- Böning, C.W., Herrmann, P., 1994. Annual Cycle of Poleward Heat Transport in the Ocean: Results from High-Resolution Modeling of the North and Equatorial Atlantic. *J. Phys. Oceanogr.* 24, 91–107. doi:10.1175/1520-0485(1994)024<0091:ACOPHT>2.0.CO;2
- Böning, C.W., Scheinert, M., Dengg, J., Biastoch, A., Funk, A., 2006. Decadal variability of subpolar gyre transport and its reverberation in the North Atlantic overturning. *Geophys. Res. Lett.* 33, L21S01. doi:10.1029/2006GL026906
- Bradshaw, A., Brewer, P., Shafer, D., Williams, R., 1981. Measurements of total carbon dioxide and alkalinity by potentiometric titration in the GEOSECS program. *Earth Planet Sci Lett* 55, 99–115. doi:10.1016/0012-821X(81)90090-X

- Brambilla, E., Talley, L.D., 2008. Subpolar Mode Water in the northeastern Atlantic: 1. Averaged properties and mean circulation. *J Geophys Res* 113, C04025. doi:10.1029/2006JC004062
- Brambilla, E., Talley, L.D., Robbins, P.E., 2008. Subpolar Mode Water in the northeastern Atlantic: 2. Origin and transformation. *J Geophys Res* 113, C04026. doi:10.1029/2006JC004063
- Branellec, P., Thierry, V., 2013. OVIDE 2010 CTD-O2 Cruise report. <http://archimer.ifremer.fr/doc/00210/32134/>.
- Brewer, P.G., 1978. Direct observation of the oceanic CO<sub>2</sub> increase. *Geophys. Res. Lett.* 5, 997–1000. doi:10.1029/GL005i012p00997
- Broecker, W.S., 1974. “NO”, a conservative water-mass tracer. *Earth Planet. Sci. Lett.* 23, 100–107. doi:10.1016/0012-821X(74)90036-3
- Broecker, W.S., Peacock, S.L., Walker, S., Weiss, R., Fahrback, E., Schroeder, M., Mikolajewicz, U., Heinze, C., Key, R., Peng, T.-H., Rubin, S., 1998. How much deep water is formed in the Southern Ocean? *J. Geophys. Res. Oceans* 103, 15833–15843. doi:10.1029/98JC00248
- Brown, P.J., Bakker, D.C.E., Schuster, U., Watson, A.J., 2010. Anthropogenic carbon accumulation in the subtropical North Atlantic. *J. Geophys. Res.* 115, C04016. doi:10.1029/2008JC005043
- Bryden, H., Imawaki, S., 2001. Ocean heat transport, in: *Ocean Circulation and Climate: Observing and Modelling the Global Ocean* [Siedler, G., J. Church and J. Gould (eds.)]. Academic Press. pp. 455–474.
- Bryden, H.L., King, B.A., McCarthy, G.D., McDonagh, E.L., 2014. Impact of a 30% reduction in Atlantic meridional overturning during 2009–2010. *Ocean Sci* 10, 683–691. doi:10.5194/os-10-683-2014
- Bubnov, V.A., 1968. Intermediate subarctic waters in the northern part of the Atlantic Ocean. *Okeanologia* 19, 136–153 (English translation, N00 Trnas 545, U.S. Nav. Oceanogr. Off., Washington, D. C., 1973).
- Byrne, R.H., Mecking, S., Feely, R.A., Liu, X., 2010. Direct observations of basin-wide acidification of the North Pacific Ocean. *Geophys Res Lett* 37, L02601. doi:10.1029/2009GL040999
- Caldeira, K., Wickett, M.E., 2005. Ocean model predictions of chemistry changes from carbon dioxide emissions to the atmosphere and ocean. *J. Geophys. Res.* 110, C09S04. doi:10.1029/2004JC002671
- Carracedo, L.I., Gilcoto, M., Mercier, H., Pérez, F.F., 2014. Seasonal dynamics in the Azores–Gibraltar Strait region: A climatologically-based study. *Prog. Oceanogr.* 122, 116–130. doi:10.1016/j.pocean.2013.12.005
- Carracedo, L.I., Pardo, P.C., Villaceros-Robineau, N., Granda, F.D. la, Gilcoto, M., Pérez, F.F., 2012. Temporal changes in the water mass distribution and transports along the 20°W CAIBOX section (NE Atlantic). *Cienc. Mar.* 38, 263–286. doi:10.7773/cm.v38i1B.1793
- Carter, B.R., Radich, J.A., Doyle, H.L., Dickson, A.G., 2013. An automated system for spectrophotometric seawater pH measurements. *Limnol. Oceanogr. Methods* 11, 16–27. doi:10.4319/lom.2013.11.16
- Carter, B.R., Toggweiler, J.R., Key, R.M., Sarmiento, J.L., 2014. Processes determining the marine alkalinity and calcium carbonate saturation state distributions. *Biogeosciences* 11, 7349–7362. doi:10.5194/bg-11-7349-2014
- Castro, C.G., Pérez, F.F., Holley, S.E., Ríos, A.F., 1998. Chemical characterisation and modelling of water masses in the Northeast Atlantic. *Prog. Oceanogr.* 41, 249–279. doi:10.1016/S0079-6611(98)00021-4
- Chen, G.-T., Millero, F.J., 1979. Gradual increase of oceanic CO<sub>2</sub>. *Nature* 277, 205–206. doi:10.1038/277205a0
- Chung, S.-N., Park, G.-H., Lee, K., Key, R.M., Millero, F.J., Feely, R.A., Sabine, C.L., Falkowski, P.G., 2004. Postindustrial enhancement of aragonite undersaturation in the upper tropical and

- subtropical Atlantic Ocean: The role of fossil fuel CO<sub>2</sub>. *Limnol. Oceanogr.* 49, 315–321. doi:10.4319/lo.2004.49.2.0315
- Ciais, P., Sabine, C., Bala, G., Bopp, L., Brovkin, V., Canadell, J., Chhabra, A., DeFries, R., Galloway, J., Heimann, M., Jones, C., Le Quéré, C., Myneni, R.B., Piao, S., Thornton, P., 2013. Carbon and other biogeochemical cycles, in: *Climate Change 2013: The Physical Science Basis. Contribution of Working Group I to the Fifth Assessment Report of the Intergovernmental Panel on Climate Change*. [Stocker, T.F., D. Qin, G.-K. Plattner, M. Tignor, S.K. Allen, J. Boschung, A. Nauels, Y. Xia, V. Bex and P.M. Midgley (eds.)]. Cambridge University Press, Cambridge, United Kingdom and New York, NY, USA. pp. 465–570.
- Clarke, R.A., 1984. Transport through the cape farewell-flemish cap section. *Rapp PV Reun Cons Int Explor Mer* 185, 120–130.
- Clayton, T.D., Byrne, R.H., 1993. Spectrophotometric seawater pH measurements: total hydrogen ion concentration scale calibration of m-cresol purple and at-sea results. *Deep Sea Res. Part Oceanogr. Res. Pap.* 40, 2115–2129. doi:10.1016/0967-0637(93)90048-8
- Cooper, L.W., McClelland, J.W., Holmes, R.M., Raymond, P.A., Gibson, J.J., Guay, C.K., Peterson, B.J., 2008. Flow-weighted values of runoff tracers ( $\delta^{18}\text{O}$ , DOC, Ba, alkalinity) from the six largest Arctic rivers. *Geophys. Res. Lett.* 35, L18606. doi:10.1029/2008GL035007
- Culberson, C.H., 1991. WOCE operations manual (WHP operations and methods), WHPO 91/1. Woods Hole Oceanogr. Inst., Woods Hole, Mass.
- Cunningham, S.A., Haine, T.W.N., 1995. Labrador Sea Water in the eastern North Atlantic. Part II: Mixing dynamics and the advective-diffusive balance. *J. Phys. Oceanogr.* 14, 103–127. doi:10.1175/1520-0485(1995)025<0666:LSWITE>2.0.CO;2
- Curry, R.G., McCartney, M.S., 2001. Ocean Gyre Circulation Changes Associated with the North Atlantic Oscillation\*. *J Phys Ocean.* 31, 3374–3400. doi:10.1175/1520-0485(2001)031<3374:OGCCAW>2.0.CO;2
- Daniault, N., Lherminier, P., Mercier, H., 2011. Circulation and Transport at the Southeast Tip of Greenland. *J. Phys. Oceanogr.* 41, 437–457. doi:10.1175/2010JPO4428.1
- De Boissésou, E., Thierry, V., Mercier, H., Caniaux, G., Desbruyères, D., 2012. Origin, formation and variability of the Subpolar Mode Water located over the Reykjanes Ridge. *J Geophys Res* 117, C12005. doi:10.1029/2011JC007519
- De Jong, M.F., van Aken, H.M., Våge, K., Pickart, R.S., 2012. Convective mixing in the central Irminger Sea: 2002–2010. *Deep Sea Res.* 63, 36–51. doi:10.1016/j.dsr.2012.01.003
- Delhez, E.J.M., Campin, J.-M., Hirst, A.C., Deleersnijder, E., 1999. Toward a general theory of the age in ocean modelling. *Ocean Model.* 1, 17–27. doi:10.1016/S1463-5003(99)00003-7
- Dengler, M., Fischer, J., Schott, F.A., Zantopp, R., 2006. Deep Labrador Current and its variability in 1996–2005. *Geophys. Res. Lett.* 33, L21S06. doi:10.1029/2006GL026702
- Denman, K.L., Brasseur, G., Chidthaisong, A., Ciais, P., Cox, P.M., Dickinson, R.E., Hauglustaine, D., Heinze, C., Holland, E., Jacob, D., Lohmann, U., Ramachandran, S., da Silva Dias, P.L., Wofsy, S.C., Zhang, X., 2007. Chapter 7: Couplings Between Changes in the Climate System and Biogeochemistry, in: *Climate Change 2007: The Physical Science Basis. Contribution of Working Group I to the Fourth Assessment Report of the Intergovernmental Panel on Climate Change*. [Solomon, S., D. Qin, M. Manning, Z. Chen, M. Marquis, K.B. Averyt, M.M.B. Tignor, and H.L. Miller (eds.)]. Cambridge University Press, Cambridge, United Kingdom and New York, NY, USA. pp. 499–587.
- Desbruyères, D., Thierry, V., Mercier, H., 2013. Simulated decadal variability of the meridional overturning circulation across the A25-Ovide section. *J Geophys Res Oceans* 118, 462–475. doi:10.1029/2012JC008342
- DeVries, T., 2014. The oceanic anthropogenic CO<sub>2</sub> sink: Storage, air-sea fluxes, and transports over the industrial era. *Glob. Biogeochem. Cycles* 28, 631–647. doi:10.1002/2013GB004739

- Dickson, A.G., 1993a. The measurement of sea water pH. *Mar. Chem.* 44, 131–142. doi:10.1016/0304-4203(93)90198-W
- Dickson, A.G., 1993b. pH buffers for sea water media based on the total hydrogen ion concentration scale. *Deep Sea Res. Part Oceanogr. Res. Pap.* 40, 107–118. doi:10.1016/0967-0637(93)90055-8
- Dickson, A.G., 1981. An exact definition of total alkalinity and a procedure for the estimation of alkalinity and total inorganic carbon from titration data. *Deep-Sea Res.* 28, 609–623. doi:10.1016/0198-0149(81)90121-7
- Dickson, A., Goyet, C., 1994. Handbook of methods for the analysis of the various parameters of the carbon dioxide system in sea water. Version 2.
- Dickson, A.G., Sabine, C.L., Christian, J.R., 2007. Guide to best practices for ocean CO<sub>2</sub> measurements. *PICES Spec Publ* 3, 191 pp.
- Dickson, A.G., Sabine, C.L., Christian, J.R., 2007. Guide to best practices for ocean CO<sub>2</sub> measurements [WWW Document]. URL [http://cdiac.ornl.gov/oceans/Handbook\\_2007.html](http://cdiac.ornl.gov/oceans/Handbook_2007.html) (accessed 8.22.13).
- Dickson, A., Millero, F., 1987. A comparison of the equilibrium constants for the dissociation of carbonic acid in seawater media. *Deep-Sea Res.* 34, 1733–1743. doi:10.1016/0198-0149(87)90021-5
- Dickson, B., Meincke, J., Vassie, I., Jungclaus, J., Østerhus, S., 1999. Possible predictability in overflow from the Denmark Strait. *Nature* 397, 243–246. doi:10.1038/16680
- Dickson, B., Yashayaev, I., Meincke, J., Turrell, B., Dye, S., Holfort, J., 2002. Rapid freshening of the deep North Atlantic Ocean over the past four decades. *Nature* 416, 832–837. doi:10.1038/416832a
- Dickson, R., Lazier, J., Meincke, J., Rhines, P., Swift, J., 1996. Long-term coordinated changes in the convective activity of the North Atlantic. *Prog. Oceanogr.* 38, 241–295. doi:10.1016/S0079-6611(97)00002-5
- Dickson, R.R., Brown, J., 1994. The production of North Atlantic Deep Water: sources, rates, and pathways. *J. Geophys. Res.* 99, 12319–12. doi:10.1029/94JC00530
- Dickson, R.R., Meincke, J., Rhines, P., 2008. Arctic–Subarctic Ocean Fluxes: Defining the Role of the Northern Seas in Climate, in: *Arctic–Subarctic Ocean Fluxes: Defining the Role of the Northern Seas in Climate*. Springer, pp. 1–13.
- Dietrich, G., 1969. Atlas of the hydrography of the northern North Atlantic Ocean Based on the Polar Front Survey during the International Geophysical Year, winter and summer 1958. Hydrographic Service of the International Council for the Exploration of the Sea, Copenhagen.
- Dlugokencky, E., Tans, P., 2015. NOAA/ESRL ([www.esrl.noaa.gov/gmd/ccgg/trends/](http://www.esrl.noaa.gov/gmd/ccgg/trends/)) [WWW Document]. URL (accessed 3.27.15).
- Doney, S.C., Fabry, V.J., Feely, R.A., Kleypas, J.A., 2009. Ocean acidification: the other CO<sub>2</sub> problem. *Annu Rev Mar. Sci* 1, 169–192. doi:10.1146/annurev.marine.010908.163834
- Dore, J.E., Lukas, R., Sadler, D.W., Church, M.J., Karl, D.M., 2009. Physical and biogeochemical modulation of ocean acidification in the central North Pacific. *Proc. Natl. Acad. Sci.* 106, 12235–12240. doi:10.1073/pnas.0906044106
- Eden, C., Willebrand, J., 2001. Mechanism of Interannual to Decadal Variability of the North Atlantic Circulation. *J Clim.* 14, 2266–2280. doi:10.1175/1520-0442(2001)014<2266:MOITDV>2.0.CO;2
- Emerson, S., Hedges, J., 2008. *Chemical oceanography and the marine carbon cycle*. Cambridge University Press.
- Falina, A., Sarafanov, A., Mercier, H., Lherminier, P., Sokov, A., Daniault, N., 2012. On the Cascading of Dense Shelf Waters in the Irminger Sea. *J Phys Ocean.* 42, 2254–2267. doi:10.1175/JPO-D-12-012.1



- Feely, R.A., Doney, S.C., Cooley, S.R., 2009. Ocean acidification: Present and future changes in a high-CO<sub>2</sub> world. *Oceanography* 22, 36–47. doi:10.5670/oceanog.2009.95
- Feely, R.A., Sabine, C.L., Lee, K., Berelson, W., Kleypas, J., Fabry, V.J., Millero, F.J., 2004. Impact of Anthropogenic CO<sub>2</sub> on the CaCO<sub>3</sub> System in the Oceans. *Science* 305, 362–366. doi:10.1126/science.1097329
- Ferron, B., Kokoszka, F., Mercier, H., Lherminier, P., 2014. Dissipation rate estimates from microstructure and finescale internal wave observations along the A25 Greenland-Portugal OVIDE line. *J. Atmospheric Ocean. Technol.* 31. doi:10.1175/JTECH-D-14-00036.1
- Fiúza, A.F.G., 1984. Hidrologia e dinâmica das águas costeiras de Portugal (Hydrology and dynamics of the Portuguese coastal waters). Ph.D. dissertation, Universidade de Lisboa, 294 pp.
- Flatau, M.K., Talley, L., Niiler, P.P., 2003. The North Atlantic Oscillation, Surface Current Velocities, and SST Changes in the Subpolar North Atlantic. *J. Clim.* 16, 2355–2369. doi:10.1175/2787.1
- Fletcher, C.G., 2005. Investigations into Seasonal Predictability of North Atlantic Winter Climate. Ph.D. dissertation, University of London, 197pp.
- Fletcher, S.E.M., Gruber, N., Jacobson, A.R., Doney, S.C., Dutkiewicz, S., Gerber, M., Follows, M., Joos, F., Lindsay, K., Menemenlis, D., Mouchet, A., Müller, S.A., Sarmiento, J.L., 2006. Inverse estimates of anthropogenic CO<sub>2</sub> uptake, transport, and storage by the ocean. *Glob. Biogeochem. Cycles* 20, GB2002. doi:10.1029/2005GB002530
- Fogelqvist, E., Blindheim, J., Tanhua, T., Østerhus, S., Buch, E., Rey, F., 2003. Greenland–Scotland overflow studied by hydro-chemical multivariate analysis. *Deep Sea Res. Part Oceanogr. Res. Pap.* 50, 73–102. doi:10.1016/S0967-0637(02)00131-0
- Fraga, F., Mouriño, C., Manríquez, M., 1982. Las masas de agua en la costa de Galicia: junio-octubre. *Res Exp Cient* 10, 51–77.
- Freiwald, A., Fosså, H., Grehan, A., Koslow, T., Roberts, J.M., 2004. Cold-water coral reefs: out of sight-no longer out of mind. UNEP-WCMC, Cambridge, UK.
- Friedlingstein, P., Prentice, I.C., 2010. Carbon–climate feedbacks: a review of model and observation based estimates. *Curr. Opin. Environ. Sustain.* 2, 251–257. doi:10.1016/j.cosust.2010.06.002
- Friis, K., Körtzinger, A., Pätsch, J., Wallace, D.W.R., 2005. On the temporal increase of anthropogenic CO<sub>2</sub> in the subpolar North Atlantic. *Deep Sea Res. Part Oceanogr. Res. Pap.* 52, 681–698. doi:10.1016/j.dsr.2004.11.017
- Friis, K., Körtzinger, A., Wallace, D.W.R., 2003. The salinity normalization of marine inorganic carbon chemistry data. *Geophys. Res. Lett.* 30, 4 PP. doi:200310.1029/2002GL015898
- Gammon, R.H., Cline, J., Wisegarver, D., 1982. Chlorofluoromethanes in the northeast Pacific Ocean: Measured vertical distributions and application as transient tracers of upper ocean mixing. *J. Geophys. Res. Oceans* 1978–2012 87, 9441–9454. doi:10.1029/JC087iC12p09441
- Ganachaud, A., Wunsch, C., 2003. Large-Scale Ocean Heat and Freshwater Transports during the World Ocean Circulation Experiment. *J. Clim.* 16, 696–705. doi:10.1175/1520-0442(2003)016<0696:LSOHAF>2.0.CO;2
- García-Ibáñez, M.I., Pardo, P.C., Carracedo, L.I., Mercier, H., Lherminier, P., Ríos, A.F., Pérez, F.F., n.d. Structure, transports and transformations of the water masses in the Atlantic Subpolar Gyre. *Prog. Oceanogr.* doi:10.1016/j.pocean.2015.03.009
- Gattuso, J.-P., Brewer, P.G., Hoegh-Guldberg, O., Kleypas, J.A., Pörtner, H.-O., Schmidt, D.N., 2014. Cross-chapter box on ocean acidification, in: IPCC, 2014: Climate Change 2014: Impacts, Adaptation, and Vulnerability. Part A: Global and Sectoral Aspects. Contribution of Working Group II to the Fifth Assessment Report of the Intergovernmental Panel on Climate Change [Field, C.B., V.R. Barros, D.J. Dokken, K.J. Mach, M.D. Mastrandrea, T.E.



- Bilir, M. Chatterjee, K.L. Ebi, Y.O. Estrada, R.C. Genova, B. Girma, E.S. Kissel, A.N. Levy, S. MacCracken, P.R. Mastrandrea, and L.L.White (eds.)). Cambridge University Press, Cambridge, United Kingdom and New York, NY, USA, Pp. 129-131.
- Gehlen, M., Gruber, N., Gangstø, R., Bopp, L., Oschlies, A., 2011. Biogeochemical consequences of ocean acidification and feedbacks to the earth system, in: *Ocean Acidification*, Vol. 1, Edited by: Gattuso, J.-P. and Hansson, L. Oxford University Press, pp. 230–248.
- González-Dávila, M., Santana-Casiano, J.M., Rueda, M.J., Llinás, O., 2010. The water column distribution of carbonate system variables at the ESTOC site from 1995 to 2004. *Biogeosciences* 7, 3067–3081. doi:10.5194/bg-7-3067-2010
- Gourcuff, C., Lherminier, P., Mercier, H., Le Traon, P.Y., 2011. Altimetry Combined with Hydrography for Ocean Transport Estimation. *J. Atmospheric Ocean. Technol.* 28, 1324–1337. doi:10.1175/2011JTECHO818.1
- Grist, J.P., Marsh, R., Josey, S.A., 2009. On the Relationship between the North Atlantic Meridional Overturning Circulation and the Surface-Forced Overturning Streamfunction. *J. Clim.* 22, 4989–5002. doi:10.1175/2009JCLI2574.1
- Gruber, N., Gloor, M., Fletcher, S.E.M., Doney, S.C., Dutkiewicz, S., Follows, M.J., Gerber, M., Jacobson, A.R., Joos, F., Lindsay, K., Menemenlis, D., Mouchet, A., Müller, S.A., Sarmiento, J.L., Takahashi, T., 2009. Oceanic sources, sinks, and transport of atmospheric CO<sub>2</sub>. *Glob. Biogeochem. Cycles* 23, GB1005. doi:10.1029/2008GB003349
- Gruber, N., Sarmiento, J.L., Stocker, T.F., 1996. An improved method for detecting anthropogenic CO<sub>2</sub> in the oceans. *Glob. Biogeochem. Cycles* 10, 809–837. doi:10.1029/96GB01608
- Gualart, E.F., Fajar, N.M., Padín, X.A., Vázquez-Rodríguez, M., Calvo, E., Ríos, A.F., Hernández-Guerra, A., Pelejero, C., Pérez, F.F., 2015a. Ocean acidification along the 24.5°N section in the subtropical North Atlantic. *Geophys. Res. Lett.* 42, 2014GL062971. doi:10.1002/2014GL062971
- Gualart, E.F., Schuster, U., Fajar, N.M., Legge, O., Brown, P., Pelejero, C., Messias, M.-J., Calvo, E., Watson, A., Ríos, A.F., Pérez, F.F., 2015b. Trends in anthropogenic CO<sub>2</sub> in water masses of the Subtropical North Atlantic Ocean. *Prog. Oceanogr.* 131, 21–32. doi:10.1016/j.pocean.2014.11.006
- Guinotte, J.M., Orr, J., Cairns, S., Freiwald, A., Morgan, L., George, R., 2006. Will human-induced changes in seawater chemistry alter the distribution of deep-sea scleractinian corals? *Front. Ecol. Environ.* 4, 141–146. doi:10.1890/1540-9295(2006)004[0141:WHCISC]2.0.CO;2
- Haine, T.W.N., Curry, B., Gerdes, R., Hansen, E., Karcher, M., Lee, C., Rudels, B., Spreen, G., de Steur, L., Stewart, K.D., Woodgate, R., 2015. Arctic freshwater export: Status, mechanisms, and prospects. *Glob. Planet. Change* 125, 13–35. doi:10.1016/j.gloplacha.2014.11.013
- Haine, T.W.N., Hall, T.M., 2002. A Generalized Transport Theory: Water-Mass Composition and Age. *J. Phys. Oceanogr.* 32, 1932–1946. doi:10.1175/1520-0485(2002)032<1932:AGTTWM>2.0.CO;2
- Häkkinen, S., Rhines, P.B., 2004. Decline of subpolar North Atlantic circulation during the 1990s. *Science* 304, 555–559. doi:10.1126/science.1094917
- Hall, T.M., Haine, T.W.N., Waugh, D.W., 2002. Inferring the concentration of anthropogenic carbon in the ocean from tracers. *Glob. Biogeochem. Cycles* 16, 1131. doi:10.1029/2001GB001835
- Hall, T.M., Plumb, R.A., 1994. Age as a diagnostic of stratospheric transport. *J. Geophys. Res. Atmospheres* 99, 1059–1070. doi:10.1029/93JD03192
- Hall, T.M., Waugh, D.W., Haine, T.W.N., Robbins, P.E., Khatiwala, S., 2004. Estimates of anthropogenic carbon in the Indian Ocean with allowance for mixing and time-varying air-sea CO<sub>2</sub> disequilibrium. *Glob. Biogeochem. Cycles* 18, GB1031.

- Hansen, B., Østerhus, S., 2000. North Atlantic–Nordic Seas exchanges. *Prog. Oceanogr.* 45, 109–208. doi:10.1016/S0079-6611(99)00052-X
- Hansen, H.P., Grassof, K., 1983. Automated chemical analysis, in: *Methods of Seawater Analysis*, 2nd Edition. [K. Grassof, Ehrhardt, M., and Kremling, K. (eds.)], Pp. 347-395. Verlag Chemie, Weinheim.
- Harvey, J., 1982. Theta-S relationships and water masses in the eastern North Atlantic. *Deep Sea Res. Part Oceanogr. Res. Pap.* 29, 1021–1033. doi:10.1016/0198-0149(82)90025-5
- Harvey, J., Arhan, M., 1988. The water masses of the central North Atlantic in 1983-84. *J. Phys. Oceanogr.* 18, 1855–1875. doi:10.1175/1520-0485(1988)018<1855:TWMOTC>2.0.CO;2
- Hátún, H., Sandø, A.B., Drange, H., Hansen, B., Valdimarsson, H., 2005. Influence of the Atlantic subpolar gyre on the thermohaline circulation. *Science* 309, 1841–1844. doi:10.1126/science.1114777
- Hauck, J., Hoppema, M., Bellerby, R.G.J., Völker, C., Wolf-Gladrow, D., 2010. Data-based estimation of anthropogenic carbon and acidification in the Weddell Sea on a decadal timescale. *J. Geophys. Res.* 115, C03004. doi:10.1029/2009JC005479
- Hoegh-Guldberg, O., Mumby, P.J., Hooten, A.J., Steneck, R.S., Greenfield, P., Gomez, E., Harvell, C.D., Sale, P.F., Edwards, A.J., Caldeira, K., others, 2007. Coral reefs under rapid climate change and ocean acidification. *science* 318, 1737–1742. doi:10.1126/science.1152509
- Hurrell, J.W., 1995. Decadal Trends in the North Atlantic Oscillation: Regional Temperatures and Precipitation. *Science* 269, 676–679. doi:10.1126/science.269.5224.676
- Imawaki, S., Bower, A.S., Beal, L., Qiu, B., 2013. Chapter 13 - Western Boundary Currents, in: Gerold Siedler, S.M.G., John Gould and John A. Church (Ed.), *International Geophysics, Ocean Circulation and Climate A 21st Century Perspective*. Academic Press, pp. 305–338.
- IPCC, 2007. *Climate change 2007: The physical science basis*. Agenda 6, 333.
- Iselin, C.O., 1936. A study of the circulation of the western North Atlantic. *Pap. Phys. Oceanogr. Meteorol. Massachusetts Inst. Tech. and Woods Hole Oceanographic Inst.*
- Ito, T., Follows, M.J., Boyle, E.A., 2004. Is AOU a good measure of respiration in the oceans? *Geophys. Res. Lett.* 31, L17305. doi:10.1029/2004GL020900
- Jackson, E.L., Davies, A.J., Howell, K.L., Kershaw, P.J., Hall-Spencer, J.M., 2014. Future-proofing marine protected area networks for cold water coral reefs. *ICES J. Mar. Sci. J. Cons.* 71, 2621–2629. doi:10.1093/icesjms/fsu099
- Jochumsen, K., Quadfasel, D., Valdimarsson, H., Jónsson, S., 2012. Variability of the Denmark Strait overflow: Moored time series from 1996–2011. *J. Geophys. Res. Oceans* 117, C12003. doi:10.1029/2012JC008244
- Johnson, K.M., Sieburth, J.M., Williams, P.J. leB., Brändström, L., 1987. Coulometric total carbon dioxide analysis for marine studies: automation and calibration. *Mar. Chem.* 21, 117–133. doi:10.1016/0304-4203(87)90033-8
- Johnson, K.M., Wallace, D.W.R., 1992. The single-operator multiparameter metabolic analyzer for total carbon dioxide with coulometric detection. *DOE Res. Summ. No 19 Carbon Dioxide Inf. Anal. Cent. Oak Ridge Natl. Lab. TN.*
- Johnson, K.M., Wills, K.D., Butler, D.B., Johnson, W.K., Wong, C.S., 1993. Coulometric total carbon dioxide analysis for marine studies: maximizing the performance of an automated gas extraction system and coulometric detector. *Mar. Chem.* 44, 167–187. doi:10.1016/0304-4203(93)90201-X
- Jonsson, S., Valdimarsson, H., 2004. A new path for the Denmark Strait overflow water from the Iceland Sea to Denmark Strait. *Geophys. Res. Lett.* 31. doi:10.1029/2003GL019214
- Joos, F., Spahni, R., 2008. Rates of change in natural and anthropogenic radiative forcing over the past 20,000 years. *Proc. Natl. Acad. Sci.* 105, 1425–1430. doi:10.1073/pnas.0707386105

- Josey, S.A., Grist, J.P., Marsh, R., 2009. Estimates of meridional overturning circulation variability in the North Atlantic from surface density flux fields. *J Geophys Res* 114, C09022. doi:10.1029/2008JC005230
- Karstensen, J., Tomczak, M., 1998. Age determination of mixed water masses using CFC and oxygen data. *J Geophys Res* 103, 18599–18609. doi:10.1029/98JC00889
- Keeling, C.D., Bacastow, R.B., Bainbridge, A.E., Ekdahl, C.A., Guenther, P.R., Waterman, L.S., Chin, J.F.S., 1976. Atmospheric carbon dioxide variations at Mauna Loa Observatory, Hawaii. *Tellus* 28, 538–551. doi:10.1111/j.2153-3490.1976.tb00701.x
- Key, R.M., Tanhua, T., Olsen, A., Hoppema, M., Jutterström, S., Schirnack, C., van Heuven, S., Kozyr, A., Lin, X., Velo, A., Wallace, D.W.R., Mintrop, L., 2010. The CARINA data synthesis project: Introduction and overview. *Earth Syst. Sci. Data* 2, 105–121. doi:10.5194/essd-2-105-2010
- Khatriwala, S., Primeau, F., Hall, T., 2009. Reconstruction of the history of anthropogenic CO<sub>2</sub> concentrations in the ocean. *Nature* 462, 346–349. doi:10.1038/nature08526
- Khatriwala, S., Tanhua, T., Mikaloff Fletcher, S., Gerber, M., Doney, S.C., Graven, H.D., Gruber, N., McKinley, G.A., Murata, A., Ríos, A.F., Sabine, C.L., 2013. Global ocean storage of anthropogenic carbon. *Biogeosciences* 10, 2169–2191. doi:10.5194/bg-10-2169-2013
- Kieke, D., Klein, B., Stramma, L., Rhein, M., Koltermann, K.P., 2009. Variability and propagation of Labrador Sea Water in the southern subpolar North Atlantic. *Deep Sea Res. Part Oceanogr. Res. Pap.* 56, 1656–1674. doi:10.1016/j.dsr.2009.05.010
- Kieke, D., Rhein, M., Stramma, L., Smethie, W.M., Bullister, J.L., LeBel, D.A., 2007. Changes in the pool of Labrador Sea Water in the subpolar North Atlantic. *Geophys. Res. Lett.* 34, L06605. doi:10.1029/2006GL028959
- Kieke, D., Rhein, M., Stramma, L., Smethie, W.M., LeBel, D.A., Zenk, W., 2006. Changes in the CFC Inventories and Formation Rates of Upper Labrador Sea Water, 1997–2001. *J. Phys. Oceanogr.* 36, 64–86. doi:10.1175/JPO2814.1
- Köhl, A., 2010. Variable source regions of Denmark Strait and Faroe Bank Channel overflow waters. *Tellus A* 551–568. doi:10.1111/j.1600-0870.2010.00454.x
- Krauss, W., 1995. Currents and mixing in the Irminger Sea and in the Iceland Basin. *J Geophys Res* 100, 10851–10871. doi:10.1029/95JC00423
- Lacan, F., Jeandel, C., 2004. Denmark Strait water circulation traced by heterogeneity in neodymium isotopic compositions. *Deep-Sea Res. Part Oceanogr. Res. Pap.* 51, 71–82. doi:10.1016/j.dsr.2003.09.006
- Lamb, M.F., Sabine, C.L., Feely, R.A., Wanninkhof, R., Key, R.M., Johnson, G.C., Millero, F.J., Lee, K., Peng, T.-H., Kozyr, A., Bullister, J.L., Greeley, D., Byrne, R.H., Chipman, D.W., Dickson, A.G., Goyet, C., Guenther, P.R., Ishii, M., Johnson, K.M., Keeling, C.D., Ono, T., Shitashima, K., Tilbrook, B., Takahashi, T., Wallace, D.W.R., Watanabe, Y.W., Winn, C., Wong, C.S., 2001. Consistency and synthesis of Pacific Ocean CO<sub>2</sub> survey data. *Deep Sea Res. Part II Top. Stud. Oceanogr., The US JGOFS Synthesis and Modeling Project: Phase 1* 49, 21–58. doi:10.1016/S0967-0645(01)00093-5
- Langdon, C., Takahashi, T., Sweeney, C., Chipman, D., Goddard, J., Marubini, F., Aceves, H., Barnett, H., Atkinson, M.J., 2000. Effect of calcium carbonate saturation state on the calcification rate of an experimental coral reef. *Glob. Biogeochem Cycles* 14, 639–654. doi:10.1029/1999GB001195
- Lawson, C.L., Hanson, R.J., 1974. Solving least squares problems, *Classics in Applied Mathematics*. Society for Industrial and Applied Mathematics (SIAM).
- Lazier, J., Hendry, R., Clarke, A., Yashayaev, I., Rhines, P., 2002. Convection and restratification in the Labrador Sea, 1990–2000. *Deep Sea Res. Part Oceanogr. Res. Pap.* 49, 1819–1835. doi:10.1016/S0967-0637(02)00064-X
- Lazier, J.R.N., 1973. The renewal of Labrador Sea Water. *Deep Sea Res.* 20, 341–353. doi:10.1016/0011-7471(73)90058-2

- Leffanue, H., Tomczak, M., 2004. Using OMP analysis to observe temporal variability in water mass distribution. *J. Mar. Syst.* 48, 3–14. doi:10.1016/j.jmarsys.2003.07.004
- Le Quéré, C., Moriarty, R., Andrew, R.M., Peters, G.P., Ciais, P., Friedlingstein, P., Jones, S.D., Sitch, S., Tans, P., Arneeth, A., Boden, T.A., Bopp, L., Bozec, Y., Canadell, J.G., Chevallier, F., Cosca, C.E., Harris, I., Hoppema, M., Houghton, R.A., House, J.I., Jain, A., Johannessen, T., Kato, E., Keeling, R.F., Kitidis, V., Klein Goldewijk, K., Koven, C., Landa, C.S., Landschützer, P., Lenton, A., Lima, I.D., Marland, G., Mathis, J.T., Metzl, N., Nojiri, Y., Olsen, A., Ono, T., Peters, W., Pfeil, B., Poulter, B., Raupach, M.R., Regnier, P., Rödenbeck, C., Saito, S., Salisbury, J.E., Schuster, U., Schwinger, J., Séférian, R., Segschneider, J., Steinhoff, T., Stocker, B.D., Sutton, A.J., Takahashi, T., Tilbrook, B., van der Werf, G.R., Viovy, N., Wang, Y.-P., Wanninkhof, R., Wiltshire, A., Zeng, N., 2014. Global carbon budget 2014. *Earth Syst Sci Data Discuss* 7, 521–610. doi:10.5194/essdd-7-521-2014
- Levitus, S., 1983. Climatological Atlas of the World Ocean. *Eos Trans. Am. Geophys. Union* 64, 962–963. doi:10.1029/EO064i049p00962-02
- Lherminier, P., Mercier, H., Gourcuff, C., Alvarez, M., Bacon, S., Kermabon, C., 2007. Transports across the 2002 Greenland-Portugal Ovide section and comparison with 1997. *J. Geophys. Res.* 112, C07003. doi:10.1029/2006JC003716
- Lherminier, P., Mercier, H., Huck, T., Gourcuff, C., Perez, F.F., Morin, P., Sarafanov, A., Falina, A., 2010. The Atlantic Meridional Overturning Circulation and the subpolar gyre observed at the A25-OVIDE section in June 2002 and 2004. *Deep Sea Res. Part Oceanogr. Res. Pap.* 57, 1374–1391. doi:10.1016/j.dsr.2010.07.009
- Liu, X., Patsavas, M.C., Byrne, R.H., 2011. Purification and Characterization of meta-Cresol Purple for Spectrophotometric Seawater pH Measurements. *Environ. Sci. Technol.* 45, 4862–4868.
- Lunden, J.J., McNicholl, C.G., Sears, C.R., Morrison, C.L., Cordes, E.E., 2014. Acute survivorship of the deep-sea coral *Lophelia pertusa* from the Gulf of Mexico under acidification, warming, and deoxygenation. *Glob. Change Future Ocean* 1, 78. doi:10.3389/fmars.2014.00078
- Lux, M., Mercier, H., Arhan, M., 2001. Interhemispheric exchanges of mass and heat in the Atlantic Ocean in January–March 1993. *Deep Sea Res. Part Oceanogr. Res. Pap.* 48, 605–638. doi:10.1016/S0967-0637(00)00033-9
- Macdonald, A.M., Baringer, M.O., Wanninkhof, R., Lee, K., Wallace, D.W.R., 2003. A 1998–1992 comparison of inorganic carbon and its transport across 24.5°N in the Atlantic. *Deep Sea Res. Part II Top. Stud. Oceanogr.* 50, 3041–3064. doi:10.1016/j.dsr2.2003.07.009
- Mackas, D.L., Denman, K.L., Bennett, A.F., 1987. Least squares multiple tracer analysis of water mass composition. *J. Geophys. Res.* 92, 2907–2918. doi:10.1029/JC092iC03p02907
- Macrander, A., Send, U., Valdimarsson, H., Jónsson, S., Käse, R.H., 2005. Interannual changes in the overflow from the Nordic Seas into the Atlantic Ocean through Denmark Strait. *Geophys. Res. Lett.* 32, L06606. doi:10.1029/2004GL021463
- Maier-Reimer, E., Hasselmann, K., 1987. Transport and storage of CO<sub>2</sub> in the ocean—an inorganic ocean-circulation carbon cycle model. *Clim. Dyn.* 2, 63–90. doi:10.1007/BF01054491
- Malmberg, S.A., 1972. Intermediate Polar Water in the Denmark Strait Overflow August 1971. *Int. Counc. Explor. Sea Conf. Meet.* 6, 44–60.
- Mantyla, A.W., 1994. The treatment of inconsistencies in Atlantic deep water salinity data. *Deep Sea Res. Part Oceanogr. Res. Pap.* 41, 1387–1405. doi:10.1016/0967-0637(94)90104-X
- Marsh, R., de Cuevas, B.A., Coward, A.C., Bryden, H.L., Álvarez, M., 2005. Thermohaline circulation at three key sections in the North Atlantic over 1985–2002. *Geophys Res Lett* 32. doi:10.1029/2004GL022281
- Matear, R.J., Lenton, A., 2014. Quantifying the impact of ocean acidification on our future climate. *Biogeosciences* 11, 3965–3983. doi:10.5194/bg-11-3965-2014

- Matsumoto, K., Gruber, N., 2005. How accurate is the estimation of anthropogenic carbon in the ocean? An evaluation of the  $\Delta C^*$  method. *Glob. Biogeochem. Cycles* 19, GB3014. doi:10.1029/2004GB002397
- Mauritzen, C., 1996. Production of dense overflow waters feeding the North Atlantic across the Greenland-Scotland Ridge. Part 1: Evidence for a revised circulation scheme. *Deep Sea Res. Part Oceanogr. Res. Pap.* 43, 769–806. doi:10.1016/0967-0637(96)00037-4
- Mazé, J.P., Arhan, M., Mercier, H., 1997. Volume budget of the eastern boundary layer off the Iberian Peninsula. *Deep Sea Res. Part Oceanogr. Res. Pap.* 44, 1543–1574. doi:10.1016/S0967-0637(97)00038-1
- McCartney, M.S., Mauritzen, C., 2001. On the origin of the warm inflow to the Nordic Seas. *Prog. Oceanogr.* 51, 125–214. doi:10.1016/S0079-6611(01)00084-2
- McCartney, M.S., Talley, L.D., 1982. The subpolar mode water of the North Atlantic Ocean. *J. Phys. Oceanogr.* 12, 1169–1188. doi:10.1175/1520-0485(1982)012<1169:TSMWOT>2.0.CO;2
- McNeil, B.I., Matear, R.J., 2008. Southern Ocean acidification: A tipping point at 450-ppm atmospheric CO<sub>2</sub>. *Proc. Natl. Acad. Sci.* 105, 18860–18864. doi:10.1073/pnas.0806318105
- Mehrbach, C., Culberson, C.H., Hawley, J.E., Pytkowicz, R.M., 1973. Measurement of the apparent dissociation constants of carbonic acid in seawater at atmospheric pressure. *Limnol. Oceanogr.* 897–907. doi:10.4319/lo.1973.18.6.0897
- Mercier, H., 1986. Determining the general circulation of the ocean: A nonlinear inverse problem. *J. Geophys. Res. Oceans* 91, 5103–5109. doi:10.1029/JC091iC04p05103
- Mercier, H., Lherminier, P., Sarafanov, A., Gaillard, F., Daniault, N., Desbruyères, D., Falina, A., Ferron, B., Gourcuff, C., Huck, T., 2015. Variability of the meridional overturning circulation at the Greenland–Portugal OVIDE section from 1993 to 2010. *Prog. Oceanogr.* 132, 250–261. doi:10.1016/j.pocean.2013.11.001
- Midorikawa, T., Ishii, M., Saito, S., Sasano, D., Kosugi, N., Motoi, T., Kamiya, H., Nakadate, A., Nemoto, K., Inoue, H.Y., 2010. Decreasing pH trend estimated from 25-yr time series of carbonate parameters in the western North Pacific. *Tellus B* 62B, 649–659. doi:10.1111/j.1600-0889.2010.00474.x
- Millero, F.J., 2007. The Marine Inorganic Carbon Cycle. *Chem. Rev.* 107, 308–341. doi:10.1021/cr0503557
- Millero, F.J., Huang, F., Woosley, R.J., Letscher, R.T., Hansell, D.A., 2010. Effect of Dissolved Organic Carbon and Alkalinity on the Density of Arctic Ocean Waters. *Aquat. Geochem.* 17, 311–326. doi:10.1007/s10498-010-9111-2
- Millero, F.J., Zhang, J.Z., Lee, K., Campbell, D.M., 1993. Titration alkalinity of seawater. *Mar. Chem.* 44, 153–165. doi:10.1016/0304-4203(93)90200-8
- Mintrop, L., Pérez, F.F., González Dávila, M., Santana-Casiano, J.M., Körtzinger, A., 2000. Alkalinity determination by potentiometry: Intercalibration using three different methods. *Cienc. Mar.* 26, 23–37. doi:10.7773/cm.v26i1.573
- Movilla, J., Gori, A., Calvo, E., Orejas, C., López-Sanz, À., Domínguez-Carrió, C., Grinyó, J., Pelejero, C., 2013. Resistance of Two Mediterranean Cold-Water Coral Species to Low-pH Conditions. *Water* 6, 59–67. doi:10.3390/w6010059
- Mucci, A., 1983. The solubility of calcite and aragonite in seawater at various salinities, temperatures, and one atmosphere total pressure. *Am. J. Sci.* 283, 780–799. doi:10.2475/ajs.283.7.780
- Murata, A., Hayashi, K., Kumamoto, Y., Sasaki, K., 2015. Detecting the progression of ocean acidification from the saturation state of CaCO<sub>3</sub> in the subtropical South Pacific. *Glob. Biogeochem. Cycles* 2014GB004908. doi:10.1002/2014GB004908
- Najjar, R.G., Keeling, R.F., 2000. Mean annual cycle of the air-sea oxygen flux: A global view. *Glob. Biogeochem. Cycles* 14, 573–584. doi:10.1029/1999GB900086

- New, A.L., Barnard, S., Herrmann, P., Molines, J.-M., 2001. On the origin and pathway of the saline inflow to the Nordic Seas: insights from models. *Prog. Oceanogr.* 48, 255–287. doi:10.1016/S0079-6611(01)00007-6
- Olafsson, J., Olafsdottir, S.R., Benoit-Cattin, A., Danielsen, M., Arnarson, T.S., Takahashi, T., 2009. Rate of Iceland Sea acidification from time series measurements. *Biogeosciences* 6, 2661–2668. doi:10.5194/bg-6-2661-2009
- Olafsson, J., Olafsdottir, S.R., Benoit-Cattin, A., Takahashi, T., 2010. The Irminger Sea and the Iceland Sea time series measurements of sea water carbon and nutrient chemistry 1983–2008. *Earth Syst. Sci. Data* 2, 99–104. doi:10.5194/essd-2-99-2010
- Olsen, S.M., Hansen, B., Quadfasel, D., Østerhus, S., 2008. Observed and modelled stability of overflow across the Greenland-Scotland ridge. *Nature* 455, 519–522. doi:10.1038/nature07302
- Olsson, K.A., Jeansson, E., Tanhua, T., Gascard, J.-C., 2005. The East Greenland Current studied with CFCs and released sulphur hexafluoride. *J. Mar. Syst.* 55, 77–95. doi:10.1016/j.jmarsys.2004.07.019
- Ono, T., Watanabe, S., Okuda, K., Fukasawa, M., 1998. Distribution of total carbonate and related properties in the North Pacific along 30°N. *J. Geophys. Res. Oceans* 103, 30873–30883. doi:10.1029/1998JC900018
- Orr, J.C., 2011. Recent and future changes in ocean carbonate chemistry, in: *Ocean Acidification*, Vol. 1, Edited by: Gattuso, J.-P. and Hansson, L. Oxford University Press, pp. 41–66.
- Orr, J.C., Fabry, V.J., Aumont, O., Bopp, L., Doney, S.C., Feely, R.A., Gnanadesikan, A., Gruber, N., Ishida, A., Joos, F., Key, R.M., Lindsay, K., Maier-Reimer, E., Matear, R., Monfray, P., Mouchet, A., Najjar, R.G., Plattner, G.-K., Rodgers, K.B., Sabine, C.L., Sarmiento, J.L., Schlitzer, R., Slater, R.D., Totterdell, I.J., Weirig, M.F., Yamanaka, Y., Yool, A., 2005. Anthropogenic ocean acidification over the twenty-first century and its impact on calcifying organisms. *Nature* 437, 681–686. doi:10.1038/nature04095
- Paillet, J., Arhan, M., McCartney, M.S., 1998. Spreading of Labrador Sea Water in the eastern North Atlantic. *J. Geophys. Res.* 103, 10223–10239. doi:10.1029/98JC00262
- Pardo, P.C., Pérez, F.F., Velo, A., Gilcoto, M., 2012. Water masses distribution in the Southern Ocean: Improvement of an extended OMP (eOMP) analysis. *Prog. Oceanogr.* 103, 92–105. doi:10.1016/j.pocean.2012.06.002
- Pelejero, C., Calvo, E., Hoegh-Guldberg, O., 2010. Paleo-perspectives on ocean acidification. *Trends Ecol. Evol.* 25, 332–344. doi:10.1016/j.tree.2010.02.002
- Pérez, F.F., Fraga, F., 1987. A precise and rapid analytical procedure for alkalinity determination. *Mar. Chem.* 21, 169–182. doi:10.1016/0304-4203(87)90037-5
- Pérez, F.F., Mercier, H., Vázquez-Rodríguez, M., Lherminier, P., Velo, A., Pardo, P.C., Rosón, G., Ríos, A.F., 2013. Atlantic Ocean CO<sub>2</sub> uptake reduced by weakening of the meridional overturning circulation. *Nat. Geosci.* 6, 146–152. doi:10.1038/ngeo1680
- Pérez, F.F., Mouriño, C., Fraga, F., Ríos, A.F., 1993. Displacement of water masses and remineralization rates off the Iberian Peninsula by nutrient anomalies. *J. Mar. Res.* 51, 869–892. doi:10.1357/0022240933223891
- Pérez, F.F., Ríos, A.F., Rellán, T., Alvarez, M., 2000. Improvements in a fast potentiometric seawater alkalinity determination. *Cienc. Mar.* 26, 463–478. doi:10.7773/cm.v26i3.592
- Pérez, F.F., Vázquez-Rodríguez, M., Louarn, E., Padín, X.A., Mercier, H., Ríos, A.F., 2008. Temporal variability of the anthropogenic CO<sub>2</sub> storage in the Irminger Sea. *Biogeosciences* 5, 1669–1679. doi:10.5194/bg-5-1669-2008
- Pérez, F.F., Vázquez-Rodríguez, M., Mercier, H., Velo, A., Lherminier, P., Ríos, A.F., 2010. Trends of anthropogenic CO<sub>2</sub> storage in North Atlantic water masses. *Biogeosciences* 7, 1789–1807. doi:10.5194/bg-7-1789-2010

- Pickart, R.S., 1992. Water mass components of the North Atlantic deep western boundary current. *Deep Sea Res. Part Oceanogr. Res. Pap.* 39, 1553–1572. doi:10.1016/0198-0149(92)90047-W
- Pickart, R.S., Smethie Jr., W.M., Lazier, J.R.N., Jones, E.P., Jenkins, W.J., 1996. Eddies of newly formed upper Labrador Sea water. *J Geophys Res* 101, 20711–20726. doi:10.1029/96JC01453
- Pickart, R.S., Straneo, F., Moore, G.K., 2003. Is Labrador Sea Water formed in the Irminger basin? *Deep Sea Res. Part Oceanogr. Res. Pap.* 50, 23–52. doi:10.1016/S0967-0637(02)00134-6
- Pickart, R.S., Torres, D.J., Fratantoni, P.S., 2005. The East Greenland Spill Jet. *J Phys Ocean.* 35, 1037–1053. doi:10.1175/JPO2734.1
- Pollard, R.T., Griffthts, M.J., Cunningham, S.A., Read, J.F., Pérez, F.F., Ríos, A.F., 1996. Vivaldi 1991 - A study of the formation, circulation and ventilation of Eastern North Atlantic Central Water. *Prog. Oceanogr.* 37, 167–192. doi:10.1016/S0079-6611(96)00008-0
- Pollard, R.T., Pu, S., 1985. Structure and circulation of the upper Atlantic Ocean northeast of the Azores. *Prog. Oceanogr.* 14, 443–462. doi:10.1016/0079-6611(85)90022-9
- Pollard, R.T., Read, J.F., Holliday, N.P., Leach, H., 2004. Water masses and circulation pathways through the Iceland Basin during Vivaldi 1996. *J Geophys Res* 109, C04004. doi:10.1029/2003JC002067
- Pörtner, H.O., Langenbuch, M., Reipschläger, A., 2004. Biological Impact of Elevated Ocean CO<sub>2</sub> Concentrations: Lessons from Animal Physiology and Earth History. *J. Oceanogr.* 60, 705–718. doi:10.1007/s10872-004-5763-0
- Quay, P., Sonnerup, R., Stutsman, J., Maurer, J., Körtzinger, A., Padin, X.A., Robinson, C., 2007. Anthropogenic CO<sub>2</sub> accumulation rates in the North Atlantic Ocean from changes in the 13C/12C of dissolved inorganic carbon. *Glob. Biogeochem. Cycles* 21, GB1009. doi:10.1029/2006GB002761
- Rahmstorf, S., 2002. Ocean circulation and climate during the past 120,000 years. *Nature* 419, 207–214. doi:10.1038/nature01090
- Raven, J.A., Falkowski, P.G., 1999. Oceanic sinks for atmospheric CO<sub>2</sub>. *Plant Cell Environ.* 22, 741–755. doi:10.1046/j.1365-3040.1999.00419.x
- Raven, J., Caldeira, K., Elderfield, H., Hoegh-Guldberg, O., Liss, P., Riebesell, U., Shepherd, J., Turley, C., Watson, A., 2005. Ocean acidification due to increasing atmospheric carbon dioxide. *R. Soc. Lond. Document No.* 12/05.
- Read, J.F., 2000. CONVEX-91: water masses and circulation of the Northeast Atlantic subpolar gyre. *Prog. Oceanogr.* 48, 461–510. doi:10.1016/S0079-6611(01)00011-8
- Reid, J.L., 1979. On the contribution of the Mediterranean Sea outflow to the Norwegian-Greenland Sea. *Deep Sea Res. Part Oceanogr. Res. Pap.* 26, 1199–1223. doi:10.1016/0198-0149(79)90064-5
- Revelle, R., Suess, H.E., 1957. Carbon Dioxide Exchange Between Atmosphere and Ocean and the Question of an Increase of Atmospheric CO<sub>2</sub> during the Past Decades. *Tellus* 9, 18–27. doi:10.1111/j.2153-3490.1957.tb01849.x
- Rhein, M., Fischer, J., Smethie, W.M., Smythe-Wright, D., Weiss, R.F., Mertens, C., Min, D.-H., Fleischmann, U., Putzka, A., 2002. Labrador Sea Water: Pathways, CFC inventory, and formation rates. *J. Phys. Oceanogr.* 32, 648–665. doi:10.1175/1520-0485(2002)032<0648:LSWPCI>2.0.CO;2
- Rhein, M., Kieke, D., Hüttl-Kabus, S., Roessler, A., Mertens, C., Meissner, R., Klein, B., Böning, C.W., Yashayaev, I., 2011. Deep water formation, the subpolar gyre, and the meridional overturning circulation in the subpolar North Atlantic. *Deep Sea Res. Part II Top. Stud. Oceanogr.* 58, 1819–1832. doi:10.1016/j.dsr2.2010.10.061



- Rhein, M., Kieke, D., Steinfeldt, R., 2015. Advection of North Atlantic Deep Water from the Labrador Sea to the southern hemisphere. *J. Geophys. Res. Oceans* n/a–n/a. doi:10.1002/2014JC010605
- Rhein, M., Kieke, D., Steinfeldt, R., 2007. Ventilation of the Upper Labrador Sea Water, 2003–2005. *Geophys. Res. Lett.* 34, L06603. doi:10.1029/2006GL028540
- Rhein, M., Rintoul, S.R., Aoki, S., Campos, E., Chambers, D., Feely, R.A., Gulev, S., Johnson, G.C., Josey, S.A., Kostianoy, A., Mauritzen, C., Roemmich, D., Talley, L.D., Wang, F., 2013. Observations: Ocean, in: *Climate Change 2013: The Physical Science Basis. Contribution of Working Group I to the Fifth Assessment Report of the Intergovernmental Panel on Climate Change.* [Stocker, T.F., D. Qin, G.-K. Plattner, M. Tignor, S.K. Allen, J. Boschung, A. Nauels, Y. Xia, V. Bex and P.M. Midgley (eds.)]. Cambridge University Press, Cambridge, United Kingdom and New York, NY, USA. Cambridge University Press, Cambridge, United Kingdom and New York, NY, USA, pp. 255–316.
- Ridgwell, A., Zeebe, R.E., 2005. The role of the global carbonate cycle in the regulation and evolution of the Earth system. *Earth Planet. Sci. Lett.* 234, 299–315. doi:10.1016/j.epsl.2005.03.006
- Riebesell, U., Zondervan, I., Rost, B., Tortell, P.D., Zeebe, R.E., Morel, F.M.M., 2000. Reduced calcification of marine plankton in response to increased atmospheric CO<sub>2</sub>. *Nature* 407, 364–367. doi:10.1038/35030078
- Ríos, A.F., Álvarez-Salgado, X.A., Pérez, F.F., Bingler, L.S., Arístegui, J., Mémerly, L., 2003. Carbon dioxide along WOCE line A14: Water masses characterization and anthropogenic entry. *J. Geophys. Res.* 108, 3123. doi:10.1029/2000JC000366
- Ríos, A.F., Pérez, F.F., Fraga, F., 1992. Water masses in the upper and middle North Atlantic Ocean east of the Azores. *Deep Sea Res. Part Oceanogr. Res. Pap.* 39, 645–658. doi:10.1016/0198-0149(92)90093-9
- Ríos, A.F., Resplandy, L., García-Ibáñez, M.I., Fajar, N.M., Velo, A., Padin, X.A., Wanninkhof, R., Steinfeldt, R., Roson, G., Pérez, F.F., Submitted. Decadal acidification in the water masses of the Atlantic Ocean. *Proc. Natl. Acad. Sci. U. S. A.*
- Rodolfo-Metalpa, R., Montagna, P., Aliani, S., Borghini, M., Canese, S., Hall-Spencer, J.M., Foggo, A., Milazzo, M., Taviani, M., Houlbrèque, F., 2015. Calcification is not the Achilles' heel of cold-water corals in an acidifying ocean. *Glob. Change Biol.* 21, 2238–2248. doi:10.1111/gcb.12867
- Rogers, J.C., 1984. The association between the North Atlantic Oscillation and the Southern Oscillation in the Northern Hemisphere. *Mon Wea Rev* 112, 1999–2015. doi:10.1175/1520-0493(1984)112<1999:TABTNA>2.0.CO;2
- Rosón, G., Ríos, A.F., Pérez, F.F., Lavin, A., Bryden, H.L., 2003. Carbon distribution, fluxes, and budgets in the subtropical North Atlantic Ocean (24.5°N). *J. Geophys. Res. Oceans* 1978–2012 108, 3144. doi:10.1029/1999JC000047
- Rossby, T., 1999. On gyre interactions. *Deep Sea Res. Part II Top. Stud. Oceanogr.* 46, 139–164. doi:10.1016/S0967-0645(98)00095-2
- Rossby, T., 1996. The North Atlantic Current and surrounding waters: At the crossroads. *Rev. Geophys.* 34, 463–481. doi:10.1029/96RG02214
- Ross, C.K., 1984. Temperature–salinity characteristics of the “overflow” water in Denmark Strait during “OVERFLOW’73.” *Rapp PV Reun Cons Int Explor Mer* 185, 111–119.
- Rudels, B., Eriksson, P., Buch, E., Budéus, G., Fahrbach, E., Malmberg, S.A., Meincke, J., Mälkki, P., 2003. Temporal switching between sources of the Denmark Strait overflow water. *ICES Mar. Sci. Symp* 319–325.
- Rudels, B., Fahrbach, E., Meincke, J., Budéus, G., Eriksson, P., 2002. The East Greenland Current and its contribution to the Denmark Strait overflow. *ICES J. Mar. Sci. J. Cons.* 59, 1133–1154. doi:10.1006/jmsc.2002.1284

- Rudels, B., J Friedrich, H., Quadfasel, D., 1999. The Arctic circumpolar boundary current. *Deep Sea Res. Part II Top. Stud. Oceanogr.* 46, 1023–1062. doi:10.1016/S0967-0645(99)00015-6
- Sabine, C.L., Feely, R.A., Gruber, N., Key, R.M., Lee, K., Bullister, J.L., Wanninkhof, R., Wong, C.S., Wallace, D.W.R., Tilbrook, B., Millero, F.J., Peng, T.-H., Kozyr, A., Ono, T., Rios, A.F., 2004. The Oceanic Sink for Anthropogenic CO<sub>2</sub>. *Science* 305, 367–371. doi:10.1126/science.1097403
- Santana-Casiano, J.M., González-Dávila, M., Rueda, M.-J., Llinás, O., González-Dávila, E.-F., 2007. The interannual variability of oceanic CO<sub>2</sub> parameters in the northeast Atlantic subtropical gyre at the ESTOC site. *Glob. Biogeochem. Cycles* 21, GB1015. doi:10.1029/2006GB002788
- Sarafanov, A., 2009. On the effect of the North Atlantic Oscillation on temperature and salinity of the subpolar North Atlantic intermediate and deep waters. *ICES J. Mar. Sci.* 66, 1448–1454. doi:10.1093/icesjms/fsp094
- Sarafanov, A., Falina, A., Mercier, H., Sokov, A., Lherminier, P., Gourcuff, C., Gladyshev, S., Gaillard, F., Daniault, N., 2012. Mean full-depth summer circulation and transports at the northern periphery of the Atlantic Ocean in the 2000s. *J Geophys Res* 117, C01014. doi:10.1029/2011JC007572
- Sarafanov, A., Falina, A., Sokov, A., Demidov, A., 2008. Intense warming and salinification of intermediate waters of southern origin in the eastern subpolar North Atlantic in the 1990s to mid-2000s. *J. Geophys. Res. Oceans* 113, C12022. doi:10.1029/2008JC004975
- Sarafanov, A., Mercier, H., Falina, A., Sokov, A., Lherminier, P., 2010. Cessation and partial reversal of deep water freshening in the northern North Atlantic: observation-based estimates and attribution. *Tellus A* 62, 80–90. doi:10.1111/j.1600-0870.2009.00418.x
- Sarmiento, J.L., Orr, J.C., Siegenthaler, U., 1992. A perturbation simulation of CO<sub>2</sub> uptake in an ocean general circulation model. *J. Geophys. Res. Oceans* 1978–2012 97, 3621–3645. doi:10.1029/91JC02849
- Saunders, M.A., Qian, B., 2002. Seasonal predictability of the winter NAO from North Atlantic sea surface temperatures. *Geophys Res Lett* 29. doi:10.1029/2002GL014952
- Saunders, P.M., 2001. The dense northern overflows, in: *Ocean Circulation and Climate*, Edited by G. Siedler, J. Church, and J. Gould. Academic, New York, pp. 401–417.
- Saunders, P.M., 1996. The Flux of Dense Cold Overflow Water Southeast of Iceland. *J Phys Ocean.* 26, 85–95. doi:10.1175/1520-0485(1996)026<0085:TFODCO>2.0.CO;2
- Saunders, P.M., 1986. The accuracy of measurements of salinity, oxygen and temperature in the deep ocean. *J Phys Ocean.* 16, 189–195. doi:10.1175/1520-0485(1986)016<0189:TAOMOS>2.0.CO;2
- Schmitz, W.J.J., 1996. On the World Ocean Circulation: Volume I: some global features/North Atlantic Circulation. Woods Hole Oceanogr. Inst. Tech. Rep. WHOI-96-03, 150 pp.[Available from Woods Hole Oceanographic Institution, Woods Hole, MA 02543.].
- Schmitz, W.J., McCartney, M.S., 1993. On the North Atlantic Circulation. *Rev. Geophys.* 31, 29–49. doi:10.1029/92RG02583
- Schott, F.A., Brandt, P., 2007. Circulation and deep water export of the subpolar North Atlantic during the 1990s, in: *Ocean Circulation: Mechanisms and Impacts*. *Geophys. Monogr. Ser.*, Vol. 173, Edited by A. Schmittner, J. Chiang, and S. Hemmings, Pp. 91-118, AGU, Washington, D.C.
- Seager, R., Battisti, D.S., Yin, J., Gordon, N., Naik, N., Clement, A.C., Cane, M.A., 2002. Is the Gulf Stream responsible for Europe's mild winters? *Q. J. R. Meteorol. Soc.* 128, 2563–2586. doi:10.1256/qj.01.128
- Shapiro, G.I., Meschanov, S.L., 1996. Spreading pattern and mesoscale structure of Mediterranean outflow in the Iberian Basin estimated from historical data. *J. Mar. Syst.* 7, 337–348. doi:10.1016/0924-7963(95)00011-9

- Smethie, W.M.J., Fine, R.A., 2001. Rates of North Atlantic Deep Water formation calculated from chlorofluorocarbon inventories. *Deep-Sea Res. Part Oceanogr. Res. Pap.* 1, 189–215. doi:10.1016/S0967-0637(00)00048-0
- Smethie, W.M.J., Swift, J.H., 1989. The tritium: krypton-85 age of Denmark Strait overflow water and Gibbs Fracture Zone water just south of Denmark Strait. *J. Geophys. Res.* 94, 8265–8275. doi:10.1029/JC094iC06p08265
- Smith, L.C., Pavelsky, T.M., MacDonald, G.M., Shiklomanov, A.I., Lammers, R.B., 2007. Rising minimum daily flows in northern Eurasian rivers: A growing influence of groundwater in the high-latitude hydrologic cycle. *J. Geophys. Res. Biogeosciences* 112, G04S47. doi:10.1029/2006JG000327
- Steinfeldt, R., Rhein, M., Bullister, J.L., Tanhua, T., 2009. Inventory changes in anthropogenic carbon from 1997–2003 in the Atlantic Ocean between 20°S and 65°N. *Glob. Biogeochem. Cycles* 23, GB3010. doi:10.1029/2008GB003311
- Stoll, M.H.C., van Aken, H.M., de Baar, H.J.W., Kraak, M., 1996. Carbon dioxide characteristics of water masses in the northern North Atlantic Ocean. *Mar. Chem.* 55, 217–232. doi:10.1016/S0304-4203(96)00058-8
- Stommel, H., 1958. A survey of ocean current theory. *Deep Sea Res.* 1953 4, 149–184. doi:10.1016/0146-6313(56)90048-X
- Stramma, L., Kieke, D., Rhein, M., Schott, F., Yashayaev, I., Koltermann, K.P., 2004. Deep water changes at the western boundary of the subpolar North Atlantic during 1996 to 2001. *Deep Sea Res. Part Oceanogr. Res. Pap.* 51, 1033–1056. doi:10.1016/j.dsr.2004.04.001
- Straneo, F., Pickart, R.S., Lavender, K., 2003. Spreading of Labrador sea water: an advective-diffusive study based on Lagrangian data. *Deep Sea Res. Part Oceanogr. Res. Pap.* 50, 701–719. doi:10.1016/S0967-0637(03)00057-8
- Strass, V.H., Fahrbach, E., Schauer, U., Sellmann, L., 1993. Formation of Denmark Strait overflow water by mixing in the East Greenland Current. *J. Geophys. Res. Oceans* 1978–2012 98, 6907–6919. doi:10.1029/92JC02732
- Strömngren, T., 1971. Vertical and Horizontal Distribution of *Lophelia Pertusa* (Linné) in Trondheimsfjorden on the West Coast of Norway. *K Norske Vidensk Sfr.*
- Sutherland, D.A., Pickart, R.S., 2008. The East Greenland coastal current: Structure, variability, and forcing. *Prog. Oceanogr.* 78, 58–77. doi:10.1016/j.pocean.2007.09.006
- Swift, J.H., Aagaard, K., 1981. Seasonal transitions and water mass formation in the Iceland and Greenland seas. *Deep Sea Res. Part Oceanogr. Res. Pap.* 28, 1107–1129. doi:10.1016/0198-0149(81)90050-9
- Swift, J.H., Aagaard, K., Malmberg, S.-A., 1980. The contribution of the Denmark Strait overflow to the deep North Atlantic. *Deep Sea Res. Part Oceanogr. Res. Pap.* 27, 29–42. doi:10.1016/0198-0149(80)90070-9
- Sy, A., Rhein, M., Lazier, J.R.N., Koltermann, K.P., Meincke, J., Putzka, A., Bersch, M., 1997. Surprisingly rapid spreading of newly formed intermediate waters across the North Atlantic Ocean. *Nature* 386, 675–679. doi:10.1038/386675a0
- Takahashi, T., Brewer, P., 1986. Hydrographic and chemistry data for the TTO/NAS expedition, April — October, 1981: Revised carbon chemistry data. *Lett. CDIAC Carbon Dioxide Inf Anal Cent Oak Ridge Natl Lab Oak Ridge Tenn.*
- Takahashi, T., Broecker, W.S., Langer, S., 1985. Redfield ratio based on chemical data from isopycnal surfaces. *J. Geophys. Res.* 90, 6907–6924. doi:10.1029/JC090iC04p06907
- Takahashi, T., Sutherland, S.C., Chipman, D.W., Goddard, J.G., Ho, C., Newberger, T., Sweeney, C., Munro, D.R., 2014. Climatological distributions of pH, pCO<sub>2</sub>, total CO<sub>2</sub>, alkalinity, and CaCO<sub>3</sub> saturation in the global surface ocean, and temporal changes at selected locations. *Mar. Chem.* 164, 95–125. doi:10.1016/j.marchem.2014.06.004

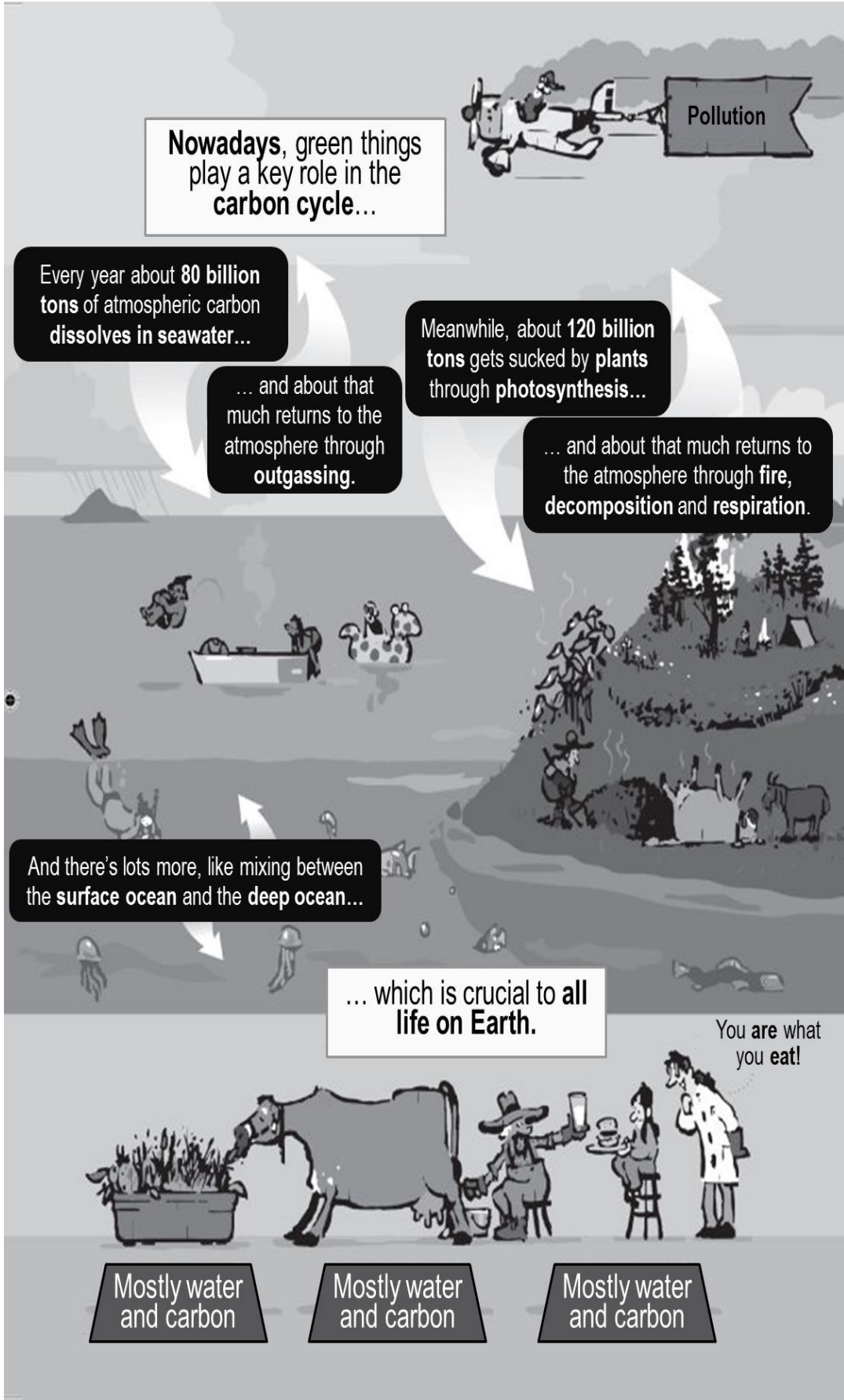
- Takahashi, T., Sutherland, S.C., Sweeney, C., Poisson, A., Metzl, N., Tilbrook, B., Bates, N., Wanninkhof, R., Feely, R.A., Sabine, C., Olafsson, J., Nojiri, Y., 2002. Global sea-air CO<sub>2</sub> flux based on climatological surface ocean pCO<sub>2</sub>, and seasonal biological and temperature effects. *Deep Sea Res. Part II Top. Stud. Oceanogr.* 49, 1601–1622. doi:10.1016/S0967-0645(02)00003-6
- Talley, L.D., McCartney, M.S., 1982. Distribution and circulation of Labrador Sea Water. *J Phys Ocean.* 12, 1189–1205. doi:10.1175/1520-0485(1982)012<1189:DACOLS>2.0.CO;2
- Talley, L.D., Pickard, G.L., Emery, W.J., Swift, J.H., 2011. *Descriptive physical oceanography: an introduction.*, 6th Edititon. ed. Elsevier, London.
- Tanhua, T., Biastoch, A., Körtzinger, A., Lüger, H., Böning, C., Wallace, D.W.R., 2006. Changes of anthropogenic CO<sub>2</sub> and CFCs in the North Atlantic between 1981 and 2004. *Glob. Biogeochem. Cycles* 20, GB4017. doi:10.1029/2006GB002695
- Tanhua, T., Olsson, K.A., Jeansson, E., 2008. Tracer Evidence of the Origin and Variability of Denmark Strait Overflow Water, in: Dickson, R.R., Meincke, J., Rhines, P. (Eds.), *Arctic–Subarctic Ocean Fluxes*. Springer Netherlands, pp. 475–503.
- Tanhua, T., Olsson, K.A., Jeansson, E., 2005. Formation of Denmark Strait overflow water and its hydro-chemical composition. *J. Mar. Syst.* 57, 264–288. doi:10.1016/j.jmarsys.2005.05.003
- Tans, P., 2012. NOAA/ESRL ([www.esrl.noaa.gov/gmd/ccgg](http://www.esrl.noaa.gov/gmd/ccgg)) [WWW Document]. URL (accessed 3.27.15).
- Tarantola, A., 2005. *Inverse problem theory and methods for model parameter estimation*. Society for Industrial and Applied Mathematics (SIAM), Philadelphia.
- Thierry, V., De Boissésou, E., Mercier, H., 2008. Interannual variability of the Subpolar Mode Water properties over the Reykjanes Ridge during 1990–2006. *J. Geophys. Res.* 113, C04016. doi:10.1029/2007JC004443
- Thompson, R.O., Edwards, R.J., 1981. Mixing and water-mass formation in the Australian Subantarctic. *J. Phys. Oceanogr.* 11, 1399–1406. doi:10.1175/1520-0485(1981)011<1399:MAWMFI>2.0.CO;2
- Tjiputra, J.F., Assmann, K., Heinze, C., 2010. Anthropogenic carbon dynamics in the changing ocean. *Ocean Sci.* 6, 605–614. doi:10.5194/os-6-605-2010
- Tomczak, M., 1999. Some historical, theoretical and applied aspects of quantitative water mass analysis. *J. Mar. Res.* 57, 275–303. doi:10.1357/002224099321618227
- Tomczak, M., 1981. A multi-parameter extension of temperature/salinity diagram techniques for the analysis of non-isopycnal mixing. *Prog. Oceanogr.* 10, 147–171. doi:10.1016/0079-6611(81)90010-0
- Tomczak, M., Godfrey, J.S., 1994. *Regional Oceanography: An Introduction*. Elsevier.
- Tomczak, M., Large, D.G., 1989. Optimum multiparameter analysis of mixing in the thermocline of the eastern Indian Ocean. *J. Geophys. Res.* 94, 16141–16149. doi:10.1029/JC094iC11p16141
- Touratier, F., Azouzi, L., Goyet, C., 2007. CFC-11, Δ14C and 3H tracers as a means to assess anthropogenic CO<sub>2</sub> concentrations in the ocean. *Tellus B* 59, 318–325. doi:10.1111/j.1600-0889.2006.00247.x
- Trigo, R.M., Osborn, T.J., Corte-Real, J.M., 2002. The North Atlantic Oscillation influence on Europe: climate impacts and associated physical mechanisms. *Clim Res* 20, 9–17. doi:10.3354/cr020009
- Tsuchiya, M., Talley, L.D., McCartney, M.S., 1992. An eastern Atlantic section from Iceland southward across the equator. *Deep Sea Res. Part Oceanogr. Res. Pap.* 39, 1885–1917. doi:10.1016/0198-0149(92)90004-D

- Turley, C., 2005. The other CO<sub>2</sub> problem [WWW Document]. openDemocracy. URL [https://www.opendemocracy.net/globalization-climate\\_change\\_debate/article\\_2480.jsp](https://www.opendemocracy.net/globalization-climate_change_debate/article_2480.jsp) (accessed 3.27.15).
- Turley, C., Eby, M., Ridgwell, A.J., Schmidt, D.N., Findlay, H.S., Brownlee, C., Riebesell, U., Fabry, V.J., Feely, R.A., Gattuso, J.-P., 2010. The societal challenge of ocean acidification. *Mar. Pollut. Bull.* 60, 787–792. doi:10.1016/j.marpolbul.2010.05.006
- UNESCO, 1981. Background papers and supporting data on the practical salinity scale, 1978. Unesco technical papers in marine science.
- Våge, K., Pickart, R.S., Thierry, V., Reverdin, G., Lee, C.M., Petrie, B., Agnew, T.A., Wong, A., Ribergaard, M.H., 2009. Surprising return of deep convection to the subpolar North Atlantic Ocean in winter 2007–2008. *Nat. Geosci.* 2, 67–72. doi:10.1038/ngeo382
- Van Aken, H.M., 2000a. The hydrography of the mid-latitude Northeast Atlantic Ocean: II: The intermediate water masses. *Deep Sea Res. Part Oceanogr. Res. Pap.* 47, 789–824. doi:10.1016/S0967-0637(99)00112-0
- Van Aken, H.M., 2000b. The hydrography of the mid-latitude northeast Atlantic Ocean: I: The deep water masses. *Deep Sea Res. Part Oceanogr. Res. Pap.* 47, 757–788. doi:10.1016/S0967-0637(99)00092-8
- Van Aken, H.M., Becker, G., 1996. Hydrography and through-flow in the north-eastern North Atlantic Ocean: the NANSEN project. *Prog. Oceanogr.* 38, 297–346. doi:10.1016/S0079-6611(97)00005-0
- Van Aken, H.M., de Boer, C.J., 1995. On the synoptic hydrography of intermediate and deep water masses in the Iceland Basin. *Deep Sea Res. Part Oceanogr. Res. Pap.* 42, 165–189. doi:10.1016/0967-0637(94)00042-Q
- Van Aken, H.M., de Jong, M.F., 2012. Hydrographic variability of Denmark Strait Overflow Water near Cape Farewell with multi-decadal to weekly time scales. *Deep Sea Res. Part Oceanogr. Res. Pap.* 66, 41–50. doi:10.1016/j.dsr.2012.04.004
- Van Vuuren, D.P., Edmonds, J., Kainuma, M., Riahi, K., Thomson, A., Hibbard, K., Hurtt, G.C., Kram, T., Krey, V., Lamarque, J.-F., Masui, T., Meinshausen, M., Nakicenovic, N., Smith, S.J., Rose, S.K., 2011. The representative concentration pathways: an overview. *Clim. Change* 109, 5–31. doi:10.1007/s10584-011-0148-z
- Vázquez-Rodríguez, M., Padin, X.A., Pardo, P.C., Ríos, A.F., Pérez, F.F., 2012a. The subsurface layer reference to calculate preformed alkalinity and air–sea CO<sub>2</sub> disequilibrium in the Atlantic Ocean. *J. Mar. Syst.* 94, 52–63. doi:10.1016/j.jmarsys.2011.10.008
- Vázquez-Rodríguez, M., Padin, X.A., Ríos, A.F., Bellerby, R.G.J., Pérez, F.F., 2009a. An upgraded carbon-based method to estimate the anthropogenic fraction of dissolved CO<sub>2</sub> in the Atlantic Ocean. *Biogeosciences Discuss.* 6, 4527–4571. doi:10.5194/bgd-6-4527-2009
- Vázquez-Rodríguez, M., Pérez, F.F., Velo, A., Ríos, A.F., Mercier, H., 2012b. Observed acidification trends in North Atlantic water masses. *Biogeosciences* 9, 5217–5230. doi:10.5194/bg-9-5217-2012
- Vázquez-Rodríguez, M., Touratier, F., Lo Monaco, C., Waugh, D.W., Padin, X.A., Bellerby, R.G.J., Goyet, C., Metzl, N., Ríos, A.F., Pérez, F.F., 2009b. Anthropogenic carbon distributions in the Atlantic Ocean: data-based estimates from the Arctic to the Antarctic. *Biogeosciences* 6, 439–451. doi:10.5194/bg-6-439-2009
- Visbeck, M., 2002. Deep Velocity Profiling Using Lowered Acoustic Doppler Current Profilers: Bottom Track and Inverse Solutions\*. *J. Atmospheric Ocean. Technol.* 19, 794–807. doi:10.1175/1520-0426(2002)019<0794:DVPULA>2.0.CO;2
- Von Appen, W.-J., Koszalka, I.M., Pickart, R.S., Haine, T.W.N., Mastropole, D., Magaldi, M.G., Valdimarsson, H., Girton, J., Jochumsen, K., Krahnemann, G., 2014. The East Greenland Spill Jet as an important component of the Atlantic Meridional Overturning Circulation. *Deep-Sea Res. Part Oceanogr. Res. Pap.* 92, 75–84. doi:10.1016/j.dsr.2014.06.002

- Wakita, M., Watanabe, S., Honda, M., Nagano, A., Kimoto, K., Matsumoto, K., Kitamura, M., Sasaki, K., Kawakami, H., Fujiki, T., Sasaoka, K., Nakano, Y., Murata, A., 2013. Ocean acidification from 1997 to 2011 in the subarctic western North Pacific Ocean. *Biogeosciences* 10, 7817–7827. doi:10.5194/bg-10-7817-2013
- Walker, G.T., Bliss, E.W., 1932. World weather V. *Mem Roy Met Soc* 4, 53–84.
- Wallace, D.W.R., 1995. Monitoring global ocean carbon inventories. Ocean Observing System Development Panel.
- Wallace, W.R., 2001. Storage and transport of excess CO<sub>2</sub> in the oceans: The JGOFS/WOCE global CO<sub>2</sub> survey, in: *Ocean Circulation and Climate*, Edited by G. Siedler, J. Church, and J. Gould. pp. 489–521.
- Wanninkhof, R., Doney, S.C., Bullister, J.L., Levine, N.M., Warner, M., Gruber, N., 2010. Detecting anthropogenic CO<sub>2</sub> changes in the interior Atlantic Ocean between 1989 and 2005. *J. Geophys. Res. Oceans* 115, C11028. doi:10.1029/2010JC006251
- Watson, A.J., Nightingale, P.D., Cooper, D.J., Leach, H., Follows, M., 1995. Modelling Atmosphere-Ocean CO<sub>2</sub> Transfer [and Discussion]. *Philos. Trans. Biol. Sci.* 348, 125–132. doi:10.1098/rstb.1995.0054
- Wauth, D.W., Haine, T.W.N., Hall, T.M., 2004. Transport times and anthropogenic carbon in the subpolar North Atlantic Ocean. *Deep Sea Res. Part Oceanogr. Res. Pap.* 51, 1475–1491. doi:10.1016/j.dsr.2004.06.011
- Weiss, R.F., 1974. Carbon dioxide in water and seawater: the solubility of a non-ideal gas. *Mar. Chem.* 2, 203–215. doi:10.1016/0304-4203(74)90015-2
- Willebrand, J., Barnier, B., Böning, C., Dieterich, C., Killworth, P.D., Le Provost, C., Jia, Y., Molines, J.-M., New, A.L., 2001. Circulation characteristics in three eddy-permitting models of the North Atlantic. *Prog. Oceanogr.* 48, 123–161. doi:10.1016/S0079-6611(01)00003-9
- Worthington, L.V., 1976. *On the North Atlantic Circulation*. Johns Hopkins University Press Baltimore.
- Wüst, G., Defant, A., 1936. Atlas zur Schichtung und Zirkulation des Atlantischen Ozeans. *Wissenschaftliche Ergebnisse : Deutsche Atlantische Expedition auf dem Forschungs- und Vermessungsschiff "Meteor" 1925–1927* 6, 103.
- Xu, X., Hurlburt, H.E., Schmitz Jr., W.J., Zantopp, R., Fischer, J., Hogan, P.J., 2013. On the currents and transports connected with the atlantic meridional overturning circulation in the subpolar North Atlantic. *J Geophys Res Oceans* 118, 502–516. doi:10.1002/jgrc.20065
- Xu, X., Schmitz Jr, W.J., Hurlburt, H.E., Hogan, P.J., Chassignet, E.P., 2010. Transport of Nordic Seas overflow water into and within the Irminger Sea: An eddy-resolving simulation and observations. *J Geophys Res* 115. doi:10.1029/2010JC006351
- Yashayaev, I., 2007. Hydrographic changes in the Labrador Sea, 1960-2005. *Prog. Oceanogr.* 73, 242–276. doi:10.1016/j.pcean.2007.04.015
- Yashayaev, I., Bersch, M., van Aken, H.M., 2007a. Spreading of the Labrador Sea Water to the Irminger and Iceland basins. *Geophys Res Lett* 34, L10602. doi:10.1029/2006GL028999
- Yashayaev, I., Dickson, R.R., 2008. Transformation and fate of overflows in the Northern North Atlantic, in: *Arctic-Subarctic Ocean Fluxes: Defining the Role of the Northern Seas in Climate*. Springer Science+Business Media B.V., P.O. Box 17, AA Dordrecht, The Netherlands, pp. 505–526.
- Yashayaev, I., Holliday, N.P., Bersch, M., van Aken, H.M., 2008. The History of the Labrador Sea Water: Production, Spreading, Transformation and Loss, in: Dickson, R.R., Meincke, J., Rhines, P. (Eds.), *Arctic-Subarctic Ocean Fluxes: Defining the Role of the Northern Seas in Climate*. Springer Netherlands, pp. 569–612.
- Yashayaev, I., Loder, J.W., 2009. Enhanced production of Labrador Sea Water in 2008. *Geophys. Res. Lett.* 36, n/a–n/a. doi:10.1029/2008GL036162

- Yashayaev, I., van Aken, H.M., Holliday, N.P., Bersch, M., 2007b. Transformation of the Labrador Sea Water in the subpolar North Atlantic. *Geophys Res Lett* 34, L22605.  
doi:10.1029/2007GL031812
- Zeebe, R.E., Wolf-Gladrow, D.A., Jansen, H., 1999. On the time required to establish chemical and isotopic equilibrium in the carbon dioxide system in seawater. *Mar. Chem.* 65, 135–153.  
doi:10.1016/S0304-4203(98)00092-9
- Zeebe, R., Wolf-Gladrow, D., 2001. CO<sub>2</sub> in seawater: equilibrium, kinetics, isotopes. Elsevier Science.
- Zenk, W., 1975. On the Mediterranean outflow west of Gibraltar. *Meteor Forschungsergeb* 16, 23–24.
- Zibrowius, H., 1980. Les scléroractiniales de la Méditerranée et de l'Atlantique nord-oriental. Mémoires de l'Institut océanographique, Monaco.





Hoy en día, "las cosas verdes" tienen un papel fundamental en el ciclo del carbono...



Cada año cerca de 80 mil millones de toneladas de carbono atmosférico se disuelven en el océano...

Cerca de 120 mil millones de toneladas son tomadas por las plantas mediante la fotosíntesis...

... y aproximadamente lo mismo vuelve a la atmósfera por desgasificación.

... y aproximadamente lo mismo vuelve a la atmósfera debido a incendios, descomposición y respiración.

Y hay mucho más, como la mezcla entre el océano superficial y profundo...

... que es crucial para toda la vida en la Tierra.

¡Eres lo que comes!



Principalmente agua y carbono

Principalmente agua y carbono

Principalmente agua y carbono

## ***Appendix A.- Acronyms, abbreviations and symbols***

---

$\theta$ : potential temperature.

$\Omega$ : saturation states for calcium carbonate.

$\sigma_x$ : potential density referenced to “x” dbar.

$\sigma_{MOC}$ : potential density that constitutes the limit between the upper and lower limbs of the Meridional Overturning Circulation.

$\rho$ : in situ density.

$u$ : velocity orthogonal to the section.

$\Delta C_{ANT}$ : difference between the mean value of anthropogenic carbon dioxide in the upper and lower limbs of the Meridional Overturning Circulation.

$\Delta pH_{C_{ANT}}$ : pH change related to the uptake of anthropogenic  $CO_2$ .

$\Delta pH_{Var}$ : pH change not directly related to the uptake of anthropogenic  $CO_2$ .

$A_T$ : total alkalinity.

AABW: Antarctic Bottom Water.

ADCP: Acoustic Doppler Current Profiler.

AIW: Arctic Intermediate Water.

AMOC: Atlantic Meridional Overturning Circulation.

AOU: Apparent Oxygen Utilization.

$B(OH)_4^-$ : borate.

BOCATS: Biennial Observation of Carbon, Acidification, Transport and Sedimentation in the North Atlantic.

$C_{ANT}$ : anthropogenic carbon dioxide.

$C_T$ : total dissolved inorganic carbon.

$CaCO_3$ : calcium carbonate.

CARINA: CARbon dioxide IN the Atlantic Ocean.

CATARINA: CARbon Transport and Acidification Rates In the North Atlantic.

CCHDO: CLIVAR & Carbon Hydrographic Data Office.

CGFZ: Charlie–Gibbs Fracture Zone.

CH<sub>4</sub>: methane.

CLIVAR: Climate and Ocean: Variability, Predictability, and Change.

CNRS: Centre National de la Recherche Scientifique.

CO<sub>2</sub>: carbon dioxide.

CO<sub>3</sub><sup>2-</sup>: carbonate ion.

CRM: Certified Reference Material.

CSIC: Consejo Superior de Investigaciones Científicas.

CTD: Conductivity–Temperature–Depth.

DSOW: Denmark Strait Overflow Water.

DWBC: Deep Western Boundary Current.

EGC: East Greenland Current.

eMLR: extended Multiple Linear Regression.

ENA: East North Atlantic (Basin).

ENACW: East North Atlantic Central Water, subpolar (ENACW<sub>p</sub>) and subtropical (ENACW<sub>t</sub>) varieties.

ESM: Eriador Seamount.

GEOVIDE: An international GEOTRACES study along the OVIDE section in the North Atlantic and in the Labrador Sea.

GHG: greenhouse gas.

GLODAP: GLObal Data Analysis Project.

GOSHIP: Global Ocean Ship-based Hydrographic Investigations Project.

GSR: Greenland–Scotland Ridge.

H<sup>+</sup>: hydrogen ions.

HCO<sub>3</sub><sup>-</sup>: bicarbonate ion.

H<sub>2</sub>CO<sub>3</sub>: carbonic acid.

IAP: Iberian Abyssal Plain.

IFREMER: Institut Français de Recherche pour l'Exploitation de la MER.

IMBER: Integrated Marine Biogeochemistry and Ecosystem Research.

IOCCP: International Ocean Carbon Coordination Project.

IRD: Institut de Recherche pour le Développement.

ISOW: Iceland–Scotland Overflow Water.

$k_0$ : solubility constant of carbon dioxide.

$k_1^*$ : first equilibrium constant of dissociation of carbonic acid.

$k_2^*$ : second equilibrium constant of dissociation of carbonic acid.

$k_{sp}$ : solubility constant of calcium carbonate.

LADCP: Lowered Acoustic Doppler Current Profilers.

LDW: Lower Deep Water.

LEMAR: Laboratoire des sciences de l'Environnement MARin.

LSW: Labrador Sea Water, classical (cLSW) and upper (uLSW) varieties.

MAR: Mid-Atlantic Ridge.

MLR: Multiple Linear Regression.

MOC: Meridional Overturning Circulation.

MOC $\sigma$ : Meridional Overturning Circulation computed in density coordinates.

MW: Mediterranean Water.

N<sub>2</sub>O: nitrous oxide.

NAC: North Atlantic Current.

NACW: North Atlantic Central Water.

NADW: North Atlantic Deep Water.

NAO: North Atlantic Oscillation.

NASPG: North Atlantic Subpolar Gyre.

NEADW: North East Atlantic Deep Water, upper (NEADW<sub>U</sub>) and lower (NEADW<sub>L</sub>) varieties.

NO<sub>3</sub>: nitrate.

O<sub>2</sub>: oxygen.

O<sub>3</sub>: ozone.

OMP: Optimum MultiParameter (analysis), classical (cOMP) and extended (eOMP).

OVIDE: Observatoire de la Variabilité Interannuelle et DÉcennale en Atlantique Nord.

$p\text{CO}_2$ : partial pressure of  $\text{CO}_2$ .

PgC: Petagrams ( $10^{15}$  g) of carbon.

PIW: Polar Intermediate Water.

PNEDC: Programme National d'Etude de la Dynamique du Climat.

$\text{PO}_4$ : phosphate.

ppm: parts per million.

$r^2$ : correlation coefficient.

S: salinity.

SADCP: Shipboard Acoustic Doppler Current Profilers.

SAIW: Subarctic Intermediate Water.

$\text{SF}_6$ : sulphur hexafluoride.

$\text{SiO}_2$ : silicate.

SOLAS: Surface Ocean Lower Atmosphere Study.

SOMMA: Single-Operator Multiparameter Metabolic Analysers.

SPMW: Subpolar Mode Water, in the Iceland (IcSPMW) and Irminger (IrSPMW) Basins.

SPNA: Subpolar North Atlantic.

STD: standard deviation.

Sv: Sverdrup ( $1 \text{ Sv} = 10^6 \text{ m}^3 \cdot \text{s}^{-1}$ ).

SWT: Source Water Type.

$T_{\text{C}_{\text{ANT}}}$ : transport of anthropogenic carbon dioxide.

$T_{\text{C}_{\text{ANT}}}^0$ : estimator of the transport of anthropogenic carbon dioxide.

$T_{\text{C}_{\text{ANT}}}^{\text{diap}}$ : diapycnal transport of anthropogenic carbon dioxide.

$T_{\text{C}_{\text{ANT}}}^{\text{isop}}$ : isopycnal transport of anthropogenic carbon dioxide.

$T_{\text{C}_{\text{ANT}}}^{\text{net}}$ : net transport of anthropogenic carbon dioxide.

UBO: Université de Bretagne Occidentale.

V: transoceanic section velocity.

WEC: Western Boundary Current.

WEB: Western European Basin.

WNACW: West North Atlantic Central Water.

WOCE: World Ocean Circulation Experiment.

$X_i$ : fraction of a source water type in a water sample.





## Appendix B.- List of Tables

Table 1.- Hydrographic cruises. ....	62
Table 2.- Main properties of each of the Source Water Types (SWTs, see footnote a) considered in the study with their corresponding standard deviation. The weights of each equation are also given, together with the square of correlation coefficients ( $r^2$ ) between the observed and estimated properties, the Standard Deviation of the Residuals (SDR) and the SDR/ $\epsilon$ ratios from the data below 400 dbar. The $\epsilon$ used to compute the SDR/ $\epsilon$ ratios are the accuracies of the measured properties listed in section 4.4.2.2. The last column accounts for the uncertainties in the SWTs contributions. Values expressed on a per one basis. ....	65
Table 3.- List of selected hydrographic cruises (Figure 26). P.I. denotes principal investigator, and #St the number of stations selected. ....	93
Table 4.- Mean values $\pm$ standard deviation of pressure (in dbar), potential temperature ( $\theta$ , in $^{\circ}\text{C}$ ), salinity, Apparent Oxygen Utilization (AOU, in $\mu\text{mol}\cdot\text{kg}^{-1}$ ), total alkalinity ( $A_T$ , in $\mu\text{mol}\cdot\text{kg}^{-1}$ ), anthropogenic $\text{CO}_2$ estimated with the $\phi C_T^0$ method ( $C_{\text{ANT}}$ , in $\mu\text{mol}\cdot\text{kg}^{-1}$ ), pH in seawater scale at $25^{\circ}\text{C}$ ( $\text{pH}_{\text{SWS}_{25}}$ ), pH change not derived from the $C_{\text{ANT}}$ uptake ( $\Delta\text{pH}_{\text{Var}}$ ) and concentration of carbonate ions ( $[\text{CO}_3^{2-}]$ , in $\mu\text{mol}\cdot\text{kg}^{-1}$ ) for the bottom waters of the Iberian Abyssal Plain sampled during the OVIDE cruises. “n” represents the number of data considered in each cruise. ....	96
Table 5.- Temporal evolution (1981–2014) of the values (average $\pm$ standard deviation) of potential temperature ( $\theta$ , in $^{\circ}\text{C}$ ), salinity, Apparent Oxygen Utilization (AOU, in $\mu\text{mol}\cdot\text{kg}^{-1}$ ), salinity normalized total alkalinity ( $\text{NA}_T$ , in $\mu\text{mol}\cdot\text{kg}^{-1}$ ), anthropogenic $\text{CO}_2$ estimated with the $\phi C_T^0$ method ( $C_{\text{ANT}}$ , in $\mu\text{mol}\cdot\text{kg}^{-1}$ ), pH in seawater scale at $25^{\circ}\text{C}$ ( $\text{pH}_{\text{SWS}_{25}}$ ), pH change not derived from the $C_{\text{ANT}}$ uptake ( $\Delta\text{pH}_{\text{Var}}$ ) and saturation state of aragonite ( $\Omega_{\text{Arag}}$ ) for the water masses considered in the Iceland Basin (Table 5a) and the Irminger Basin (Table 5b). All values listed here were obtained by vertically and horizontally integrating each property within each water mass. $x\text{CO}_2$ represents the atmospheric $\text{CO}_2$ excess (in ppm) with respect to the preindustrial atmospheric $\text{CO}_2$ concentration (278.5 ppm). See water mass acronyms in Figure 27. ....	99
Table 6.- Long-term trends (1981–2014) of anthropogenic $\text{CO}_2$ estimated with the $\phi C_T^0$ method ( $C_{\text{ANT}}$ , in $\mu\text{mol}\cdot\text{kg}^{-1}$ ), parameter $C^*$ obtained with the $\Delta C^*$ method (in $\mu\text{mol}\cdot\text{kg}^{-1}$ ), saturation state of aragonite ( $\Omega_{\text{Arag}}$ ), pH in seawater scale at $25^{\circ}\text{C}$ ( $\text{pH}_{\text{SWS}_{25}}$ ), pH change related to the $C_{\text{ANT}}$ penetration ( $\Delta\text{pH}_{C_{\text{ANT}}}$ ) and pH change not derived from the $C_{\text{ANT}}$ uptake ( $\Delta\text{pH}_{\text{Var}}$ ) versus atmospheric $x\text{CO}_2$ excess (in ppm; difference between the atmospheric $\text{CO}_2$ concentration at the time of the cruise and the preindustrial atmospheric $\text{CO}_2$ concentration (278.5 ppm)) for the water masses considered in the Irminger and Iceland Basins. The column “Preindustrial” compiles the intercepts of the trends. See layer acronyms in Figure 27. ....	106
Table 7.- Estimations of transport of anthropogenic $\text{CO}_2$ ( $T_{C_{\text{ANT}}}$ ; in $\text{kmol}\cdot\text{s}^{-1}$ ) in the North Atlantic Ocean from literature. The $T_{C_{\text{ANT}}}$ is often given in $\text{PgC}\cdot\text{yr}^{-1}$ ( $1 \text{ Pg}\cdot\text{Cyr}^{-1} = 2642 \text{ kmol}\cdot\text{s}^{-1}$ ). ....	118
Table 8.- Hydrographic cruises. ....	120



## Appendix C.- List of Figures

- Figure 1.- At the top, monthly average instrument data for atmospheric carbon dioxide ( $\text{CO}_2$ ) mixing ratios determined from the continuous monitoring programs at the four Baseline Observatories of Barrow (cyan triangle), Mauna Loa (red dot), American Samoa (green square) and South Pole (purple inverted triangle). At the bottom, locations of the observatories. Modified from Tans (2012)..... 14
- Figure 2.- Scheme of the global carbon cycle. Numbers represent mass reservoirs in PgC (1 PgC =  $10^{15}$  gC) and annual carbon exchange fluxes (in PgC $\cdot\text{yr}^{-1}$ ). Black numbers and arrows indicate mass reservoirs and exchange fluxes estimated for the time prior to the Industrial Era (~1750). Red arrows and numbers indicate annual anthropogenic fluxes averaged over the 2000–2009 time period. These fluxes are a perturbation of the carbon cycle during Industrial Era (post 1750). The red arrows parts of Net land flux and Net ocean flux are the uptake of anthropogenic  $\text{CO}_2$  by the ocean and by terrestrial ecosystems (carbon sinks). Red numbers in the reservoirs denote cumulative changes of anthropogenic carbon over the Industrial Period 1750–2011. By convention, a positive cumulative change means that a reservoir has gained carbon since 1750. Uncertainties are reported as 90% confidence intervals. Source: Ciais et al. (2013)..... 15
- Figure 3.- A topographic and feature nomenclature map for the North Atlantic. The dotted white line between Greenland and Scotland represents the Greenland–Scotland Ridge. Modified from Schmithz and McCartney (1993)..... 16
- Figure 4.- Simplified sketch of the Meridional Overturning Circulation (MOC). The red lines represent the surface currents (MOC upper limb), and the blue and purple lines the deep and bottom currents (MOC lower limb), respectively. The black arrows indicate the direction of the circulation. The dark areas indicate high salinity waters ( $> 36$ ) and the white areas low salinity waters ( $< 34$ ). The yellowish circles indicate the main regions of deep water formation. Source: Bollmann et al. (2010). ..... 17
- Figure 5.- Surface circulation scheme. NEC and SEC denote the Northern and Southern Equatorial Currents, NEUC and NECC are the Northern Equatorial Under and Counter Currents, respectively. Source: Talley et al. (2011). ..... 19
- Figure 6.- Map of Absolute Dynamic Topography (in dynamic cm; colour shading) on September 21, 2011 for the western North Atlantic from AVISO (Archiving, Validation, and Interpretation of Satellite Oceanographic Data) Web site (<http://www.aviso.oceanobs.com>), with a scheme of the currents in the Gulf Stream System, including the Northern and Southern Recirculation gyres (NRG and SRG). Source: Imawaki et al. (2013)..... 20
- Figure 7.- Topographic map of the Nordic Seas and subpolar basins with schematic circulation of surface currents (solid curves) and deep currents (dashed curves) that form a portion of the Atlantic Meridional Overturning Circulation. Colours of curves indicate approximate temperatures. Source: R. Curry, Woods Hole Oceanographic Institution/Science/USGCRP. .... 22
- Figure 8.- Potential temperature ( $^{\circ}\text{C}$ ) vs. salinity for the Atlantic Ocean. Colours indicate the latitude range. Data are from the World Ocean Circulation Experiment (1988–1997). Contours are potential density referenced to 0 dbar. Acronyms indicate the principal water masses: Antarctic Bottom Water (AABW), Antarctic Intermediate Water (AAIW), Denmark Strait Overflow Water (DSOW), Iceland–Scotland Overflow Water (ISOW), Labrador Sea Water (LSW), Mediterranean Water (MW), North Atlantic Deep

- Water (NADW), North East Atlantic Deep Water (NEADW) and Subtropical Underwater (STUW). Source: Talley et al. (2011)..... 24
- Figure 9.- Scheme showing the regional climatic impacts of the positive (left) and negative (right) phases of North Atlantic Oscillation (NAO). Surfaces mark sea surface temperatures and sea ice extension, arrows show the flow systems in ocean, atmosphere and rivers, blue and red lines indicate near-surface sea-level pressures and white rectangles describe characteristic climate conditions or important processes. Source: Fletcher (2005). ..... 28
- Figure 10.- Bjerrum plot showing the relative proportions of  $[\text{HCO}_3^-]$ ,  $[\text{CO}_3^{2-}]$  and  $[\text{CO}_2]$  to the total dissolved inorganic carbon in seawater at different salinities (S), temperatures (T), and pressures (P) (heavy curves are for S = 35, T = 25°C, P = 0 dbar; narrow curves are S = 35, T = 0°C, P = 0 dbar; dashed curves are S = 35, T = 0°C, P = 3000 dbar). The shaded region reflects the range of modern ocean surface (annual average), with the hashed region reflecting the corresponding projected year 2100 range taken from the global ocean geochemistry model projections of Turley et al. (2010). Modified from Barker and Ridgwell (2012). ..... 32
- Figure 11.- Effect of various processes on total dissolved inorganic carbon ( $C_T$ ) and total alkalinity ( $A_T$ ) at 1 atm, 15°C and salinity of 35. Solid lines indicate levels of constant dissolved  $\text{CO}_2$  (in  $\mu\text{mol}\cdot\text{kg}^{-1}$ ) and dashed lines indicate levels of constant pH as a function of  $C_T$  and  $A_T$ . Modified from Zeebe and Wolf-Gladrow (2001)..... 33
- Figure 12.- The geographical distribution of the Revelle factor in ocean surface waters in 1994, averaged for the upper 50 m of the water column. Source: Sabine et al. (2004)..... 34
- Figure 13.- Global ocean surface average of atmospheric partial pressure of  $\text{CO}_2$  ( $p\text{CO}_2$ ) (left) and pH at Seawater Scale ( $\text{pH}_{\text{sws}}$ ) (right). Source: Turley et al. (2010). ..... 36
- Figure 14.- The climatological mean distribution of aragonite saturation level ( $\omega$ ) in the global ocean surface water in August for the reference year 2005. The pink curves indicate the positions of the mean equatorward front of seasonal ice fields. The “+” symbol indicates the box areas affected by the El Niño events, and no value is given. The boxes with black dots indicate transition zones between oceanographic regimes (such as subtropical to subpolar regimes), where the  $\omega$  values are highly variable. These values are interpolated from the adjacent box values. Note that the Arctic Ocean is slightly undersaturated ( $\omega < 1$ ), whereas the seasonal ice zone in the Southern Ocean is 10% to 20% above the saturation. Source: Takahashi et al. (2014). ..... 37
- Figure 15.- Cruises conducted in the North Atlantic Ocean included in the international database CARINA (CARbon dioxide IN the Atlantic Ocean). Source: <http://cdiac.ornl.gov/oceans/CARINA>. ..... 47
- Figure 16.- Repeated sections conducted in the North Atlantic Ocean included in the international database CCHDO (CLIVAR and Carbon Hydrographic Data Office). Source: <http://cchdo.ucsd.edu>. ..... 48
- Figure 17.- Location of the 4x and OVIDE hydrographic stations and major topographical features of the Subpolar North Atlantic. .... 49
- Figure 18.- Location of the 4x and OVIDE hydrographic stations plotted on bathymetry (500 m intervals). The North Atlantic circulation scheme, the major topographical features of the Subpolar North Atlantic, as well as the main water masses are also shown: East Greenland Current (EGC), West Greenland Current (WGC), Labrador Current (LC), Deep Western Boundary Current (DWBC), North Atlantic Current (NAC), Denmark Strait Overflow Water (DSOW), Iceland–Scotland Overflow Water (ISOW), Labrador Sea Water (LSW), Mediterranean Water (MW), North East Atlantic Deep Water (NEADW), Charlie–Gibbs Fracture Zone (CGFZ), Bight Fracture Zone (BFZ), Mid-Atlantic Ridge

- (M.A.R.) and Iberian Abyssal Plain (I.A.P.). Schematic diagram of the large-scale circulation compiled from Schmitz and McCartney (1993), Dengler et al. (2006), Schott and Brandt (2007, Plate 1), Sutherland and Pickart (2008, Figure 16), Lherminier et al. (2010, Fig. 1b) and Sarafanov et al. (2012)..... 61
- Figure 19.- Mean (a) potential temperature ( $\theta$ ), (b) salinity, (c) oxygen, (d) nitrate, (e) silicate and (f) phosphate along the OVIDE section, from the Iberian Peninsula (right) to Greenland (left)..... 64
- Figure 20.- (A) Potential temperature ( $\theta$ )/Salinity (S)-diagram including the Source Water Types (Table 2) used in the analysis and (B) zoomed for bottom waters. The mixing figures are shown in the (C) legend (see Table 2 for the acronyms of the source water types). The isopycnals referenced in the chapter are also plotted, i.e.,  $\sigma_1 = 32.15$  and  $\sigma_1 = 32.42$  (where is  $\sigma_1$  potential density referenced to 1000 dbar)..... 65
- Figure 21.- Total residual from the extended Optimum MultiParameter (eOMP) analysis (a) and individual residuals from each eOMP equation (see Eq. 4.2): (b) potential temperature ( $\theta$ , in °C) and salinity (S); (c) silicate ( $\text{SiO}_2$ ) and nitrate ( $\text{NO}_3$ ) (both in  $\mu\text{mol}\cdot\text{kg}^{-1}$ ); and (d) phosphate ( $\text{PO}_4$ ) and oxygen ( $\text{O}_2$ ) (both in  $\mu\text{mol}\cdot\text{kg}^{-1}$ )..... 72
- Figure 22.- Water mass distributions of the mean result for the OVIDE sections (2002–2010), from the Iberian Peninsula (right) to Greenland (left). The water mass contributions are expressed on a per unit basis (see Table 2 for the acronyms of the source water types). The dashed horizontal lines represent isopycnals:  $\sigma_1 = 32.15$  (plot a), which marks the limit between the upper and lower limb of the Atlantic Meridional Overturning Circulation; and  $\sigma_1 = 32.42$  (very similar to  $\sigma_0 = 27.8$ ; plot e), which marks the lower limit of Labrador Sea Water (LSW) on the classic works and approximately crosses the potential temperature/salinity definition of the source water type for LSW (Figure 20a).  $\sigma_1 = 32.42$  has the advantage of not varying rapidly in the eastern half of the sections..... 74
- Figure 23.- Water mass distributions along the WOCE A25 sections, from 1997 (4x section, upper plots) to 2010 (OVIDE section, lower plots), from the Iberian Peninsula (right) to Greenland (left). The water mass contributions are expressed on a per unit basis. Note that  $\text{SPMW} = \text{IrSPMW} + \text{IcSPMW}$ . The dashed white line on the DSOW plots represents the limit of the PIW contributions (5% isoline) (see Table 2 for the acronyms of the source water types)..... 78
- Figure 24.- Net water mass volume transports perpendicular to the OVIDE section for the mean result of the period (2002–2010). Transports (in Sv;  $1 \text{ Sv} = 10^6 \text{ m}^3\cdot\text{s}^{-1}$ ) are positive northwards (see Table 2 for the acronyms of the source water types)..... 81
- Figure 25.- Schematic diagram of the water mass circulation, transformation and transports in the North Atlantic Subpolar Gyre, based on a two-layer box model in between the OVIDE section and the Greenland–Iceland–Scotland sills (GISS). The transports (in Sv;  $1 \text{ Sv} = 10^6 \text{ m}^3\cdot\text{s}^{-1}$ ) at the southern boundary are the mean transports across the OVIDE sections as obtained in the present study. The transports at the northern boundary (GISS) are defined as explained in section 4.7. The boundary between the western (East North Atlantic (ENA) Basin) and eastern (Irminger Basin) boxes is the Reykjanes Ridge (RR). RR is closed (open) for the deep (upper-ocean and mid-depth) circulation. The diapycnal volume fluxes (crossed and point circles) and the transports across the RR are inferred from the condition of volume conservation. The uncertainties are shown in grey. Note that CW accounts for Central Waters, AW for Atlantic waters (see Table 2 for the acronyms of the source water types) and I.P. for Iberian Peninsula. .... 84
- Figure 26.- Tracks of the twelve cruises of seawater  $\text{CO}_2$  system measurements used in this study (1981–2014). The black line represents the boundary between the Irminger and the

Iceland Basins constituted by the Reykjanes Ridge. CGFZ = Charlie-Gibbs Fracture Zone.  
 ..... 93

Figure 27.- Limits of the layers and basins considered in this study plotted on the mean salinity of the sections. The boundary isopycnals are represented in potential density ( $\sigma$ , in  $\text{kg}\cdot\text{m}^{-3}$ ), and the vertical white line represents the limit (Reykjanes Ridge) between the Irminger (left) and Iceland Basins (right). The acronyms of the layers account for: Subpolar Mode Water (SPMW), upper and classical Labrador Sea Water (uLSW and cLSW, respectively), Iceland–Scotland Overflow Water (ISOW) and Denmark Strait Overflow Water (DSOW)..... 97

Figure 28.- Mean properties for the studied period (1981–2014) along the cruise track, from Greenland (left) to the Iceland Basin (right): (a) Potential temperature ( $\theta$ , in  $^{\circ}\text{C}$ ), (b) salinity, (c) Apparent Oxygen Utilization (AOU, in  $\mu\text{mol}\cdot\text{kg}^{-1}$ ), (d) total alkalinity ( $A_T$ , in  $\mu\text{mol}\cdot\text{kg}^{-1}$ ), (e) pH in seawater scale at  $25^{\circ}\text{C}$  ( $\text{pH}_{\text{sws}}$ ), (f) anthropogenic  $\text{CO}_2$  estimated with the  $\phi C_T^0$  method ( $C_{\text{ant}}$ , in  $\mu\text{mol}\cdot\text{kg}^{-1}$ ), (g) pH change not derived from the  $C_{\text{ant}}$  uptake ( $\text{pH}_{\text{var}}$ ) and (h) saturation of  $\text{CaCO}_3$  in terms of aragonite ( $\Omega_{\text{arag}}$ ). ..... 101

Figure 29.- Temporal evolution between 1981 and 2014 of the average values of (a and b) Salinity and (c and d) Apparent Oxygen Utilization (AOU, in  $\mu\text{mol}\cdot\text{kg}^{-1}$ ) in main water masses of the Irminger (a and c) and Iceland (b and c) Basins. Each point represents the average property of a particular water mass (SPMW (red dots), uLSW (blue dots), cLSW (black dots), ISOW (green dots) and DSOW (magenta dots)) at the time of each cruise (Table 5). The error bars represent the error of the mean. The inset boxes give the trends  $\pm$  standard error of the estimate and the correlation coefficients ( $r^2$ ). \*\* denotes that the trend is statistically significant at the 95% level (p-value < 0.05). See water mass acronyms in Figure 27..... 102

Figure 30.- Temporal evolution between 1981 and 2014 of the average salinity normalized total alkalinity ( $NA_T$ , in  $\mu\text{mol}\cdot\text{kg}^{-1}$ ) values in main water masses of the Irminger (a) and Iceland (b) Basins. Each point represents the average  $NA_T$  of a particular water mass (SPMW (red dots), uLSW (blue dots), cLSW (black dots), ISOW (green dots) and DSOW (magenta dots)) at the time of each cruise (Table 5). The error bars represent the error of the mean. The inset boxes give the trends  $\pm$  standard error of the estimate and the correlation coefficients ( $r^2$ ). \* denotes that the trend is statistically significant at the 90% level (p-value < 0.1), \*\* at the 95% level (p-value < 0.05), and \*\*\* at the 99% level (p-value < 0.01). See water mass acronyms in Figure 27. .... 103

Figure 31.- Temporal evolution between 1981 and 2014 of the average values of (a and b) anthropogenic  $\text{CO}_2$  estimated with the  $\phi C_T^0$  method ( $C_{\text{ANT}} - \phi C_T^0$ , in  $\mu\text{mol}\cdot\text{kg}^{-1}$ ) and (c and d) the parameter  $C^*$  obtained with the  $\Delta C^*$  method (in  $\mu\text{mol}\cdot\text{kg}^{-1}$ ) in main water masses of the Irminger (a and c) and Iceland (b and c) Basins. Each point represents the average property of a particular water mass (SPMW (red dots), uLSW (blue dots), cLSW (black dots), ISOW (green dots) and DSOW (magenta dots)) at the time of each cruise (Table 5). The error bars represent the error of the mean. The inset boxes give the trends  $\pm$  standard error of the estimate and the correlation coefficients ( $r^2$ ). \*\*\* denotes that the trend is statistically significant at the 99% level (p-value < 0.01). See water mass acronyms in Figure 27..... 105

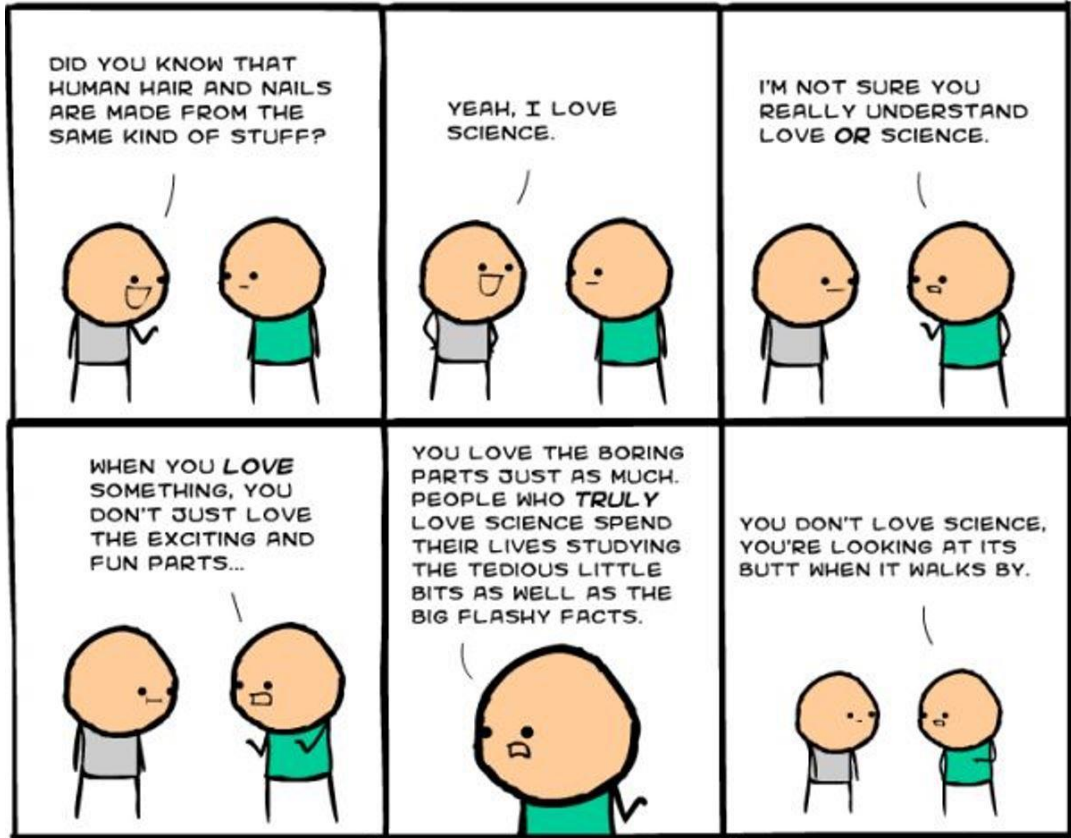
Figure 32.- Temporal evolution between 1981 and 2014 of the average values of (a and b) pH in seawater scale at  $25^{\circ}\text{C}$  ( $\text{pH}_{\text{sws}25}$ ) and (c and d) pH change derived from the uptake of anthropogenic  $\text{CO}_2$  ( $\text{pH}_{C_{\text{ant}}}$ ) in main water masses of the Irminger (a and c) and Iceland (b and c) Basins. Each point represents the average property of a particular water mass (SPMW (red dots), uLSW (blue dots), cLSW (black dots), ISOW (green dots) and DSOW (magenta dots)) at the time of each cruise (Table 5). The error bars represent the error of the mean. The inset boxes give the trends  $\pm$  standard error of the estimate and the



- correlation coefficients ( $r^2$ ). \*\* denotes that the trend is statistically significant at the 95% level (p-value < 0.05), and \*\*\* at the 99% level (p-value < 0.01). See water mass acronyms in Figure 27. .... 108
- Figure 33.- Temporal evolution between 1981 and 2014 of the average pH change not derived from the uptake of anthropogenic  $\text{CO}_2$  ( $\text{pH}_{\text{var}}$ ) values in main water masses of the Irminger (a) and Iceland (b) Basins. Each point represents the average  $\text{pH}_{\text{var}}$  of a particular water mass (SPMW (red dots), uLSW (blue dots), cLSW (black dots), ISOW (green dots) and DSOW (magenta dots)) at the time of each cruise (Table 5). The error bars represent the error of the mean. The inset boxes give the trends  $\pm$  standard error of the estimate and the correlation coefficients ( $r^2$ ). \* denotes that the trend is statistically significant at the 90% level (p-value < 0.1), \*\* at the 95% level (p-value < 0.05), and \*\*\* at the 99% level (p-value < 0.01). See water mass acronyms in Figure 27..... 109
- Figure 34.- Temporal evolution between 1981 and 2014 of the average saturation of  $\text{CaCO}_3$  in terms of aragonite ( $\Omega_{\text{Arag}}$ ) values in main water masses of the Irminger (a) and Iceland (b) Basins. Each point represents the average  $\Omega_{\text{Arag}}$  of a particular water mass (SPMW (red dots), uLSW (blue dots), cLSW (black dots), ISOW (green dots) and DSOW (magenta dots)) at the time of each cruise (Table 5). The error bars represent the error of the mean. The inset boxes give the trends  $\pm$  standard error of the estimate and the correlation coefficients ( $r^2$ ). \* denotes that the trend is statistically significant at the 90% level (p-value < 0.1), \*\* at the 95% level (p-value < 0.05), and \*\*\* at the 99% level (p-value < 0.01). See water mass acronyms in Figure 27..... 111
- Figure 35.- Schematic circulation in the North Atlantic Ocean. The main pathways of warm and salty waters originating from the Subtropical Atlantic Ocean are shown in red lines while the deep currents are displayed in dark blue. The cyan lines represent the fresh and cold currents over the shelves (Eastern Greenland Coastal Current (EGCC) and Labrador Current (LC)). The grey lines indicate the spreading of the Labrador Sea Water (LSW). The hydrographic stations of the OVIDE and 4x (FOUREX) sections are represented with black dots. The other abbreviations are DSOW = Denmark Strait Overflow Water, ISOW = Iceland–Scotland Overflow Water, WBC = Western Boundary Current, NAC = North Atlantic Current, GS = Gulf Stream, ESM = Eriador Seamount, and IAP = Iberian Abyssal Plain. .... 119
- Figure 36.- OVIDE sections of 2002 and 2010 of (a, d) potential temperature in  $^{\circ}\text{C}$ , (b, e) salinity and (c, f) anthropogenic  $\text{CO}_2$  (CANT) in  $\mu\text{mol}\cdot\text{kg}^{-1}$ . The isopycnals referenced in the chapter are plotted in all the figures; their specific values are indicated in (b) and (e). All the water masses cited in the chapter are localized in the section in (c) and (f): DSOW = Demark Strait Overflow Water, ISOW = Iceland–Scotland Overflow Water, LSW = Labrador Sea Water, MW = Mediterranean Water, AABW = Antarctic Bottom Water. The other abbreviations in (a) and (d) are RR = Reykjanes Ridge, ESM = Eriador Sea Mount and ABR = Azores–Biscay Ridge. The numbers at the top of each plot indicate the station numbers..... 121
- Figure 37.- Transport of anthropogenic  $\text{CO}_2$  ( $T_{\text{cant}}$ ; in  $\text{kmol}\cdot\text{s}^{-1}$ ) (black) and its components (diapycnal in blue, isopycnal in red and net in green) across the A25 section as a function of time. The dashed grey line is the  $T_{\text{cant}}$  due to the Ekman transport, which is dispatched between the other three components. The cyan lines are the mean value (2002–2006) and the error bars of the  $T_{\text{cant}}$  representative of the mid-2000s..... 125
- Figure 38.- Transport of anthropogenic  $\text{CO}_2$  ( $C_{\text{ant}}$ ) caused by the isopycnal component ( $T_{\text{cant}}^{\text{isop}}$ ) averaged over time. (A) The  $T_{\text{cant}}^{\text{isop}}$  (in  $\text{kmol}\cdot\text{s}^{-1}$ ) accumulated from the bottom to each specific density level. (B) The  $T_{\text{cant}}^{\text{isop}}$  horizontally accumulated from Greenland to each station along the section, and vertically integrated for the whole water column

(continuous line) and for waters denser than  $\sigma_1 = 32.14$  (dashed line). (C) On the left axis: isopycnal volume transport (in Sv; where  $1 \text{ Sv} = 10^6 \text{ m}^3 \cdot \text{s}^{-1}$ ) accumulated from Greenland to each station, and vertically integrated for the whole water column (continuous black line) and for waters denser than  $\sigma_1 = 32.14$  (dashed black line). On the right axis: mean value of Cant anomalies vertically averaged all along the section (grey line; in  $\mu\text{mol} \cdot \text{kg}^{-1}$ ). (D) The  $T_{\text{cant}}^{\text{isop}}$  horizontally but not vertically integrated (see Figure 35 for the abbreviations). Note that in plots (A) and (D) the vertical axes do not have the same scale. .... 127

- Figure 39.- The diapycnal component of the transport of anthropogenic  $\text{CO}_2$  ( $T_{\text{cant}}^{\text{diap}}$ ) and the different elements by which it was computed (see Eq. 6.7). (A) Profile of anomalies of volume transport (in Sv) integrated into density ( $\sigma_1$ ) layers with a  $0.01 \text{ kg} \cdot \text{m}^{-3}$  resolution. (B) Mean profile of anthropogenic  $\text{CO}_2$  ( $C_{\text{ant}}$ ; in  $\mu\text{mol} \cdot \text{kg}^{-1}$ ) averaged at each density layer. (C)  $T_{\text{cant}}^{\text{diap}}$  profile (in  $\text{kmol} \cdot \text{s}^{-1}$ ). All the data represented in this figure are the averages of the six surveys analysed in the present study. In the formulation,  $S$  means the area of each density layer along the section and replaces the overbar given in Eq. (6.7), since there is no vertical integration in the data displayed in the figure. .... 128
- Figure 40.- (A) Time evolution of the intensity of the Meridional Overturning Circulation computed in density coordinates ( $\text{MOC}\sigma$ , in green; in Sv) and the difference in anthropogenic  $\text{CO}_2$  ( $C_{\text{ant}}$ ) between the upper and lower limbs of the  $\text{MOC}\sigma$  (delta Cant, in pink; in  $\mu\text{mol} \cdot \text{kg}^{-1}$ ). (B) Time evolution of the transport of  $C_{\text{ant}}$  ( $T_{\text{cant}}$ ; black line), the diapycnal transport of  $C_{\text{ant}}$  ( $T_{\text{CANT}}^{\text{diap}}$ ; blue line) and the Tcant computed by the estimator ( $T_{\text{CANT}}^0$ ; cyan line) (all in  $\text{kmol} \cdot \text{s}^{-1}$ ). (C) Time evolution of anomalies of the Tcant (black line), the  $T_{\text{CANT}}^{\text{diap}}$  (blue line), the  $T_{\text{CANT}}^0$  (cyan line) in relation to the mean value computed over 1997–2010 (all in  $\text{kmol} \cdot \text{s}^{-1}$ ). .... 130
- Figure 41.- Time evolution of anthropogenic  $\text{CO}_2$  ( $C_{\text{ant}}$ ) concentrations (in  $\mu\text{mol} \cdot \text{kg}^{-1}$ ): upper limb of the Meridional Overturning Circulation computed in density coordinates ( $\text{MOC}\sigma$ ; black circles), section average value (grey circles), and lower limb of the  $\text{MOC}\sigma$  (triangles). .... 131



Cyanide and Happiness © Explosm.net



Cyanide and Happiness © Explosm.net